NORTHWESTERN UNIVERSITY

Recent Stress History Effects on Compressible Chicago Glacial Clay

A DISSERTATION

SUBMITTED TO THE GRADUATE SCHOOL

IN PARTIAL FULFILLMENT OF THE REQUIREMENTS

for the degree

DOCTOR OF PHILOSOPHY

Field of Civil Engineering

By

Wan Jei Cho

EVANSTON, ILLINOIS

June 2007

ABSTRACT

Recent Stress History Effects on Compressible Chicago Glacial Clay

Wan Jei Cho

In urban areas, an accurate evaluation of ground deformations from various construction activities requires one to properly consider both the probable ground strain level under expected working conditions and the recent stress history of the soil. For well-designed projects, the levels of ground strains typically are less than 0.5%, emphasizing the need to investigate soil behavior at small strains. This dissertation presents the results and analysis of a laboratory investigation of the very small, small and large strain behaviors of compressible, lightly overconsolidated Chicago glacial clays.

Triaxial tests were performed with bender elements and local LVDTs on high quality block samples taken from an excavation in Evanston, IL. Results of two types of drained stress probe tests with different pre-shear stress paths, "post-K_0" and "post-unloading" probes, are compared in terms of general stress-strain, modulus degradation, and directional stiffness dependence to investigate the effects of recent stress history. Stress probes also were performed on specimens of the same clay reconstituted in a slurry consolidometer. Results were presented in terms of Strain Response Envelopes (SRE) to illustrate the directional dependence.

Based on comparisons of the stress-strain data and moulus degradation curves of the two types of stress probe tests, the effects of recent stress history were apparent not only in shear and volumetric responses, but also in the cross-coupling between the shear and volumetric responses.

The significant variability of the shear, bulk and cross-coupling moduli with stress path direction and strain level shown in the SREs provide experimental evidence that the Chicago clays are incrementally nonlinear.

Results of tests conducted with three sets of bender elements show that compressible Chicago glacial clay is a cross-anisotropic material. An empirical correlation was established based on the elastic shear stiffness from bender element tests, "$G_{BE,}$" during K_0-reconsolidation. By comparing the empirical correlation with the measured G_{BE} in the stress region during probing, the deviation of G_{BE} from values computed by the empirical relation directly relates to the yielding characteristics of the clay. Also, the shear modulus based on the shear wave velocity in axial direction agrees well with the field measured shear wave velocity by seismic CPT tests and the modulus from shear stress unloading types of stress paths in triaxial tests.

Results of reconstituted samples can be used to investigate the effective stress at failure conditions of compressible Chicago clays, but the overall softer stress-strain responses, bender element results and smaller yield surface of the reconstituted samples suggest that reconstituted specimen behavior does not represent that of high quality natural samples of compressible Chicago glacial clays.

Acknowledgement

First, I would like to thank my dissertation advisor, Professor Richard Finno for giving me the opportunity to come to Northwestern University and conduct research in geotechnical engineering. His insight and advice was invaluable to my research and I appreciate his guidance, encouragement during this process. I would also like to thank Professors Charles H. Dowding and Raymond J. Krizek, members of my dissertation committee, for their valuable advice, comments, and good conversation. Also, I want to express my appreciation to Professors Choong-ki Chung, Myoung Mo Kim and Junbum Park at Seoul National University, for bring up my interests in soil mechanics and geotechnical engineering.

I would like to thank Terrence Holman for his lessons in the laboratory work. I learned a lot from him not only in the laboratory work but also staying in the United States. Without his help and advice, it would be much harder to learn how to perform TX tests and make the second TX systems.

Also, my gratitude extends to my fellows during Ph.D course, Jill Roboski, Tanner Blackburn, Laura Sullivan, Xuxin Tu, Luke Erickson, Izzat Katkuhda, Greg Andrianis and Brandon Hughes for their cares, understanding and friendships.

I would like to show my "*agradecimiento*" to my friend, "Dr." Cecilia Rechea Bernal for her friendship and help. In my entire stay in US, she was like my sister and it was a real pleasure to work, play and have a trip with her. Also, I want to express my "*επαύξηση*" to my fellow greek, Miltos Langousis for adding bright colors in my grey life. It was a wonderful experience

spending time with him in and out of the laboratory and my Ph.D work became much more enjoyable and delightful because of him.

My very special and great thanks should be given to my "crushers," Luke Erickson, Miltos Langousis, Izzat Katkuhda and Taesik Kim for their dust-breathing, back-hurting and time-taking crushing work at the basement. With their great efforts, I could make the "reconstituted samples," which are apparently not remolded samples.

I would like to thank my Korean friends, Young-hoon Jung, Taesik Kim, Namhong Min and Sangwon Lee for sharing their feelings and ideas not only in the academic research but also "Life in US." I have met so many great people during my stay at Seoul National University and Northwestern University. I really appreciate their friendships and cares and I hope this relationship continues.

I also thank my girl friend, future wife Yeonjoo for her thoughtful and endless supports and all other things she has done for me. I hope she can also finish her Ph.D work nice and smooth soon so that she can join the Ph.D club.

I don't know how I could express all my appreciation to my mother, brother and grandmother. Without their support and love, I could not even think about starting my Ph.D work. Also, I would like to thank my new family members, my sister-in-law and nephew. And lastly I would like to dedicate this thesis to my father.

TABLE OF CONTENTS

LIST OF FIGURES

LIST OF TABLES

CHAPTER 1 INTRODUCTION

An accurate evaluation of ground deformations from various construction activities requires one to properly consider the probable ground strain level under expected working conditions. Except in cases where the excessive deformation induces the failure in the ground, the levels of ground strains associated with the safe design of a structure typically is less than 0.5%, emphasizing the need to investigate soil behavior at small strains. Therefore, the understanding of small strain behavior is a key element to the successful design and the analysis of soil deformations under working conditions.

When analyzing effects of construction in urban areas where the ground experiences applied stresses other than that from one dimensional deposition, one of the important factors affecting the small strain behavior, "recent stress history," becomes more critical. Consequently, the effect of recent stress history on small strain response of soils has been studied rather extensively over the last 20 years. Unfortunately, conflicting experimental results on this subject have been reported based on studies of a number of clays, including London, Bothkennar and Gault clays. Furthermore, no studies have been performed on freshwater, lightly overconsolidated clays, such as the compressible Chicago glacial clays.

The objective of this thesis is to provide detailed experimental results of the general, axisymmetric stress-strain behavior of compressible Chicago clays. Tests were conducted on block samples taken from an excavation in Evanston, IL. The experiments were designed to develop data not only related to the small strain response, but also to the large strain responses embodied in yield, and failure criteria. The experiments were designed to investigate stiffness directionality, current stress path dependency and pre-shear stress path dependency. In addition,

the stress-strain responses of the samples reconstituted from cuttings and spent block samples, are compared to that of the natural block samples to evaluate the acceptability of using reconstituted samples in lieu of the more difficult to obtain block samples. Data from this thesis can be used to develop constitutive models that describe the incrementally nonlinear behavior of this clay.

This dissertation presents the results and analysis of a laboratory investigation of the very small, small and large strain behaviors of compressible, lightly overconsolidated Chicago glacial clays. The laboratory testing program incorporates two types of drained directional stress probing tests; one is designed for the investigation of general behavior of *in-situ* soils and involves 10 different stress paths, including many commonly encountered effective stress paths and the other is designed specifically to investigate recent stress history effects, involving 5 different stress paths. Stress probing tests were conducted on high quality block samples using bender elements and local LVDTs to measure the very small and small strain response. Six stress probes were performed on reconstituted specimens of the same clay created in a slurry consolidometer.

Chapter 2 summarizes the previous experimental research on small strain behavior of cohesive soils. It explains why small strain stiffness and the effects of recent stress history became major topics of interest. The laboratory and field measurement devices which can measure small strain responses are summarized. The factors affecting small strain stiffness are summarized including disturbance, current stress, stress history and creep and ageing. In particular, previous research on recent stress history effects are discussed in detail.

Chapter 3 presents a detailed description of the experimental program to characterize the small strain response of compressible Chicago glacial clays. The sources of the natural block and

reconstituted samples are discussed. The equipment used to measure small strain responses, bender elements for very small strains and sensitive subminiature LVDTs for small to large strains, is described with emphasis on the accuracy, precision and data analysis. The experimental procedures are summarized, including specimen preparation and mounting, residual effective stress measurement, K_0 reconsolidation and creep, and triaxial stress probing. Data analysis methods also are described.

Chapter 4 presents an analysis of the general stress-strain data in terms of shear, volumetric and cross coupling behaviors. Stress probe tests in this chapter are based on specimens that are K_0-consolidated to the *in-situ* vertical effective stress of the block samples. These results are thought to represent *in-situ* behavior. These stress probes are called "post-K_0" probes. Specimen behavior prior to and during K_0 reconsolidation and creep also is described as a function of the residual effective stresses, saturation strains, reconsolidation strains and creep stress paths. A study on the effects of swelling during saturation in triaxial tests in clays is included separately in Appendix A. Directional responses are discussed with respect to the stress-strain gradients at very small, small and large strains. Modulus degradation curves are presented for each stress probe. Directional stiffness diagrams are created from the degradation curves, and the dependence of the shear and bulk moduli on stress probe direction is discussed. Strain response envelopes are developed that graphical analysis of the general stiffness behavior can be performed on the stress-strain response to investigate the stiffness evolution based on strain level. The limit state points are determined for each stress probe and compared to strain energy contour.

In Chapter 5, the results of the stress probing tests which were conducted of the unloading from the K_0-condition, herein called "post-unloading" probes, are analyzed and

compared to quantify recent stress history effects. The responses are extensively compared in the context of deviatoric, volumetric and cross coupling behaviors. Directional stiffness diagrams are created from the degradation curves, and the dependence of the shear and bulk moduli on stress probe direction with respect to recent stress history are discussed. Strain response envelopes are generated for the data set to describe the material stiffness and nonlinearity in general terms.

Chapter 6 presents results of the bender element tests performed on natural specimens during K_0 reconsolidation, creep, and directional stress probing. The empirical relationship between the stress state and the dynamic shear moduli is established based on the bender element test results. The limit state obtained from the bender element tests is compared with that based on the stress-strain data presented in Chapter 4. The anisotropy ratio during K_0 reconsolidation and the evolution of the anisotropy during shearing are presented. Dynamic shear stiffness reflected in the bender element results is compared with in-situ sCPT test results and the mechanical shear stiffness obtained from the stress-strain data.

Chapter 7 compares the experimental responses of the reconstituted samples with that of natural samples in terms of index properties, stress history, residual effective stress, K_0 consolidation behavior and stress-strain responses during shear. Stress-strain data are compared in terms of shear, bulk and cross coupling responses. Modulus degradation and stress paths dependency of reconstituted samples also are discussed. Relationships between dynamic modulus and effective stress for reconstituted samples are developed and compared to those for natural samples presented in Chapter 6. Limit states and the failure conditions of the natural and reconstituted samples also are compared.

Chapter 8 presents a summary of the dissertation and its conclusions.

CHAPTER 2 EFFECTS OF RECENT STRESS HISTORY ON SMALL STRAIN BEHAVIOR

Field measurements of the ground behavior caused by construction of a number of types of structures highlighted the importance of accurately simulating the behavior of soils at small strains. Consequently, there has been various research that focused on the small strain stiffness and the factors that influence the responses of different geomaterials. In particular, the previous research on the small strain stiffness of cohesive materials is the focus of this chapter. Section 2.1 summnarizes the beginnings of small strain research. This section shows why small strain stiffness became a major topic of interest and also why the recent stress history became an issue in this research. Section 2.2 describes the laboratory or field measurement devices which can measure small strain responses. In particular, emphasis is placed on the devices applied in this experimental program, bender elements and the on-specimen measurement systems. Previous research on the comparisons between the laboratory and field measurements is presented. Section 2.3 summarizes previous research on the factors affecting small strain stiffness, including disturbance, current stress, stress history and creep and ageing. Section 2.4 deals solely with the recent stress history effects. Finally, Section 2.5 summarizes the previous research on small strain stiffness and effects of recent stress history.

2.1. SMALL STRAIN STIFFNESS

It is well known that detailed information on the highly non-linear stress-strain behavior of the ground is crucial to make realistic predictions for the displacements induced by excavations, tunnels and foundations in different types of soils (e.g. Burland 1989, Jardine et al. 1991;

Atkinson 2000). Case studies on a variety of examples derived from field measurements or based on analytical predictions demonstrate the predominance of small-strain deformations within the affected soil. Based on these previous studies, it was concluded that most of the overall ground movement at typical working loads is developed within regions of the ground where the major principal strain ranges between 0.001% and 0.5% (Jardine 1995). Furthermore, inverse-analyses of foundation settlements and deep excavations have also indicated that shear strain levels in the soils surrounding adequately performing structures are typically less than 0.1% (Burland 1989).

Numerical modeling and finite element analysis are becoming more commonly employed for deformation estimates of deep excavations, foundations, tunnels, cut slopes, and embankments. The strengths of the finite element method as a tool for geotechnical deformation analysis are its ability to simultaneously model complex geometries, boundary and loading conditions, loading and unloading processes and fluid flow. One major weakness of the finite element method is rooted in the constitutive models used to mathematically describe the stress-strain-strength behavior of geomaterials. Constitutive models generally require significant numbers of parameters and numerous assumptions about the soil behavior in order to provide convenient mathematical formulations for inclusion into computer codes. The majority of the available constitutive models does not account for the small strain-level dependent nature of soil stiffness and as a result, commonly overpredict ground deformations within some portion of a deforming soil mass.

Furthermore, the parameters used in numerical modeling are based on common laboratory test results, where tangent and secant moduli are estimated in the strain range of 0.1 to

2%. As a result, use of laboratory-determined moduli values for predictions is one of the primary causes for overestimation of deformations.

However, recent advances in soil testing have resulted in new capabilities for investigating stiffness at small strains. Probing tests with triaxial cells fitted with both local strain instrumentation and multi-directional bender elements allow both static and dynamic test probes to be performed and offer the possibility of measuring all the terms in an initial elastic stiffness matrix. The understanding and consideration of the small strain non-linearity enhanced the predictive capabilities of a constitutive model for soil (e.g., Whittle and Hashash 1995; Atkinson 2000).

As the interest in the small strain stiffness grew, there have been many attempts to investigate the factors that can affect the small strain stiffness (e.g., Atkinson and Sallfors, 1991; Tatsuoka et al., 1997; Santagata et al., 2005). Sample disturbance, current stress state and stress history, stress path direction and reversals, anisotropy, and aging/creep have been shown to be factors that influence very small and small strain moduli parameters most significantly, and are discussed hereafter.

2.1.1. Ground strain induced under working conditions

Burland (1989) detailed a series of case histories in the United Kingdom in which soil and rock moduli were back-calculated from observed settlements of large foundations and deformations around deep supported excavations. Burland (1989) indicated that the initial interest in small strain behavior resulted from the higher obeserved stiffness and lower strains generated during full scale footing and plate load tests on weathered Chalk. The small strain modulus of London clay, a heavily overconsolidated deposit, was evaluated in light of small foundation settlements

and deep excavation ground movements. The result of these initial studies was a realization that the ground strain levels were significantly less than expected, and that, conversely, the moduli were much greater that predicted.

The measured or calculated ground strain levels surrounding foundations and retaining structures are typically less than predicted by analytical, empirical, or finite element methods. This behavior is intimately related to the mobilization of very high moduli in the field and is thought to be a primary reason for the overprediction of vertical settlements at some distances behind deep excavations. Figures 2-1 and 2-2 present calculated shear strain distributions behind real and finite element model deep excavations in stiff London Clay. Figure 2-3 demonstrates the differences between finite element-predicted ground settlement distributions and measured values for a 19 m deep secant pile excavation in London Clay (Hight and Higgins, 1995). Figure 2-4 illustrates similar behavior for a tunnel excavated through stiff clay for which non-linear constitutive models were employed to predict the deformation profile.

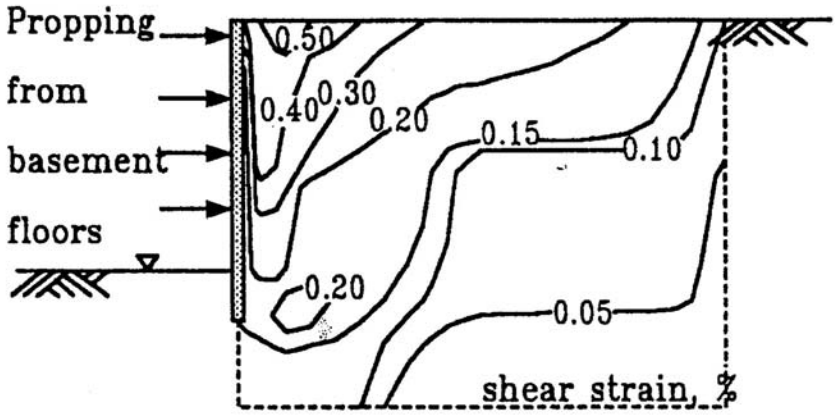

Figure 2-1 Shear strain distribution behind deep excavation with four basement levels (Atkinson and Sallfors, 1991)

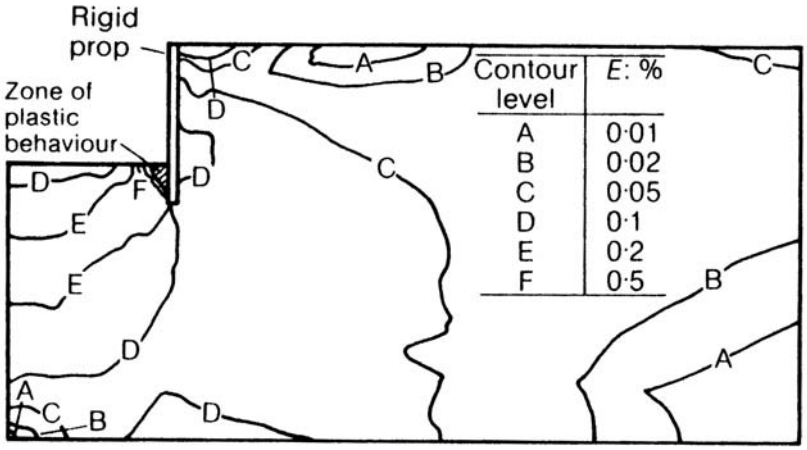

Figure 2-2 Finite element predictions of deviatoric strain distribution behind 15 m deep excavation (Jardine et al, 1986)

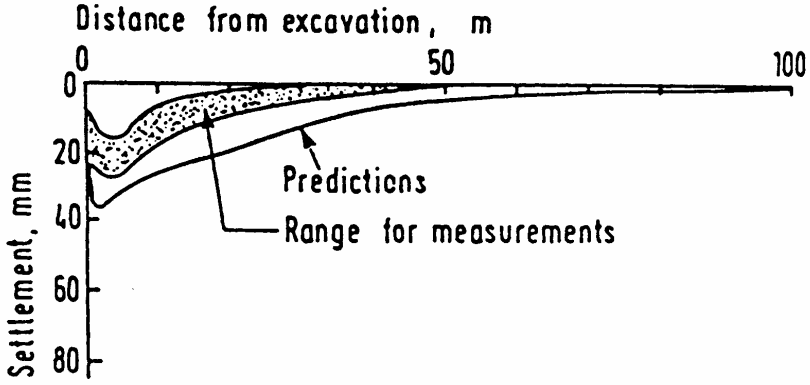

Figure 2-3 Predicted versus measured ground surface settlement profile behind a 19 m deep excavation (Hight and Higgins, 1995)

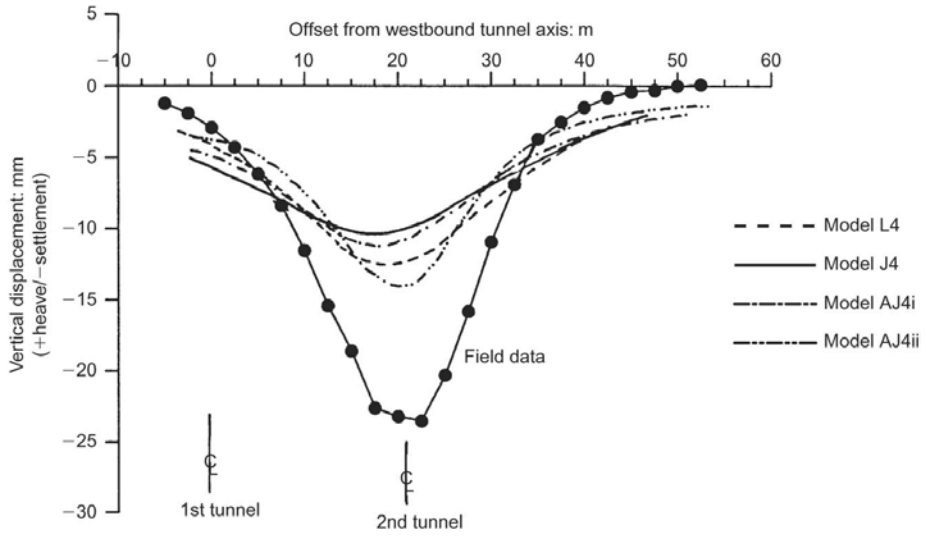

Figure 2-4 Measured displacement profile over tunnel in stiff clay versus predicted profile using nonlinear constitutive models (Addenbrooke et al, 1997)

Examination of Figures 2-1 and 2-2 and many of the case histories presented by Burland (1989) suggest that the mobilized strains beneath foundations and around deep excavations are typically less than 0.2%. Somewhat higher strains may be observed immediately beneath shallow foundations or immediately adjacent to deep excavations due to high local shear stresses and development of limited plastic failure zones. The strains appear to decrease with distance away from the excavation wall. Tunneling may induce higher shear strains (up to 1%) in the overlying soils because of poor workmanship, overexcavation, and stress redistribution and yielding of tunnel supports. The displacement fields presented in Figures 2-3 and 2-4 demonstrate that the predicted deformation distribution is dissimilar to that measured in the field. It is of great interest that the measured distributions show a more rapid decrease with distance from the excavation or tunnel than the predictions. One reason for the difference between measured versus predicted settlement profiles is the mobilization of high soil stiffness at low strains. A comparative chart of mobilized shear strains versus type of structure is presented in

Figure 2-5. The strain measurement capabilities for conventional triaxial tests are also included in the graph.

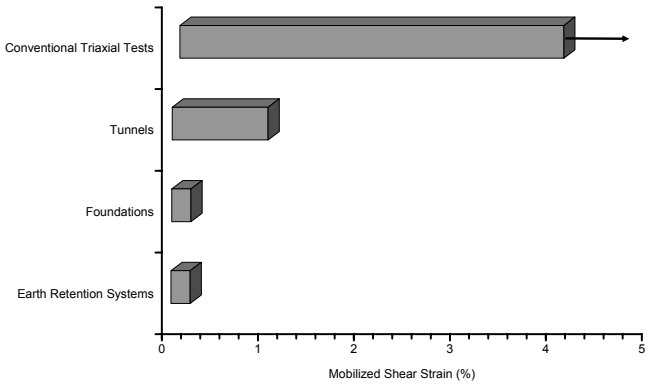

Figure 2-5 Comparative plot of typically mobilized shear strains around structures (adapted from Atkinson, 2000)

The ranges of mobilized strains in Figure 2-5 are applicable to foundations, tunnels, and earth retention systems that have not undergone deformations resulting in loss of serviceability. It is most interesting to note that conventional triaxial testing can only begin to accurately measure strains at about 0.1 to 0.2%. This is widely believed a result of bedding errors and limitations of the conventional external instrumentation employed to measure axial and radial displacements and vertical loads (Scholey et al, 1995).

2.1.2. Strain Levels and Characteristics

The initial field and laboratory work on small strain behavior of soils resulted in the realization that the stiffness behavior of soils under static loading could be classified according to strain levels. Atkinson and Sallfors (1991) divided strain levels into three categories: Very Small Strains (VSS), Small Strains (SS), and Large Strains (LS), as delineated in Table 2-1.

Table 2-1 Strain level categories and limits (after Atkinson and Sallfors, 1991)

Strain Category	Strain Limits (%)
Very Small Strain (VSS)	<0.001
Small Strain (SS)	0.1 to 0.001
Large Strain (LS)	>0.1

The delineation of the upper boundary of very small strains as 0.001% was based on the assumption that strains below this value could only be induced by geophysical means, and stress-strain properties can be reliably measured above this value using mechanical means. The stress-strain behavior is thought to be linear elastic in the Very Small Strain range. Upon reaching a strain level threshold value near 0.001%, the stress-strain behavior becomes markedly nonlinear and the secant and tangent moduli begin to degrade in a hyperbolic fashion with increasing strain. This behavioral zone is designated as Small Strain and terminates at a strain of about 0.1%. The onset of Large Strain behavior occurs at about 0.1%, marking the zone where the secant and tangent moduli become relatively small, and the soil begins to approach failure. Soil moduli in the LS range may be only 10 to 20% of that in the VSS region. Figure 2-6 depicts the idealized shear modulus degradation behavior of real soils based on the strain levels given in Table 2-1. Ishihara (1996) also suggested similar categories of the shear strains in terms of the mechanical states of soils. Infinitesimal strains where the strain range below the order of 0.001%, are defined exactly same as Very Small Strain range in Table 2.1. The soil deformation in this region is purely elastic and recoverable. The second zone is intermediate strains (0.01% ~ 1%) where the behavior of soils is elasto-plastic and the irrecoverable permanent deformation and dilation begin to appear. And the large strains is defined as the strains exceeding a few percent where failure takes place in the soils.

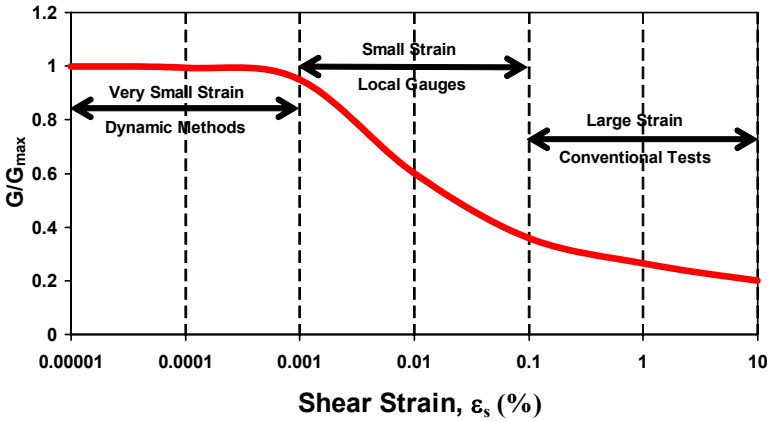

Figure 2-6 Idealized modulus degradation behavior (after Atkinson and Sallfors, 1991)

The stiffness characterization based on the strain level might not be applicable to all soils because the range of linear elastic zone, for example, can be larger than 0.001% in soft rocks and very stiff clays and there is little physical meaning in the large strain limit for these materials.

Another interpretation of these behaviors is the kinematic strain-hardening plasticity framework suggested by Jardine (1995). In his model, two kinematic surfaces were defined, named Y_1 and Y_2, existing within the conventional main yield surface, termed Y_3. A schematic diagram of this model is shown in Figure 2-7. Within the zone limited by the Y_1 surface the soil response is linear elastic and the strains are fully recoverable. In general, the size of Y_1 for soft soils is extremely small in stress space and the corresponding strain level is less than 0.001% which is smaller than the reliable range of strains obtained by the on-specimen instrumentation. The Y_2 surface corresponds to the contour of a zone beyond which the strain increment vector may change direction and the rate of plastic strain development accelerates. It has been speculated that this surface corresponds to the limit beyond which particle contacts fail and particle movements occur. The conventional yield surface Y_3 represents the current bounding

surface. The zone between Y_2 and Y_3 shows highly non-linear stress-strain response, significant irrecoverable plastic straining and continuous degradation of mechanical properties.

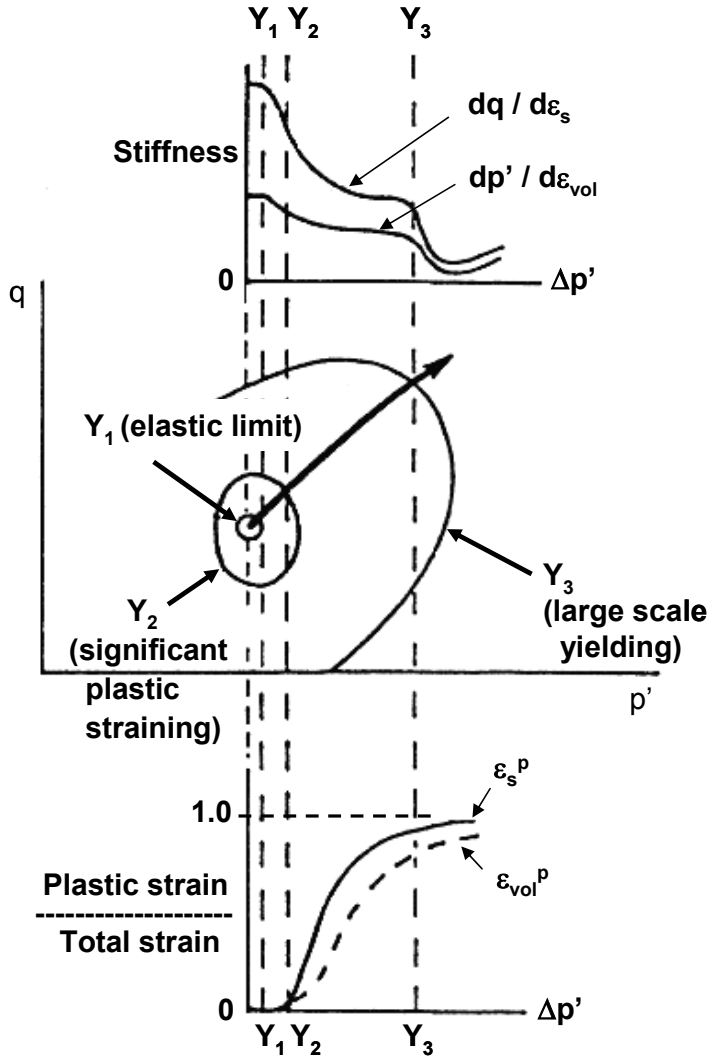

Figure 2-7 Scheme of multiple yield surfaces (Jardine, 1995)

The terminology in Table 2-1 is employed to describe the range of strains in this thesis.

Figure 2-8 presents actual undrained Young's modulus degradation behavior of soft marine clay from the Bothkennar test site in the United Kingdom (Heymann et al, 2000), including an expanded view of the stress-strain behavior at small strains. Figure 2-8 shows

clearly the degradation of secant Young's modulus with increasing axial strain under undrained triaxial compression loading, as well as a zone of apparent constant modulus at small strains. The data below about 0.005% show a trend of constant modulus followed by a 75% decrease in modulus up to an axial strain of 1%. Although not corresponding exactly to the characterstics of Atkinson and Sallfors (1991), the general trend of initial linear portion at modulus degradation conforms reasonably well to the previously-mentioned conceptual model.

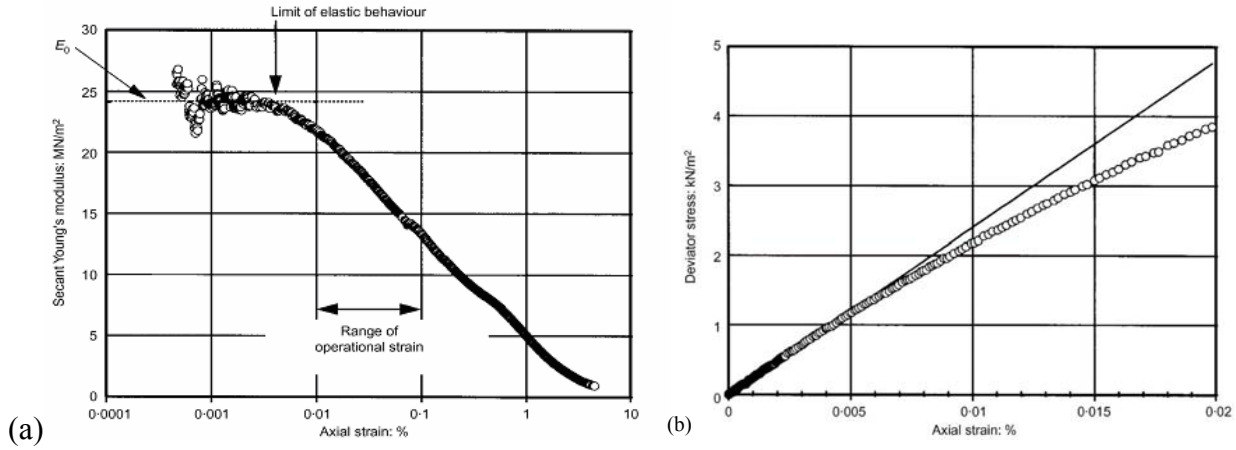

Figure 2-8 (a) Modulus degradation curve for soft Bothkennar Clay in undrained triaxial compression, (b) Stress-strain data at small strain levels (Matthews et al, 2001)

The interesting characteristics of modulus degradation curves are found from stress probing tests. Smith et al (1992) presented triaxial testing results for a stress probing program on lightly overconsolidated natural clay indicating that the shear and bulk modulus degradation varied with stress path direction. Amorosi et al (1999) also found that for active and passive stress paths typical of idealized excavations (i.e. reduced triaxial compression (RTC) and reduced triaxial extension (RTE)), the secant shear modulus degradation for reconstituted clays was different for the two stress path directions. Modulus degradation curves for normally consolidated specimens tested for RTC and RTE stress paths are shown in Figure 2-9a. The

active stress path resulted in a relatively less stiff response than the passive stress path. The overconsolidated specimens shown in Figure 2-9b indicate stiffer behavior for the active (A) tests than for the passive (P) tests.

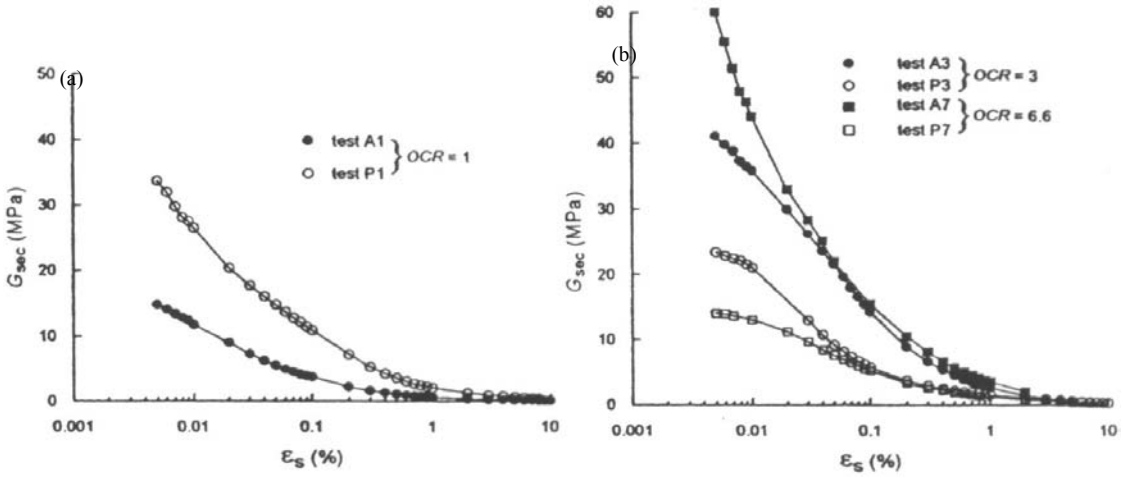

Figure 2-9 Secant shear stiffness for active and passive triaxial tests on reconstituted specimens of (a) normally consolidated clay, (b) overconsolidated clay (Amorosi et al, 1999)

2.1.3. Recent Stress History

As mentioned in the previous section, the modulus degradation characteristics depend on the previous stress path direction and current path direction. Atkinson et al. (1990) found that the stress-strain behavior of overconsolidated clays was influenced by the recent stress history, which was defined in terms of the angular difference between a new stress path direction and the previous path direction. Through a series of experiments involving constant deviatoric stress q and constant mean normal effective stress p', the gradient of the stress strain curves was determined to be different depending on the recent stress history, indicating that the modulus degradation behavior is also different. In particular, Atkinson et al. (1990) concluded that complete stress reversals yielded the stiffest soil response, while continuations of the previous

stress path direction resulted in the softest soil response. Also, the influence of the rotation angle was not distinguishable after 0.5% strain where all the curves converged into a unique value. Figure 2-4 presents plots of gradient versus strain for the constant q tests for stress path rotations of 0°, ±90°, and 180°, illustrating the stiff response generated by the stress path reversal.

The various experimental results will be further discussed in Section 2.4 because there have been conflicting results on the stress path dependency and recent stress history effects since the work of Atkinson et al. (1990).

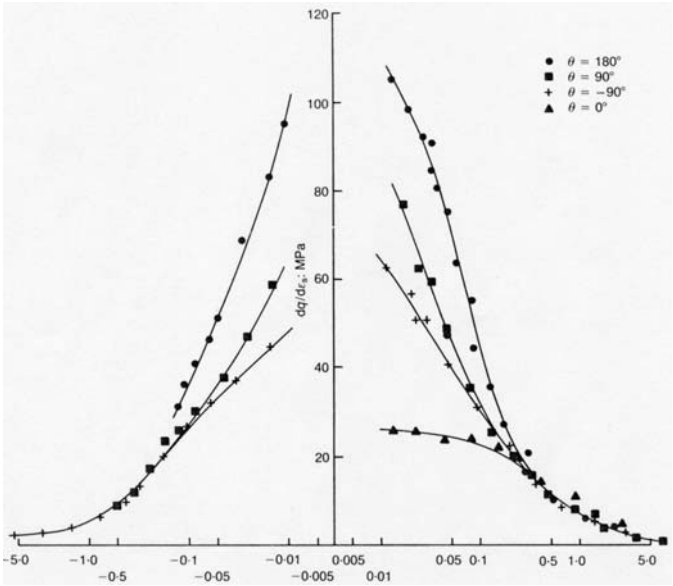

Figure 2-10 Gradient dq/dε_s versus ε_s for constant q triaxial tests (Atkinson et al. 1990)

2.2. MEASUREMENT OF SOIL MODULI

As discussed in section 2.1, there is strong evidence in the literature that the investigation of the small strain behavior of soils is important for the prediction of ground movements and the interpretation of field data. However, the stiffness values obtained from the laboratory were

consistently smaller than the values measured in situ or back calculated from the field movements. This discrepancy was contributed to the effects of sampling disturbance (e.g. Lambe and Whittman 1967, Burland 1989).

Due to the on-specimen instrumentation techniques for triaxial systems developed in early 1980's, there has been a major improvement in laboratory stiffness measurement (Burland and Symes 1982, Costa Filho 1985). It was found that the discrepancy of the stiffness value between the laboratory and field measurement is also due to bedding errors occurring at the end platens. Furthermore, the employment of bender element in a triaxial system can close the gap between the field measurement and laboratory measurement of the stiffness in the very small strain range.

2.2.1. Laboratory tests

There are many types of laboratory equipment to investigate stiffness of the soil in small strain regions. Those devices can be categorized as either static or dynamic tests. Dynamic tests use fast and cyclic loading conditions where the mass of the soil element cannot be neglected and acceleration of the soil mass is a key controlling factor. In dynamic tests, the stiffness of the soil is determined by the dynamic properties of the specimen or the system including the specimen. For example, dynamic properties in bender element tests are shear wave velocities within a specimen and the resonant frequency of the specimen and driving apparatus in a resonant column test. Both resonant column and bender element tests apply cyclic loading of the soil at significantly higher strain rates than those in static tests. Static tests are defined as those in which monotonic or cyclic loading is applied at a rate slow enough that the effects of inertia can be ignored (Woods 1991). The most commonly used static tests to investigate the stiffness in small

strain range are the triaxial and the torsional shear tests. Of these tests, bender element tests and triaxial tests with on-specimen instrumentation will be described in more detail.

2.2.1.1. Bender elements

Investigation of soil stiffness in the very small strain range ($\varepsilon<0.001\%$) is typically accomplished through wave propagation techniques. Bender element (BE) systems are employed to measure wave propagation velocity as a function of stress state and path because bender elements offer a relatively simple non-destructive method for estimating the elastic modulus of soils. Their main advantage is that they allow multiple measurements on the same specimen under a range of tests conditions, i.e. during consolidation and shearing.

Bender elements are piezoceramic electro-mechanical transducers capable of converting electrical energy into mechanical movement and vice versa. A bender element consists of two piezoceramic plates bonded together in series or parallel with a brass electrode plate in between (Dyvik and Madshus, 1985). They typically are mounted in the base pedestal and top cap of a triaxial cell and act as miniature cantilever beams. When excited by an input voltage, the source element bends, emitting a horizontally polarized wave, assumed to be a shear wave, which travels through the soil sample at an assumed shear wave velocity V_s. The wave motion causes the receiver element to mechanically vibrate, inducing a voltage signal that is captured by an oscilloscope or high-speed digital data acquisition system. The shear wave velocity is calculated by determining the travel time of the shear wave between the tips of the source and receiver elements. The very small strain shear modulus, G_{max}, is then calculated using the one-dimensional wave propagation relationship:

$$G_{\max} = \rho V_s^2 \tag{2-1}$$

where ρ is the mass density of the sample and V_s is the shear wave velocity. Since the shear modulus is direct function of shear wave velocity, the travel distance and the travel time for the velocity are the key parameters to be determined reliably. Viggiani and Atkinson (1995) concluded from several tests on triaxial samples of different heights that the tip to tip distance between the bender elements was the most adequate measure of travel distance. Brignoli et al. (1996) supported the use of tip to tip distance based on laboratory measurements using both conventional bender elements and non-penetrating shear plates.

Methods of estimating the shear wave travel time from the input and receiver signals include 1) first arrival, 2) first significant peak, and 3) cross-correlation analysis. Methods 1 and 2 rely on visual interpretation of the waveform, while Method 3 is a digital signal processing method that relies on numerical integration of a time-shifted signal to determine the shift that causes the maximum amplitude of a cross-correlation function. The selection of wave travel time by Methods 1 and 2 can introduce errors up to 20% in G_{max} (Viggiani and Atkinson, 1995a).

Initially, a square wave was used as the transmitted signal. Typical oscilloscope signals from bender element tests with a square pulse excitation are shown in Figure 2-11. The point of transmission of the shear wave is very clear, but the arrival at the receiving element is not, because of the near field effect (Viggiani and Atkinson 1995) by which the true arrival time of the shear wave is mixed by the arrival of the by-product compressive wave.

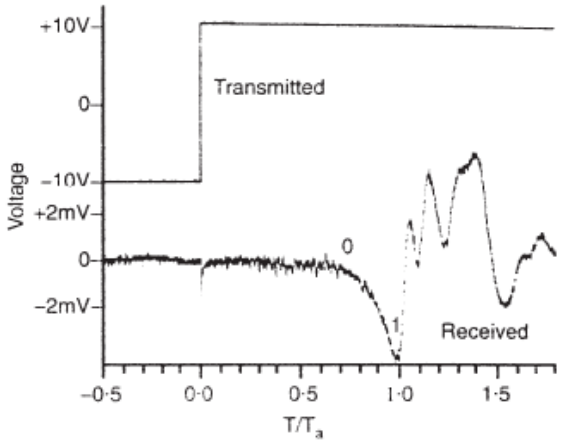

Figure 2-11 Typical response of square wave (Rolo 2003)

Viggiani and Atkinson (1995) suggested using a sine pulse wave to reduce the subjectivity in the interpretation of the square wave, because the square wave is composed of a spectrum of different dominant frequencies which results in the near field effect. Furthermore, the use of sinusoidal excitation of the source bender element reduces the near field effects and enables the application of simple, yet accurate, methods of interpretation, such as the cross correlation technique.

With regard to the frequency of the shear wave, the use of relatively high frequency waves was desirable since the near field effect was reduced and error in the interpretation methods was minimized (Viggiani and Atkinson 1995; Brignoli and Gotti 1992). It was proved both numerically and experimentally that near field effects are attenuated with distance and number of wavelengths (higher frequencies imply more wavelengths) suggested that the optimum number of wavelengths was around 4 to 5 (Jovicic et al. 1996; Brignoli et al. 1996).

This frequency dependency of the bender element tests results is suggested by research at Northwestern University. The theoretical group wave velocity based on the numerical solutions,

assuming a specimen is a wave guide, is dispersive and frequency-dependent (Wang 2004). Based on these results, the propagation velocity being measured during a bender element test does not necessarily correspond to that of a shear wave, except within a relatively narrow range of non- dimensional frequency Ω ($=2\pi fr/V_s$, where f is frequency, r is the cylinder radius and V_s is the true shear wave velocity) from 1.25 to 2.5.

One important consideration to bear in mind is that the voltage is a direct consequence of the displacement of the tip of the element. Kuwano (1999) estimates that the output voltage of 1 to 10 mV represents a displacement of the receiving element of the order of 0.0015 to 0.0025 μm for the bender element of 13 mm in length and 3 mm penetration into soil. This in turn represents a shear strain between 1.5 to 2.0×10^{-4}% at the receiver element and between 3 to 7×10^{-2}% at the source element. This indicates that the input amplitude should be carefully chosen not to exceed the elastic range of the material.

Common bender element orientations in the triaxial test apparatus produce shear waves that propagate vertically within the sample, but are polarized in the horizontal direction to measure G_{vh}, commonly thought of as G_{max} as shown in Figure 2-12. Natural soils, especially soft normally consolidated to lightly overconsolidated clays, are inherently anisotropic due to depositional history and induced stresses. The measurement of G_{vh} is not sufficient to describe the complete stiffness behavior for a cross-anisotropic soil. The bender element method can be used to evaluate the anisotropy in shear stiffness, as the bender element orientations can be changed to induce shear waves that propagate in the horizontal direction. The shear moduli in the horizontal plane, G_{hh} and G_{hv}, can be evaluated by mounting bender elements on the side of a

specimen as shown in Figure 2-12 or cutting horizontal samples from blocks (Jovicic and Coop, 1998; Pennington et al, 1997).

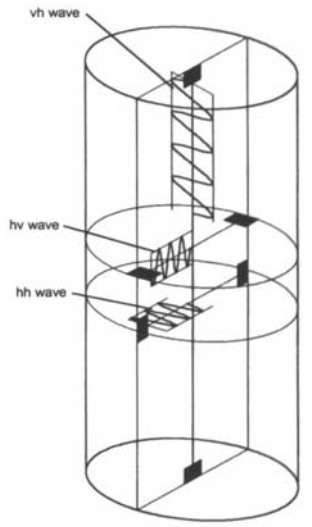

Figure 2-12 Bender element wave propagation and polarization directions for triaxial specimens (Callisto and Rampello, 2002)

2.2.1.2. On-specimen instrumentation (Internal measurement)

Investigation of the small strain behavior of soils in the triaxial apparatus requires on-specimen measurement of the strains. Accurate small strain moduli estimations cannot be made using externally measured axial and radial displacements because of a multitude of experimental errors, including seating, alignment, bedding, and compliance errors (Scholey et al, 1995). While conventional systems with external measuring devices can provide reliable estimates of the stiffness, at best, for strains larger than 0.05~0.1%, significant advances have been made by using devices such as proximity sensors, miniature LVDT and local deformation transducers mounted directly on the specimen. Accurate strain measurement can be made from strains on the order of 0.001% to failure.

Figure 2-13 shows the results of some unconsolidated undrained tests on London clay in which locally measured strains are compared with globally-measured strains (Costa Filho and Vaughan 1980). Local measurement gave much larger stiffness because they were not affected by the above mentioned errors. Therefore, local measurements of axial and radial strain are required over the middle one-third of the specimen to make accurate estimations of small strain moduli and degradation behavior in the triaxial apparatus.

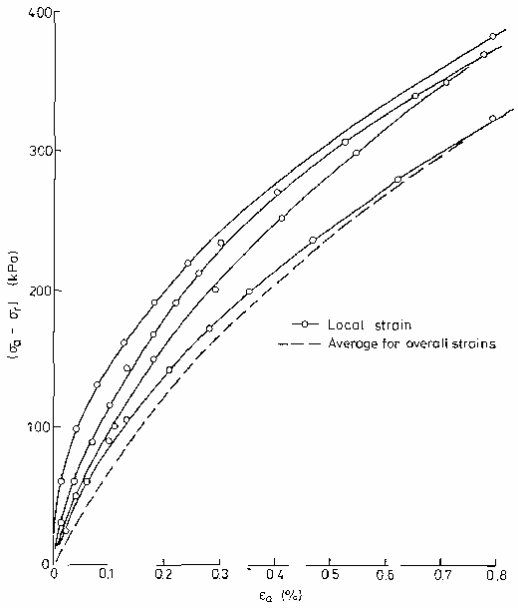

Figure 2-13 Comparison between local measurement and overall strain measurement (Costa Filho and Vaughan 1980)

Axial and radial strains can now be measured directly on a triaxial sample rather than from external gauges. Since the early 1980s, a number of systems have been developed to make local displacement measurements inside the triaxial cell. Earlier types of LVDTs were used but found to be too cumbersome and inaccurate, and were followed by electrolevel inclinometer gauges (Jardine et al, 1984), Hall Effect gauges (Clayton and Khatrush, 1986), and local displacement transducers (Goto et al, 1991). With advances in transducer technology, data

acquisition systems, and calibration methods, LVDTs became the gauge of choice for local strain measurements. LVDTs have infinite electrical resolution, high accuracy/linearity, and are now very compact and lightweight. Miniature LVDTs available on the commercial market are easily capable of accurate displacement measurements of 5 μm, data acquisition system resolution on the order of 0.003% of full scale, with overall strain accuracies of 0.01% or better. Additional accuracy and resolution can be achieved by more detailed calibration (Clayton et el, 1997) or specially-designed data acquisition systems (Da Re et al, 2001).

For the accurate measurement of axial and radial measurement, there have also been also efforts to improve the configuration of the measurement devices. For axial measurements, Santagata (2005) used the extension of the LVDT cores and Kevlar string to hang the cores inside the LVDT body to allow free movement of the core in the transducer and reduce stick-slip problems at extremely small displacements as shown in Figure 2-14(a). As a result, axial strain can be accurately measured less than 0.0001%.

For radial strain measurement, Kuwano (2000) used a LVDT installed in rectangular frame as shown in Figure 2-14 (b). The LVDT is supported by a rectangular frame and the frame and the armature rod of the LVDT are glued onto the membrane. The radial caliper proposed by Bishop and Henkel (1957) is commonly used for its simple design and easy installation (Figure 2-14 (c)). The measurement occurs right in the middle of the specimen to be relatively free from the end restraint errors. Based on their research, these two different frames of the radial strain measurement do not seem to affect the accuracy of the radial strain. The accuracy of the radial strain measurement solely depends on the accuracy of the measuring gage.

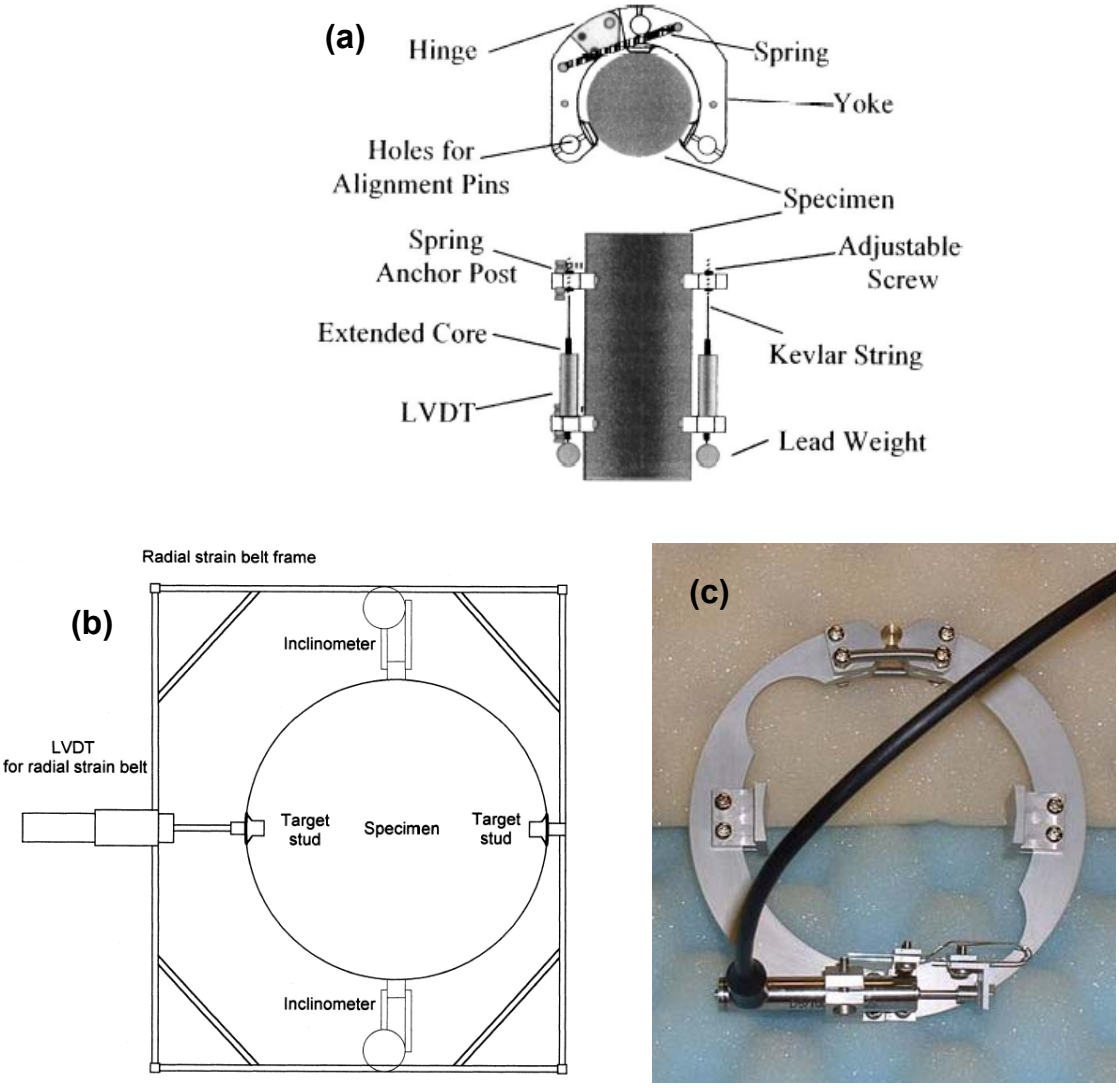

Figure 2-14 Configuration of axial and radial measurement device: (a) Hanging LVDTs (Santagata 1998), (b) Radial strain belt frame (Kuwano 2000), (c) Radial caliper designed by Bishop and Henkel (1957) (Holman 2003)

2.2.2. Field Tests

Field tests to obtain the stiffness of the ground can be categorized as two types; conventional methods and geophysical method. Conventional in-situ test results can be correlated to large strain measurements with a moderate degree of certainty. For example, conventional Cone Penetration test results can be correlated to constrained moduli (Lunne et al, 1997). Menard-type

or Self Boring Pressuremeter tests can be employed to give estimates of the initial or unload-reload shear modulus at varying small to large strain levels (Mair and Wood, 1987). Self-Boring Pressuremeter tests provide more reliable large strain moduli measurements, and may be used to estimate moduli in the upper end of the small strain range (near 0.1%) in some geomaterials (Fahey, 1999).

On the other hand, in-situ tests that use geophysical techniques to measure shear wave propagation can evaluate the very small strain shear stiffness. The induced strain level is comparable to that in bender element tests. Two methods can be employed to measure G_{max} in the field are the Seismic Cone Penetration Test (SCPT) and the Cross Hole Seismic Test (CHST) (Sully and Campanella 1995). The SCPT is conducted using a conventional 10 or 15 cm^2 piezocone fitted with one or more accelerometers. Shear waves are introduced into the ground from surface impacts (downhole test) and the travel times are measured based on wave arrivals at the accelerometers, as shown in Figure 2-11. Preferably, the true travel time will be estimated between two accelerometers approximately 1 m apart in the cone to eliminate dependence on trigger sensitivity. Stiffness anisotropy cannot be measured with the conventional downhole SCPT. CHST involves transmission of shear waves between three parallel boreholes and measurement of travel times between the source and two receivers. The source and receiver are typically located at the same depth and can be oriented to measure anisotropy of G_{max} in the horizontal plane. The SCPT is preferred for the advantage of the conventional field test and additional information of seismic properties.

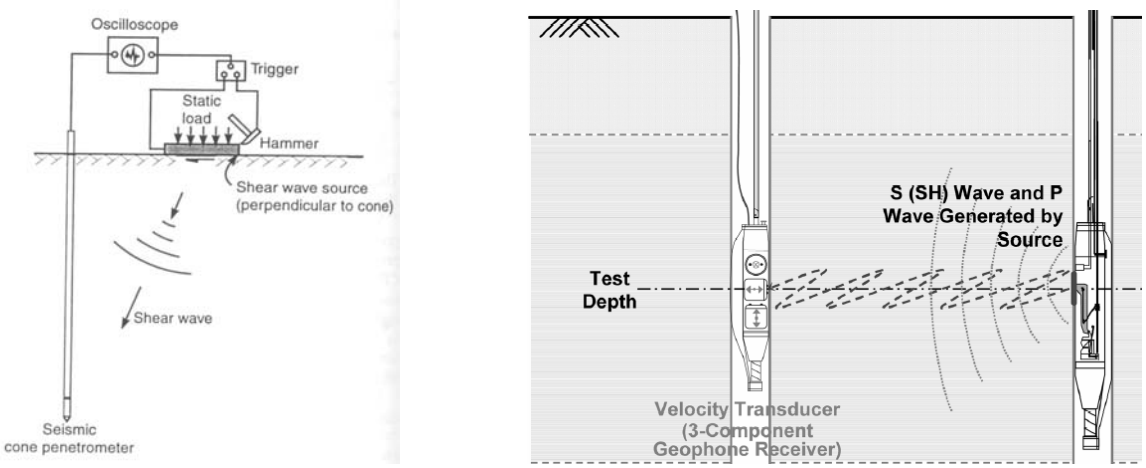

Figure 2-15 Schematic diagrams of seismic cone penetration test and cross hole seismic test (Lunne et al, 1997; Sun and Mok 2006)

2.2.3. Initial stiffness comparisons between laboratory and field test results

The shear modulus values from both in-situ seismic tests and bender element tests can be compared to clarify the sampling effects in laboratory tests and also whether the anisotropy measured in the field is maintained in laboratory measurement.

As mentioned before, the stiffness values obtained from the laboratory are believed to be consistently smaller than the values measured in situ or back calculated from the field movements. This discrepancy was contributed to the effects of sampling disturbance (e.g. Lambe and Whittman 1967, Burland 1989). For example, the G_{vh} values of London clay were approximately 35% lower than the corresponding in-situ G_{vh} data from down-hole shear wave velocity measurements (Hight et al. 1997). However, it was concluded that the hollow cylinder samples in the torsion shear tests were mechanically disturbed due to complex trimming procedures.

Other research has shown that G_{max} measured in-situ is approximately equal to that measured in laboratory tests on very high quality specimens (Clayton and Heymann, 1999; Matthews et al, 2001).

Due to the location of the source and the receiver and the wave propagation and polarization direction, the down hole test or the seismic cone penetration test results are compared to V_{vh} from the bender element test results and the cross-hole seismic test results are compared to V_{hh} and V_{hv} depending on the orientation of the source wave. Recent research on London Clay (Hight et al. 2003) shows both G_{hh}/G_{hv} and G_{vh}/G_{hv} compare favorably with the laboratory measurements by Jovicic and Coop (1998). However, Pennington et al. (1997) pointed out the discrepancy between G_{vh} and G_{hv} from field measurements on Gault clays as shown in Figure 2-16. Pennington et al. (1997) explained that this is possibly due to layering of the in-situ condition, because the vertically propagated waves have to pass through each layer while the horizontally propagated waves will tend to travel along layers of highest stiffness, therefore, G_{hv} values are consistently higher than G_{vh} values.

With recent development of high resolution measurement device, the strain can resolve down to less than 0.0001% and the very small strain stiffness value in the triaxial tests can compare with the stiffness from the bender element test results. In some research based on field seismic and on-specimen instrumentation, the static and dynamic stiffness are broadly consistent (e.g. Smith et al, 1992; Gasparre et al. 2007). Considering that the major difference between the static and dynamic measurement is the strain rate, it can be inferred that the very small strain stiffness value is hardly influenced by rate of shear straining.

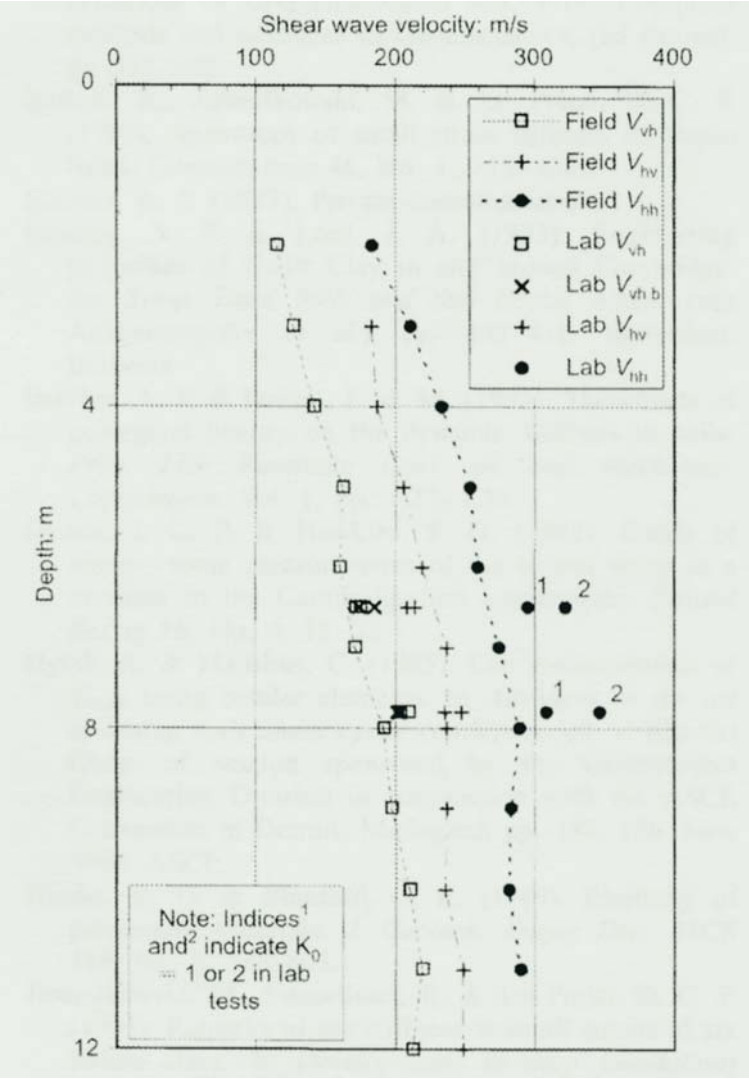

Figure 2-16 Comparison between field measurements of shear wave velocity plotted against depth and laboratory measurements on natural samples from K_0 =1 and 2 conditions (Pennington et al. 1997)

2.3. FACTORS INFLUENCING VERY SMALL STRAIN SOIL MODULI

There are multiple factors that significantly influence the moduli of soils at very small and small strains. These factors can be separated into two categories (Jardine 1995). The first one is related to the soil's nature and history and included factors such as the composition, grading and particle properties, the soil fabric, void ratio or density, chemical alterations related to bonding and

cementing of the particles, stress history, current stress state. The second category arises due to the changes applied to the current stress condition, including the perturbing stress path, drainage conditions, loading rates, boundary conditions and so on. Among the most pertinent factors for normally consolidated to lightly overconsolidated clays are sample disturbance, current state and stress history, stress path directions and reversals, anisotropy, and age/creep (Atkinson and Sallfors, 1991; Tatsuoka et al, 1997).

2.3.1. Sample Disturbance

Sample disturbance is one of the most significant impedances to the characterization of very and small strain behavior for soft clays. Disturbance is caused by many factors, including but not limited to: borehole instability, reduction of effective stress, and shear strains induced by tube penetration, sample extrusion and trimming (Hight, 2001). Disturbance causes a variety of different effects on soft soils, but typically, results in a flatter modulus degradation curve due to progressive destructuring and shrinkage of the limit state surface (Clayton et al, 1992). However, it is also possible for the moduli of a somewhat disturbed sample to become greater after reconsolidation due to significant decreases in void ratio. Using high quality block samples and trimming the triaxial specimens with a fine wire saw can minimize the effects of disturbance. However, even block samples can suffer from some measure of disturbance due to excavation method, stress relief, sample mounting and re-saturation methods.

2.3.2. Current State and Stress History

The current state and stress history of a normally consolidated to lightly overconsolidated clay have major effects on the shear moduli at very small and small strains. A number of researchers

focusing on the dynamic properties of soils had investigated the factors influencing shear modulus at very small strains. From a series of resonant column tests on sands and clays, Hardin and Black (1966, 1968) and Hardin and Blandford (1989) suggested an empirical correlation of elastic shear modulus in the very small strain region:

$$G_{ij}^{0} = S_{ij} f(e)(\mathrm{OCR})^{k} (\sigma'_{i})^{ni} (\sigma'_{j})^{nj} \qquad (2\text{-}2)$$

where G_{ij}^{0} is the elastic shear modulus in the $i-j$ plane, S_{ij} is a material constant (or fabric constant), $f(e)$ is a void ratio function, e is the void ratio, OCR is the overconsolidation ratio, σ'_{i} is the normal effective stress in the i-direction, and ni, nj and k are exponents for σ'_{i}, σ'_{j} and OCR, respectively. While numerous testing data have supported the applicability of Eq. (1), further effort has been devoted to simplify it. For instance, a number of researchers (e.g. Ishihara 1982; Jamiolkowski et al. 1994; Santagata et al. 2005; Shibuya et al. 1997; Tatsuoka and Shibuya 1992) ignored the effect of OCR on the elastic shear modulus, and proposed alternative expressions with different void ratio functions. Furthermore, Viggiani (1992) replaced $f(e)$ with a function of the mean normal effective stress based on the plastic hardening of clays under isotropic stress (Houlsby and Wroth 1991). Rampello et al. (1997) extended Viggiani's equation to anisotropic stress conditions based on experimental results of a reconstituted clay subjected to a constant stress ratio. One may conclude that the elastic stiffness of normally to lightly overconsolidated soils can be expressed simply by the stress components, as well as by relationships between void ratio and stresses as shown in Equation (2-3)

$$\frac{G_{BE}}{p_a} = A f(e) \left(\frac{\sigma'_{a}}{p_a} \right)^{na} \left(\frac{\sigma'_{r}}{p_a} \right)^{nr} \qquad (2\text{-}3)$$

where p_a is atmospheric pressure (101.3kPa), used as a normalizing constant, $f(e)$ is the void ratio function, and A, na, and nr are material constants. Thus, this empirical equation is related not only to the stress components but also to the corresponding value of void ratio. Unlike tests conducted on reconstituted specimens where void ratio can be closely controlled, the effects of void ratio on G_{BE} values should be carefully examined for undisturbed natural samples because minor fluctuations in void ratio is inevitable due to inherent inhomogeneity (Jung et al. 2007)

2.3.3. Anisotropy

Laboratory test data are usually interpreted assuming that the soil behaves in an isotropic manner. In general, soil is unlikely to be isotropic, because of the way in which it was originally deposited. In fact, it is only likely to be isotropic in the plane normal to its direction of deposition because during deposition and subsequent consolidation under gravity, soil particle contacts are directionally dependent, or anisotropic, and the response depends on the direction of the applied changes of stress or strain. Such material is usually called 'cross anisotropic' or 'transversely isotropic'. Under the assumption of cross anisotropy, two of the modulus can be regarded as the same due to the presumed isotropic nature of the plane normal to its direction of deposition.

However, laboratory bender element measurements and cross hole and down hole tests have shown that G_{vh} and G_{hv} are not necessarily equal (Pennington et al. 1997). The shear wave velocity is mostly dependent on the stress acting on the direction of the wave travel and that explains why G_{vh} and G_{hv} can be different under anisotropic stress conditions. Differences between these stiffnesses can arise due to the development of force chains and stiffer particle networks that originate not only because stress states, but also because of the inherent structure

of the system such as deposition, particle size and shape. Thus one must remember that where soil can be assumed to behave as a cross anisotropic material, it is not always true.

The modulus ratio, $n = E_v/E_h$ or $m = G_{hh}/G_{vh}$ is commonly in use to report the degree of anisotropy for a cross anisotropic material in a given stress condition. Table 2-2 summarizes the reported values of n and m for clays in the literature. According to Table 2-2, the modulus ratio ranges from 1.3 to 4 and is higher in heavily overconsolidated clays than in normally consolidated clays.

Table 2-2 Anisotropy of very small-strain (VSS) stiffness in clays (Yimsiri and Soga, 2002)

Soil type	Reconst. method	Test method	Stress condition	SS anisotropy	References
Panigaglia clay	Undisturbed	m = 1.4 (Ko = 1.0)	1-D consolidation	m = 1.4 (NC)	Jamiolkowski et al. (1995)
				m = 1.5 (OCR=1.7~5)	
				m = 2.0 (OCR=12~27)	
				m = 1.7 (Ko = 1.0)	
Pisa clay	Undisturbed		1-D consolidation	m = 1.3 (NC)	
Gault clay	Reconstituted	Bender element in triaxial test	Iso at p'=50-500kPa	m = 1.5 (NC & OCR<10)	Pennington et al. (1997)
	UD (OCR>30)		In-situ stress state	m = 2.0	
Speswhite kaolin	Reconst. (NC)		Iso	m = 1.7	Jovicic and Coop (1998)
London clay	UD (heavily OC)		Iso at p'=in-situ	m = 1.5	
	Reconst. (NC)		Iso	m = 1.24	
Gault clay	UD (heavily OC)		Consolidated in-situ stress state	m = 2.25	Ling et al. (2000)
		Multiple drained		n = 4.0	

2.3.4. Age and Creep

It has been observed that prolonged secondary compression causes the stiffness to increase in an approximately linear manner with the logarithm of time (e.g., Anderson and Stokoe 1978). As seen with the increase in pre-consolidation pressure and undrained strength caused by prolonged aging, the increase in stiffness cannot be explained solely by the reduction in void ratio that occurs during secondary compression. Another important factor is the evolution of the soil's microstructure due to the rearrangement of the soil structure and strengthening of physical-chemical bonds (Anderson and Stokoe 1978).

Tatsuoka et al. (1997) indicated that creep periods significantly increased the regions of quasi-elastic behavior for all soils. Small creep periods at a given constant state of stress resulted in an increase in the modulus along the current stress path direction. Furthermore, recent study on reconstituted Boston blue clay (Santagata et al. 2007) shows that an increase in the duration of the pre-shear aging period at a constant stress causes a stiffening of the soil at all strains, a larger linear threshold, and a higher shear stress at all strains up to 0.1% as shown in Figure 2-17. Correspondingly, a slightly reduced nonlinearity is also observed. These results extend the existing knowledge based on the effects of aging on the stiffness of soils beyond the initial region of maximum stiffness.

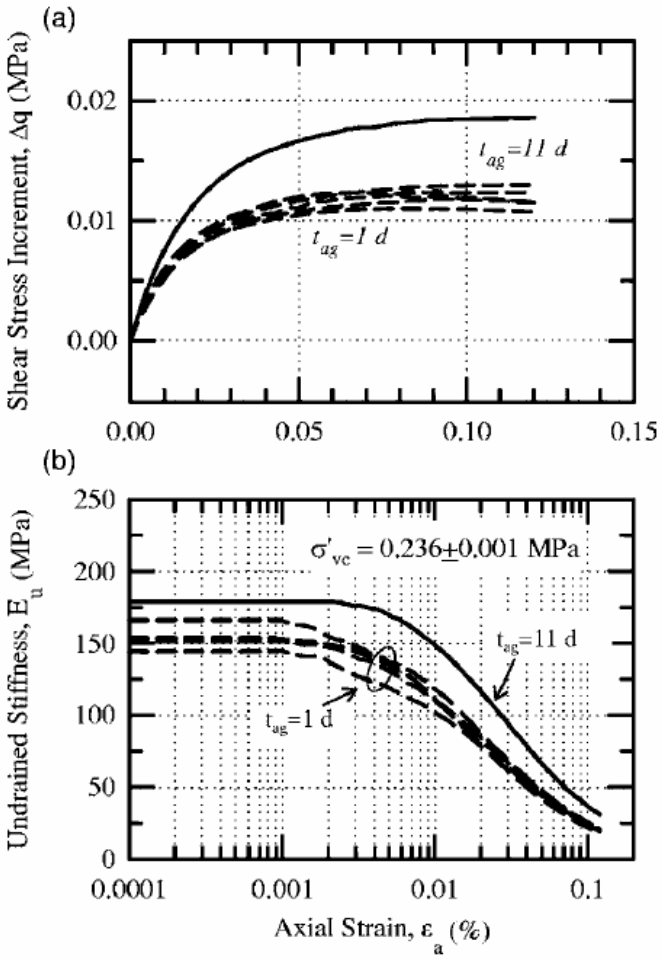

Figure 2-17 Effect of laboratory aging on small-strain behavior of K_0 normally consolidated resedimented Boston blue clay: (a) stress-strain behavior (b) stiffness degradation curve

2.4. RECENT STRESS HISTORY EFFECTS

2.4.1. Previous Research on Recent Stress History Effects

As briefly mentioned in Section 2.1.3, Atkinson et al. (1990) found that the stress-strain behavior of overconsolidated clays depends on their current state and on the loading history followed to reach that state, in particular the relative directions of the current and previous loading paths. Atkinson et al. (1990) defined "recent stress history" as the current path load undertaken by the

soil in relation to the previous stress path, which might be a result of a stress path direction change or a prolonged period of rest under constant stress.

Through a series of experiments involving constant deviatoric stress q and constant mean normal effective stress p' on reconstituted samples of London clay, the gradients of the stress strain curves were determined to be different depending on the recent stress history, indicating that the modulus degradation behavior is also different. In particular, Atkinson et al. (1990) concluded that complete stress reversals yielded the stiffest soil response, while continuations of the previous stress path direction resulted in the softest soil response. Also, the influence of the rotation angle was not distinguishable after 0.5% strain where all the curves converged into a unique value.

There have been many experiments with various soils and testing equipments to unveil these effects. Figure 2-18 shows the stiffness against strain for undrained and drained triaxial probing tests on anisotropically consolidated, low OCR, and soft Bothkennar clay by Smith et al. (1992). From the stress probing tests, the differences in shear and bulk stiffness were observed. The results showed that a stress path with less angle change from the previous consolidation path has lower stiffness than the stress path experiencing the stress reversal path. This tendency became more distinct in bulk moduli than the shear moduli. Jardine (1992) performed a set of tests in London Clay starting from isotropic and anisotropic stress states and investigating the stiffness of the soil and the size of the kinematic surfaces. Natural and reconstituted specimens were consolidated to their initial in-situ stress points following different stress paths, before shearing to failure, as shown in Figure 2-19. Without reloading, the undrained stiffness in compression (stress reversal) at 0.01% strain was higher than that in extension at the same strain

level, as shown in the table in Figure 2-18. In the case of heavily overconsolidated specimen, it showed stiffer response in extension.

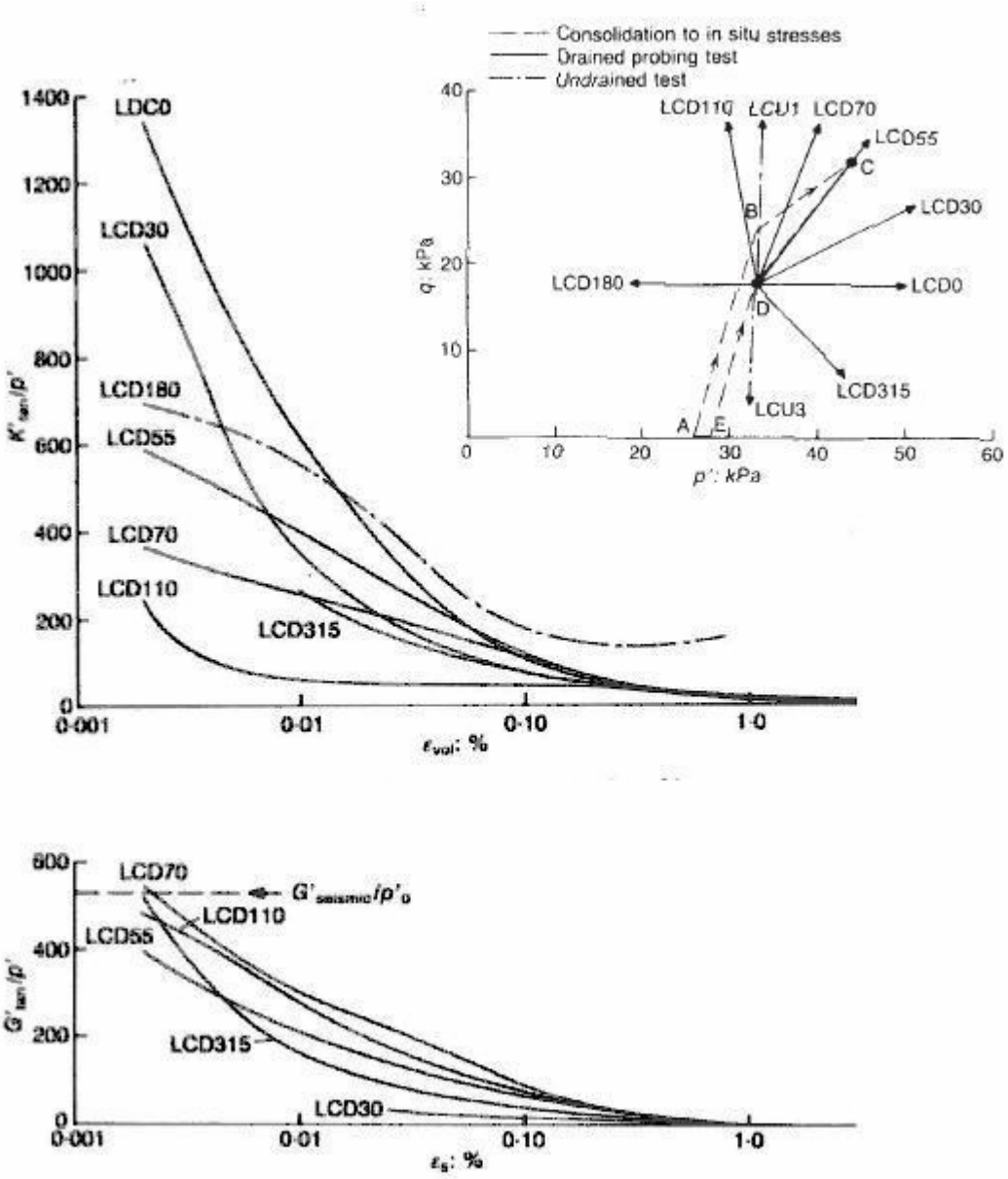

Figure 2-18 Tangent bulk and shear modulus degradation curves from stress probe tests on Bothkennar clays (Smith et al, 1992)

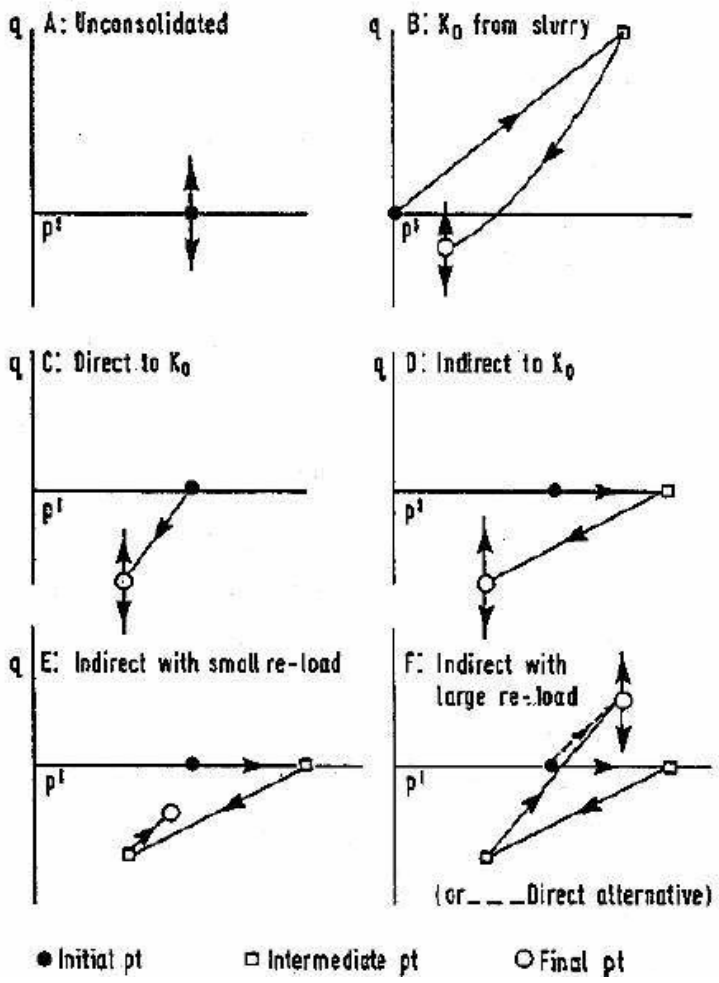

Test Series	Consolidation Path	$\frac{Eu_{0.01}c}{Eu_{0.01}e}$	$\frac{Eu_{0.01}(c+e)}{p'}$
(1) Means, 3 sites, thin-wall samples	A	1.67	1000
(2) Reconstituted, K_0 consolidated $OCR=7$	B	2.52	1480
(3) Bell Common (means), Hellings (1988)	C	1.40	1545
(4) Whitefrairs (means)	E	1.59	1435
(5) Lambeth (means)	F	0.79	1565
(6) City of London (means)	E/F	0.75	1330

Figure 2-19 Compression paths and small strain stiffnesses for natural and reconstituted London Clay samples (Jardine 1992)

Similar results are presented by Zdravkovic (1996) and Zdravkovic and Jardine (1997) from Hollow Cylinder and triaxial tests on anisotropically consolidated, non-plastic silt with OCR of 1.3. Figure 2-20 (a) shows the drained and undrained stress paths applied for the experimental program. Special care was taken to have the strain rates at the end of creep dropped to around 1/100 of the strain rate applied during shearing. Different modes of shearing showed the differences of up to 300% between the maximum and minimum values of G_{oct}[1] at small strains. Figure 2-20 (b) shows the directional shear stiffness derived from these tests. The test results show the stiffer response in the stress-reversal direction, supporting the previously mentioned experiment results.

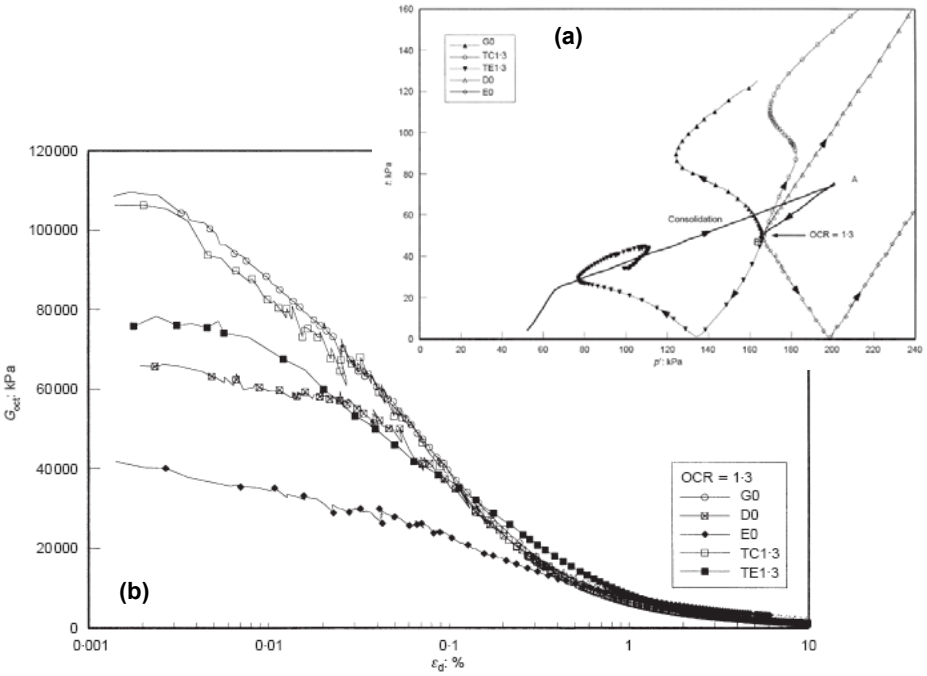

Figure 2-20 Stiffness of an artificial silt subjected to various stress paths after K_0 consolidation and swelling to OCR = 1.3 (Zdravkovic 1996)

[1] Octahedral shear stiffness $G_{oct} = \frac{\Delta J}{\Delta \varepsilon_d}$, where ΔJ and $\Delta\varepsilon_d$ are defined from Hollow cylinder test.

Lings et al. (2000) observed similar results in the heavily overconsolidated Gault clay. The pre-shear stress path and the angle of rotation influenced the elastic parameters of the material and their degradation. Two sets of tests were performed on natural samples including a different angle of rotation of the pre-shear stress path. Figure 2-21 shows the stiffness value normalized by respective initial effective stress strongly depends on the angle of rotation.

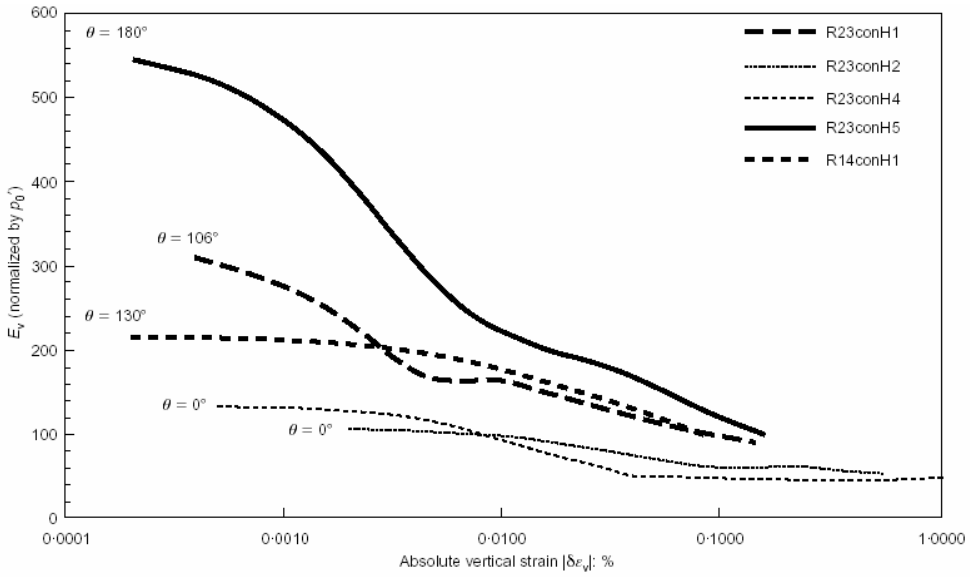

Figure 2-21 Normalized stiffness E_v of heavily overconsolidated Gault clay plotted against logarithm of absolute vertical strain (Lings et al. 2000)

From the stress probing tests from the in-situ stress state of compressible Chicago Glacial clays with OCR of 1.3 (Holman 2003), recent stress history effects and stress path dependency also were found at shear strain levels of 0.001%. No particular attempt was made to discriminate the effect of the current stress path direction from the recent stress history effects because the two effects were not distinguishable with one stress probing tests starting from the same stress state and could have overlapped preventing any clear conclusion being made. However, the trend is clearly shown between the shear or bulk stiffness and the angle change between the previous

and current stress paths as shown in Figure 2-22. In both shear and bulk modulus, unloading stress paths (stress reversal cases) show stiffer responses. The stiffness variation is large at small strain and diminishes significantly when the strain near 0.1%.

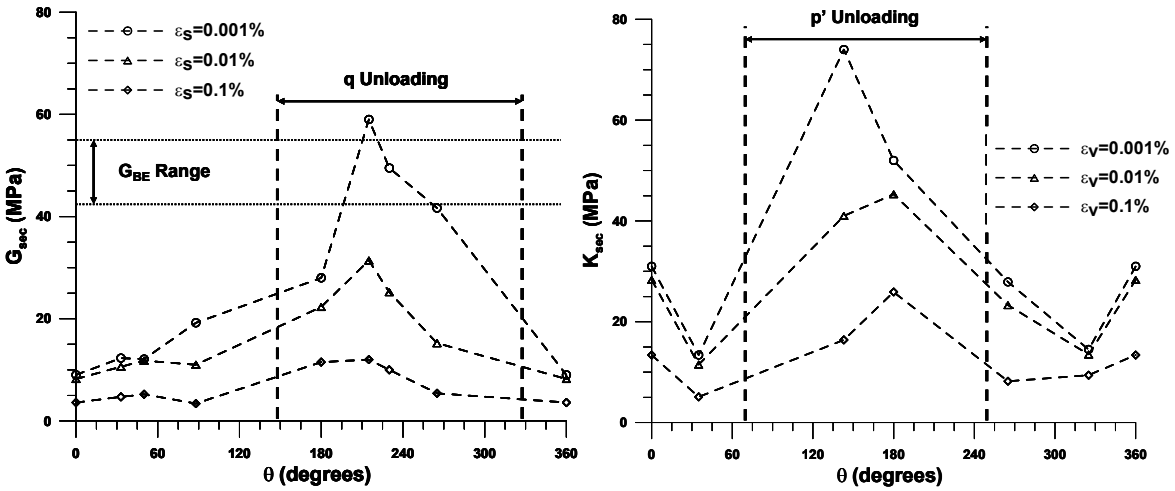

Figure 2-22 Shear and bulk modulus variation with the angle change between the previous and current stress path directions

Callisto and Rampello (2002) conducted drained true triaxial stress probes on natural stiff clays and utilized subminiature LVDTs to measure normal strains on cubical specimens. Their work on block samples of overconsolidated specimens indicated that when interpreted in terms of isotropic elasticity, there was not a very significant difference between equivalent shear moduli as a function of stress probe direction, as shown in Figure 2-23. According to the data in the figure, there was only a 20 MPa difference in equivalent shear modulus G_{eq} at 0.001% shear strain for two stress probes only 60° apart, and a 10 MPa difference for probes 180° apart.

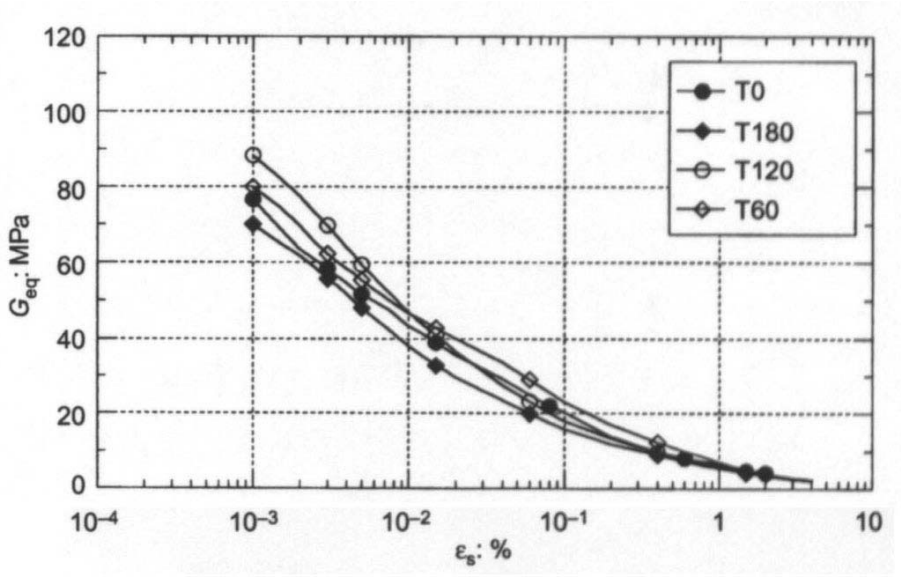

Figure 2-23 Equivalent shear modulus degradation curves from true triaxial tests on stiff overconsolidated natural clay specimens (Callisto and Rampello, 2002).

Clayton and Heymann (2001) performed a set of tests on Bothkennar clay as shown in Figure 2-24. The undrained shear probes started from an initial isotropic state to which the sample had been consolidated following three different approach directions. Clayton and Heymann (2001) considered that Atkinson (1990) allowed only 3 hours of creep before starting the probes, which was long enough so that no volumetric strain changes could be measured at that time, creep for their experimental program was allowed before each shear probe until neither axial nor volumetric strain could be measured. As shown in Figure 2-24, there is no appreciable difference in the stiffness curves from all the shear probes, regardless the different approach stress paths. It was believed that creep might erase any memory of the approach stress path, so that the time spent at constant stress became the recent stress history for the tested material.

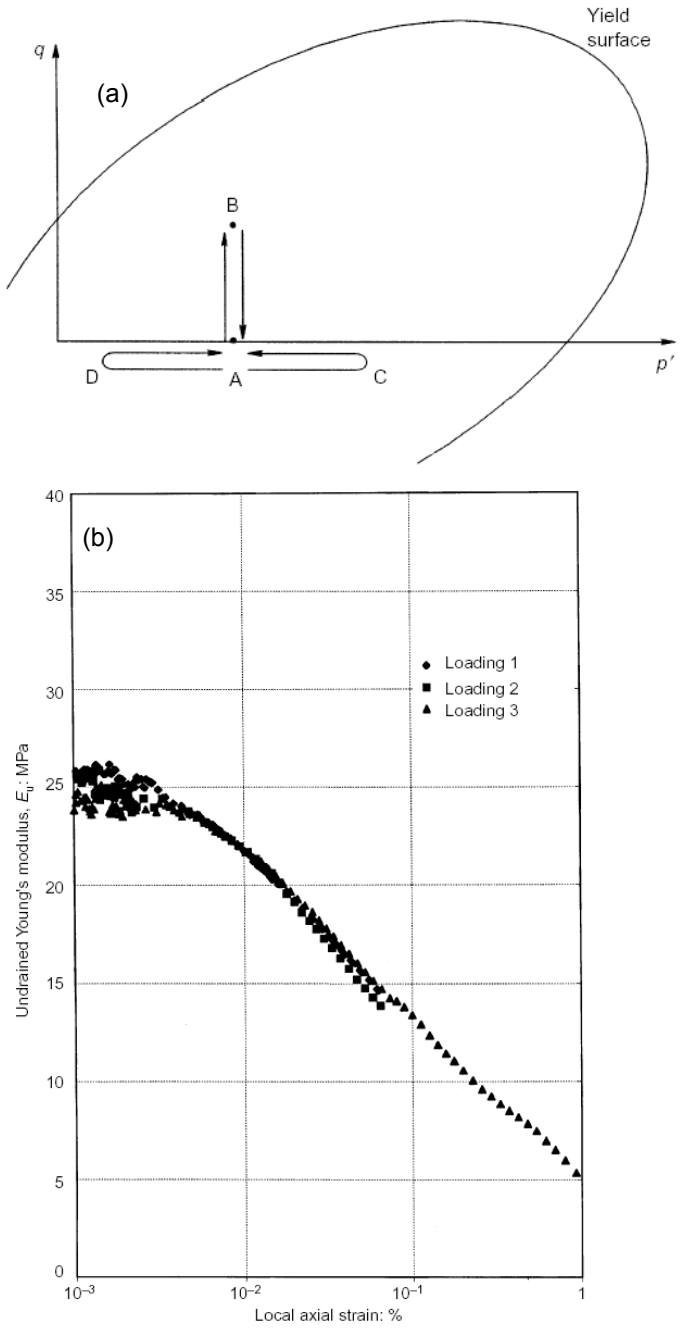

Figure 2-24 Stress probes and stiffness degradation curves for Bothkennar clay (a) pre-shear stress path (b) stiffness response (Clatyon and Heymann 2001)

Tatsuoka et al. (1997) explain that when creep periods are short, the effects of recent stress history become more important. The regions of elastic and relatively stiff behavior extend

as the relative angle between the recent effective stress path trajectory and the direction of the current stress path decreases. After prolonged ageing/creep, the size, shape and location of the elastic and relatively stiff region becomes less dependent on the previous stress history. Similar results were obtained by Santagata et al.(2005) for resedimented Boston Blue clays, a marine illitic (CL) clay. In undrained triaxial compression tests with the axial strain resolution less than 0.0001%, the stress path used to reach the K_0-consolidation stresses does not significantly affect the small strain behavior if enough creep is allowed so that the shearing rate is 25-30 times larger than the creep rate.

Shear probes in compression and extension on natural block samples from Bothkennar clay and London clay were also performed starting from their in-situ stresses (Clayton and Heymann 2001). For both clays, specimens were anisotropically reconsolidated to their estimated in-situ stress states and the creep periods were applied before shearing for 1-3 days for Bothkenna clays and 6-12 days for London clays. These creep periods provided shearing rates 50 to 100 times faster than the creep rate for the London and Bothkennar clays, respectively. The extension probe is the stress reversal path for Bothkennar clay, which has K_0 value less than 1. The stiffness at 0.001% axial strain was very similar for both compression and extension cases, but the degradation was faster in compression than in extension. For the London clay, which has K_0 value larger than 1, the degradation was faster in extension. Clayton and Heymann (2001) concluded that since the initial stiffness of both Bothkennar clay and London clay did not change for the different stress path rotations, the current stress path direction influenced the soil response. This conclusion brought another point of view on recent stress history effects on small strain stiffness that the direction of current stress path from current stress state is the main reason of

apparent recent stress history effect. The main idea is that when loading from an anisotropic stress state soils show a stiffer response in the stress path that moves away from the failure line.

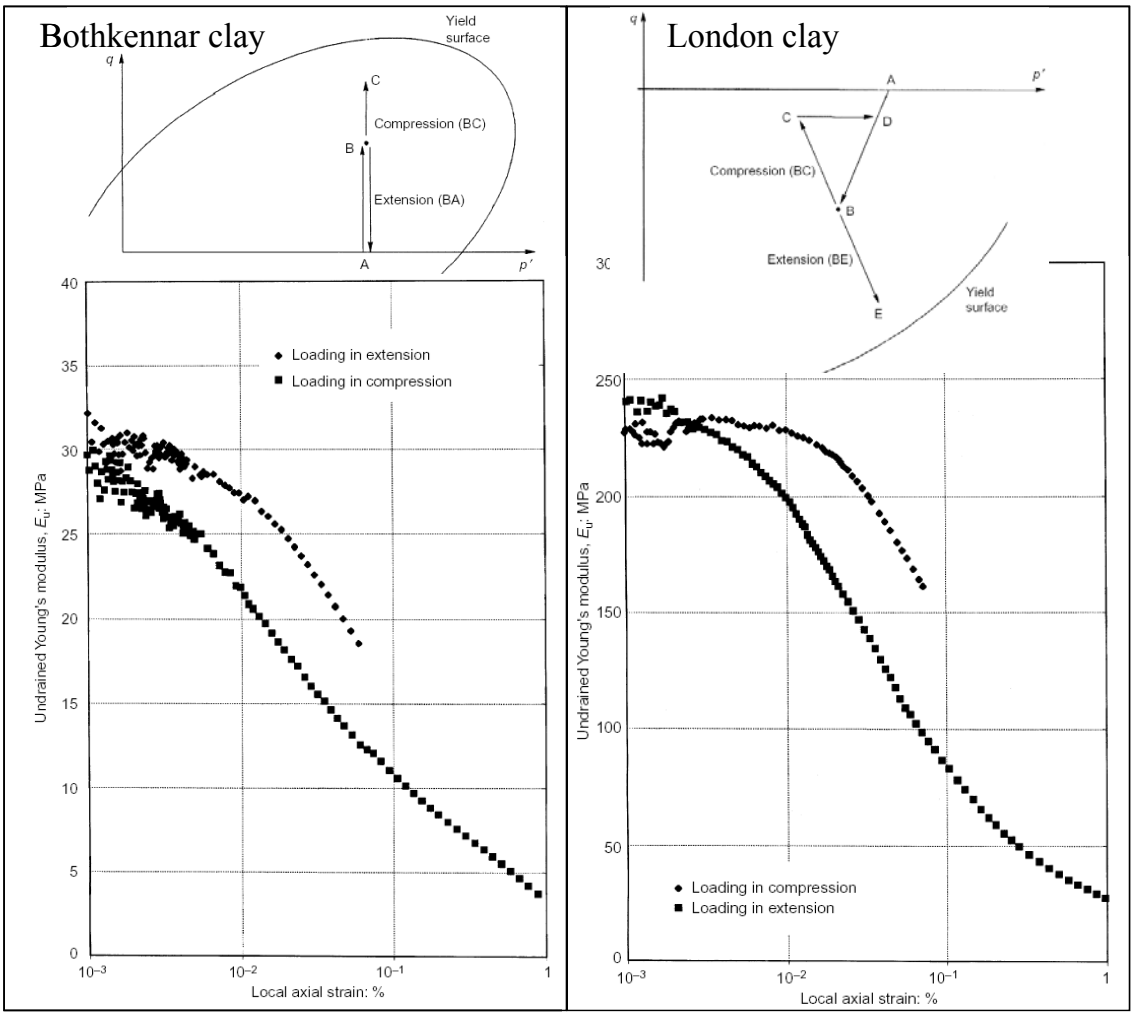

Figure 2-25 Stiffness degradation curves of Bothkennar clays (Left) and London clays (Right) subjected to two different loading paths (compression and extension).

Gasparre et al. (2007) performed a systematic experimental program with natural London clay to clarify the interaction between recent stress history, creep/aging periods and probing path directions. The theory behind these stress probing tests were based on the conceptual model suggested by Jardine (1992).

Three sets of undrained stress probing tests were performed from the same near isotropic initial stress point approached by a constant mean normal stress drained compression or extension path. The reason to choose the nearly isotropic initial stress was to avoid being close to either the compression or extension failure envelopes to discriminate the stiffness directionality mentioned by Clayton and Heymann (2001). Figure 2-26 shows the schematic diagrams of each stress probe and its response. Figure 2-26 (a) shows the case the pre-shear stress path within the Y_2 with 7 days of creep. It is clearly shown that there is little recent stress history effect. However, in the same situation with less creep period (3 hours) shows an obvious effect of recent stress history as shown in Figure 2-26 (b). It can be concluded that if the pre-shear stress path is in the original Y_2 region, the creep period becomes a key parameter for the recent stress history effects confirming the absence of stress history effects noted by Clayton and Heymann (2001) in tests on London clay with comparably short pre-shear stress path and long creep periods.

However, when the pre-shear stress path is outside of the current Y_2 region, the recent stress history affects the stiffness at small strain despite the extended creep period (10 days) as shown in Figure 2-27. Thus, once the pre-shear stress path engaged or relocate the Y_2 surface, the recent stress history effects become evident despite the extended creep periods.

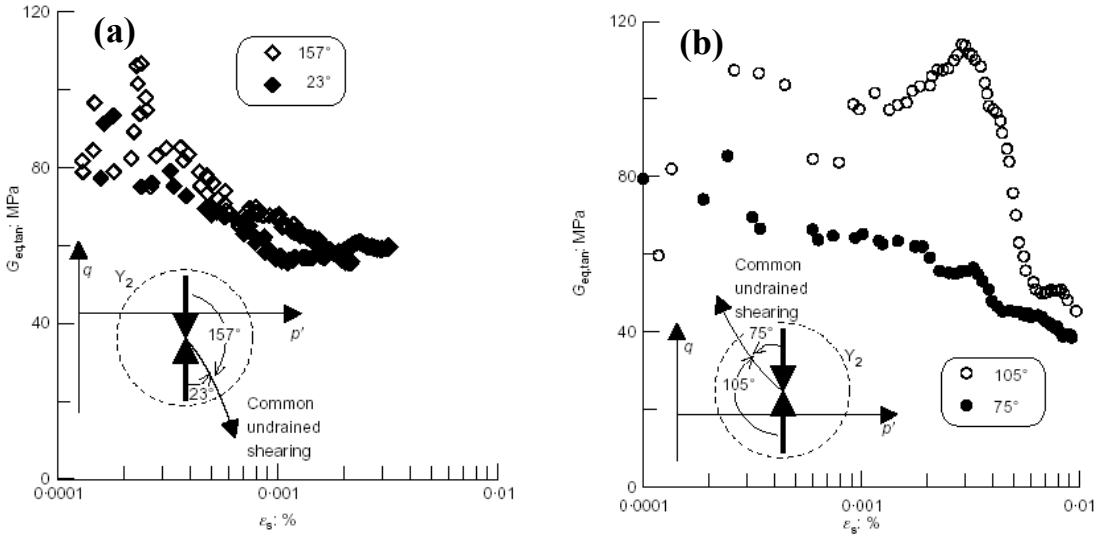

Figure 2-26 Tangent stiffness degradation curves for probes with different pre-shear stress path within Y_2 region: (a)Creep allowed (7 days) (b)Creep allowed (3 hours)

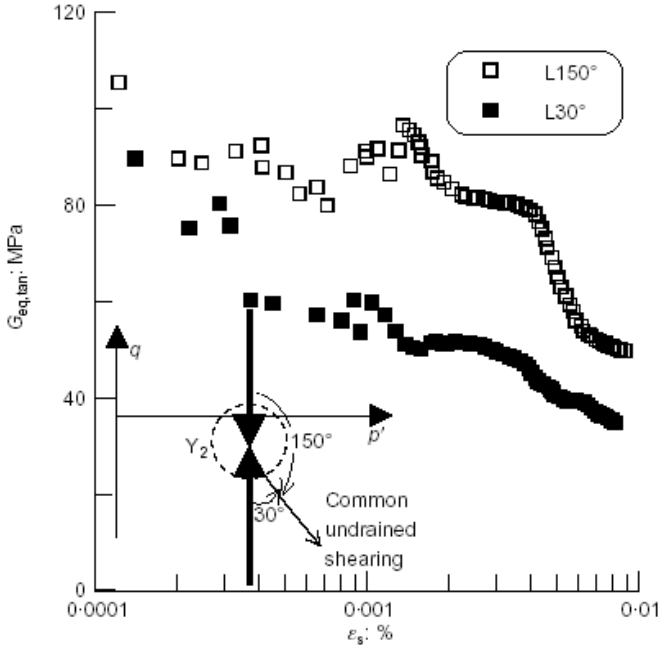

Figure 2-27 Tangent stiffness degradation curves for probes with different pre-shear stress path above Y_2 region and creep allowed (10 days)

2.4.2. Discussions of Previous Research

Section 2.4.1 presents previous work on recent stress history, pre-shear stress path and current stress path effects on the soil stiffness. It is necessary to define those effects clearly. "Recent stress history" is originally from Atkinson (1990)'s work defined as the current path undertaken by the soil in relation to the previous stress path, which might be a result of a stress path direction change or a prolonged period of rest under constant stress. Atkinson (1990) included "a prolonged period of rest under constant stress" in the category of "recent stress history." In contrast, the term "pre-shear stress path" includes only the directional change between the current and previous stress path. The effect of "current stress path" considers only the current stress path directions regardless of the previous stress path. This concept came from Clayton and Heymann (2001) based on the experimental results showed that only the current stress path direction affected the stiffness of soil. The main idea is that when loading from an anisotropic stress state, soils exhibit a stiffer response in the stress path that moves away from the failure line. It might be worth discriminating between the effects of pre-shear and current stress path directions on the soil stiffness in a modeling framework, but it is impossible to differentiate those two effects under real ground conditions. Thus, those two effects are combined in this dissertation as "directionality" because in reality those two effects do not exist separately.

After Atkinson (1990), all of the research concerning these directional effects on soil stiffness excluded the creep effects. When the strain rate during creep becomes 30-50 times slower than the strain rate during subsequent shearing, the possible creep effects on stiffness variations based on the stress paths are negligible (Santagata 2005). However, in this case, the creep occurred at a condition of constant effective stress, which may not represent field ground

conditions. To simulate the field conditions, creep should be considered in many cases as occurring under K_0 conditions, which, in many cases results in horizontal stress changes. Thus, when trying to simulate many field conditions the question arises whether the directionality should consider the stress path direction during K_0 creep.

None of the work summarized in this Chapter clearly presented the strains that developed during K_0 reconsolidation and saturation. From the experimental work on the swelling effect on compressible clays presented in Appendix A, it is proved that the information of pre-shear stages, including the saturation stage, can have a large impact on the subsequently-measured stress-strain responses.

Gasparre et al. (2007) experimentally proved that the recent stress history effects for stiff London clay depends on the "length" of the pre-shear stress path within the context of Jardine's (1992) 3 yield surface model. However, in their experimental program, the same specimen was used to simulate the small length of pre-shear stress path (Figure 2-26) and the longer pre-shear stress path (Figure 2-27). When the pre-shear stress path stays within the Y_2 surface, a zone of recoverable strains, then no pre-shear stress path effects are observed. Defining the Y_2 yield surface is not an easy task, especially for softer clays like those that are the subject of this investigation. For example, Figure 2-26 presents only shear strain less than 0.01%. In particular, the data only showed shear strains as large as 0.003% in the undrained extension test.

Furthermore, all the work related to recent stress history is based on the experimental results from marine clays. It is well known that the structure or the response of the fresh-water based clays such as Chicago clays are different in a number of aspects than marine clays. Thus, it

is worth investigating the "directionality" of compressible Chicago clays in light of data collected during the pre-shear stages, including saturation, K_0 reconsolidation and K_0 creep.

2.5. SUMMARY

Geotechnical engineering analyses of deformations around new or existing structures requires consideration of the strain-level dependent nature of soil stiffness (i.e. modulus degradation), effects of stress path directions and recent stress history. Significant modulus degradation occurs for all soils, even for soft, compressible clays and at strain levels as low as 0.001%. Stress path direction impacts the soil stiffness and degradation, causing initial increases in moduli when paths are reversed with respect to the recent stress history.

Strain fields around well-designed structures such as deep excavations and tunnels demonstrate that strains are typically lower than anticipated, with common values on the order of 0.1 to 0.2% or lower. Strains are commonly seen to decrease with distance away from an excavation support system or tunnel centerline, resulting in decreased deformations or ground surface settlements. The decrease in strains and deformations is due to the strain-level dependency of soil stiffness and stress path direction.

Complete characterization of soil small strain behavior requires the measurement of soil moduli from below 0.001% to above 0.1%. Bender elements may be used in the lab to measure the very small strain shear modulus, or seismic cone penetration testing may be conducted in-situ. Very sensitive LVDTs may be mounted directly on soil specimens to make measurements of strains in the small strain range between 0.001% and 0.1%. Conventional laboratory stress-strain tests or in-situ tests are used to gauge the large strain response (>0.1%).

The modulus of cohesive soils at very small and small strains are influenced by sample disturbance, current state and stress history, stress path direction and reversals, anisotropy, and age/creep. Among these, the recent stress history effects have various issues related to the creep effect and the stress path dependency of the stiffness. There have been many attempts to investigate the effects with various soil types and those results are conflicting with regard to the stress path dependency of stiffness and recent stress history effects. The conceptual model with three yield surfaces suggested by Jardine (1995) explained those conflicts of the existence of the recent stress history effects. The recent stress history effects started to affect the stiffness when the pre-shear stress path was long enough to pass the Y_2 surface regardless of the creep period.

CHAPTER 3 EXPERIMENTAL PROGRAM

The experimental program presented in this research is designed to investigate general small strain responses of compressible Chicago clays. This chapter describes the sample sources, the testing devices, testing procedures and data reduction methods.

Section 3.1 presents an overview of sample sources employed for this experimental program. It includes a brief geological background of Chicago clay and descriptions of natural undisturbed block samples hand-cut from a bottom of the excavation site and reconstituted samples obtained from a large diameter slurry consolidometer.

Section 3.2 describes the triaxial testing devices, focusing on the small strain measurement systems, subminiature axial and radial LVDTs mounted directly on the specimen, an internal load cell and bender elements. Also the accuracy and precision of the system components are presented.

Section 3.3 explains experimental testing procedures applied in this research. It describes how to set up the triaxial test. Two sets of stress probe test are used; one for general stress-strain response and the other to evaluate the effects of pre-shear stress paths.

Section 3.4 discusses the data reduction and analysis techniques, and compares the external and internal measurement data.

Section 3.5 summarizes the performed tests for the two types of stress probing tests explained in Section 3.3.

Section 3.6 summarizes the material presented in this chapter.

3.1. SAMPLE SOURCES

3.1.1. Geological Background of Compressible Chicago Glacial Clay

The soils in the Chicago area primarily are glacially derived and composed of six fairly distinct till sheets deposited during the Wisconsin stage of the Pleistocene epoch (Peck and Reed 1954; Finno and Chung 1992). Among those six till sheets, the lightly overconsolidated clay used in this research is categorized as Deerfield till due to its uniform water contents and composition. Geologically, the Deerfield tills are subglacial ice margin deposits that originated from an advance and retreat of the ice front. The degree of overconsolidation depends on the thickness of the glacier, drainage conditions, permeability and the duration of the ice remained in place while soil was deposited. The details regarding the geology of these compressible Chicago glacial clays are found in Chung and Finno (1992)

After the soils at the site where the block samples were excavated, were deposited, a large drop in the water table with a subsequent recovery occurred about 8000 years ago. In the late 1800s, about 4 m of fill was placed to raise the grade to its current level. Thus, the most recent event that affected the *in situ* clay's stress history prior to the excavation for the Ford Building can be represented as a one-dimensional loading of fill, similar to the path of the reconsolidated clay in the laboratory.

3.1.2. Undisturbed block samples

Three undisturbed block samples of Chicago clay were obtained in April 2004 from the excavation for the Ford Motor Company Engineering Design Center deep in Evanston. This project consisted of an 8.5 m deep excavation, 44 m by 37 m in plan, supported by steel sheet

pile walls and two levels of internal bracing (Blackburn, 2005). Figure 3-1 shows a plan view of the site with the location of the block sampling area. The sampling location was approximately 2 m from the southern sheeting line and 12 m from the eastern sheeting line as shown in Figure 3-1. A small trench was made with a small back-hoe before hand-cutting each sample. Three block samples, approximately 0.3 m in each dimension were hand-cut and removed from a depth of about 8.3 m below street level (Elev. -5 m Evanston City Datum). All three block samples were immediately adjacent to each other.

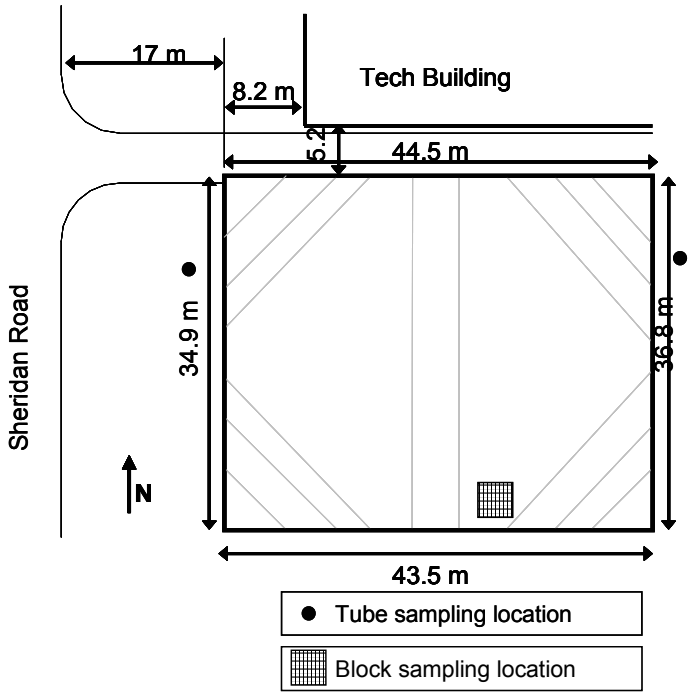

Figure 3-1 Plan view of the Ford Motor Company Engineering Design Center site with location of block sample

Photographs of the block sampling location, the small trench for sampling, and a block sample prior to plastic wrapping are shown in Figure 3-2. The blocks were wrapped and transported to the Technological Institute in Evanston, IL right next to the excavation site. Then,

cheese cloth was wrapped prior to waxing to have better sealing. Coats of wax were applied then stored in the refrigerator at 4°C. The block samples were designated as FB1, FB2, and FB3.

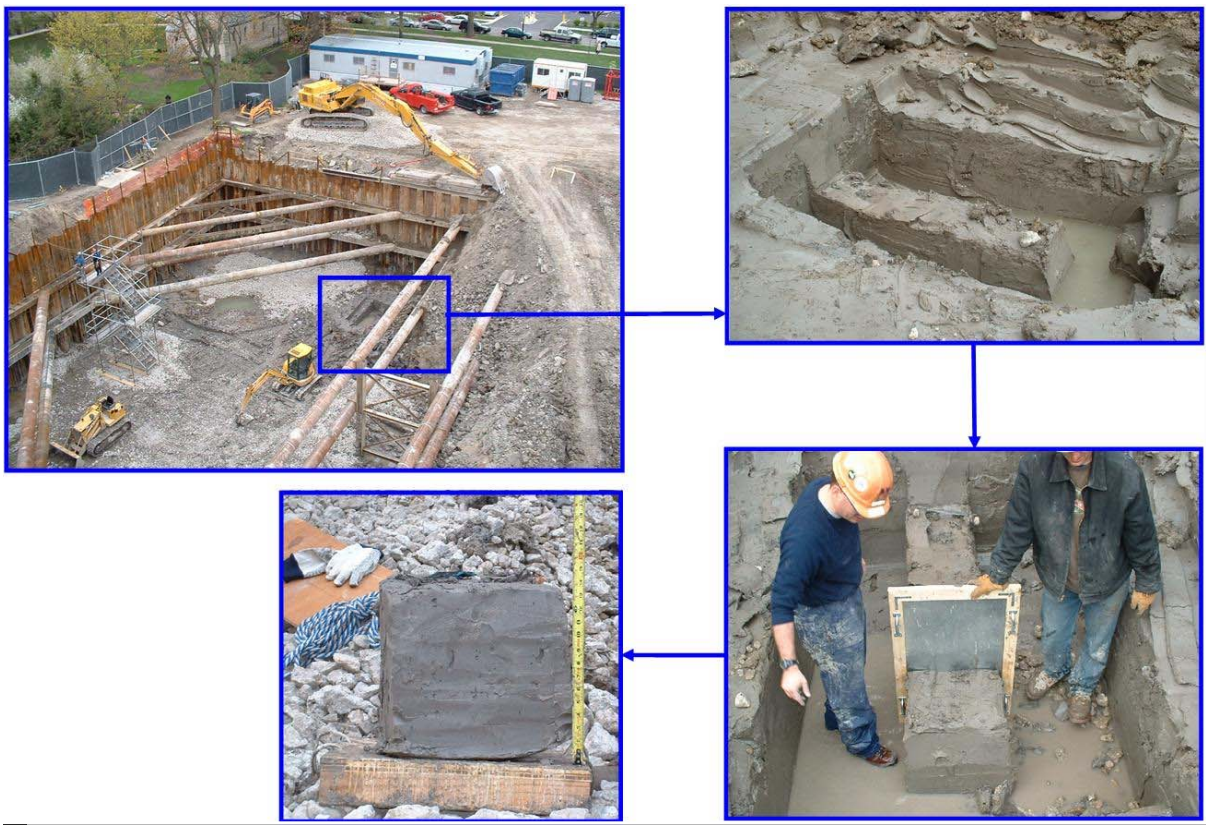

Figure 3-2 Photographs of block sampling location, small trench for sampling, cutting and the block sample prior to plastic wrapping

3.1.3. Reconstituted samples

To clarify the effect of inhomogeneity and ageing, a series of reconstituted block samples were created with a known stress history. Comparison between natural and reconstituted samples is helpful not only to quantify those effects but also to understand the mechanical behavior of natural soils.

Reconstituted samples were created using slurry consolidation techniques (Sheeran and Krizek 1971). Dried Chicago clay, consisting of trimmings and tested specimens from the block

samples, was crushed and dry-sieved through a 0.425 mm sieve to remove coarse and medium sand particles, which leads to 10% loss of total weight of dried soil. The slurry with a water content of twice the liquid limit of the block samples was placed into a large consolidometer (203.2 mm diameter) and loaded in several stages until the applied pressure reached the maximum past pressure previously determined from standard oedometer tests on the block samples. This last load was maintained for a week after the specimen had fully consolidated under the final vertical stress. During this research, total of 7 block samples were made in a slurry consolidometer similar to that described by Sheeran and Krizek (1971) and shown in Figure 3-3. The consolidometer consists of a smooth bore stainless steel cylinder with inside diameter of 203 mm, aluminum top and bottom caps, stainless steel loading rod and platen, and 183 mm diameter porous stones.

Details of the consolidation behavior and comparisons with natural samples for the reconstituted samples will be given in Chapter 7. At the end of the creep period, the vertical consolidation stress was reduced to zero and the sample was carefully extruded from the consolidometer, wrapped in cheesecloth, coated with paraffin wax, and stored at approximately 4°C until ready for use. The typical size of each reconstituted sample was 203 mm diameter and about 260 mm in height. From the top 60 to 80 mm, two samples were taken to perform 1-D consolidation tests to obtain stress history of each block. Individual triaxial specimens were obtained by quartering the larger reconstituted sample.

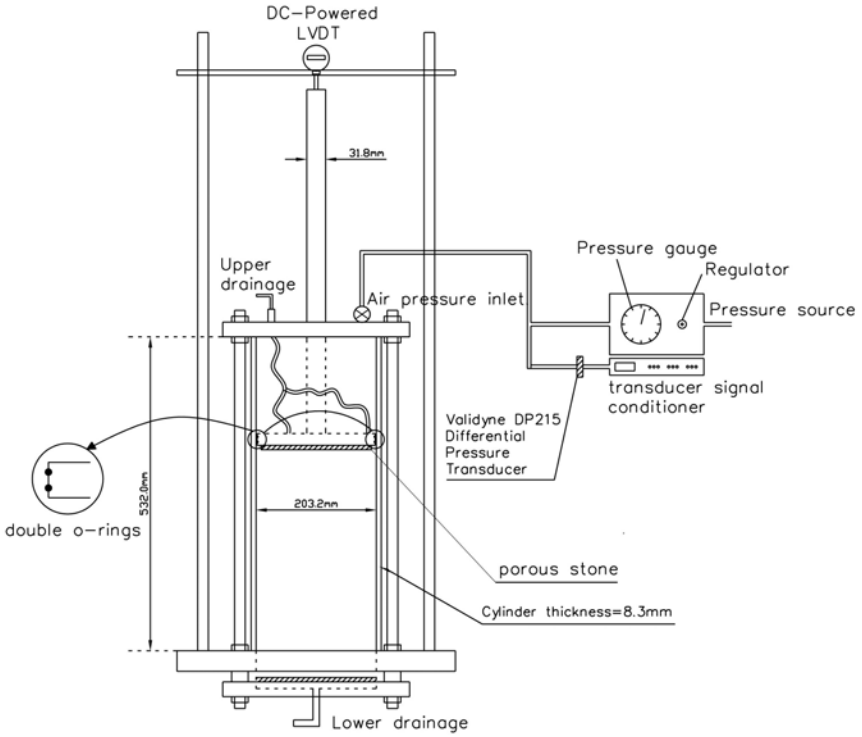

Figure 3-3 Schematic diagram of slurry consolidometer device

3.2. EQUIPMENT AND IMPLEMENTATION

3.2.1. Automated Triaxial Testing Equipment (CKC e/p Cyclic Loader)

The CKC e/p Cyclic Loader, an automated, feedback-controlled triaxial testing system designed and manufactured by Clarence K. Chan of Soil Engineering Equipment Co. was used for all stress path testing in this research program. The components, calibration, and general operation of this testing system have been described in great detail by Li et al (1988) and Chung (1991). Modifications to the system for the current research program include the use of an air cylinder versus an oil-filled Bellofram for better axial loading control because the small strain response can not be shown clearly in the closed loop strain controlled test with the Bellofram. Also, the size of the triaxial cell was increased to accommodate the internal instrumentation.

In this research, the control of the CKC system was based on the external measurement (external LVDT, external load cell, differential pressure transducer of total and effective cell pressure and conventional volume change device rather than the internal devices). The K_0 consolidation module operates by applying the vertical effective consolidation stress σ_{vc}' at a user-specified rate and maintaining zero radial strain ε_r (within a tolerance) by varying the total radial stress σ_r and deviatoric stress σ_d. The condition of zero radial strain is enforced by continuous comparison of externally measured axial strains ε_a and volumetric strains ε_v, followed by computer-controlled changes in σ_r or σ_d. All directional stress probes are carried out under drained stress-controlled conditions where total radial stress σ_r and deviatoric stress σ_d changes can be imposed incrementally or continuously.

3.2.2. Small Strain measurement system

The small strain instrumentation employed in this experimental program consists of highly accurate linear variable differential transformer transducers (LVDTs) to measure local axial and radial deformations of specimens and a high precision internal load cell to measure applied axial forces. Specifications for the small strain instrumentation were developed as part of this research program and the equipment was manufactured by GDS Instruments, Ltd. (GDS) of the United Kingdom.

While the CKC system was used to conduct the conventional triaxial test based on the external measurement of strain and stress, the GDS system was used solely to measure the small strain behavior based on the data collected by the internal load cell and three on-specimen high-resolution LVDTs. This engineered conventional triaxial system also allows one to recognize the

errors that existed in the conventional triaxial systems. The detailed comparisons of the results from both systems will be shown in Section 3.4.3.

The small strain measurement system itself has much higher precision and accuracy than CKC triaxial testing system, and the system also uses direct measurements of strains on the specimen. The deformation is measured directly on the middle third of the specimen to eliminate complicated boundary effects and possible seating errors associated with conventional triaxial testing.

Of the LVDTs attached to the triaxial specimen, two measure axial deformations and one measures radial deformation. A photograph of the GDS calipers and LVDTs is shown in Figure 3-4. Each LVDT has a linear range of ±2.5 mm about the electrical zero. LVDT calipers are constructed of lightweight anodized aluminum and are attached to the specimen using either pins or contact adhesive. The radial caliper is styled after that proposed by Bishop and Henkel (1957) and measures exactly twice the diameter change at the transducer location that occurs at the mounting pads on the specimen diameter. The initial gauge length of the axial LVDT calipers are 46.0 mm, while the initial diameter of the specimen controls the gauge diameter of the radial LVDT caliper.

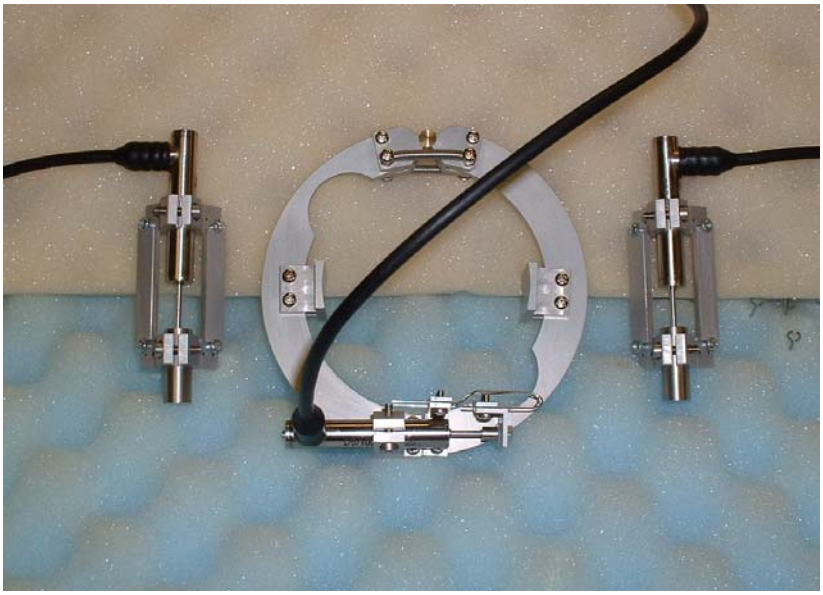

Figure 3-4 Photograph of the GDS calipers and LVDTs

3.2.3. Bender Elements

Bender elements are electrical-mechanical transducers constructed of piezoelectric ceramic bimorphs that can be used to induce and sense perturbations in soils so that wave propagation velocities can be calculated. Full descriptions of the design and construction of bender elements have been given by various authors (e.g. Dyvik and Madshus, 1985). The construction of the GDS elements is such that they are capable of producing both distortional (S-wave) and dilational (P-wave) waves within the triaxial specimen, similar to the bender/extender elements described by Lings and Greening (2001).

Each element, once encapsulated in a waterproof epoxy coating, measures approximately 1 mm in thickness, 11 mm in width, and 13 mm in length. As shown in Figure 3-5, once mounted within the steel or titanium insert, each bender element is clamped for about 5 mm of its length and unclamped for about 8 mm. Approximately 7 mm of the unclamped length is encased

in flexible silicone sealant, and 1 mm protrudes into the clay specimen. This short protruded length was made possible by fixing the element further down inside the insert and then filling the remaining volume with flexible material. This allows the element to achieve maximum flexure at its tip without compromising the power transmitted to or received by the elements.

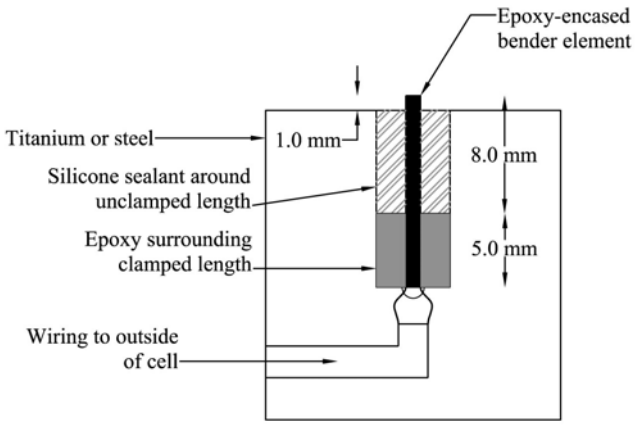

Figure 3-5 Schematic diagram of GDS bender element insert showing bender element dimensions

The transmitter element is excited by means of an applied voltage, causing it to vibrate in the direction normal to the face of the piezo-ceramic plates. The generated wave passes through the specimen and then is detected by the receiving element. The time differences between the output and input wave represents the travel time of the induced wave, V_s. This wave is conventionally thought to be shear wave. Thus, the small strain shear stiffness can then be calculated using the following relationship:

$$G_{max} = \rho V_s^2 \qquad (3\text{-}1)$$

where ρ represents the bulk density.

Since the shear modulus is direct function of shear wave velocity, the travel distance and the travel time for the velocity are key parameters that must be determined reliably. As discussed in Chapter 2.2.1.1, the tip to tip distance between the two elements was adopted as the effective wave travel distance and cross-correlation method was used to determine the travel time. It was used in this research because of its simplicity and objectivity. Sine waves with frequency of 2 kHz for the axial direction and those with 10 kHz for the horizontal direction are used as the input wave. This frequency ranges make the generated waves as shear waves and provide enough wave lengths to propagate as discussed in Chapter 2.2.1.1.

Wave stacking is used to minimize electrical noise. It is a useful tool that averages multiple waveforms taken at relatively short time intervals. This stacking eliminates much of the typical output signal noise seen in other bender element studies without resorting to signal filtering, which can cause distortions in the true signal that alter the actual response. In this study, 5 to 25 waves were stacked with 1 second delay between each wave depending on the noise level.

Table 3-1 summarizes the sizes and mode of propagation of each of the elements. The bender elements used for the three different directions are identical and the input frequencies were different to obtain enough wave lengths.

Table 3-1 Summary of bender elements used in the experiments

Types of Wave		S_{vh}	S_{hv}	S_{hh}
Dimensions (mm)	Length	13	13	13
	Width	12	12	12
	Thickness	1	1	1
Installation		Top cap and bottom pedestal	Side	Side
Shape of Wave		Sine	Sine	Sine
Frequency (Hz)		5	10	10
Amplitude (kV)		14	14	14
Wave propagation		Vertical	Horizontal	Horizontal
Wave polarisation		Horizontal	Vertical	Horizontal

3.2.4. Measurement Accuracy and Precision

It is very important to understand the measurement accuracy and precision of the triaxial system instrumentation since the main focus of this investigation is the small strain response of Chicago clays. In addition, the equipment used in this study has two measuring systems, the CKC triaxial testing equipment that controls the overall testing program and the small strain measurement system consisting of on specimen LVDTs and submersible load cell.

The CKC triaxial testing equipment uses five transducers, an axial load cell, an axial LVDT, chamber and effective stress (differential pressure) transducers, and a volume change (differential pressure) transducer. The GDS instrumentation consists of an internal axial load cell and three subminiature LVDTs (two axial, one radial). The GDS instrumentation is used solely for measuring local deformations and axial forces, which are then used to calculate local axial and radial strains, ε_{al} and ε_{rl}, as well as internally-measured deviatoric stress σ_{dl}.

Both instrument accuracy and electrical precision play a significant role in the successful characterization of small strain behavior for soft clays. The level of accuracy is tied to the nonlinearity and hysteresis within the linear range of measurement, commonly expressed as a percentage of full scale output (FSO). Electrical precision is a function of the range of a transducer and the analog to digital (A/D) conversion rate of the data acquisition system.

The measurement range, manufacturer accuracy, and electrical resolution of each transducer from the CKC and GDS systems are listed in Table 3-2 in terms of engineering units. In addition, the A/D conversion rates of the data acquisition systems are also listed for each transducer. The values listed for the GDS axial LVDTs are the average of the two transducers. The manufacturer accuracy is commonly calculated as a percentage of Full Scale Output (FSO).

The electrical resolution is calculated by dividing the FSO by 2^N, where N is the Analog to Digital (A/D) conversion rate in bits. The load cells for each system provide identical levels of accuracy, but the GDS load cell has a precision 5 times smaller than the CKC cell. Comparison of the axial LVDT values for the CKC and GDS transducers indicates that the GDS LVDT has accuracy 35 times smaller than the CKC LVDT and a precision 150 times smaller. No direct comparison can be made for the CKC volume change transducer, used to directly compute volumetric strains and indirectly compute radial strains, and the GDS radial deformation transducer, which is used to directly compute radial strains.

Table 3-2 Measurement characteristics of stress path testing system instrumentation

	Transducer Type	Measurement Range	Manufacturer Accuracy	Electrical Precision	A/D Conversion Rate (bits)
Global Transducers (CKC)	Axial Load Cell (kN)	+/- 2.225	0.0013	0.0005	12
	LVDT (mm)	+/- 25.4	0.105	0.012	12
	Chamber and Effective Pressure (kPa)	0-1400	3.5	0.342	12
	Volume Change (mm H_20)	560	0.14	0.014	12
Local Transducers (GDS)	Axial Load Cell (kN)	+/- 4.0	0.0013	0.0001	16
	Axial LVDTs (mm)	+/- 2.5	0.0032	0.0001	16
	Radial LVDT (mm)	+/- 2.5	0.0045	0.0001	16

The measurement range, accuracy, and precision values listed in Table 3-2 were used to calculate the range, accuracy, and precision of stress and strain for the CKC and GDS instrumentation. These computed values are presented in Table 3-3. A typical sample diameter of 72.5 mm and length of 152.0 mm were used to calculate the values for the axial load cells in both systems, the CKC LVDT and Volume Change transducers, and the GDS radial LVDT. For the GDS axial

transducers, the typical gauge length was taken as 46.0 mm. The directly calculated values of greatest importance in Table 3-2 are those of the axial LVDTs for both systems. The GDS LVDTs provide a level of axial strain accuracy 10 times that of the CKC LVDT and a precision more than 40 times greater. The CKC LVDT cannot theoretically resolve axial strains less than 0.008% or provide accuracy better than 0.07%, which significantly restricts the ability of the CKC system alone to measure small strain behaviors. The volumetric strain information by local transducer is based on the axial strain and radial strain information assuming the local axial and radial measurements are statistically independent. It is necessary to define the accuracy of each LVDT because typically manufacturer specifies a maximum error as the accuracy. The evaluation of accuracy needs a more accurate device but one can estimate the accuracy by checking the precision, the difference between the instrument's reported values during repeated measurements of the same quantity. The precision of the axial and radial LVDTs and the accuracy of the LVDTs used in this program will be evaluated after the stability check.

Table 3-3 Calculated typical stress-strain measurement characteristics of stress path testing system instrumentation

	Transducer Type	Quantity	Measurement Range	Accuracy	Electrical Resolution	A/D Conversion Rate (bits)
Global Transducers (CKC)	Axial Load Cell (kPa)	1	+/- 539	0.315	0.131	12
	LVDT (%)	1	+/- 16.9	0.07	0.0083	12
	Chamber and Effective Pressure (kPa)	1	0-1400	3.5	0.342	12
	Volume Change (%)	1	5.5	0.019	0.0019	12
Local Transducers (GDS)	Axial Load Cell (kPa)	1	+/- 969	0.31	0.015	16
	Axial Strain (%)	2	+/- 5.4	0.007	0.0002	16
	Radial Strain (%)	1	+/- 3.4	0.003	0.0001	16
	Vol. Strain (%)	1	+/- 12.2	0.013	-	-

It is also necessary to evaluate the stability of the LVDT-signal conditioning system for the long term. The long term stability is important for the accurate measurements of creep behavior. The electrical stability of the small strain system was evaluated by monitoring the transducer output for 12 hours at room temperature (20 ^{o}C). For this test, LVDTs and load cell were inside the triaxial cell to avoid the other environmental changes. Figure 3-6 shows the electrical stability of two axial LVDTs, one radial LVDT and one internal load cell for 12 hours. For the LVDTs, the average noise band corresponds to a displacement of 0.001 mm and translates into a strain of about 0.002% for the axial strain and 0.001% for the radial strain since the radial LVDT measures twice of the displacement in diameter. The internal load cell has an average fluctuation of 0.0003 N which corresponds to about 0.7×10^{-4} kPa of axial stress for the average sample diameter of 72.5 mm. There was no signal drift in the measurements for the times shown in Figure 3-6.

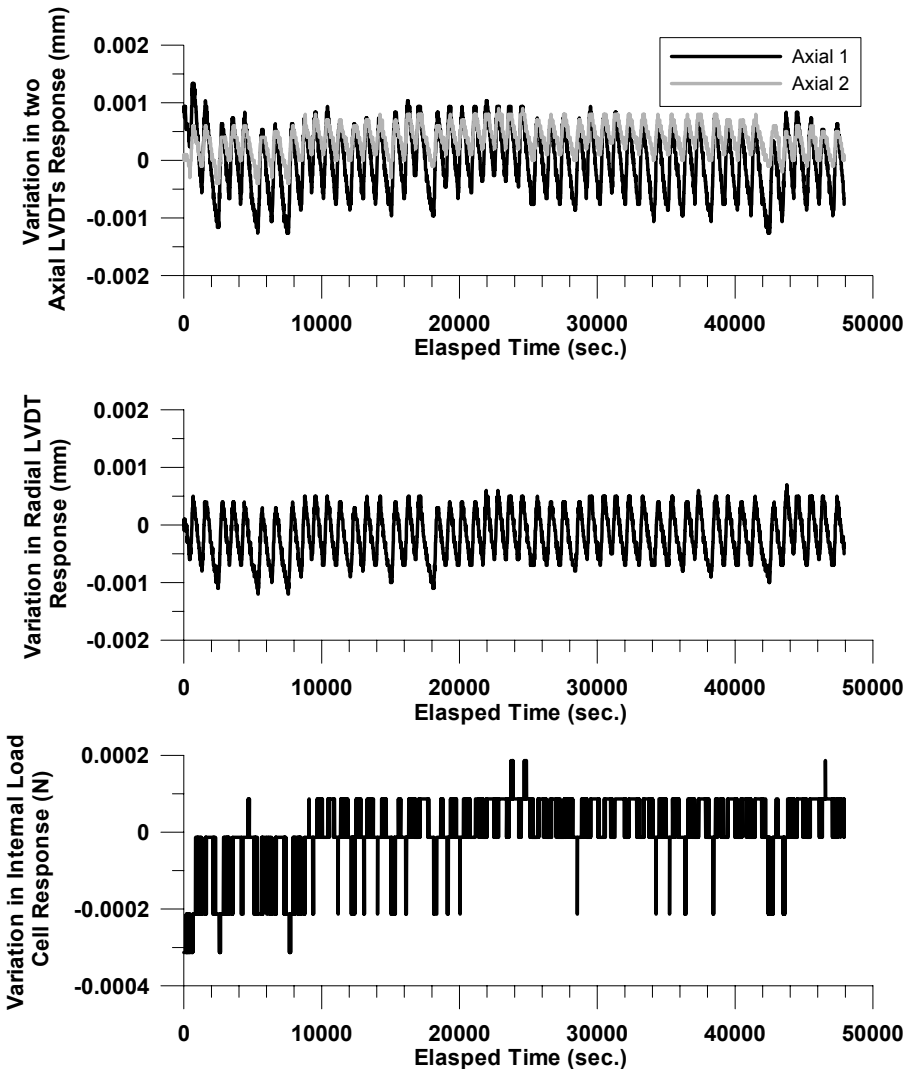

Figure 3-6 GDS transducer response for 12 hour period under static conditions of zero displacement and zero axial load

The precision can be checked based on data collected during the stability check of the "zero set" of each element. Figure 3-7 shows histograms of axial and radial measurement and the standard normal distribution. The true value is zero, but the mean value of axial measurements is 0.00018 mm with a standard deviation of 0.00038 and that of axial measurement is -0.00018 mm with a standard deviation of 0.00040. Here, the axial measurement values are averaged from the two axial LVDTs. Assuming a standard normal distribution, both axial and radial LVDTs can

measure reliable values with 95% of confidence of ±0.0008 mm. This value is smaller than the manufacturers' accuracies, 0.0032 mm and 0.0045 mm for axial and radial LVDTs.

Based on the results shown in Figure 3-7, shear strains and volumetric strains on the order of 0.002% and 0.004%, respectively can be reliably determined.

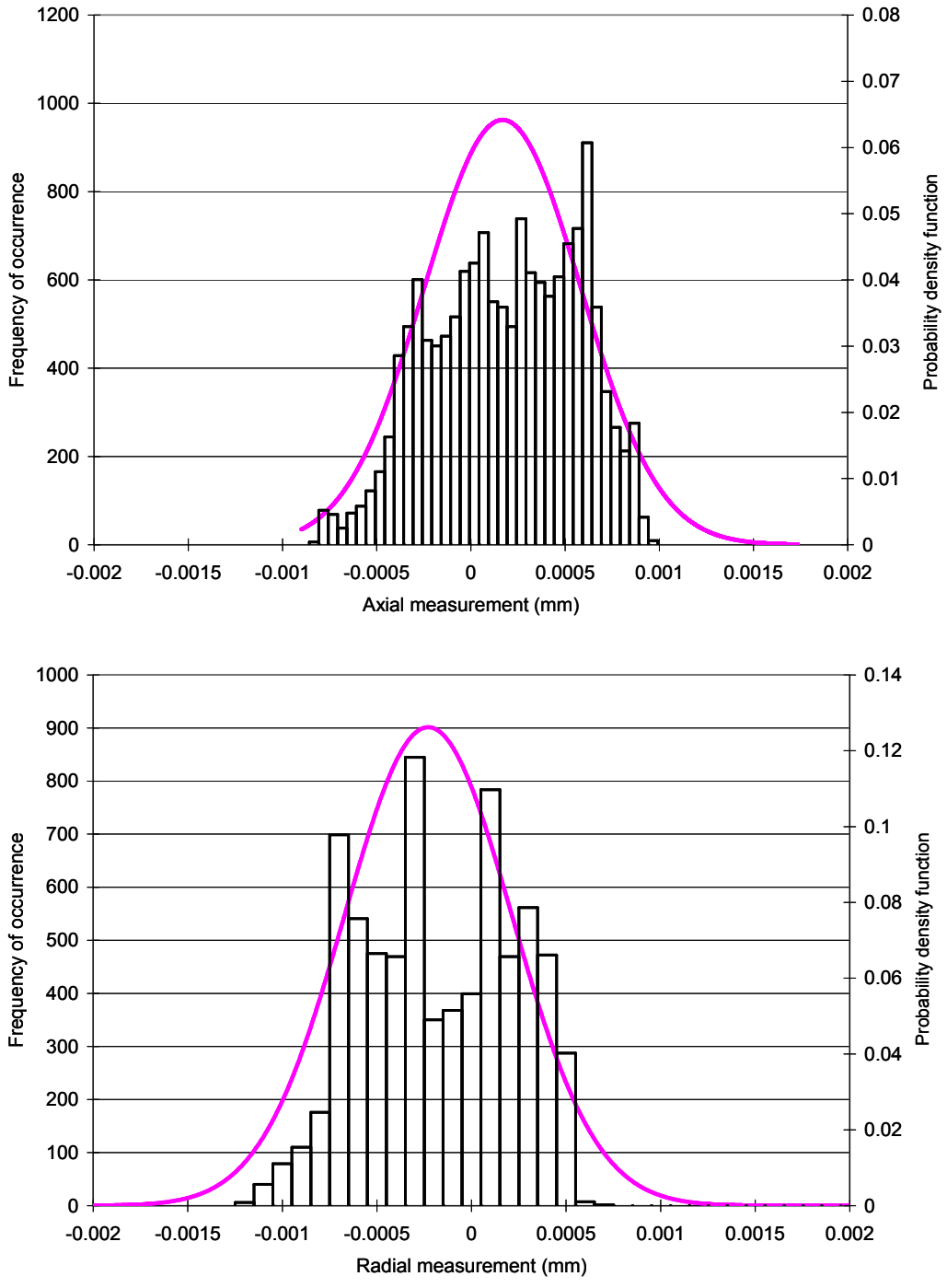

Figure 3-7 Histogram of axial and radial measurement with assumed standard normal distribution

3.3. EXPERIMENTAL TESTING PROCEDURE

3.3.1. Specimen Preparation

Each triaxial specimen was hand trimmed from a 100 mm wide x 100 mm deep x 180 mm hight portion of the block samples described previously. Uniform diameter samples were created using a rotary trimming device with vertical guide bars and a thin wire saw (0.46 mm diameter). To minimize eccentric loading of the specimen during consolidation, sample ends were cut perpendicular to the axis of the specimen using a split mold; verticality was then checked with a bulls-eye level. The average trimmed sample length and diameter of all block-cut specimens were 152.12 mm and 72.25 mm, respectively.

The glacially derived clays typically contain shale and dolomite fragments and rounded gravel in sizes generally ranging from 1 mm to 19 mm but sometimes larger than 50 mm. Figure 3-8 shows the selected shale and dolomite fragments from the block samples. Where encountered along the sample periphery or ends, these particles were carefully removed and replaced with remolded cuttings. The center on the both ends and peripheral of each sample was inspected for rock fragments very carefully in the areas where the bender elements would be in direct contact with the soil. Any small gravel or rock fragments found in these areas were removed and replaced with remolded cuttings to ensure that the bender elements would be free to deflect during transmission or reception of the propagating waves.

Figure 3-8 Selected shale and dolomite fragments from the block samples

Immediately after trimming, the sample was mounted on the base platen of the triaxial cell, surrounded by lateral filter paper drains, and a latex rubber membrane was placed over the specimen. Disks of filter paper were placed between the top and bottom surfaces of the specimen and the smooth sides of the sintered brass porous stones. The lateral drains were placed so that they did not provide any additional tensile resistance during extension-type stress probes by using either spiraled drains or by cutting the drains. The top, bottom, and lateral filter papers, as well as the sintered brass pore stones, were placed in a dry condition. The top cap was then carefully aligned with the specimen top and seated using light pressure to embed the transmitter bender element. The top cap was oriented such that the transmitter bender element was correctly aligned with the receiver bender element in the base platen. If misalignment occurred, the transmitted and received waveforms would be out of phase and the amplitude of the propagated

wave would be less than the maximum that occurs when the elements are in-phase. This is because the wave produced by the bender elements is polarized; theoretically, if the elements were 90º out of phase, the receiver element will not be able to sense the incoming wave. Once the transmitter and receiver bender elements were determined to be in-phase, rubber O-rings were placed to seal the membrane around the base platen and top cap.

The horizontal bender elements are identical to the vertical ones except that they are mounted in a smooth canister of smaller diameter (12mm) to allow the inserts to be mounted to the sides of the sample. To install the horizontal bender elements on the specimen, two holes for each polarization direction were cut in the sample membrane which was already located on the specimen. By pinching a small piece of the membrane with small pliers, a very small cut was made in the end of the stretched membrane. Care was taken to cut not too large a hole because the hole would appear larger when the membrane relaxed. The rubber grommet was then located in the hole, and the bender element insert was pushed into the grommet. Lining the insert with a small amount of silicon grease made it easier to insert the bender element. Before inserting the bender elements, the alignments of the bender element were checked so that those two pair elements would be in line. Especially, great care was taken to have good contact between the element and the specimen. Then, an O-ring was placed around the grommet. To ensure a good seal so that the membrane would not leak throughout the test, the additional sealing (silicon sealant) was used around the joint between the grommet and the membrane. The elements appeared slightly loose on the sample, however, bedding pressure of the horizontal elements increased when the light vacuum pressure was applied later.

A schematic drawing of a typical specimen with attached small strain instrumentation is shown in Figure 3-9. The axial and radial LVDT calipers were attached to the specimen after it was mounted on the triaxial cell's base platen. A light vacuum (on the order of 250 to 300 mm Hg) was first applied to the specimen and membrane through the drainage lines to remove any slack in the membrane and lock the specimen firmly against cell's base platen. The calipers were attached so that the zone of displacement measurement was concentrated in the middle 1/3 of the specimen for the axial LVDTs and exactly at the middle of the specimen for the radial LVDT. The axial calipers were placed diametrically opposite each other. The calipers were attached to the specimen using a combination of stainless steel pins and silicone adhesive. The adhesive was placed on the axial caliper pads, which were then aligned with pre-marked points on the membrane. Each axial caliper was then pressed carefully against the specimen, held in place, then securely anchored using a total of four pins inserted into the specimen through machined holes in the caliper pad. The minimum set time for the sealant was 3 hours, after which the spacer bars on the axial calipers were released. The radial caliper was attached to the specimen using the same sealant type and pins. The attachment of axial and radial calipers was performed on the same day as specimen trimming and mounting, followed by overnight curing of the sealant. The following day, the vacuum pressure applied to the specimen was checked to ensure there was no leak on the membrane. Triaxial cell assembly was completed the following day. The total time for specimen trimming, mounting, and LVDT attachment was approximately 24 hours, including overnight curing time for the sealant.

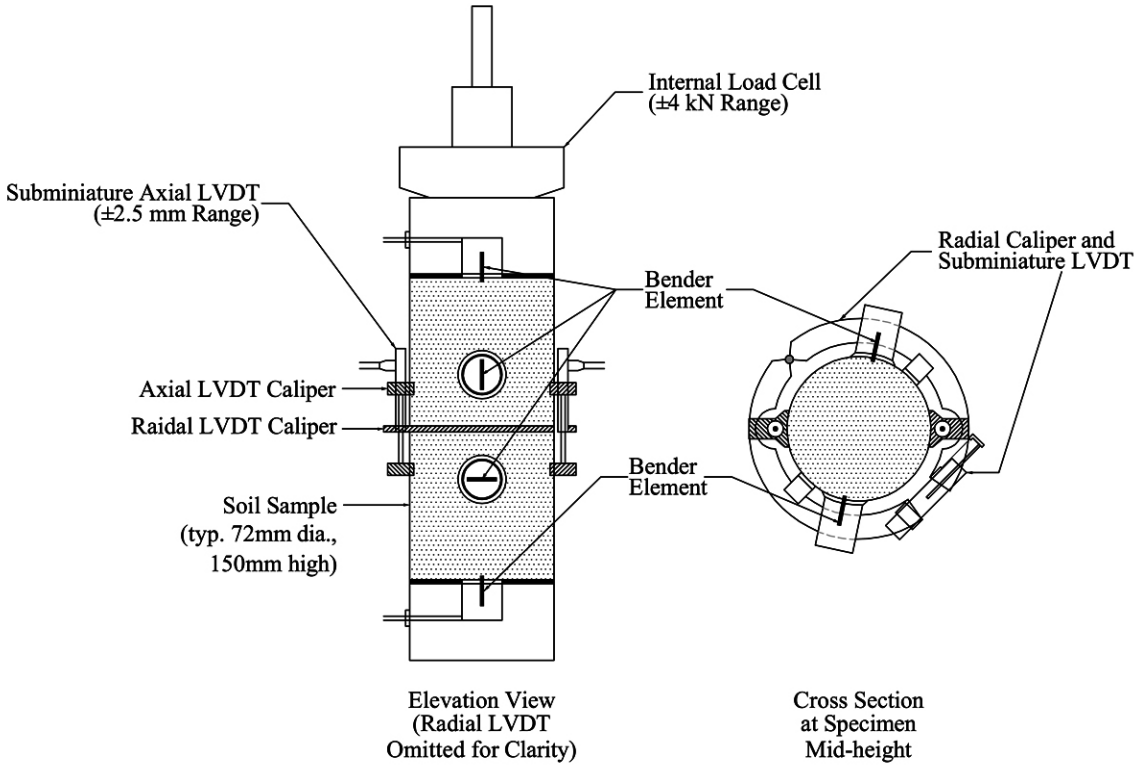

Figure 3-9 Schematic diagram of specimen with small strain measurement systems and three sets of bender elements

3.3.2. Index and Oedometer testing

A series of index and oedometer tests were conducted on specimens cut from the natural block samples, reconstituted samples and tube samples during the course of the research program. The index tests included natural water content, Atterberg limits (liquid and plastic limits), and specific gravity. A limited number of grain size analysis tests were performed. A series of oedometer, or one-dimensional consolidation, tests were conducted on natural samples to estimate the maximum past pressure σ_p' and to make estimates of block sample disturbance by evaluating the vertical strain ε_{v0} to the in-situ vertical effective stress σ_{v0}'. The consolidation tests were performed using variable load increment ratios (LIR) less than or equal to 1.0 to better

define the yield point. Oedometer cells with integral cutting rings were employed to minimize any additional disturbance due to trimming and sample transfer. Oedometer tests were also performed on reconstituted samples to confirm the maximum past pressure σ_p' imposed while consolidating in the slurry consolidometer.

3.3.3. Residual Effective Stress Measurement

Residual effective stress, also called stored effective stress, initial mean effective stress, or effective stress after sampling, is the effective stress remaining in the soil sample after sampling, storage and handling (Hight 2003; Ladd and Lambe 1964; Skempton and Sowa 1963). This concept is rooted in the perfect sampling concept (Ladd and Lambe 1964) where there is no other disturbance, but that from the stress relief. The difference between the perfect sampling effective stress and the residual effective stress, p_r', is caused by disturbance rather than stress relief, implying that the residual stress can be used as a qualitative measure of sample disturbance (Baldi and Hight 1988; Ladd and Lambe 1964).

The residual effective stress, p_r', was evaluated prior to saturation via the response of excess pore-water pressure as isotropic stress increments are applied to a specimen with the drainage lines closed (Ladd and Lambe 1964; Skempton and Sowa 1963). Typically, the total confining stress, σ_c, was increased in 50 kPa increments until the total stress reached 300 kPa, and then σ_c was decreased in 100 kPa increments to 100 kPa. In each step, the pore-water pressure, u, was allowed to equilibrate and then was recorded. Pore pressures usually stabilized within 30 to 60 minutes in each loading step. Typical responses of u to σ_c are shown in Figure 3-10. Using linear regression on this data, the matric suction within the soil sample, u_m, was taken

as the value of u at σ_c=0. Following the general concept of effective stress, the residual effective stress, p_r', is defined as:

$$p_r' = -u_m \tag{3-2}$$

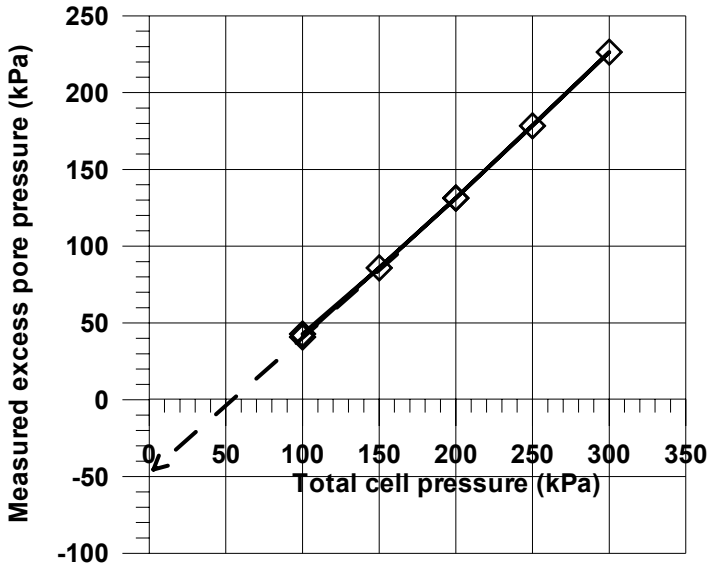

Figure 3-10 Linear regression method to determine residual effective stress

3.3.4. Saturation and K_0 Reconsolidation

After measuring the residual effective stress, each specimen was backpressure saturated in the triaxial cell under isotropic conditions. The effective radial stress σ_r' during the saturation process was maintained at the measured residual effective stress. When the applied effective stress is close to the measured residual effective stress, theoretically, the volumetric strain during saturation becomes negligible, because the applied effective stress equalizes the matric suction. Test results show that the volumetric strain of all samples during saturation varied between

0.01% and 0.2%, which is much less than the 0.3% to 2.5% when saturated at 10 kPa in previous research (Holman 2003).

Those relatively large strains during saturation may alter the original structure of natural clay, which can be crucial for the small strain behavior. Thus, it is important to maintain original structure as intact as possible since this research is focused on the small strain response of natural Chicago clays. In every triaxial test, axial and radial strains were recorded to quantify the deformation prior to consolidation and after the initial measurement during set up. Commonly, only two cycles of backpressure saturation (100 kPa and 200 kPa) were required to produce a B-value, defined as $\Delta u/\Delta\sigma_r$, greater than or equal to 0.98. The total time for backpressure saturation was generally 18 to 24 hours.

After backpressure saturation, the specimen was consolidated under conditions of zero radial strain to the in-situ stress state. The recompression method (Bjerrum, 1973; Jamiolkowski et al, 1985) was used here to reproduce the in-situ stress state. The reason why this method was chosen over the SHANSEP method (Ladd and Foott 1974) is that the main focus of the work is on the small strain response which is closely related to the original structure of the sample. Furthermore, the unloading process inherent in SHANSEP method for lightly overconsolidated clays before the drained directional shear may alter the original structure thereby affecting the small strain stiffness. Therefore, in this study, the specimens were reconsolidated in zero radial strain condition back to the estimated in-situ vertical effective stress of 137 kPa in the field. The reconsolidation was carried out by the CKC e/p Cyclic Loader by maintaining a user-specified effective vertical consolidation stress rate, $d\sigma_{vc}'/dt$ while varying the total lateral confining stress (σ_r) to maintain an average radial strain (ε_r) equal to zero. Radial strains were not directly

measured, but were calculated by the CKC software based on globally measured axial and volumetric strains. The vertical stress rate was maintained at 1.25 kPa per hour to minimize excess pore pressure development. The total time for primary reconsolidation varied from 3800 to 4600 minutes depending on the measured residual stress. Once σ_{vc}' reached 137 kPa, a creep cycle was initiated while maintaining constant vertical effective stress and zero lateral strain to bring the sample to rest prior to stress path testing. This creep cycle is applied to avoid any confusing interactions related to previous loading history. It usually took 36 to 40 hours to obtain a vertical creep rate more than 30 times slower than initial shear strain rate during stress probing.

During the creep cycle, the mean normal effective stress, $p'=(\sigma_v'+2\sigma_h')/3$, typically increased while the deviatoric stress, $q=\sigma_v'-\sigma_h'$, decreased as the CKC system maintained $\varepsilon_r=0$ conditions. Local specimen deformations and axial load were recorded by the GDS system at 120 second intervals throughout the reconsolidation and creep phases. The same data collection rate was maintained for the CKC system.

During the course of the K_0 reconsolidation and creep phases for each specimen, an average of 13 bender element tests were performed. Typically, 10 tests were conducted during the primary reconsolidation and 3 during the creep phase. Measurements of current sample length, L, diameter, D, effective radial stress, σ_r', and deviatoric stress, q, were made and recorded at the time of each bender element test. At the starting of the testing program, only vertical shear wave velocity was measured with bender elements embedded in top cap and bottom pedestal. After the implementation of the two horizontal bender elements, the other two shear waves, the horizontally-propagated, horizontally-polarized and the horizontally-propagated,

vertically-polarized shear wave velocities were also measured throughout the reconsolidation and creep stages.

Each bender element test consisted of 5 to 50 individual shots at one-second intervals, which were stacked by the GDS BES software to create an averaged output waveform. The number of shots per test making up a complete stack was increased as the mean normal stresses on the sample increased to filter out some of the signal noise and provide a cleaner output signal.

3.3.5. Triaxial Testing Program

Two types of directional stress probe tests were employed to characterize the general stress-strain response of soft Chicago glacial clay and to investigate the effect of pre-shear stress path. The major differences between the two types of tests were the stress state at the beginning of the directional shear and the pre-shear stress path direction. The first types of stress probe test, "post-K_0" probes, starts from the in-situ stress state to characterize the general stress-strain behavior. For the second types of stress probe tests, "post-unloading" probes, the starting stress state is unloaded by an RTE stress path to the stress state where the deviatoric stress is a half that of the *in-situ* stress state. The second type of stress probe was designed to simulate the stress state of soils in urban areas which experienced various stress changes due to adjacent construction activity such as tunneling, or excavation.

Similar to previous works by Holman (2003) that characterized the general small strain behavior of block samples Chicago clays taken from the Blodgett stratum, the first stress probe test, "post-K_0" probes consisted of a series of drained directional stress paths starting from the estimated in-situ K_0 stress state. A schematic diagram of these stress probes is shown in Figure

3-11 (a). Stress probe directions encompassed common triaxial testing paths such as compression (TC), reduced compression (RTC), reduced extension (RTE), and triaxial extension (TE). Less common stress path directions included constant mean normal stress compression (CMS), constant mean normal stress extension (CMSE), constant shear stress loading (CQL) and unloading (CQU), and general anisotropic loading (AL) and unloading (AU). The slopes $\eta=dq/dp'$ of paths AL and AU were 0.6 and 0.4, respectively. The slopes for AL and AU were decided from each reconsolidation end point. Several stress paths were duplicated to check the variability between the samples even though those blocks showed identical index properties and 1-D consolidation characteristics.

This first type of stress probe tests also was applied to reconstituted specimens to ascertain the behavioral differences between samples with a known, simple stress history and limited amounts of ageing or creep and natural samples. Probe directions were limited to TC, CMS, CMSE, CQL, CQU, and RTE. The comparisons between the natural and reconstituted samples will be extensively made in Chapter 7.

As shown in Figure 3-11 (b), for the second type of probe tests, "post-unloading" probes, only 5 stress paths were applied due to the limited quantities of block samples. CMS, CMSE, CQL, CQU and AU paths were selected to characterize shear, bulk and two coupling moduli.

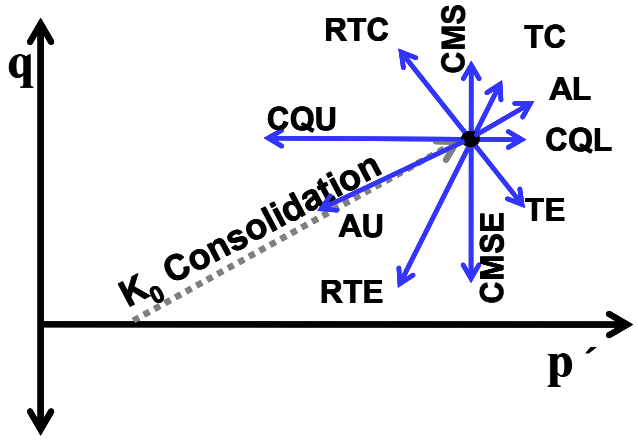

(a) stress probe starting from in-situ K_0 stress state, "post- K_0" probes

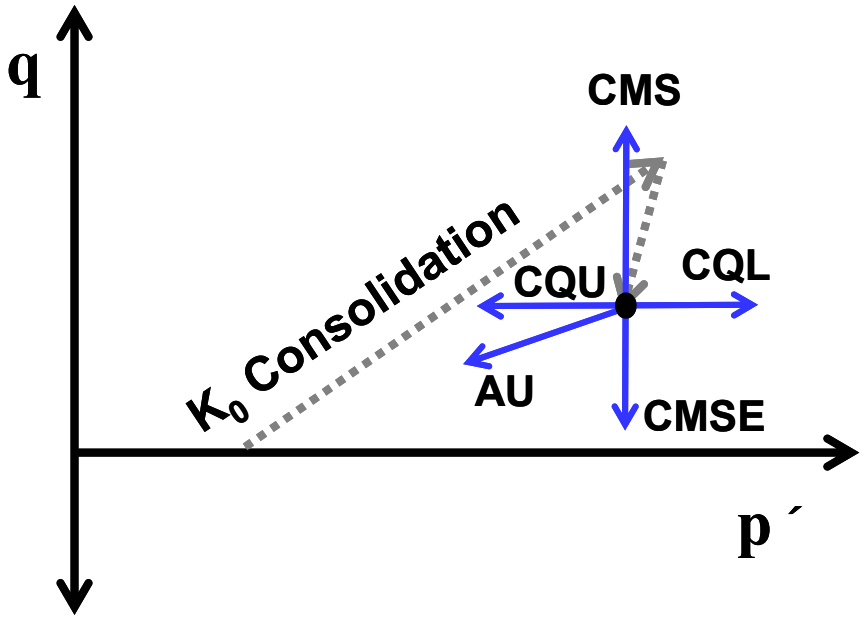

(b) stress probe starting from unloading stress path, "post-unloading" probes

Figure 3-11 Two triaxial testing programs; (a) stress probe starting from in-situ K_0 stress state, "post- K_0" probes and (b) stress probe starting from unloading stress path, "post-unloading" probes

All directional stress probes were performed using the stress path module of the CKC system under stress-controlled conditions. Stress changes were automatically applied by the CKC system by varying the total radial stress σ_r and deviatoric axial stress σ_d according to preprogrammed rates and endpoints. Endpoints for the probes were selected to ensure that sufficient strains were induced and that the entirety of the small strain response could be measured. The duration of the stress paths was sellected to maintain a stress change rate of $d\sigma/dt$ of ±1.2 kPa per hour so that the effects of excess pore pressure accumulation would be minimized.

Stress and strain data were collected by both the CKC and GDS systems during the directional stress probes. The CKC system acquired and stored values of axial strain, volumetric strain, total radial stress, total pore water pressure, and axial stress at intervals ranging from 30 to 120 seconds. The GDS data acquisition system collected and stored values of local axial deformation, radial deformation, and axial load from the internal load cell at 5 to 20 second intervals. During the course of the testing program, a method was devised to allow the data from CKC system transducers to be read by the GDS system serial pad and data acquisition program. Bender element tests were conducted during the directional stress probes on each sample to examine the effects of general stress and strain changes on the propagation velocities. Tests were made at intervals of 3 to 12 hours during the stress probing, correlating to stress-based intervals of about 4 to 14 kPa.

3.4. DATA ANALYSIS TECHNIQUES

3.4.1. Stress and Strain Definitions

The stress invariants that are employed to describe the triaxial stress paths are the mean normal effective stress, p′, and deviatoric stress, q, defined as:

$$p' = \frac{\sigma_v' + 2\sigma_r'}{3} = \sigma_r' + \frac{q}{3} \tag{3-3}$$

$$q = \sigma_v - \sigma_r \tag{3-4}$$

where σ_v' is the effective axial stress, σ_r' is the effective radial stress.

The deviatoric stress is defined by the current load cell value and sample area excluding the rod area connected to the piston. Sample strains in the triaxial apparatus are described using work conjugate quantities to the stress measures defined above. The two infinitesimal strain invariants are the volumetric strain ε_{vol} and the triaxial shear strain ε_{sh} defined as:

$$\varepsilon_{vol} = \varepsilon_a + 2\varepsilon_r \tag{3-5}$$

$$\varepsilon_{sh} = \frac{2}{3}(\varepsilon_a - \varepsilon_r) \tag{3-6}$$

where ε_a is the axial strain ($\Delta L/L_0$) and ε_r is the radial strain ($\Delta R/R_0$).

Pseudo-elastic secant shear moduli G_{sec} and bulk moduli B_{sec} are calculated from these stress and strain invariants by the following:

$$G_{sec} = \frac{\Delta q}{\varepsilon_{sh}} \tag{3-7}$$

$$K_{\sec} = \frac{\Delta p'}{\varepsilon_{vol}} \tag{3-8}$$

3.4.2. Comparison between External and Internal Measurements

Both internal and external measurements were made throughout this experimental program. As explained in 3.2.4, there is significant difference in accuracy and precision between theses two systems. The comparison between the two systems in terms of measurement values and stress-strain values will show the limitations and inherent errors, such as seating errors, in the conventional triaxial testing device.

The comparisons of axial strain and deviatoric stress with time in triaxial compression test are shown in Figure 3-12. Axial strains were calculated directly from the displacement measurement either externally from the outside of the cell or internally on the specimen. It clearly indicates that the external measurement is not appropriate for the small strain range, as suggested by the much larger variation in Figure 3-12 (a). Furthermore, the deviatoric stress comparison in Figure 3-12 (b) shows that,the externally measured deviatoric stress is 1-2 kPa higher than the internally measured value, from which can be inferred that there is either some loss of the load transferred to the specimen or error in calculation of area based on the estimation from the volumetric and axial strains. Note that the deviatoric stress is calculated from the internal load cell value and the calculated area of the specimen at the time of measurement based on the direct measurement in diameter in GDS systems or from the external load cell value and the calculated area of the specimen based on the indirect estimation of diameter which is calculated from the volumetric strain and axial strain in CKC systems. This difference may not crucial for the failure and yield characteristics but can be important for the small strain stiffness.

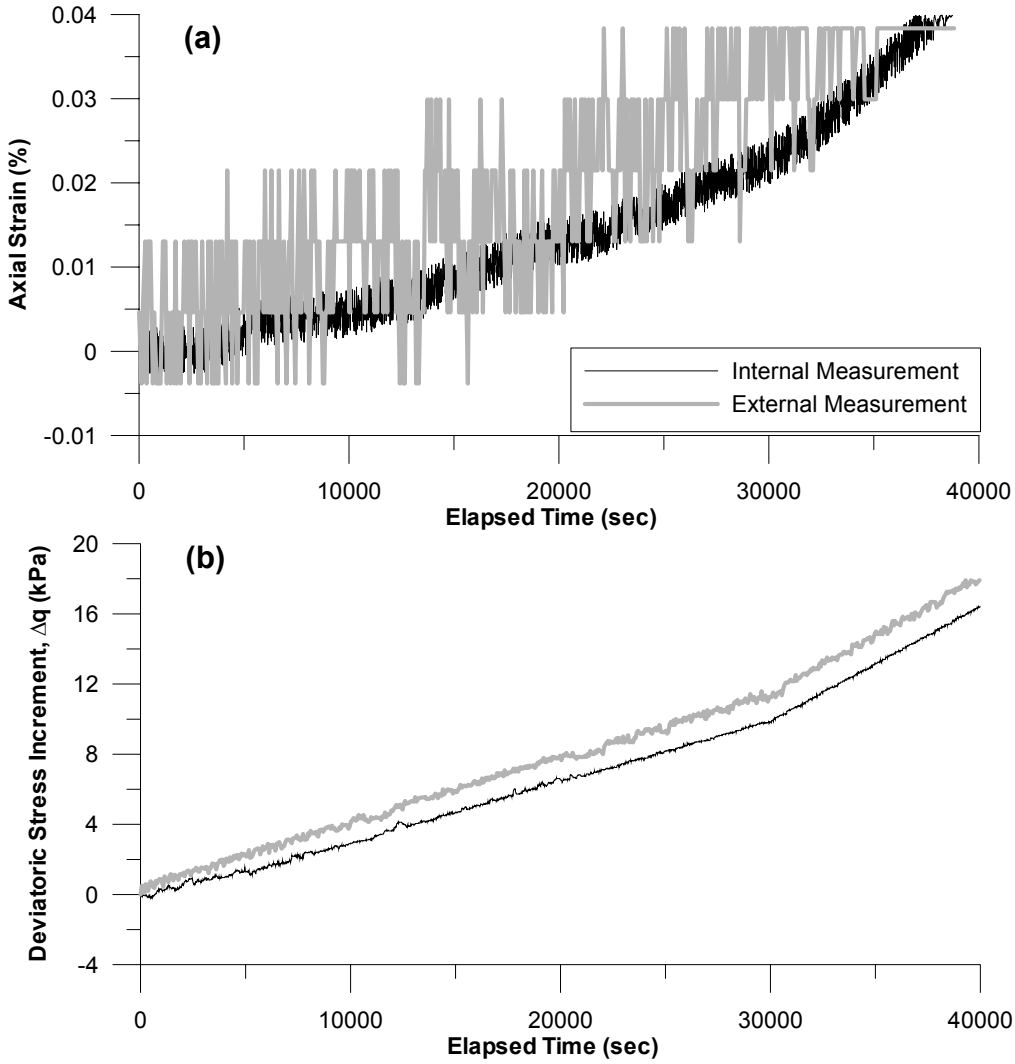

Figure 3-12 Axial strain and deviatoric stress comparison between external and internal measurements

Figure 3-13 shows the comparisons between the external and internal measurements in terms of stress-strain response. The deviatoric stress based on the internal measurement system shows stiffer responses before the failure, but smaller deviatoric stress at failure. This is likely because of the different area calculation methods between external and internal measurement. While the external measurement system calculates the sample area based on the radial strain assumed in uniform deformation, the internal system directly measures the radial deformation to

calculate the area. The different response between the two systems also implies that the internal measurement is more suitable for the small strain analysis due to its high precision and accuracy. Furthermore, this figure suggests that the data from external measurement can underestimate the stiffness before the failure.

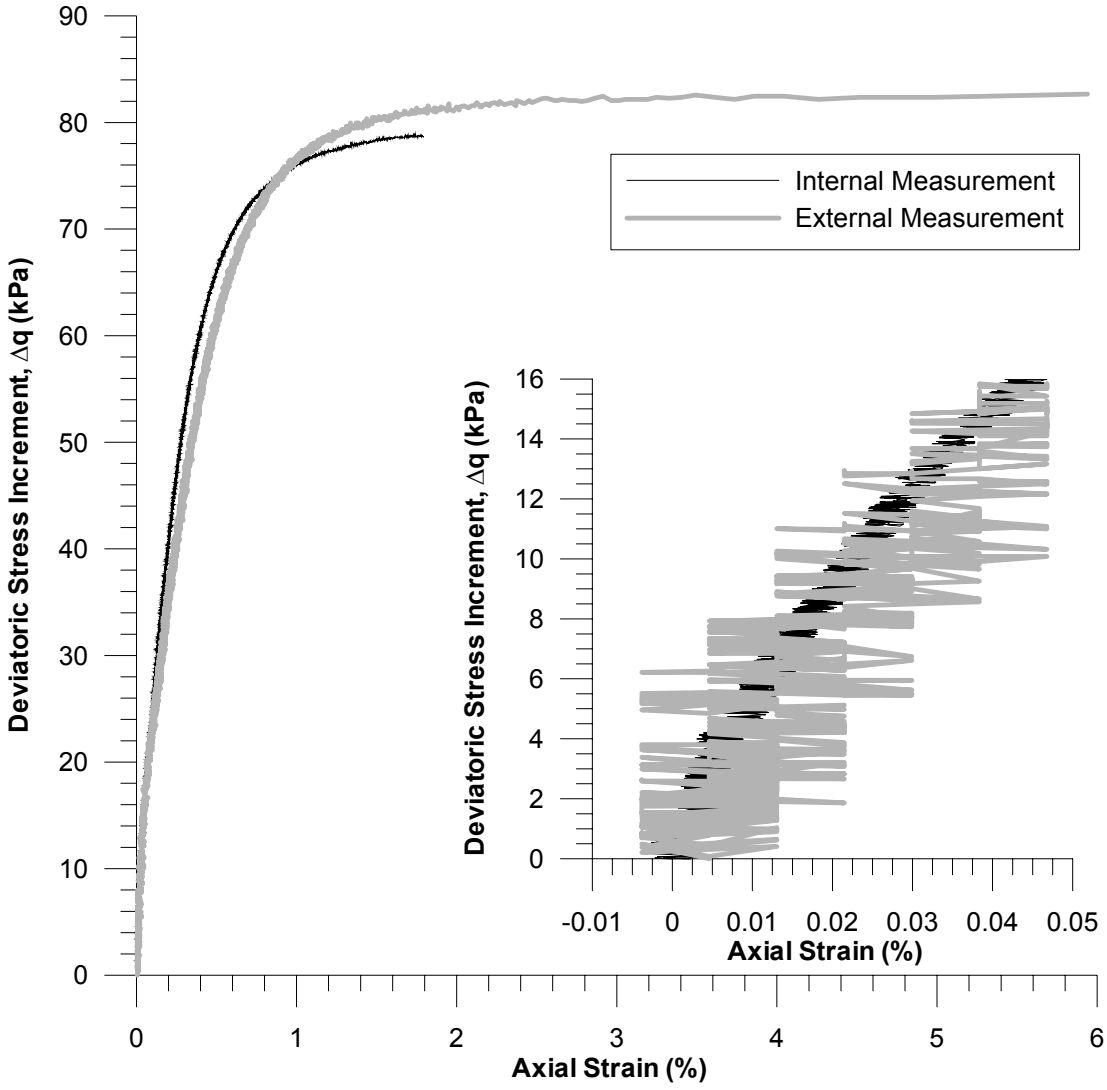

Figure 3-13 Comparison of stress-strain response between internal measurement systems (GDS) and external measurement systems (CKC)

3.4.3. Small Strain Measurement System Stress-Strain Data

Data analysis for the GDS stress-strain data requires calculation of stresses and strains from the raw transducer data. Since the triaxial testing is controlled by CKC loading systems, CKC loading system instability and the inherent electrical noise at very small displacement and load levels causes significant scatter in the stress and strain data, obscuring the smooth response. Regression techniques with polynomial function were employed to reduce the influence of the noise and data scatter at small displacements and loads and smooth the entire data set.

3.4.3.1. Raw data analysis

Raw data from the GDS instrumentation included local displacements from two local axial LVDTs and the radial LVDT, and axial load from the internal load cell. Raw axial strains were computed by dividing the average axial displacements by the initial gauge length of the axial LVDT calipers. Raw radial strains were computed by dividing the change in specimen diameter from the radial LVDT by the initial sample diameter. The current diameter was computed from the measured diameter changes and used to calculate the current sample area. The raw deviatoric stress was calculated using the internal load cell readings.

3.4.3.2. Curve Fitting using Polynomial Function

To eliminate the influence of electrical noise-based data scatter, all GDS data was processed by a regression technique with polynomial function. Since five transducers were used to measure five different quantities, axial strain A and B, radial strain, applied load from internal load cell and the effective stress measured from the differential pressure transducer in CKC machine, regression techniques were applied separately to each of the 5 measured quantities. The external

axial LVDT and the external load cell values were not used to analyze the small strain behavior. It is difficult for one polynomial function to represent the measured quantity throughout the whole testing time because the duration of the tests was as much as 150 hours for the CQL test. Even in the test with the shortest testing time, 20 hours for the RTC path, it was hard to adequately fit one polynomial function due to the non-linearity of the responses. Thus, the entire testing time first was divided into several sections of, for example, 40,000 seconds through all the data. Figure 3-13 shows the five measured quantities and the applied polynomial functions in the first 40,000 seconds of a test. Generally, 4^{th} to 6^{th} order polynomial functions were used to obtain a good R^2 value and good visual agreement. To prevent discontinuities between the two consecutive sections, 20% overlap was used between each 40,000 seconds section. For example, the polynomial functions shown in Figure 3-14 were based on the test data up to 48,000 seconds. In similar way, the polynomial functions applied in the next 40,000 seconds section were obtained from the data between 32,000 seconds and 88,000 seconds to maintain the 20% overlap at both ends of the data. Figure 3-15 shows the raw data and fitted data in 3 sections. With 20% overlaps, the possible absurdities at the connections become negligible. After obtaining the polynomial functions for the entire test, the representative values of each measurement at increment of 1,000 seconds were calculated from the functions. With this process, the total data in one test were reduced to 200 to 500 points for each measurement. Processed data from the two axial LVDTs were averaged to produce a single axial displacement response, assumed to be representative of the centerline deformations within the zone of local measurement.

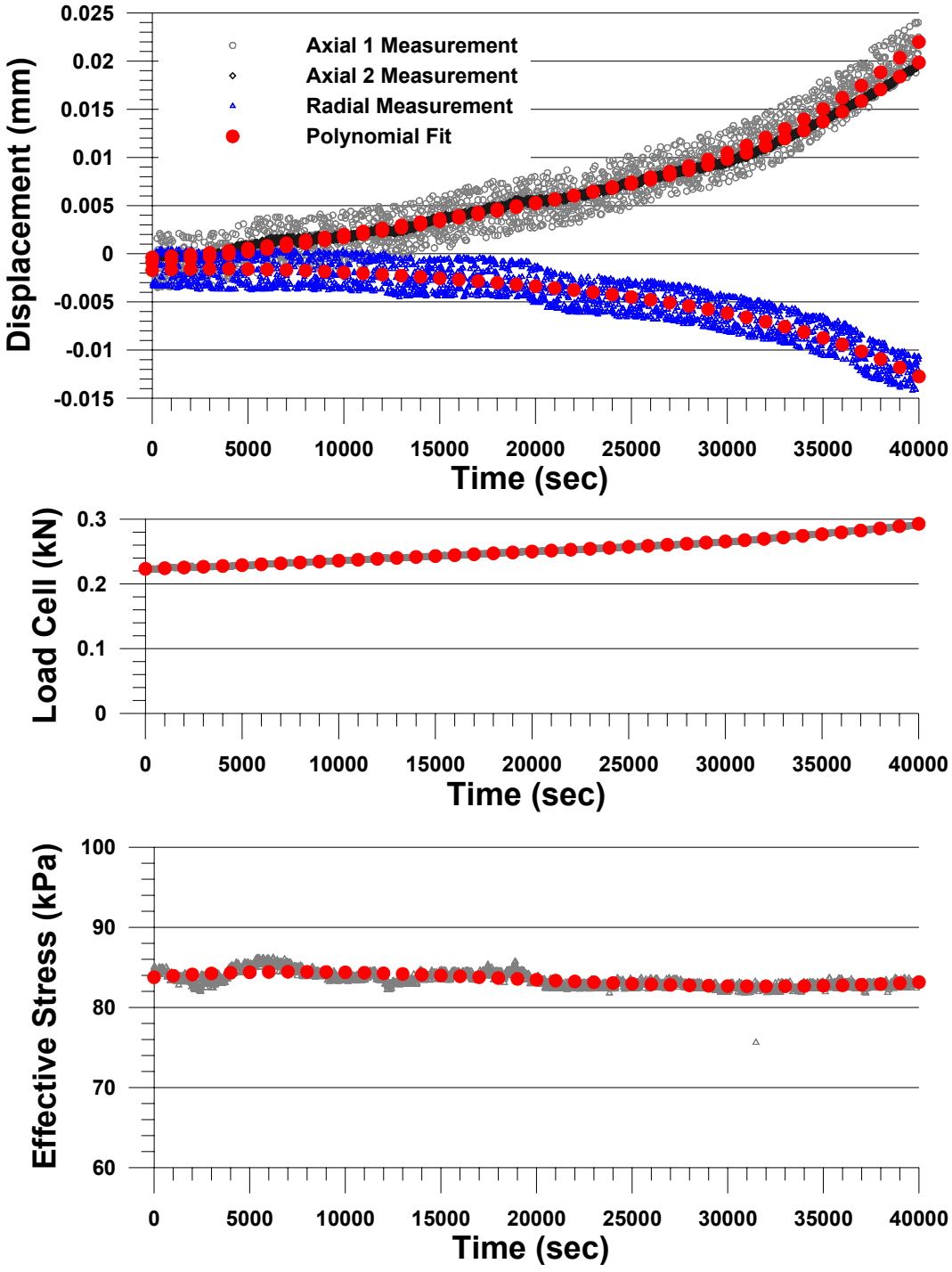

Figure 3-14 Five measured quantities and their polynomial fitted data in one section (0-40,000 sec)

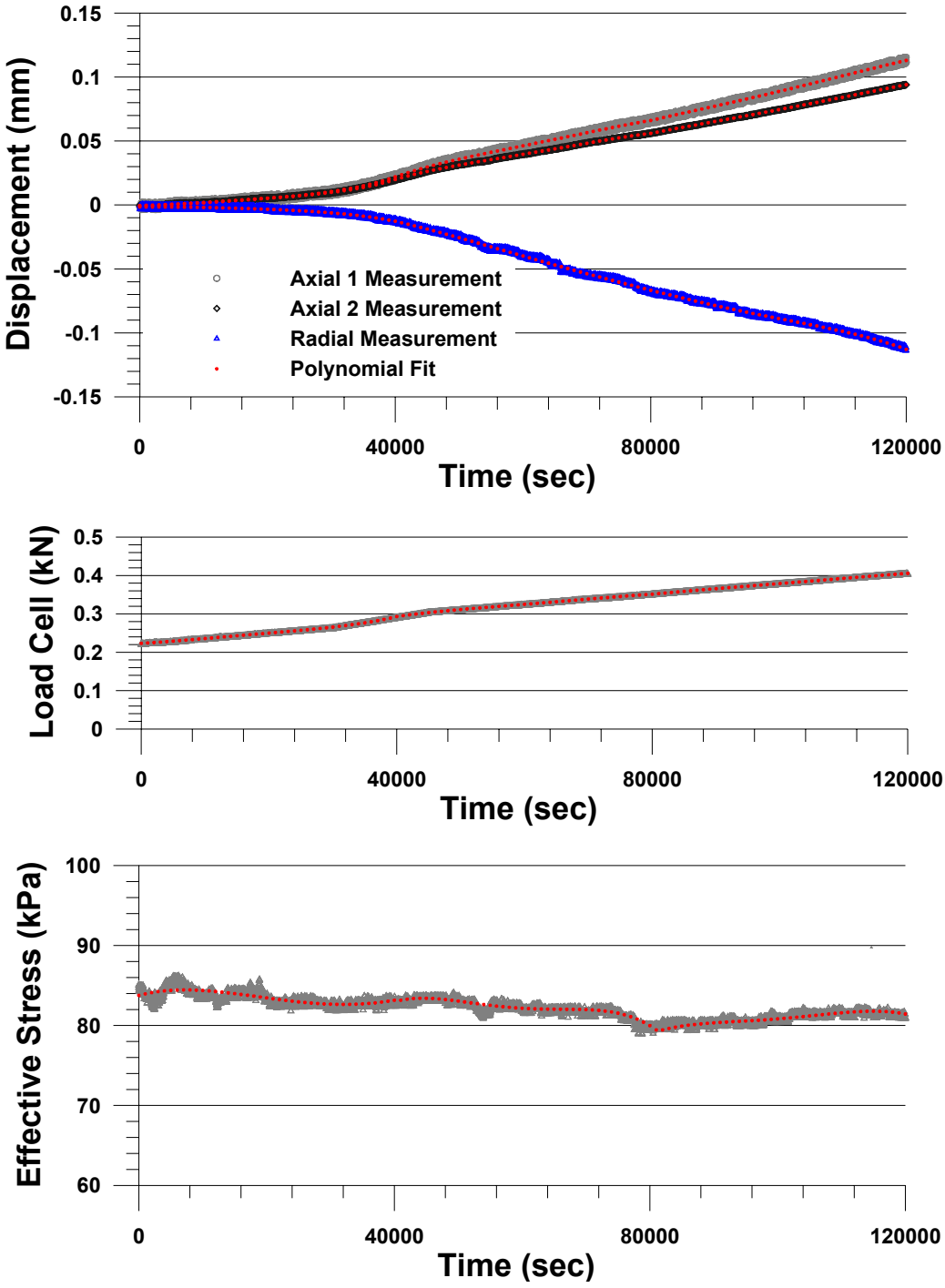

Figure 3-15 Five measured quantities and their polynomial fitted data in 3 sections (0-120,000)

3.4.4. Bender Element Test Analysis

The analysis of bender element tests entails the determination of the wave travel time t_{BE} between the transmitter and receiver element, which is then used to calculate the propagation velocity, V_{BE}, given a known length L_t between the two elements. As mentioned before, the determination of the wave travel time is the crucial step in the calculation of V_{BE}. The dimension L_t was computed from the global axial strain ε_{ag} calculated by the CKC triaxial system at the time of each bender element test and the initial sample length L_0. In this dissertation, the travel time t_{BE} was calculated using cross-correlation, a digital signal processing technique commonly used in field and laboratory wave propagation studies and recommended by Viggiani and Atkinson (1995a), and Arulnathan et al (1998). Cross correlation consists of the integration over time and total signal length of the product of two time-domain signals *S1* and *S2* that have been shifted by a time τ.

$$CC_{S1-S2}(\tau) = \lim_{T\to 0} \frac{1}{T} \int_{T} S1(t) S2(t+\tau) dt \qquad (3\text{-}9)$$

where T is the total recorded time, commonly 5 ms for the present study. Each value of τ and subsequent integration produces a cross correlation value $CC_{S1\text{-}S2}$. For two signals of a similar nature, the maximum value of $CC_{S1\text{-}S2}$ occurs at the time shift τ representing the travel time t_{BE} between the bender elements. The primary benefit of using cross correlation to estimate the travel time is that it utilizes both signals to find the travel time for the entire waveform, not just an individual point or peak. The impact of near-field effects on the selection of wave arrival times is minimized by cross correlation.

As is very common in modern digital signal processing, it is more convenient to perform cross correlation in the frequency domain rather than the time domain (Arulnathan et al, 1998). This requires the use of the Fast Fourier Transform (FFT) operation on each time-domain signal S1 and S2 to form the linear spectra representations *L1(f)* and *L2(f)*. The product of $L1(f)\cdot L2^{*}(f)$, where $L2^{*}(f)$ is the complex conjugate of *L2(f)*, is defined as the cross-power spectrum $G_{S1\text{-}S2}(f)$. Using $G_{S1\text{-}S2}(f)$, the cross correlation value is defined in terms of the frequency domain as

$$CC_{S1-S2}(\tau) = IFFT[G_{S1-S2}(f)] \tag{3-10}$$

Figure 3-16 presents typical bender element data from a simple cross correlation routine programmed in MATLAB 6.5, a commercially available mathematical analysis program. The data presented in Figure 3-14 are from the bender element test on sample FB1TC2 during the K_0 reconsolidation stage. The results indicate that t_{BE} from the cross correlation analysis of the two signals equals 0.89 ms, corresponding to a V_{BE} of 167.64 m/s. The t_{BE} selected from peak-peak points of the input and output signals equals 0.93 ms, approximately 4% slower than the cross correlation value in this example. This difference between the two methods of estimating t_{BE} is generally within 5% for all of the experiments performed in the current study,

The propagation velocities V_{BE} determined from cross correlation analyses of the bender element tests were then used to calculate a dynamic modulus G_{BE} at each stress point during the K_0 reconsolidation and stress probe process. As previously mentioned in Section 3.1.7, G_{BE} was calculated using the Equation 3-1(Timoshenko and Goodier, 1970) by assuming that the triaxial specimen represented an infinite, isotropic, elastic medium

$$G_{BE} = \rho V_{BE}^{2} \tag{3-1}$$

where ρ is the total mass density of the soil sample at the particular time when V_{BE} is being measured.

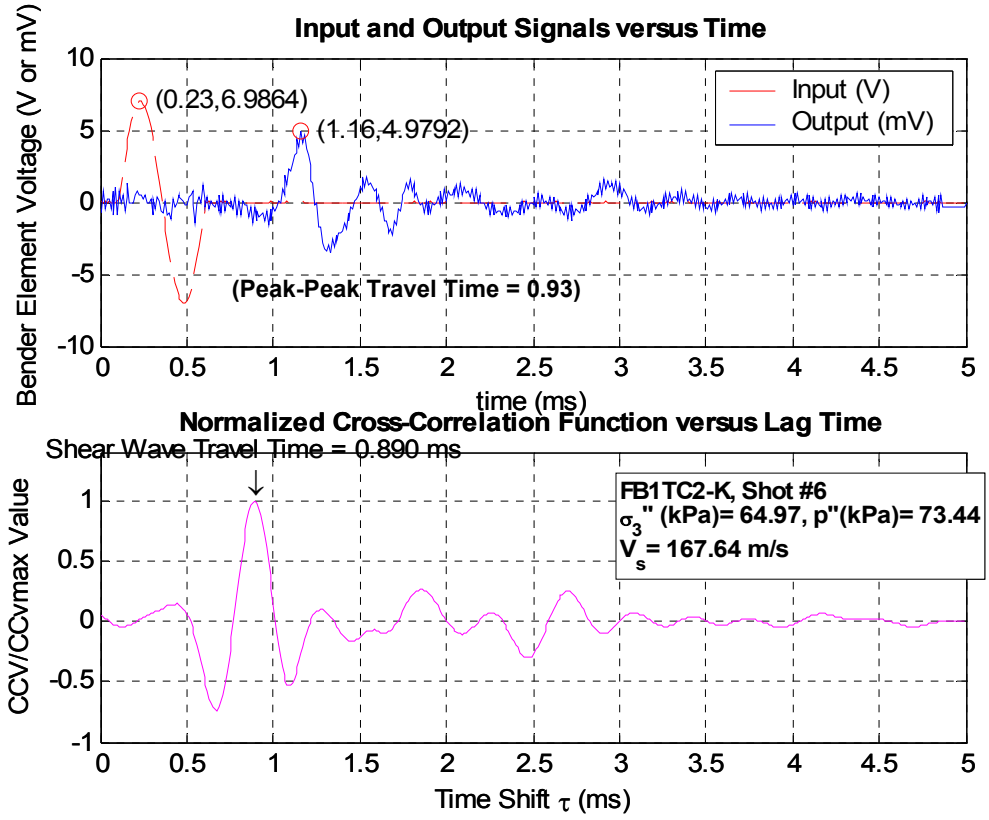

Figure 3-16 Example output from MATLAB program used to determine bender element wave propagation travel time using cross-correlation signal processing method

3.5. SUMMARY OF EXPERIMENTS

Table 3-4 summarizes the two types of stress probing tests. For the first type of the stress probing tests, specimens were K_0 consolidated to the in-situ stress state and sheared in 10 directions. For the second type of stress probe, specimens were K_0 reconsolidated to their in-situ stress states

with K_0 creep and then unloaded via a RTE path to the stress state where the deviatoric stress is half of the in-situ stress state also with the creep period. Due to the availability of the natural samples, 5 stress path tests were performed for the second type of the probing tests. Stress probing tests with 6 directions were performed with reconstituted samples to compare the responses of the natural samples.

Table 3-4 Summary of triaxial testing program

Stress probing	Initial	Stress Path	Block sample	Reconstituted Sample
"post-K_0" stress probing test	In-Situ K_0	Compression	5(1)	1
	In-Situ K_0	Reduced Compression	2	-
	In-Situ K_0	Reduced Extension	1	1
	In-Situ K_0	Extension	1	-
	In-Situ K_0	Constant p' loading & unloading	3	2
	In-Situ K_0	Constant q loading & unloading	3	2
	In-Situ K_0	Anisotropic loading & unloading	3	1
"post-unloading" stress porbing tests	Exc (unloading)	Constant q loading & unloading	2	1
	Exc (unloading)	Constant p' loading & unloading	2	-
	Exc (unloading)	Anisotropic unloading	1	-
		Total	24	8

3.6. SUMMARY

This chapter has described in detail the experimental program undertaken to investigate the small strain properties of compressible Chicago glacial clays. Three hand-cut block samples of these clays were obtained from the Ford Engineering Design Center deep excavation. A total of 27 high quality triaxial specimens were trimmed from block samples for stress path testing. Reconstituted specimens with a simple one-dimensional stress history and known maximum apparent preconsolidation pressure σ_p' were also successfully created using pulverized Chicago clay. A slurry consolidometer was used to create these specimens with initial water content approximately twice the liquid limit for these clays.

The K_0 reconsolidation and stress probe testing were conducted using a CKC e/p Cyclic Loader and custom-designed small strain testing equipment manufactured by GDS Instruments. The CKC device was used to control the manner in which the stress were applied, while the GDS instrumentation was used to make internal, on-specimen measurements of axial and radial deformations and axial loads. The accuracy and precision of the GDS LVDTs were 35 and 150 times greater than that of the CKC system, respectively. The lower-bound accuracy of the GDS LVDTs enabled accurate measurements of local shear and volumetric strains to 0.002% and 0.005%. The internal load cell was capable of accurately measuring axial stresses to ±0.3 kPa. A bender element system was also incorporated into the triaxial apparatus to make measurements of propagation velocity throughout the consolidation and stress probe testing phases. For some of the stress path tests, 3 sets of bender elements are installed to characterize the anisotropic nature of Chicago clays.

Each natural and reconstituted specimen was subjected to K_0 reconsolidation to a vertical effective stress of 137 kPa, a drained creep period, and then drained directional stress probing. Prior to consolidation, residual effective stresses were measured using a pore water pressure technique. The measured residual stress was used as an effective stress value to saturate the specimen. The reconsolidation was carried out at an average vertical stress rate of about 1.25 kPa per hour, followed by a 36 hour creep period under K_0 conditions. The measured strain rate at the end of creep period is less than 0.002%/day, which is generally 30 times slower than the shearing rate during stress probing.

Two types of stress probe tests were performed. The first type was intended to allow for the assessment of small strain behavior under general stress conditions. Duplicate probes were performed for several of these stress paths to examine the natural variability of block samples. The second type was performed to simulate the stress state of soils experiencing an unloading type of stress change. Bender element tests were performed during consolidation, creep, and stress probing for each test.

The data analysis for this experimental program required signal processing methods for the bender element data and smoothing of an extremely large number of data points for each stress probe. Cross-correlation techniques were used to calculate the propagation velocity for each bender element tests. A regression technique with polynomial functions was used to reduce the influence of electrical noise and data scatter at small displacements and loads during the stress probes. Stress-strain data are generated from the data fitted by the polynomial functions.

CHAPTER 4 GENERAL STRESS-STRAIN BEHAVIOR

Small strain stiffness and stiffness anisotropy are now recognized as important features of soil behavior related to the ground movements and the interpretation of field data both in earthquake engineering and soil structure interaction problems. Since Burland (1989) suggested that working strain levels in soil around well-designed tunnels and foundations were typically less than 0.2 %, there have been a number of attempts (e.g. Atkinson et al. 1990; Clayton and Heymann 2001; Santagata et al. 2005) to characterize the stiffness variation in small strain region. These studies also found that the stiffness anisotropy plays an important role in soil behavior. Simpson et al. (1996) showed the importance of initial stiffness anisotropy on predicted deformations due to tunneling in stiff clays.

There have been a number of studies concerning the stress strain response of stiff soils such as London clay or Gault clay, in terms of the small strain non-linearity and stiffness anisotropy using on-specimen LVDTs and bender elements (Jamiolkowski et al. 1995; Pennington et al. 1997; Jovicic and Coop 1998; Lings et al. 2000). However, there have been no data reported for lightly overconsolidated clays deposited in fresh water environments. The experimental program described in this thesis is performed with high quality hand-cut block samples and focuses not only on the small strain non-linearity, but also the yield characteristics at larger strains.

This chapter presents test results and analyses of an experimental program to define the stress-strain responses of block samples under axi-symmetric conditions of compressible, fresh-water Chicago glacial clays from strain levels as low as 0.002%.

Section 4.1 presents the index properties and oedometer test results. Results provide a

measure of the natural variation within the block samples. Section 4.2 shows the residual effective stress, saturation and K_0 reconsolidation behaviors. Recompression strains are used to analyze the quality of the undisturbed block samples, and are shown to be related to the residual effective stress. Section 4.3 presents the stress-strain response of the block samples measured from the internal measurement system. The results of the directional stress probes are presented for both large and small strain levels, and analyzed separately in terms of shearing and volumetric behaviors. Section 4.4 summarizes the limit state and the failure behavior. Finally, Section 4.5 summarizes the previous sections and draws conclusions.

4.1. INDEX PROPERTIES AND OEDOMETER TEST RESULTS

Index tests were conducted on block samples of FB1, FB2 and FB3. The index test results were used for initial assessments of block sample similarities and for identification of the geologic unit. Oedometer tests were performed to evaluate their stress history and initial void ratios.

Figure 4-1 shows the oedometer test results from 2 specimens taken from each block sample. The consolidation tests were performed using variable load increment ratios (LIR) less than or equal to 1.0 in order to better define the yield point. Oedometer cells with integral cutting rings were employed to minimize any additional disturbance due to trimming and sample transfer. Even though there is natural variation of the void ratio, the overall characteristics are very similar in each block sample.

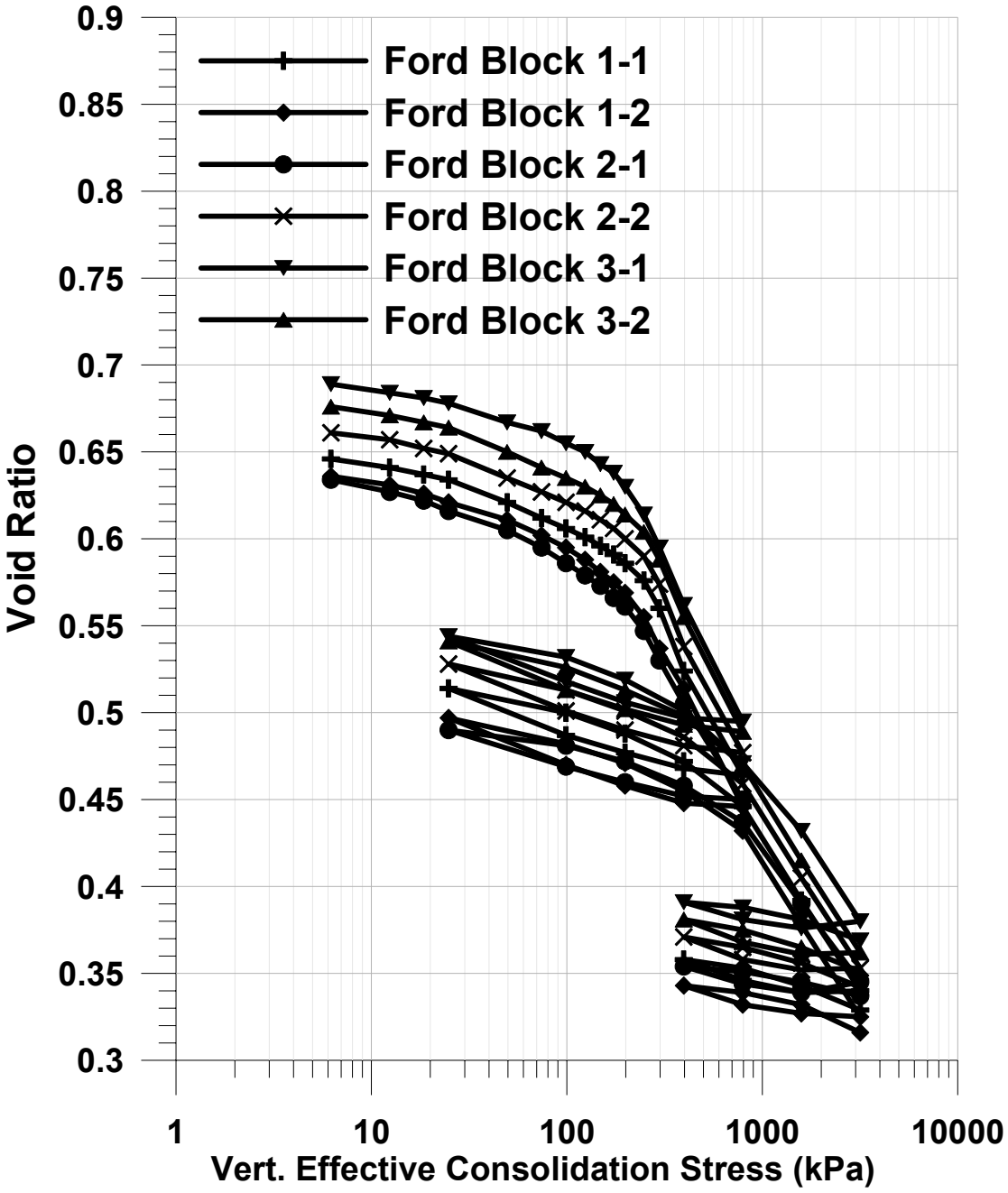

Figure 4-1 Oedometer test results for block samples FB1, FB2 and FB3

Table 4-1 presents a summary of the mean properties measured from the triaxial specimens and standard deviations. The mean natural water contents and Atterberg limits are very similar for specimens from all 3 blocks. In addition, the consolidation characteristics and

stress histories of block samples are almost identical. The standard deviations of the index properties are low, suggesting little variation within each block and between blocks. According to the previous research on Chicago clays (Peck and Reed 1954; Finno and Chung 1992; Chung and Finno 1992), the block samples are from the Deerfield till unit, which is a waterlain paratill, characterized by its uniform texture.

Table 4-1 Summary of index properties and 1D consolidation characteristics of block samples

	Block 1	Block 2	Block 3	Average
Natural Water Content (%)	24.3-25.7	24.9-25.3	25-25.3	24.9 (0.3)
Liquid Limit (%)	29.5-31.8	30.5-31.8	31.5-32	30 (1.1)
Plasticity Index (%)	14.2-16.4	14.9-16.1	15-15.8	15.1 (0.8)
Specific Gravity	2.71-2.72	2.71-2.72	2.71-2.72	2.72 (0.06)
Max. Past Pressure (kPa)	225-230	220-235	235	235 (10)
OCR	1.65-1.7	1.65-1.7	1.65-1.7	1.7
Compression Index, C_c	0.19	0.19	0.21	0.2 (0.01)
Recompression Index, C_r	0.023	0.030	0.027	0.028 (0.002)

4.2. SATURATION AND K_0 RECONSOLIDATION BEHAVIOR OF BLOCK SAMPLES

4.2.1. Residual Effective Stress and Saturation Behavior

The residual effective stress, p_r', was determined for all natural triaxial specimens using the pore water pressure method detailed in Section 3.3.3. Results for each specimen are listed in Table 4-2. The mean p_r' for specimens trimmed from FB1 was 43 kPa, with a range of 33 to 64 kPa. The mean p_r' for FB2 specimens was 41 kPa and the range was from 38 kPa to 51 kPa. The mean p_r' for FB3 specimens was 47 kPa and the range was from 35 kPa to 54 kPa. When considering all

of the specimens, the mean value of p_r' was 47 kPa and the standard deviation was 6 kPa, corresponding to a coefficient of variation (COV) of 0.13.

As explained in Section 3.3.3, the residual stress concept is rooted in the perfect sampling concept. The "perfect sampling" effective stress, σ_{ps}', was first discussed by Ladd and Lambe (1963). The value of σ_{ps}' can be determined either in the laboratory through undrained unloading tests along stress paths assumed to be the same as that experienced by samples in the field, or by the equation set up with the assumption of Skempton pore-pressure parameter, A, and earth pressure coefficient at rest, K_0. For lightly overconsolidated, low plasticity clays such as the Chicago glacial clays, the expected ratio of $\sigma_{ps}'/\sigma_{v0}'$ would be in the range of 0.58 to 0.62 based on a K_0 value from 0.50 to 0.55 and an assumed A_u value of 0.15 for lean clays. However, the average p_r'/σ_{v0}' ratio is around 0.34 and maximum value is 0.47. This indicates that even though the block samples were carefully hand-carved, it is inevitable to experience disturbance arising from causes other than stress relief.

In addition to providing a qualitative indicator of sample disturbance, the residual effective stress can be used as the effective stress during the saturation. Because the physical meaning of residual stress is the negative pore pressure in the specimen, the least amount of strain is developed during saturation if the specimen is saturated at the measured residual stress. Figure 4-2 compares the axial and radial strains of Ford block specimens saturated at values of 10 kPa and the p_r'. As shown in Figure 4-2, negligible strains developed when a specimen was saturated at the residual stress, whereas the specimen saturated at 10 kPa swelled to produce 0.5% radial strain and 0.2% axial strain. This swelling alters the structure of the clay which affects the overall behavior. The detailed effect of swelling during the saturation is presented in Appendix A.

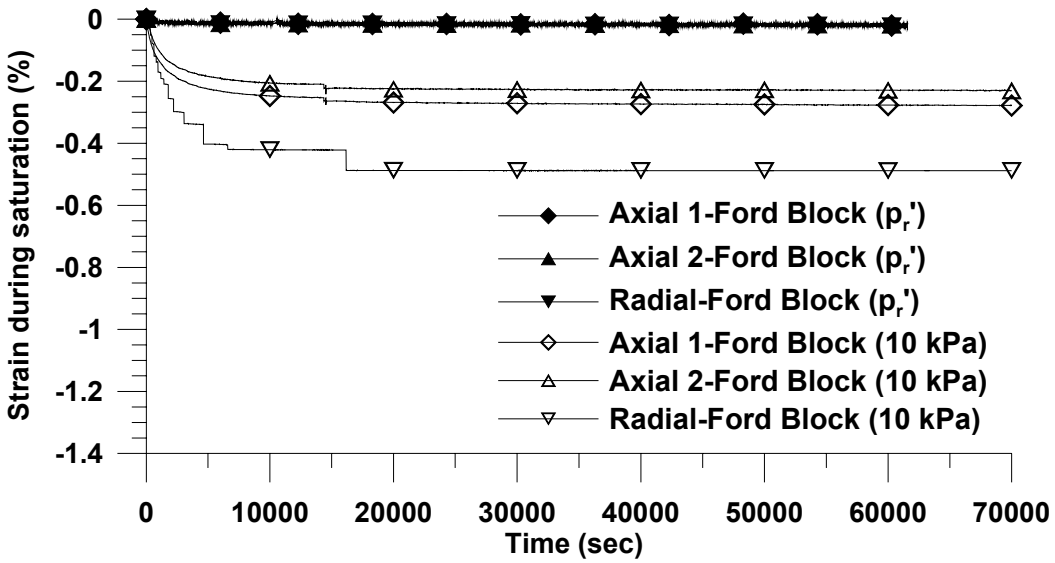

Figure 4-2 axial and radial strain comparison between residual effective stress saturation and 10 kPa saturation

Table 4-2 Residual effective stress data for block samples

Test	Residual stress (p_r')	Test	Residual stress (p_r')
FB1TC1	37.42	**FB2TC1**	37.42
FB1RTC1	44.30	**FB2CQL1**	42.07
FB1RTE1	38.27	**FB2CMSE1**	42.04
FB1TE1	49.65	**FB2CQU1**	39.00
FB1TC2	51.15	**FB2TC2**	51.00
FB1RTC2	33.45	**FB2AU1**	42.00
FB1CMS1	38.30	**FB2TC3**	38.42
FB1CMS2	64.21	**FB2 Average**	41.71 (4.53)
FB1CQL1	32.66		
FB1 Average	43.27 (10.22)		
FB3AL1	47.00		
FB3sCMS1	47.71		
FB3sCQL1	47.17		
FB3sCMSE1	35.28		
FB3sCQU1	54.26		
FB3AU1	51.82		
FB3sCQU2	40.26		
FB3sAU1	49.25		
FB3 Average	46.59 (6.13)		
Average	43.92 (6.20)		

4.2.2. K_0 Reconsolidation Behavior

4.2.2.1. K_0 Stress Paths

Each specimen was reconsolidated under K_0 conditions from p_r' to a σ_{vc}' of 137 kPa. As explained in Section 3.3.4, the K_0 reconsolidation process allows the soil sample to reach a predetermined vertical effective stress while changing the effective radial stress to maintain one-dimensional consolidation conditions. Figure 4-3 shows the radial effective and deviatoric stresses during K_0 reconsolidation and creep period based on both internal and external measurement systems. The effective radial stress σ_r' is measured by the external transducers and used in stress calculations for the internal system. At the start of the consolidation stage, the deviatoric stress increases while the radial effective stress decreases to find the stress point where the axial strain shows different value than the volumetric strain. Then, the deviatoric and effective radial stresses are back to the residual stress state. After that initial loop, the radial effective stress is adjusted with small deviatoric stress increments to minimize the difference between the axial and volumetric strains. Here, the effective radial and deviatoric stresses are controlled based on the external measurements.

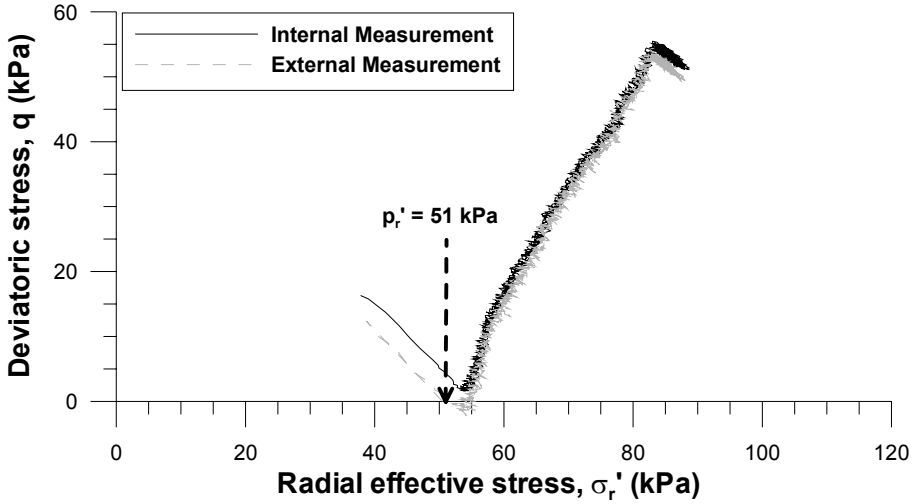

Figure 4-3 Deviatoric stress and radial effective stress during K_0 reconsolidation and creep

The overall responses from internal and external measurement system are very similar with the exception of the deviatoric stresses, which differ by 3 to 4 kPa difference. This difference comes from the different measurement of deviatoric stress in the external and internal systems. The deviatoric stress in the external system is calculated from the force measured from the external load cell and the area based on the initial diameter and the radial strain from the axial and volumetric strain measured in the external system while deviatoric stress in the internal system is measured from the force measured in the internal load cell and the area based on the initial diameter and the radial strains directly measured from the radial LVDT.

The effect of the different residual effective stresses and the method of test control is that the effective radial stress σ_r' is not forced to be the same for each "identical" specimen, but is allowed to change as a function of the constitutive behavior of the specimen. As a result, the principal stress difference or deviatoric stress, q at the final σ_{vc}' is not necessarily the same, nor is the mean normal effective stress p'. Stress paths of block samples during the K_0 reconsolidation and creep periods are presented in Figure 4-4. The stress paths indicate that the stress at the end of K_0 consolidation and creep is directly influenced by the residual stress.

Examination of the stress data at the end of consolidation and creep in Table 4-3 indicates that the natural specimens generally reached the same end stress states. The mean σ_{vc}' measured with the internal measurement system was 139.42 kPa with a standard deviation of 1.33 kPa. The mean K_0 value at this σ_{vc}' was 0.58, with a range from 0.48 to 0.66. The values of p' varied from 90 to 108 kPa with an average of 100.43 kPa and a standard deviation was 4.6 kPa. The values of q varied from 48.0 to 73.0 kPa, with an average of 58.48 kPa and a standard deviation of 6.5. Based on the COV for p' (4.59%) and q (13.92%), it is reasonable to conclude that each natural specimen reached similar final stress points. Note that FB2TC3 was saturated at 10 kPa,

which is much lower than the measured residual effective stress. As a result, it experienced more swelling during saturation. As mentioned in the previous section, swelling can alter the structure of the clay, and affect the overall behavior. Thus, the stress condition of FB2TC3 at the end of consolidation and creep was not considered in the calculation of mean and standard deviation.

Table 4-3 Stress state at the end of K_0 consolidation and creep

Test	p' (kPa)	q (kPa)	σ_{vo}' (kPa)	K_0 value
FB1TC1	96.32	63.12	138.40	0.54
FB1RTC1	98.95	60.04	138.98	0.57
FB1RTE1	98.35	60.60	138.75	0.56
FB1TE1	104.30	52.20	139.10	0.62
FB1TC2	103.03	54.30	139.23	0.61
FB1RTC2	90.22	68.35	135.79	0.50
FB1CMS1	97.78	59.94	137.74	0.56
FB1CMS2	104.82	50.26	138.33	0.64
FB1CQL1	92.10	67.13	136.85	0.51
FB1 Average	**98.43 (5.11)**	**58.44 (8.60)**	**138.13 (1.15)**	**0.57 (0.05)**
FB2TC1	106.79	51.99	141.45	0.63
FB2CQL1	107.94	48.35	140.17	0.66
FB2CMSE1	103.93	54.53	140.28	0.61
FB2CQU1	99.82	62.65	141.59	0.56
FB2TC2	105.35	49.77	138.53	0.64
FB2AU1	97.87	61.22	138.68	0.56
FB2TC3*	84.72	84.14	140.81	0.40
FB2 Average	**103.62 (3.98)**	**54.75 (5.96)**	**140.12 (1.31)**	**0.61 (0.04)**
FB3AL1	98.53	63.62	140.94	0.55
FB3sCMS1	101.00	61.26	141.84	0.57
FB3sCQL1	100.44	59.72	140.25	0.57
FB3sCMSE1	92.93	73.47	141.91	0.48
FB3sCQU1	98.24	60.24	138.40	0.56
FB3AU1	101.89	54.22	138.04	0.61
FB3sCQU2	100.13	59.06	139.50	0.58
FB3sAU1	109.15	48.98	141.80	0.65
FB3 Average	**100.29 (4.52)**	**60.07 (7.09)**	**140.34 (1.56)**	**0.57 (0.05)**
Average	**100.43 (4.61)**	**58.48 (6.48)**	**139.42 (1.33)**	**0.58 (0.05)**
COV (%)	**4.59**	**13.92**	**0.96**	**8.62**

During the creep period, deviatoric and radial effective stresses are still controlled to maintain the K_0 condition. As a result, radial effective stress increased as the vertical effective stress remained constant during the creep to maintain zero lateral strain. Consequently, the deviatoric stress decreased during this period.

Based on the difference in mean slopes of the recompression and creep stages, the change in stress path direction was approximately 88 to 95 degrees. The stress path lengths were computed to vary from approximately 6 to 10 kPa. Given the relatively small length of the creep path compared to the length of stress path during K_0 reconsolidation (65-100 kPa), a minimal impact on the directional stress-strain behavior was expected. Significantly longer creep periods yielding longer creep stress path lengths would be expected to have a larger effect on stress-strain response, particularly in the small strain range.

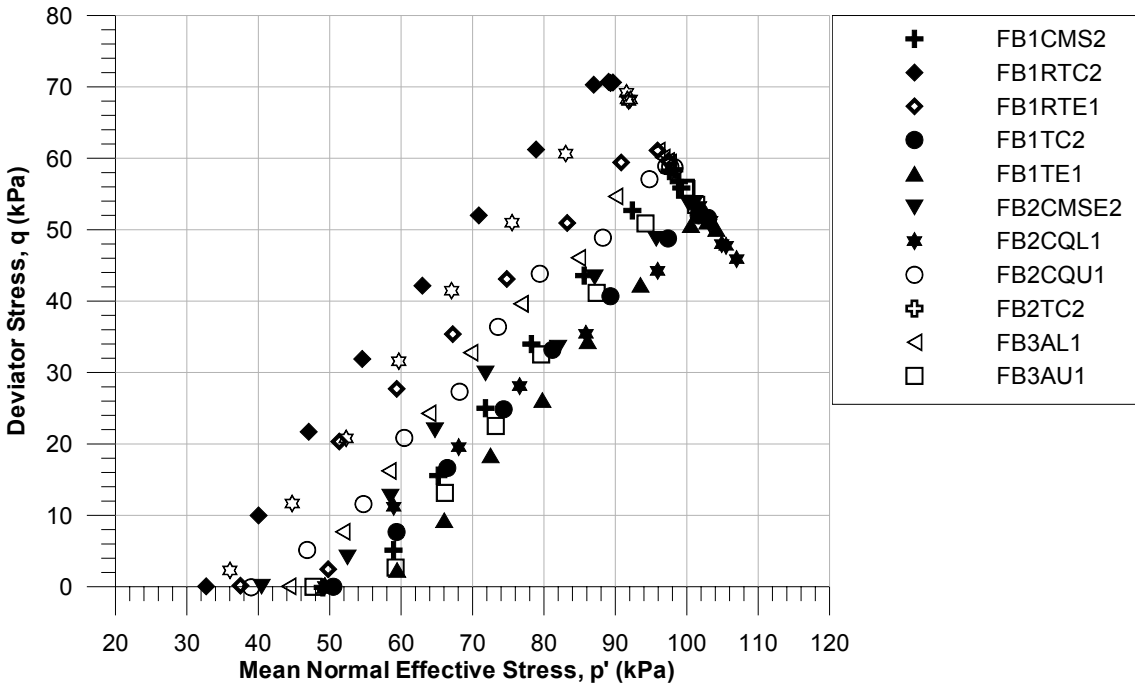

Figure 4-4 Stress paths of block samples during K_0 reconsolidation and creep period

4.2.2.2. Strain response during K_0 reconsolidation

The axial, radial and volumetric strains at the end of K_0 reconsolidation and creep are presented in this section. Computed strains for both the external and internal measurement systems are presented to illustrate the difference between the two sets of measurements.

Figure 4-5 shows (a) axial and radial strain and (b) axial and volumetric strain during K_0 reconsolidation and creep. The data shows the fluctuation inherent in each system. Clearly, the internal system measures the strains with less fluctuation. The initial stress loop explained in the previous section results in a loop in the strain response. Both systems show similar axial strains during the loop, but the external system shows larger radial strains possibly because the radial strain is computed indirectly based on the axial and volumetric strains assuming uniform deformation within the specimen.

Since the deviatoric stress and the radial effective stress are controlled based on the external measurement system, axial and volumetric strains are essentially the same in the external measurement system, indicating that the computed external radial strain is marginally zero and that one-dimensional consolidation conditions had been maintained. The internally measured radial strain is less than 0.1% throughout the K_0 reconsolidation and creep period. While the magnitude of this strain is considered small, the accumulation of any amount of radial strains in the central portion of the specimens could serve to introduce an additional degree of destructuring prior to the directional stress probes.

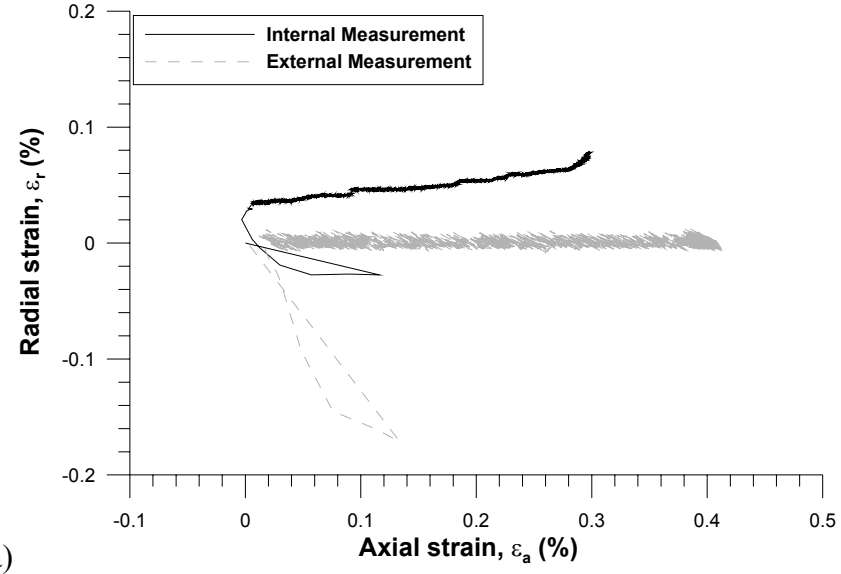

(a)

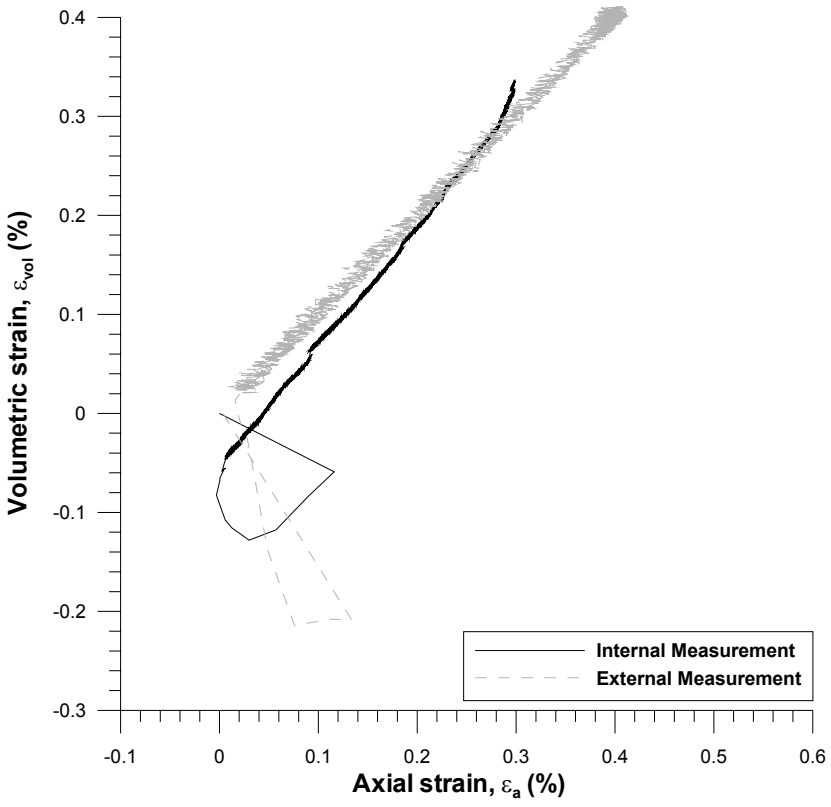

(b)

Figure 4-5 Strains developed during K_0 reconsolidation and creep (a) axial and radial strain (b) axial and volumetric strain

Table 4-4 summarizes axial and volumetric strain measured in the internal system during K_0 reconsolidation and creep period. The difference between the axial and volumetric strains in each block sample is less than 0.05%, which means the radial strain is minimized less than 0.025%. The axial or volumetric strains in each block show similar range with a standard deviation of less than 0.15%. Here, note again that FB2TC3 is the test saturated at 10 kPa. Relatively large axial and volumetric strains occurred during consolidation in this test due to the excessive swelling during the saturation process.

The axial strain occurred during creep was separately reported in Table 4-5. The creep strain is less than 5% of reconsolidation strain in most cases. FB2TC1, which had a one week creep period, showed a creep strain of more than 9% of reconsolidation strain. FB2TC3, which was saturated at 10 kPa, showed a large creep strain of about 45% of the reconsolidation strain. Again, the saturation at an inappropriate effective stress can affect the overall response of Chicago clays.

The axial and volumetric strains during K_0 reconsolidation can be used to qualitatively assess the sample disturbance (Terzaghi et al 1994; Lunne et al 1997). The use of large triaxial specimens over consolidation specimens to assess the sample disturbance is more appropriate because the greater specimen size is less likely to be affected by small zones of disturbance. Based on the Sample Quality Designations (SQD) according to Terzaghi et al (1994), all of the natural block simples have SQDs of "A," which is very good or excellent. However, the specimen saturated at 10 kPa (FB2TC3) shows a SQD of "B." The strain response shows that the saturation at effective stress significantly lower than p_r' affects the consolidation response of Chicago clays.

Table 4-4 Strains at end of K_0 consolidation and creep for natural samples

Test	ε_a (%)	ε_{vol} (%)	ε_a (Creep) (%)
FB1TC1	0.330	0.325	0.015
FB1RTC1	0.198	0.197	0.012
FB1RTE1	0.262	0.416	0.011
FB1TE1	0.177	0.333	0.014
FB1TC2	0.287	0.340	0.013
FB1RTC2	0.331	0.387	0.015
FB1CMS1	0.419	0.430	0.011
FB1CMS2	0.440	0.295	0.014
FB1CQL1	0.414	0.477	0.015
FB1 Average	**0.317 (0.096)**	**0.355 (0.083)**	**0.013 (0.002)**
FB2TC1**	0.157	0.215	0.020
FB2CQL1	0.263	0.183	0.016
FB2CMSE1	0.139	0.143	0.013
FB2CQU1	0.128	0.108	0.015
FB2TC2	0.121	0.120	0.018
FB2AU1	0.272	0.277	0.011
FB2TC3*	1.164	1.107	0.500
FB2 Average	**0.18 (0.069)**	**0.174 (0.064)**	**0.016 (0.003)**
FB3AL1	0.251	0.313	0.014
FB3sCMS1	0.210	0.112	0.012
FB3sCQL1	0.190	0.173	0.011
FB3sCMSE1	0.491	0.489	0.023
FB3sCQU1	0.220	0.210	0.013
FB3AU1	0.056	0.048	0.015
FB3sCQU2	0.513	0.493	0.035
FB3sAU1	0.285	0.213	0.022
FB3 Average	**0.277 (0.154)**	**0.256 (0.164)**	**0.018 (0.008)**
Average	**0.268 (0.109)**	**0.274 (0.106)**	**0.016 (0.004)**

4.3. STRESS-STRAIN RESPONSE OF NATURAL SPECIMENS

4.3.1. Stress Paths

Typical stress path data for each probe direction are illustrated in Figure 4-6 in q-p' space; the notations used in the figure are summarized in Table 4-6. Figure 4-6(a) shows the stress paths from the end of K_0 consolidation and creep, whereas Figure 4-6(b) shows incremental stress

paths beginning at a common point ($\Delta p'$, Δq) = (0, 0). Each path's data were zeroed as a result of the relatively small variation in the end stress states following K_0 consolidation and creep stages reported in the previous section. The length and direction of each stress path represents the actual data. All paths follow straight lines of constant slope η due to the drained nature of the testing program. Small variations in intended path directions and straightness resulted from minor fluctuations in the CKC e/p loading system and the development of small excess pore pressures, generally no more than 2 to 3 kPa, measured at the ends of the specimen.

Table 4-6 Notation for directional stress probe

Label	Description	Label	Description
AL	Anisotropic loading ($\eta = 0.6$)	AU	Anisotropic unloading ($\eta = -0.4$)
TC	Triaxial compression	RTE	Reduced triaxial extension
CMS	Constant mean normal stress compression	CMSE	Reduced constant mean normal stress
RTC	Reduced triaxial compression	TE	Triaxial extension
CQL	Constant shear loading	CQU	Constant shear unloading

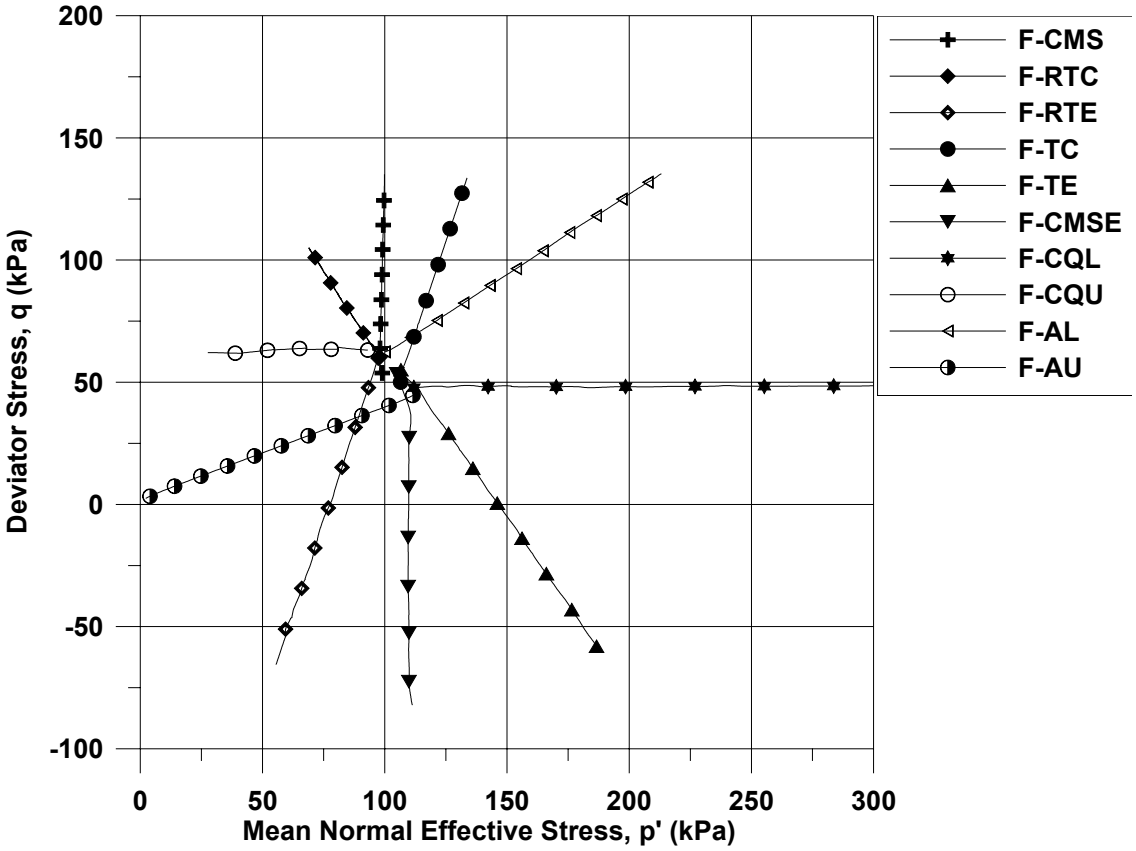

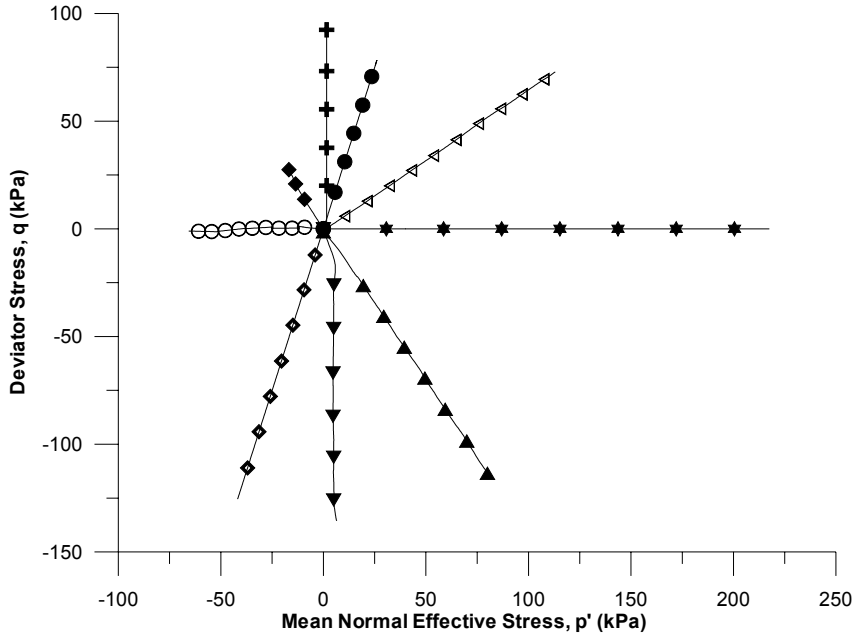

Figure 4-6 Stress paths for selected natural specimens in *p'*-*q* space (a) in the original stress state (b) in rezeroed state

4.3.2. Stress-Strain Response of Ford Block Samples

The stress probes included typical stress paths, such as triaxial compression and extension, as well as stress paths for investigating coupling effects, such as constant q loading and constant mean normal stress compression.

Under axisymmetric conditions like those in triaxial or oedometer tests, the soil response can be divided into volumetric and shear behavior and their cross-coupling explicitly described as shown in Equation (4-1) (Tu 2007).

$$\begin{Bmatrix} \Delta\varepsilon_v \\ \Delta\varepsilon_s \end{Bmatrix} = \begin{bmatrix} 1/K & 1/J_v \\ 1/J_s & 1/3G \end{bmatrix} \begin{Bmatrix} \Delta p' \\ \Delta q \end{Bmatrix} \tag{4-1}$$

where ε_v and ε_s are volumetric strain and shear strain, while p′ and q are mean normal effective stress and deviatoric stress, respectively.

In this section, the general stress-strain behaviors of the stress probe tests in terms of shear, bulk and two cross coupling moduli are presented. For the purpose of analysis, interpretation and discussion of the stress-strain data, the following isotropic elastic definitions of shear, bulk and two cross coupling secant moduli are employed:

$$G_{\text{sec}} = \frac{\Delta q}{3\Delta\varepsilon_s} \tag{4-2}$$

$$K_{\text{sec}} = \frac{\Delta p'}{\Delta\varepsilon_v} \tag{4-3}$$

$$J_{v\,\text{sec}} = \frac{\Delta q}{\Delta\varepsilon_v} \tag{4-4}$$

$$J_{s\,\text{sec}} = \frac{\Delta p'}{\Delta\varepsilon_s} \tag{4-5}$$

Figure 4-7 presents the deviatoric stress-axial strain responses and volumetric-axial strain responses based on the internal measurements for TC, RTE, CMS, CMSE, RTC and TE paths. For CQL and CQU paths, mean normal effective stress-axial strain response and volumetric-axial responses are plotted because the deviatoric stress does not change in those tests.

In triaxial compression (TC) and constant mean normal stress compression (CMS) stress paths, there are duplicate test results to check the natural variability. Two TC specimens show almost identical stress-strain response while CMS data show that the initial stiffness can vary 10-15% and the mobilized friction angle differs about 2^{o}. As was the case for index properties and stress history obtained from oedometer tests, duplicate block samples show little variation in responses, and thus differences in responses for various paths can be attributed primarily to constitutive behavior and not material variability.

Due to the limited range of the internal measurement system, stress strain responses based on the external measurements are used for those paths reached failure, TC, CMS, RTC, CQU, RTE, CMSE and TE.

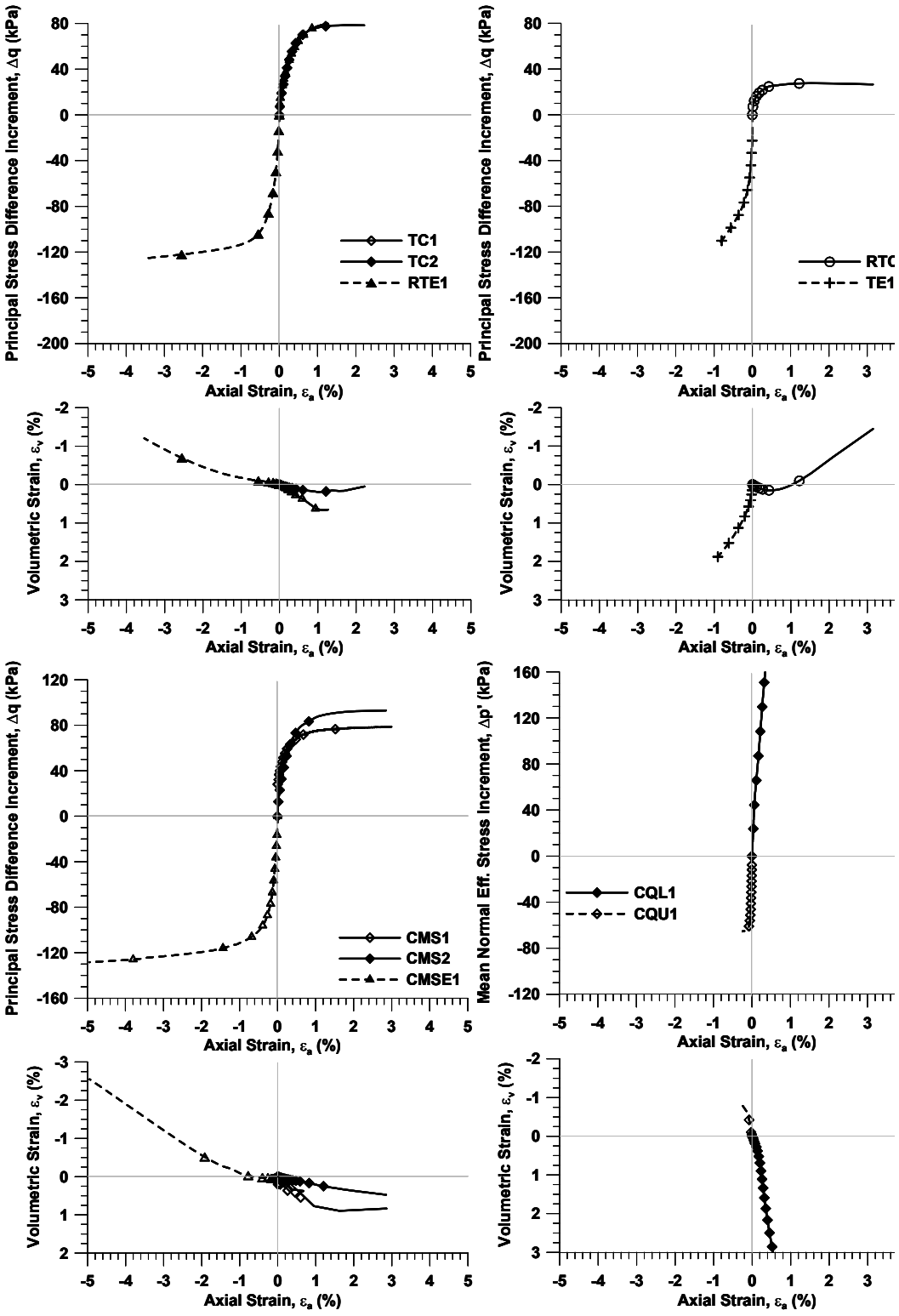

Figure 4-7 stress-strain data for stress probe tests

4.3.3. Deviatoric Stress-Shear Strain Behavior

Directional stress probe data were processed to plot the change in invariant deviatoric stress Δq, versus the local invariant shear strain, ε_{sh}.

Figure 4-8 shows a series of Δq-ε_{sh} plots for the same specimens whose stress paths were shown in Figure 4-6. The test data in Figure 4-8 are presented at two shear strain scales: large strain up to ±2% and at small strains up to ±0.01%. Multiple strain scales are used to illustrate the effects of stress path directions on large and small strain behavior.

At a large strain scale, all of the stress paths shown in Figure 4-8(a) show the yield occurs at strains less than 0.5%. While the deviatoric stresses at failure are different, computations show similar mobilized friction angles. All the responses are very similar in this scale up to ±0.1%. Failure was achieved for paths TC, CMS, RTC, and CQU and will be discussed in greater detail in Section 4.5.2.

The small-strain response to the directional stress probes is presented in Figure 4-8(b). The data are plotted for $-0.01\% \leq \varepsilon_{sh} \leq 0.01\%$ to accentuate the behavior just beyond ±0.002% strain, the lower limit of accurately measured small strains with the experimental system used herein. At this level of strain detail, the differences in Δq-ε_{sh} behavior are much more visible than in Figure 4-8(a). The probe data generally indicates that at small ε_{sh}, the slopes of the Δq-ε_{sh} curves are relatively smaller in compression than in extension for all path directions, except the RTC path. To investigate the shear stiffness in this small strain range, secant shear modulus degradation of the stress probe tests are plotted in Figure 4-9.

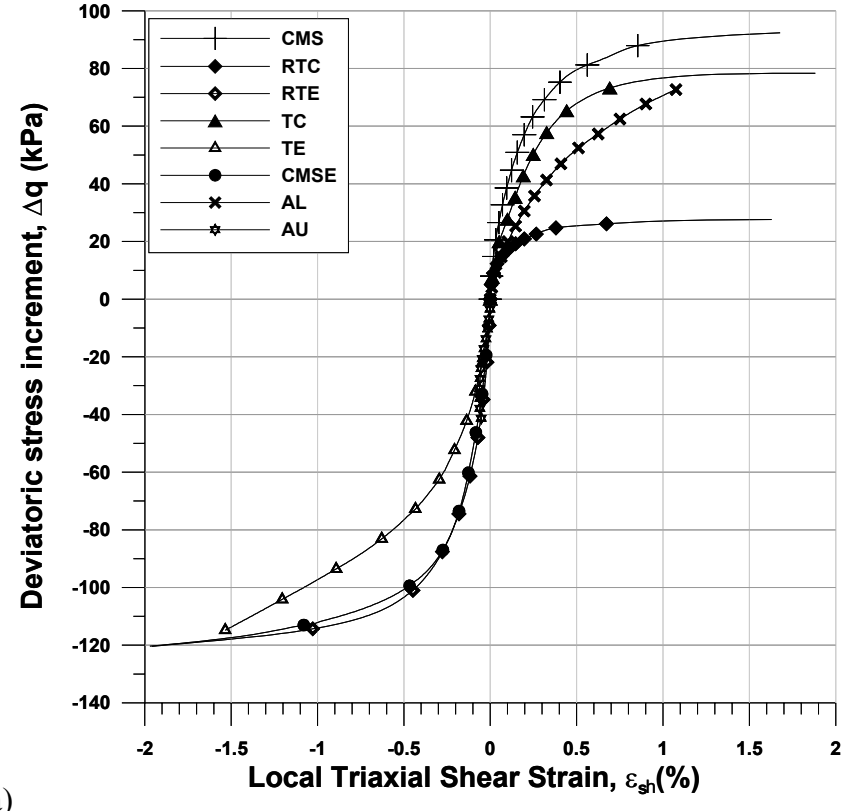

(a)

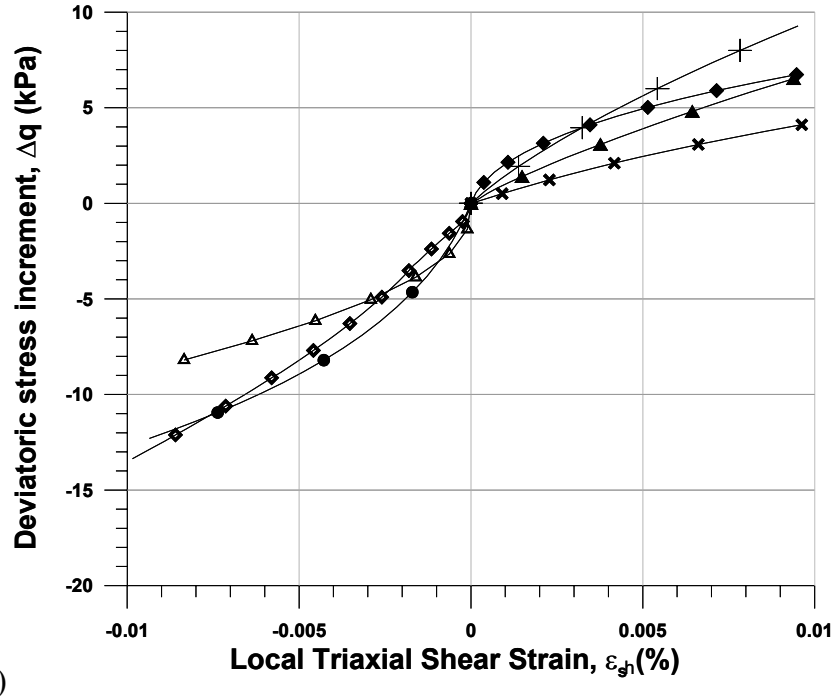

(b)

Figure 4-8 Change in deviatoric stress q versus local triaxial shear strain ε_{sh} for selected natural specimens (a) complete test data, (b) test data for ε_{sh} ±0.01%

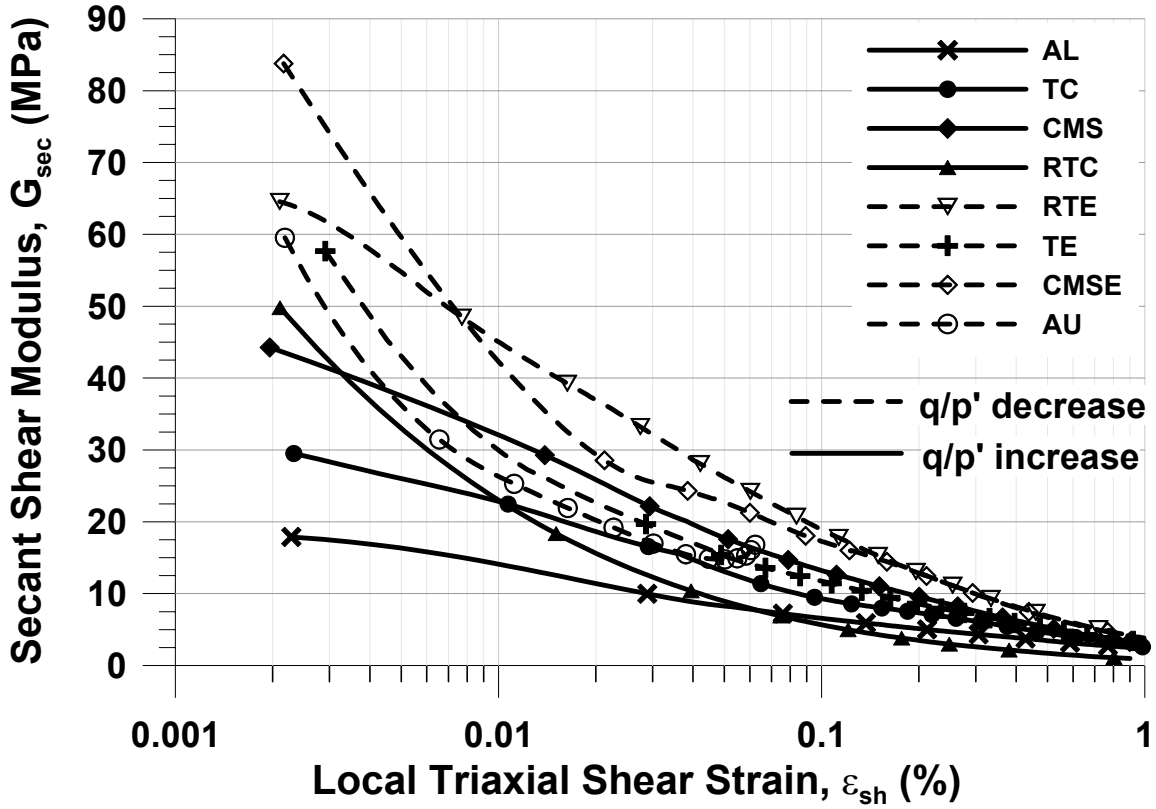

Figure 4-9 Shear stiffness degradation curves of block samples for stress probe tests

The maximum and minimum calculated G_{sec} values at ε_{sh} of 0.002% are 85 MPa and 18 MPa for probes CMSE and AL, respectively. Various researchers have referred to the strain level beyond which the modulus degrades rapidly as an elastic threshold strain (e.g., Santagata 1998; Clayton and Heymann 2001) but the data show no a region wherein the shear moduli are constant (and can be interpreted as a linear elastic region), at least at strain levels larger than 0.002%.

As shown clearly, the shear moduli of soft Chicago glacial clay strongly depends on the stress path direction. Overall, the shear moduli in the stress probes wherein q and the stress ratio, $\eta = q/p'$, is increased ("loading") are smaller than those in the stress

probes where q and η initially decrease ("unloading"). The pattern of shear moduli is more distinct when they are plotted against the angular difference from the CQL path (i.e. horizontal path), as shown in the upper left inset in Figure 4-10. In Figure 4-10, the values of G_{sec} for 0.002%, 0.01%, and 0.1% strains are plotted versus the angle θ calculated for each of the stress probe. The path CQL would plot at both 0° and 360°. The variation in G_{sec} is nonlinear with respect to stress path rotation angle θ for all small strain levels. The dependence of shear modulus on θ is large at 0.002% and 0.01% ε_{sh}, but the apparent directional dependence decreases as the strains reach and exceed 0.1%. The secant shear modulus is technically indeterminate at CQU path at 180^{o} because there is no change in q for the probe. The curves should be discontinuous at this point, but the data trend is clear to either side.

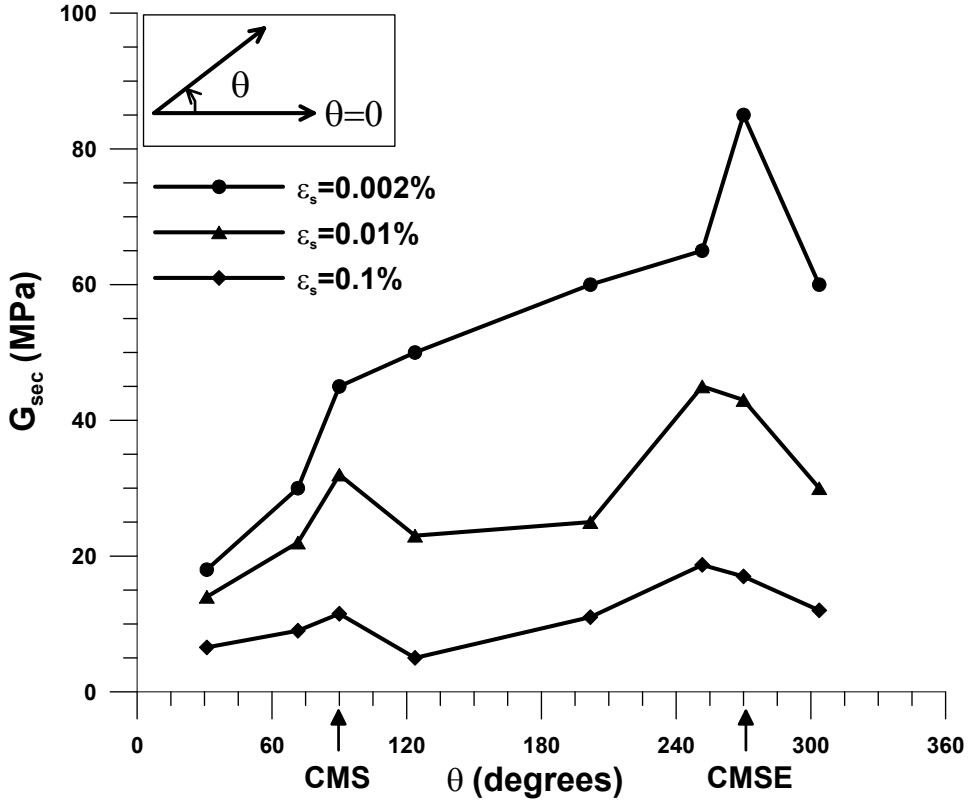

Figure 4-10 Variation of secant shear modulus G_{sec} as a function of angular difference in stress probe direction

4.3.4. Mean Normal Effective Stress-Volumetric Strain Behavior

Directional stress probe data were processed to allow plotting of the change in mean normal effective stress $\Delta p'$ versus the internally-measured volumetric strain ε_{vol}.

Figure 4-11 shows a series of $\Delta p'$-ε_{vol} plots for the same specimens whose stress paths were shown in Figure 4-6. The test data in Figure 4-11 are presented at two strain scales: large volumetric strain up to ±2%, and at small strains up to ±0.01%. Multiple strain scales again are employed to illustrate the effects of stress path directions on large and small strain behaviors. For the present discussion, "loading" paths will refer to

probes for which $\Delta p'$ increased (CQL, AL, TC, and TE), and "unloading" paths are designated by probes for which $\Delta p'$ decreased (RTC, CQU, AU, and RTE).

Paths CQL, AL, and TE resulted in the development of compression strains because of the changes in $\Delta p'$ caused by the stress probe. The changes in $\Delta p'$ for probe TC (Figure 4-11a) are much smaller than for the other loading probes, and subsequently resulted in the development of less volumetric strain prior to failure. At large strains, the loading paths continue to increase unlike deviatoric stress-shear strain response, wherein q becomes constant at failure. The response for unloading paths CQU, AU, and RTE indicates that the initial behavior is stiff, followed by volumetric yielding and the achievement of failure conditions for probes CQU and RTE.

Stress probe RTC resulted in ε_{vol} of 0.2% at failure, but it is notable that the volumetric strain was still positive for an unloading path that resulted in a reduction of $\Delta p'$. This behavior resulted from a significantly larger positive axial strain component than the radial strain component, rendering a positive ε_{vol} even though $\Delta p'$ was negative. Presumably, this behavior suggests coupling of the shear stress and volumetric strain.

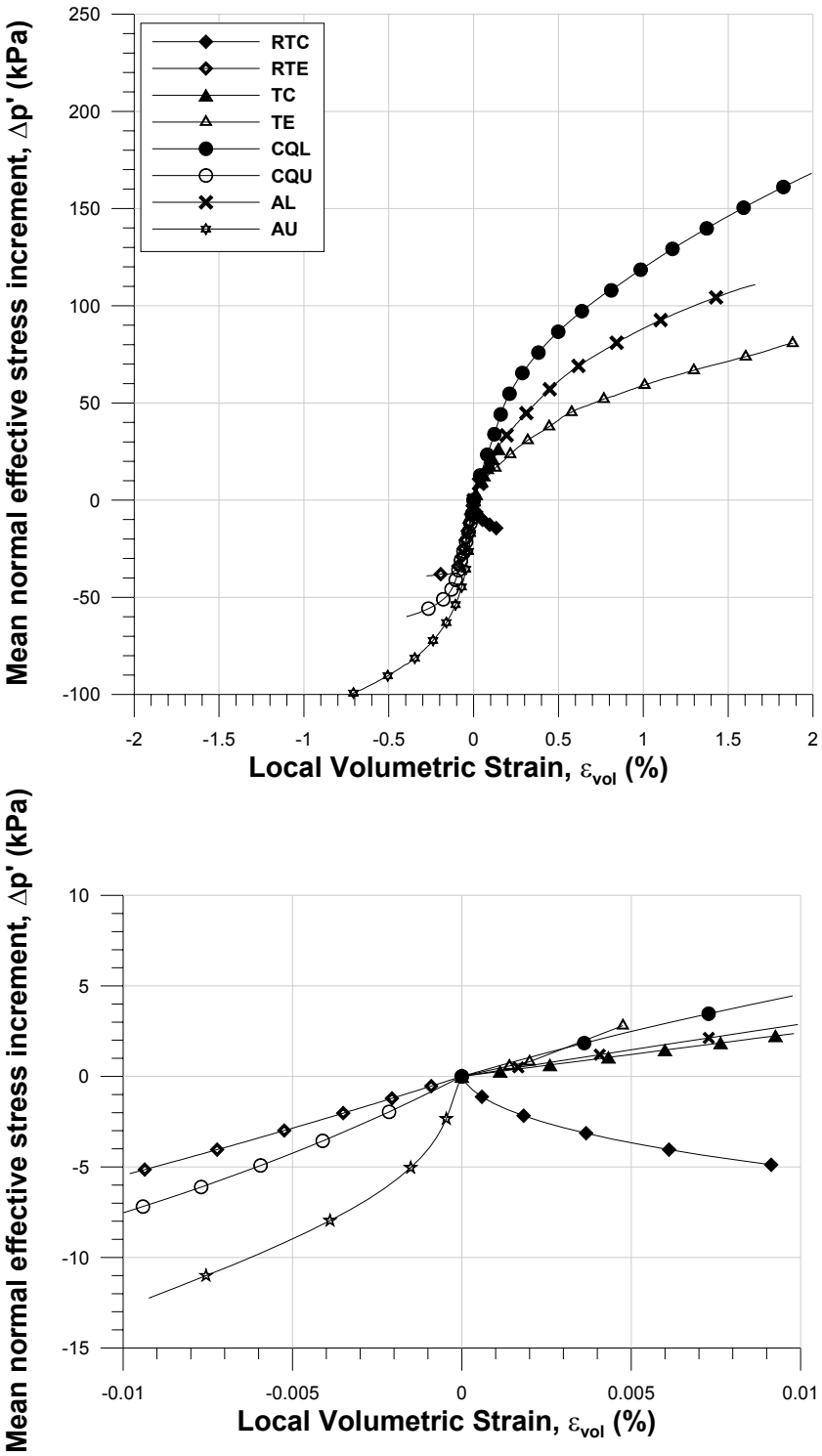

Figure 4-11 Change in mean normal effective stress p' versus local volumetric strain ε_{vol} for selected natural specimens (a) complete test data, (b) test data for ε_{vol} ±0.01%

The volumetric behavior at small strains is shown in Figure 4-11b for $\Delta p'$ loading and unloading stress probes. Note that the reliable range for volumetric strain is larger than 0.005% as mentioned in Chapter 3. In general, loading paths TC, CQL, AL, and TE and unloading path RTE contain zones of constant slope, indicating that the volumetric stiffness is approximately at small strain levels for each path. Unloading moduli show a relatively stiffer response.

In addition, Figure 4-12 shows the comparisons of $\Delta p'$-ε_{vol} based on the measurements between the internal and external systems. The RTE and CQU paths failed at stress conditions noted by end points of the external measurements. The internally-measured volumetric strains on the horizontal plateaus in the figure do not reflect actual material responses; rather they reflect data points that occurred when global failure was reached. Thus, the dashed lines are not to be considered as material responses.

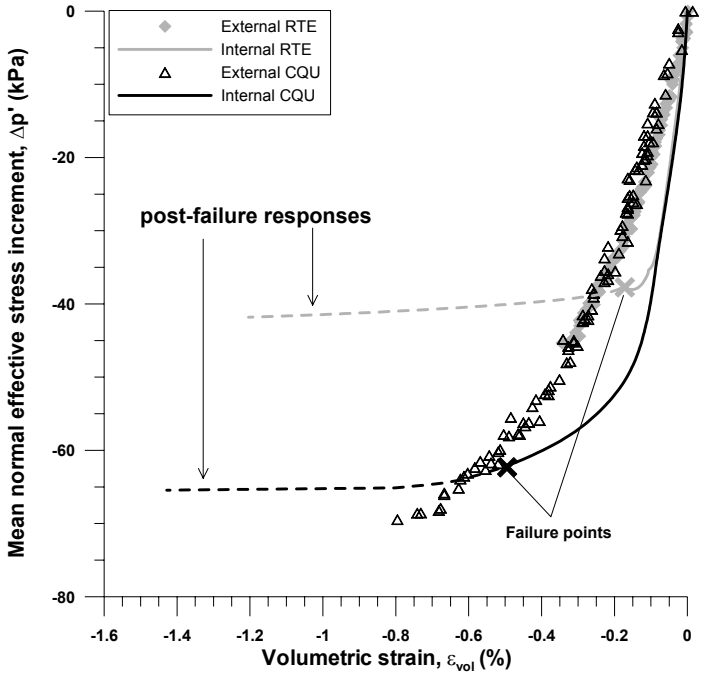

Figure 4-12 $\Delta p'$-ε_{vol} for RTE and CQU paths from internal and external measurements

To investigate the volumetric behavior in the small strain range, secant bulk moduli are plotted versus volumetric strain in Figure 4-13.

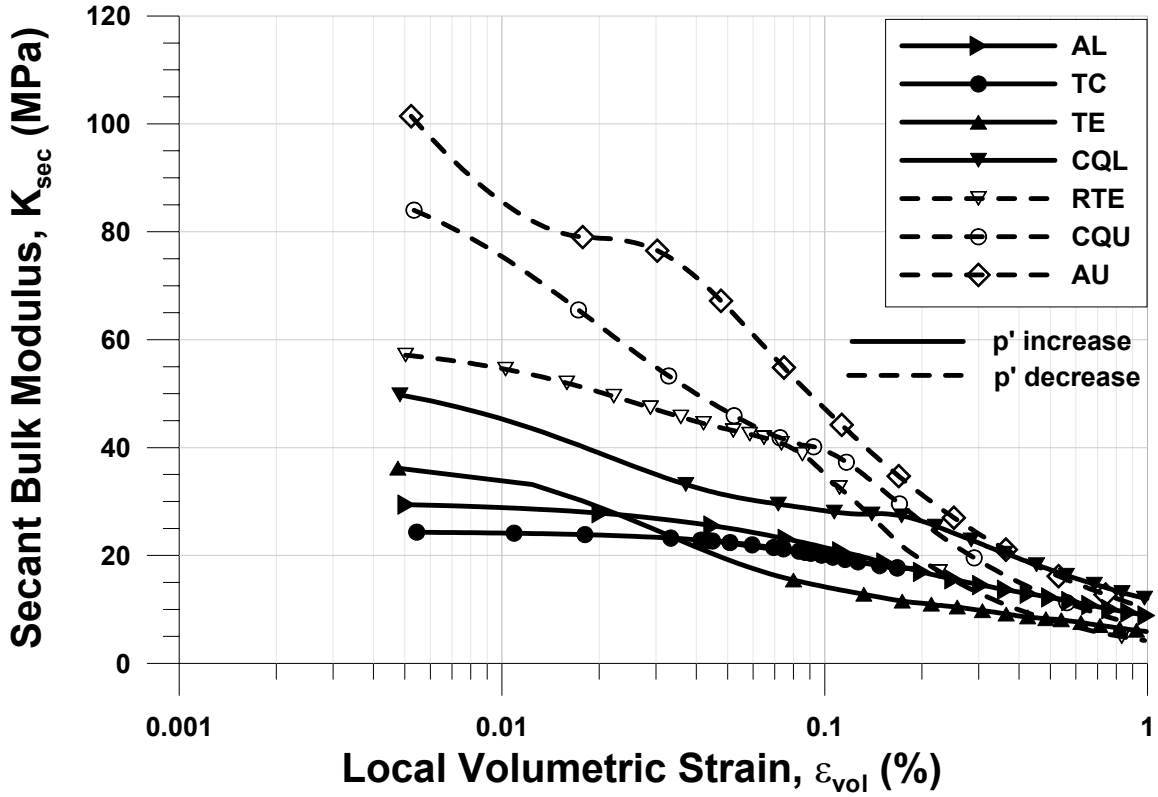

Figure 4-13 Bulk modulus degradation curves of block samples for stress probe tests

The maximum and minimum calculated K_{sec} values at ε_{vol} of 0.005% are 100 MPa and 23 MPa for probes AU and TC, respectively. Unlike the secant shear moduli, TC and AL paths show a zone of constant bulk moduli, which can be interpreted as a linear elastic response.

The bulk moduli of soft Chicago glacial clay also strongly depend on the stress path direction. Overall, the bulk moduli in the stress probes wherein p' is increased ("loading") are smaller than those in the stress probes where p' initially decrease ("unloading"). The pattern of bulk moduli is also very similar to shear moduli when they

are plotted against the angular difference from the CMS path as shown in the inset in Figure 4-14. In Figure 4-14, the values of K_{sec} for 0.005%, 0.01%, and 0.1% strain are plotted versus the angle θ. Data points for path CMS would plot at 0° and 360°. The variation in K_{sec} is nonlinear with respect to stress path rotation angle θ for all small strain levels. The dependence of bulk modulus on θ is large at 0.005% and 0.01% ε_{vol}, but the apparent directional dependence decreases as the strains reach and exceed 0.1%. The secant bulk modulus is technically indeterminate both the CMS path at 0^o and the CMSE path at 180^o because there is no change in p' for the probe. The curves should be discontinuous at these points. The data trend is clear to either side of the CMSE path. Note that bulk modulus of RTC path is not included in Figure 4-12 and 4-13 because it shows positive volumetric strain with decrease of mean normal effective stress, likely as a result of coupling phenomena.

These discrepancies in the trends of the secant shear and bulk moduli data illustrate the limitations of interpreting the stress-strain data solely in terms of isotropic secant shear and bulk moduli, without considering the effects of coupling.

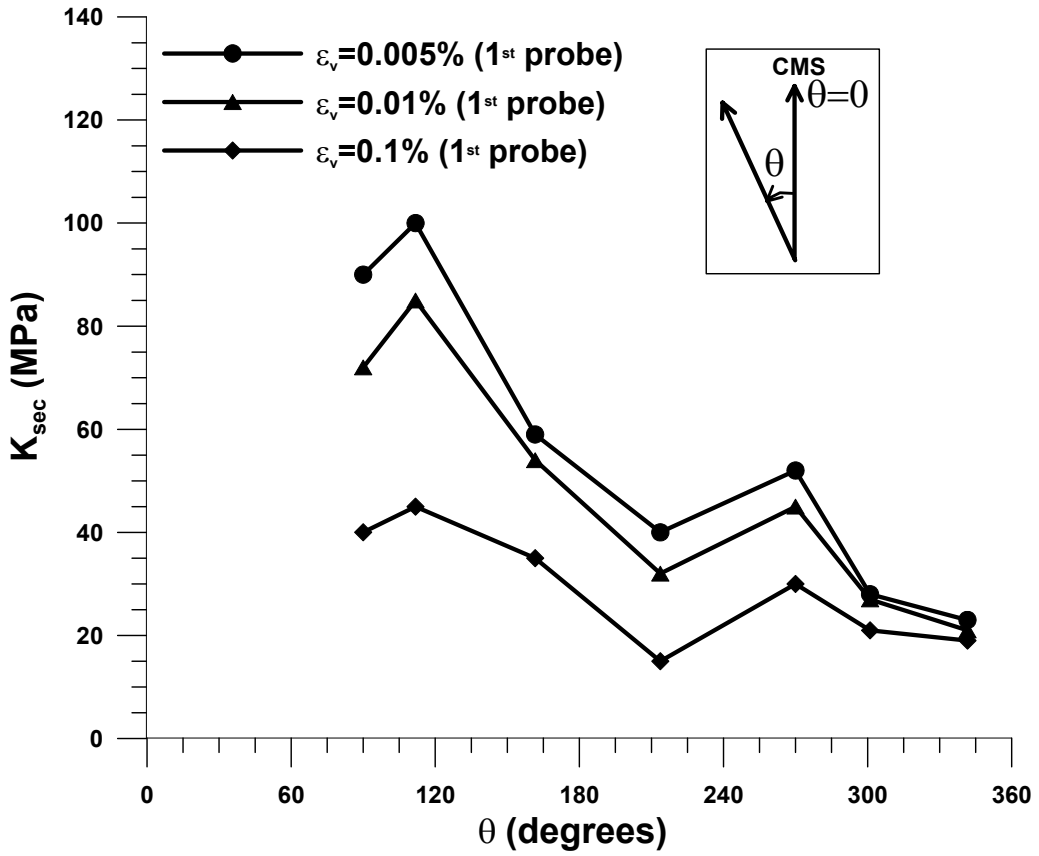

Figure 4-14 Variation of secant bulk modulus K_{sec} as a function of angular difference in stress probe direction

4.3.5. Coupling Stress-Strain Behavior

Figure 4-15 shows the mean normal effective stress and shear strain relationship. At a large strain scale, the CQL path shows very stiff response indicating no apparent coupling up to 90 kPa increase of mean normal effective stress. At large strains (Figure 4-14(a)), there is no "apparent" coupling from -50 to 90 kPa. However, at small strains for the closer look (Figure 4-14(b)), the response of CQL path shows an initially positive shear strain (0.02%) up to 90 kPa increase in $\Delta p'$, followed by a transition to negative shear strain. The CQU path also shows very stiff response up to $\Delta p'$ of -50 kPa, then softer

responses afterwards. Also, the $\Delta p'$ and ε_{sh} responses in the CQL and CQU paths are clearly different as are the volumetric and shear behaviors.

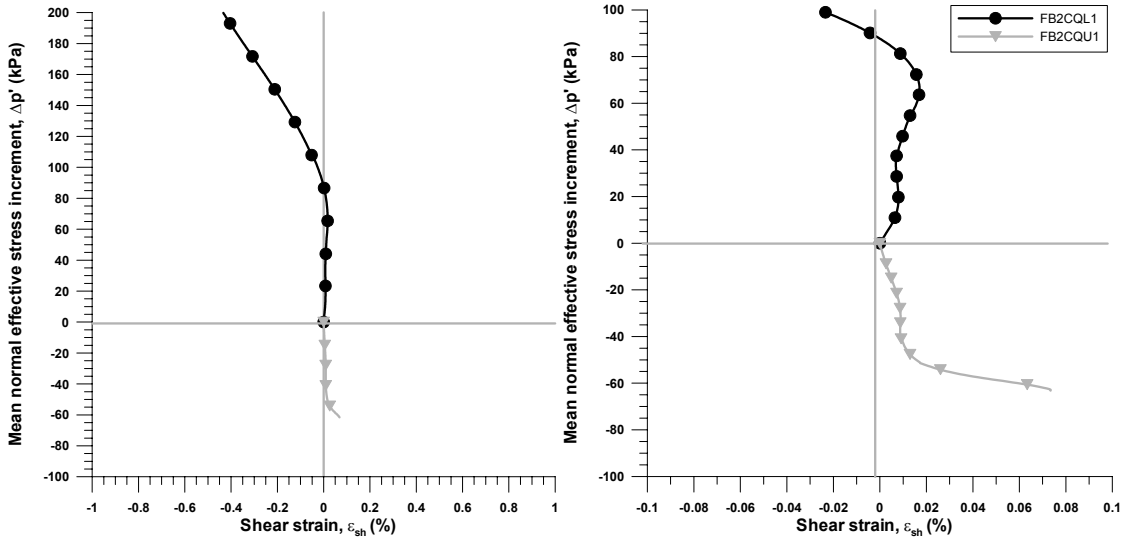

Figure 4-15 $\Delta p'$ versus ε_{sh} for CQL and CQU stress paths (a) large strain data up to 1%, (b) small strain data for ε_{vl} ±0.01%

Figure 4-16 shows the deviatoric stress and volumetric strain relationship. At a large strain scale, unlike the mean normal effective stress and shear strain relationship, both the CMS and CMSE paths show that changes in shear stress result in volumetric strains from the beginning of the shear. The CMSE path shows a stiffer response than that of the CMS path. In general, increases in shear stress result in volumetric contraction, and decreases in shear stress result in volumetric expansion, as one might expect for lightly overconsolidated clays.

As clearly stated in the modeling framework on Chicago clays (Tu 2007), the cross-coupling moduli, J_s and J_v should be considered independently because the responses between the two can not be correlated to each other. The cross-coupling relationship between the shear and volumetric behaviors observed in this program also

support the idea that compressible Chicago clays are not an isotropic elastic material and the each coupling effect should be considered exclusively for the modeling framework.

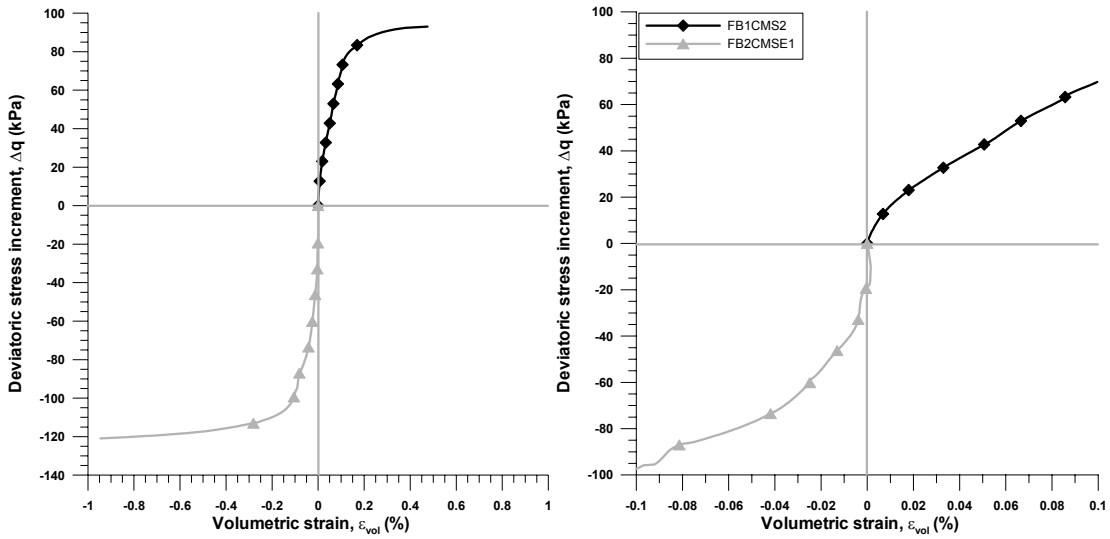

Figure 4-16 Δq versus ε_{vol} for CMS and CMSE stress paths (a) large strain data up to 1%, (b) small strain data for ε_{vl} ±0.01%

4.4. STRAIN RESPONSE ENVELOPE

Modulus degradation curves and directional stiffness diagrams are useful to help understand shear and volumetric components of soft Chicago clay behavior, but cannot be used to graphically represent general stress-strain-stiffness behavior, including the cross-coupling behavior. Strain response envelopes (SREs) can be generated to depict stress-strain response for all possible strain path directions and incremental stress probe magnitudes. Nonlinear and irreversible soil response also can be seen in the SREs.

4.4.1. Theory and Development

Gudehus (1979) advocated the use of stress response envelopes as a tool to visualize the performance of various rate-type constitutive equations under axisymmetric conditions.

A stress response envelope was defined as the image in stress-rate space of a unit sphere in strain-rate space, mapped by the constitutive equation. Stress response envelopes can be created in either Rendulic stress space (σ_a':$\sqrt{2}\sigma_r'$ plane) or general p′-q space for the axisymmetric conditions of a triaxial test by probing constitutive equations with incremental strain probes of known length and direction and computing the incremental stress response.

Incremental strain response envelopes (SREs) are the inverse of a stress response envelope and may be defined as the image in the strain-rate space of the unit sphere in stress-rate space mapped by the constitutive equation (Costanzo et al, 2006). Schematic diagrams of input stress probes and their SRE in strain paths in Rendulic stress space (($\sqrt{2}\Delta\varepsilon_r$, $\Delta\varepsilon_a$ plane) are shown in Figure 4-17. SREs are generated from the results of directional stress probe investigations on identical specimens, such as that described in this dissertation. When coupled with accurate small strain measurements, the SRE becomes a powerful tool to help visualize the complete nonlinear, irreversible and directionally-dependent responses for the entire group of stress probes about a single initial stress state.

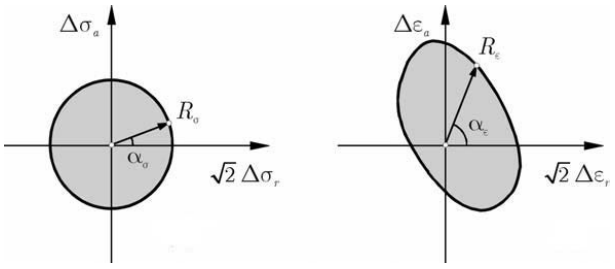

Figure 4-17 Construction of strain response envelopes for directional stress probes (after Costanzo et al, 2003)

General p′-q space can be also used to present stress response envelopes, and in the same way, a SRE can be generated in shear strain and volumetric strain space. It is advantageous to use the SRE in terms of the volumetric and shear strains because it can be related to the analysis of the stress-strain data presented in Section 4.3. The SRE with volumetric and shear strains can be understood in terms of shear, bulk and two cross-coupling behaviors. Hereafter, the term SRE will be applied to the strain response envelope generated in shear and volumetric strain space.

The construction of a SRE essentially consists of mapping stress probe vector magnitudes R_σ onto strain paths in the general p′-q space ($\Delta\varepsilon_{vol}$: $\Delta\varepsilon_s$) for each probe, then contouring like values of R_σ (Costanzo et al. 2006). The input stress probe of magnitude R_σ takes the form of a circle in p′:q space, with R_σ calculated as

$$R_\sigma = \sqrt{(\Delta p)^2 + (\Delta q)^2} \tag{4-6}$$

As an example, Figure 4-18 presents a SRE constructed for an isotropic linear elastic material with K = 60 MPa, G = 50 MPa and no cross coupling, i.e. $J_v = J_s = \infty$. The same compliance matrix as given in Equation (4-1) is employed:

$$\begin{pmatrix} d\varepsilon_{vol} \\ d\varepsilon_s \end{pmatrix} = \begin{pmatrix} 1/K & 1/J_v \\ 1/J_s & 1/3G \end{pmatrix} \begin{pmatrix} dp \\ dq \end{pmatrix} \tag{4-7}$$

where G is the shear modulus, K is bulk modulus, and J_v and J_s are the cross-coupling modulus. The elastic SRE normalized by R_σ is an ellipse centered at ($\Delta\varepsilon_{vol}$, $\Delta\varepsilon_s$)=(0, 0), with its major axis aligned with the horizontal axis. The major and minor axes represent the purely volumetric and shear behaviors, respectively.

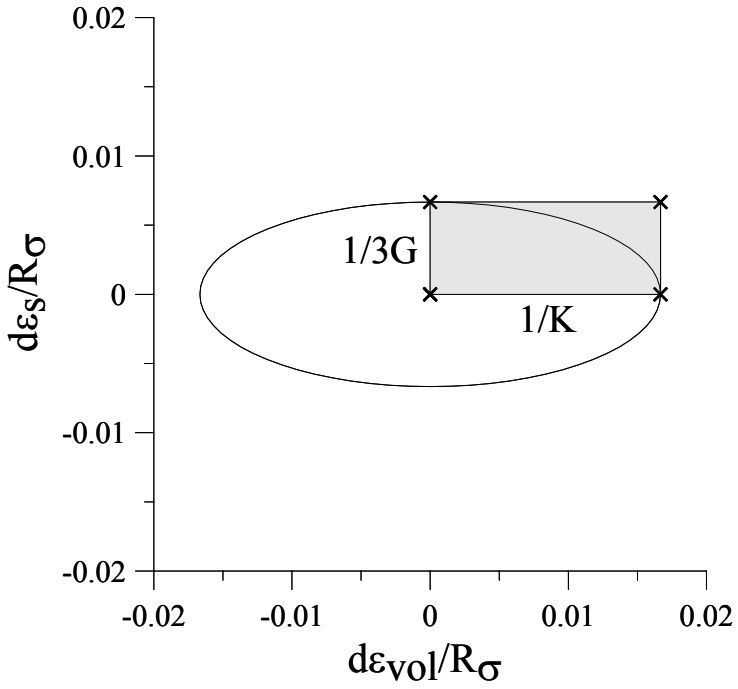

Figure 4-18 Isotropic elastic strain response envelope for *G* = 50 MPa, K = 60 MPa

To investigate the cross-coupling presented on the SREs, SREs of an anisotropic elastic material with K = 60 MPa, G = 50 MPa, J_s, the coupling between $\Delta p'$ and ε_{sh}, and $J_v=\infty$, are presented in Figure 4-19. Figure 4-19 shows the SRES of an anisotropic elastic material varying the magnitude of J_s. With regard to the rotation of the major axis, as the J_s increases, the axis rotates clockwise. In addition to the rotation, the area of the ellipse also decreases with increased J_s.

Similarly, Figure 4-20 presents the anisotropic elastic material with the same K and G (K= 60 MPa, G= 50 MPa) as in Figure 4-18, but with J_v, and $J_s=\infty$. The major axis of the ellipse is rotated clockwise, but the rotation angle with the same amount of the change in the coupling moduli, J_v is smaller than that with J_s change. Again, the reduction of the size in SREs with increase of stiffness is also observed.

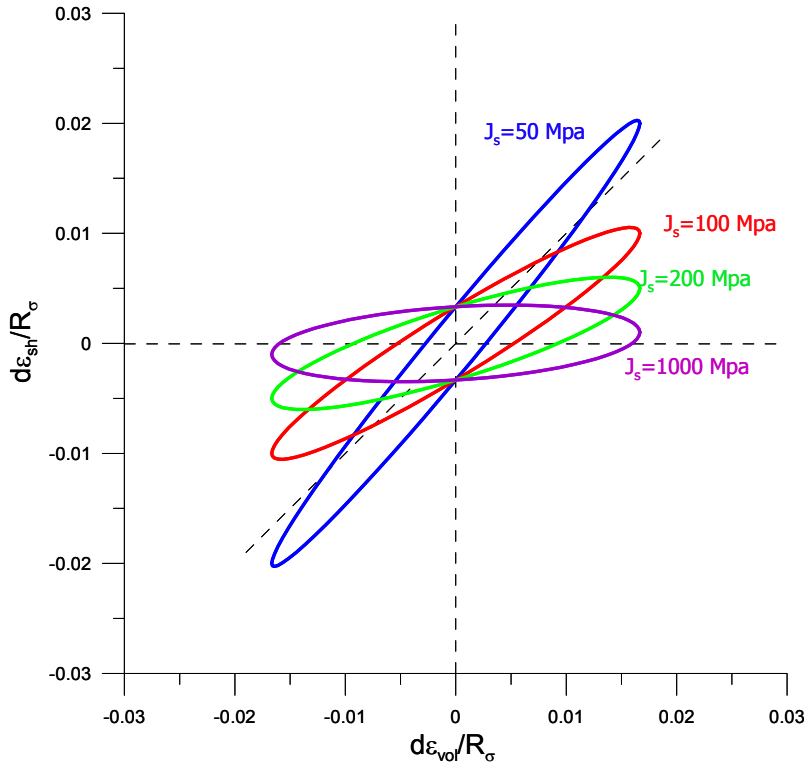

Figure 4-19 SREs for anisotropic elastic material with K = 60 MPa, G = 50 MPa, J_s and $J_v=\infty$

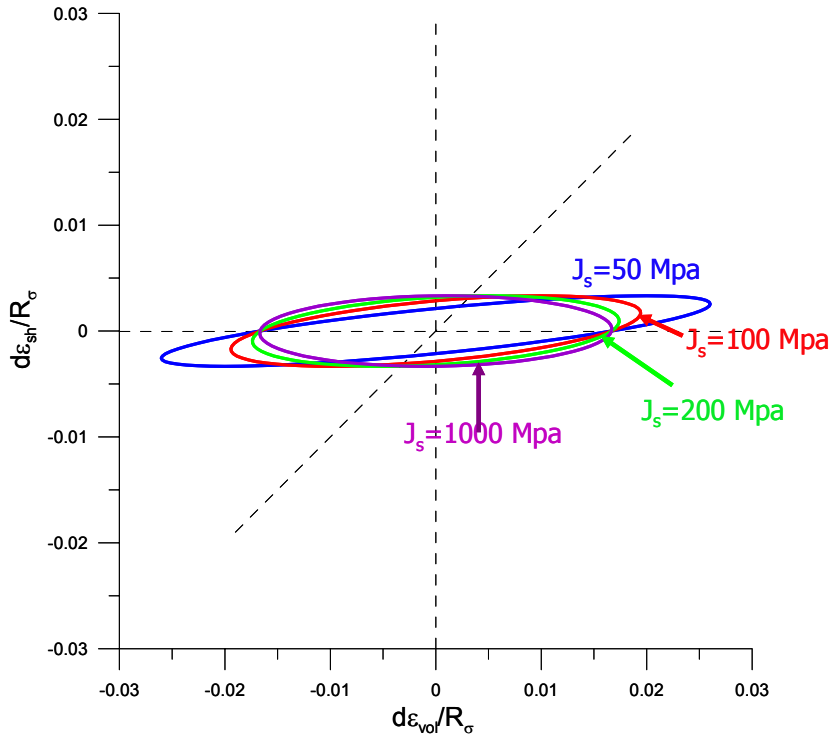

Figure 4-20 SREs for anisotropic elastic material with K = 60 MPa, G = 50 MPa, J_v and $J_s=\infty$

As a final example, a SRE with different cross-coupling moduli was constructed for K = 60 MPa, G = 50 MPa, J_v = 100 MPa, and J_s =200 MPa. Figure 4-21 shows the SRE of the material with cross-coupling. The cross-coupling makes the major axis of the ellipse rotate. Thus, the rotation of the major axis can be a quantitative measure of cross coupling. However, as shown in previous examples, it is not possible to quantify the each cross-coupling effect on the rotation of the major axis.

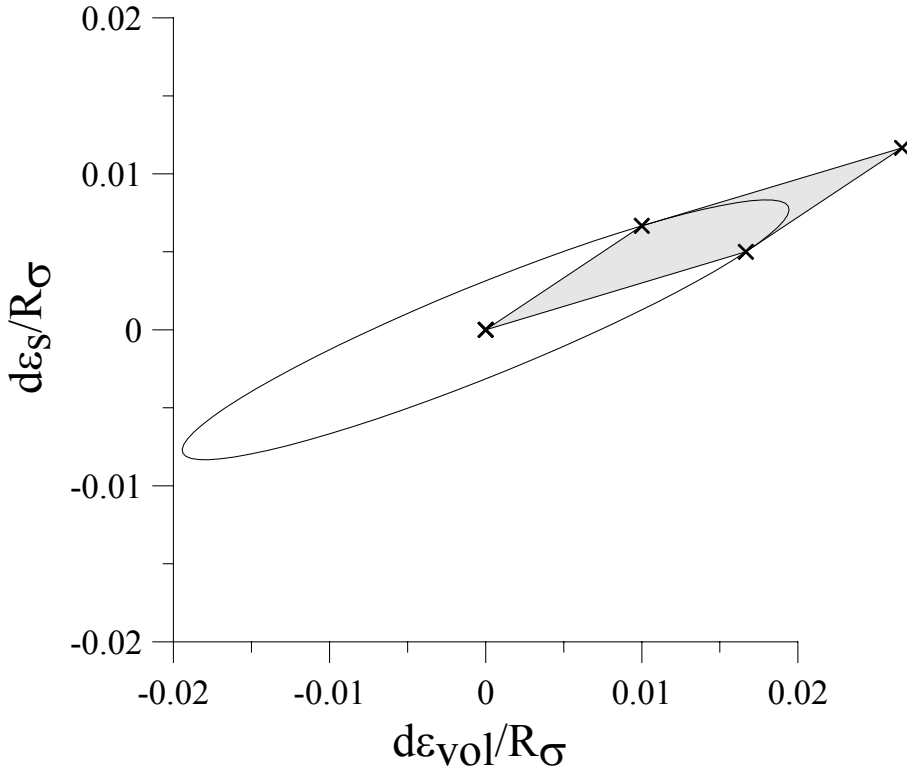

Figure 4-21 strain response envelope for K = 60 MPa, G = 50 MPa, J_v = 100 MPa, and J_s =200 MPa

The examples have symmetric elliptical shapes because they do not have different moduli in loading and unloading. However, if soil exhibits different moduli in loading and unloading, then the ellipse becomes asymmetric and, as a result, the origin of the ellipse shift towards the direction where the soft response occurs.

4.4.1.1. Strain Response Envelopes of Compressible Chicago Glacial Clays

Strain response envelopes were created using the stress-strain data reported in Section 4.3. SREs are plotted at various strain levels to illustrate the evolution of the shear, bulk and the two cross-coupling moduli of Chicago clay as a function of strain level. The SREs can be used to provide insight into the irreversible, nonlinear response of these

compressible Chicago clays, as well as to illustrate the general secant compliance as a function of stress path direction. The secant stiffness that is indicated by an SRE is related to the typical isotropic definitions for modulus (i.e. shear or bulk).

Values of R_σ of 1, 2, 5, 10, 15, 30, 40 and 50 kPa were applied to investigate the non linearity and directional dependence of stiffness. For clarity, Figure 4-22 presents the stress probe input circles for R_σ=10, 15, 30, 40, and 50 kPa.

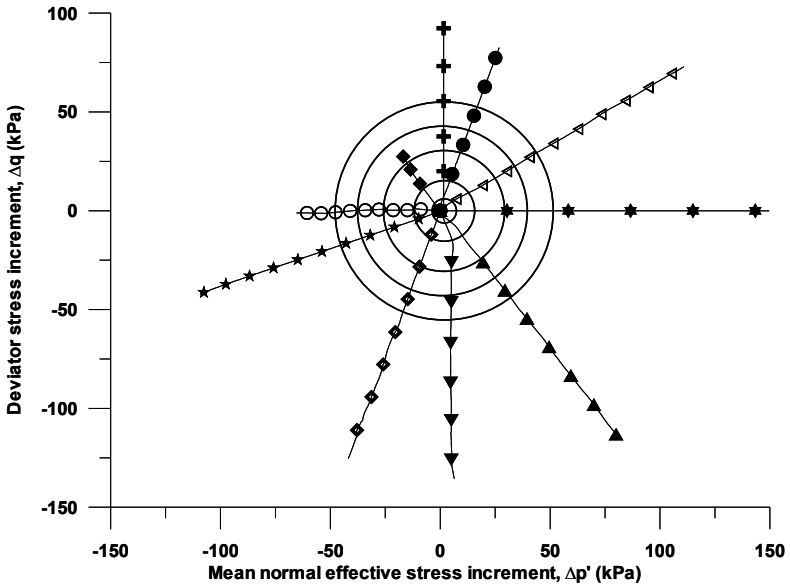

Figure 4-22 Stress probe input circles for R_σ=10, 15, 30, 40 and 50 kPa

Figure 4-23 shows the SREs at strains as large as 0.3% for R_σ= 30, 40 and 50 kPa. Symbols in the figures herein represent actual data points at specified stress contour. It shows different behaviors between loading and unloading probes even at relatively large strain levels. The spacing between contours is a function of the general stiffness of the soil for a given loading direction. It is apparent that the softest response as indicated by the largest spacing between contours, occurs when the probe points are in the direction of

continued loading (AL) and stiffest response as indicated by the smallest spacing between contours, occurs for unloading paths (AU and RTE). This is consistent with the results presented in the previous sections for G_{sec} and K_{sec}. All SREs are markedly asymmetric about the origin of the strain increment space, which represents genuine experimental evidence of incremental non-linearity. In particular, the lack of symmetry strongly suggests that soil response is inelastic (Costanzo et al 2006).

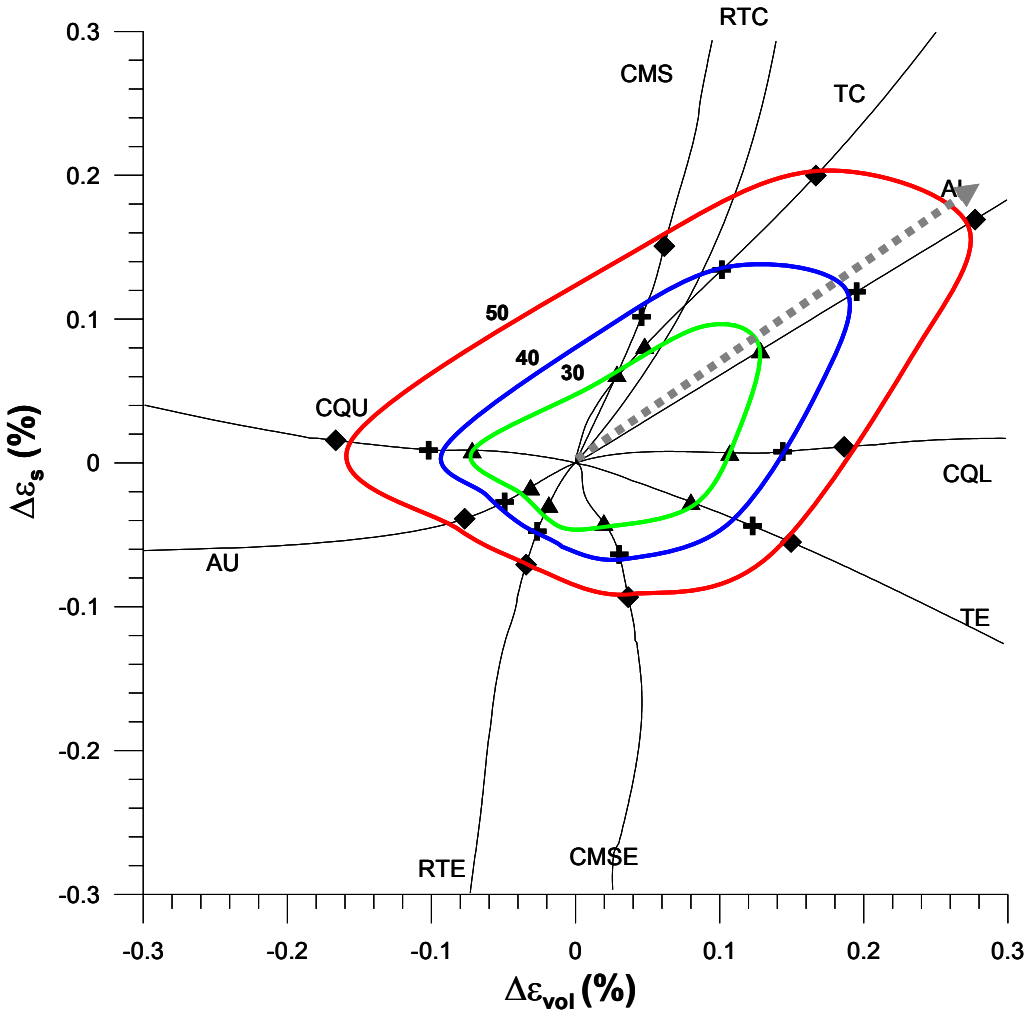

Figure 4-23 Strain response envelopes for large-strain levels, R_σ=30, 40 and 50 kPa

Furthermore, assuming the SRE has an elliptical shape, the major axis is approximately aligned with the AL path as shown as a grey dotted arrow. As explained

before, this indicates that the cross-coupling exists. This rotation of major axis indicates the existence of two positive cross-coupling moduli which means that positive increment of normal effective stress induces the positive shear strains and the deviatoric stress increase develops positive volumetric strain.

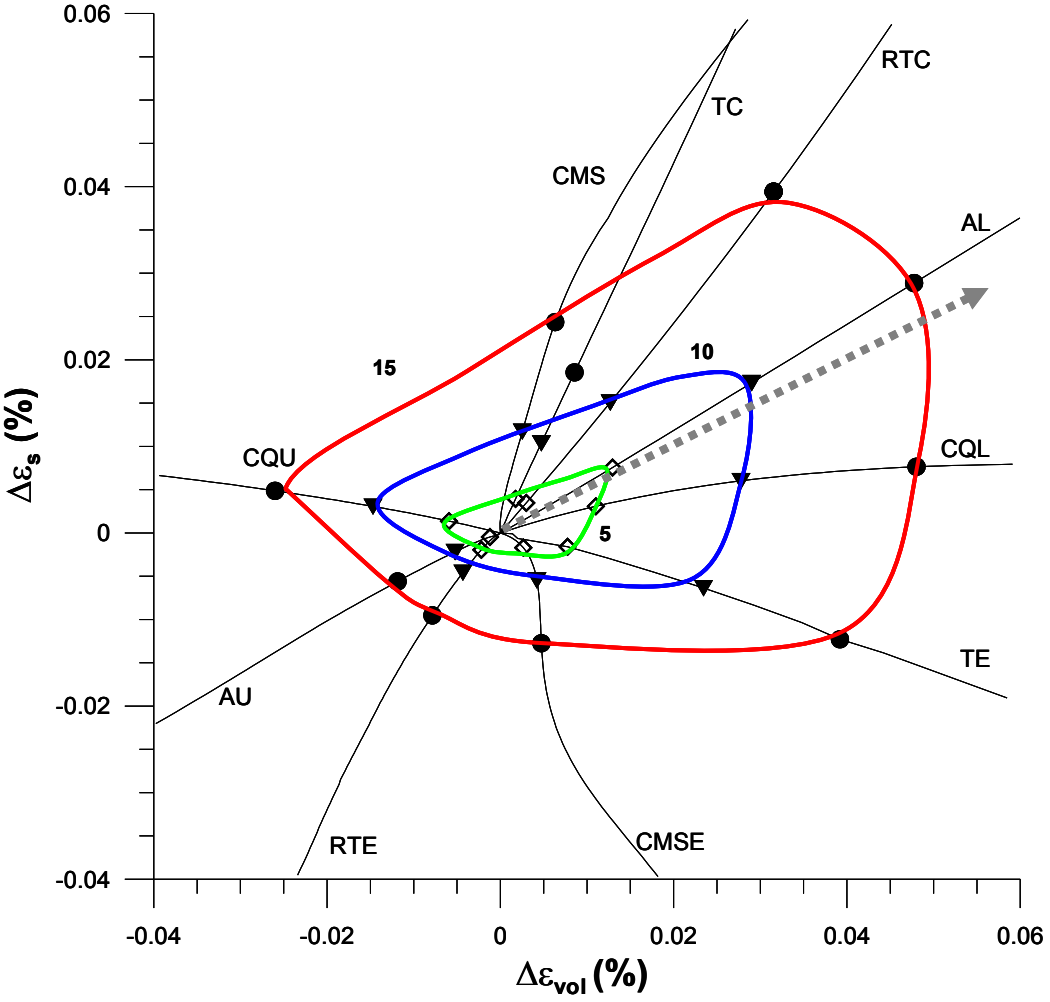

Figure 4-24 Strain response envelopes for intermediate strain levels, R_σ= 5, 10, and 15 kPa

To illustrate the evolution of SREs during stress probe tests, SREs are plotted in Figure 4-24 for an intermediate strain range (-0.04%<ε<0.06%) with R_σ of 5, 10 and 15

kPa. The difference in spacing between the loading paths and unloading paths are more noticeable than those at the higher strain ranges in Figure 4-23. Assuming an elliptical shape of the SREs, the major axes are oriented at a shallower angle with the horizontal compared to the SREs in the large strain range. This trend suggests that cross coupling is less pronounced in the intermediate strain range than in the large strain range. The data in small strain range (±0.01%) presented in Figure 4-25 also supports this trend. The major axes shown as dotted arrows rotate countclockwise as R_σ increases. The different spacing for the loading and unloading paths also is distinctly shown in this small strain level. Note that SRE with R_σ = 1 and 2 kPa are drawn even though some of the strain points are smaller than can be guaranteed to be accurate because the trend of the smaller SRE with R_σ of 1 and 2 follows the overall trend.

Examination of the SREs at the 3 different strain levels in Figure 4-23~25 shows that the difference in spacing of the SREs in loading and unloading directions decreases with increased strain levels. This behavior agrees with the findings of Atkinson (1990) that the stiffness differences between loading and unloading stress path becomes negligible after 0.5% strain. Moreover, under the assumption of an elliptical SRE shape, the data show that the angle of the major axis of the SREs from the horizontal becomes larger as strains increases, and approaches that corresponding to the AL path. This suggests that the cross-coupling effects become larger as strain increases.

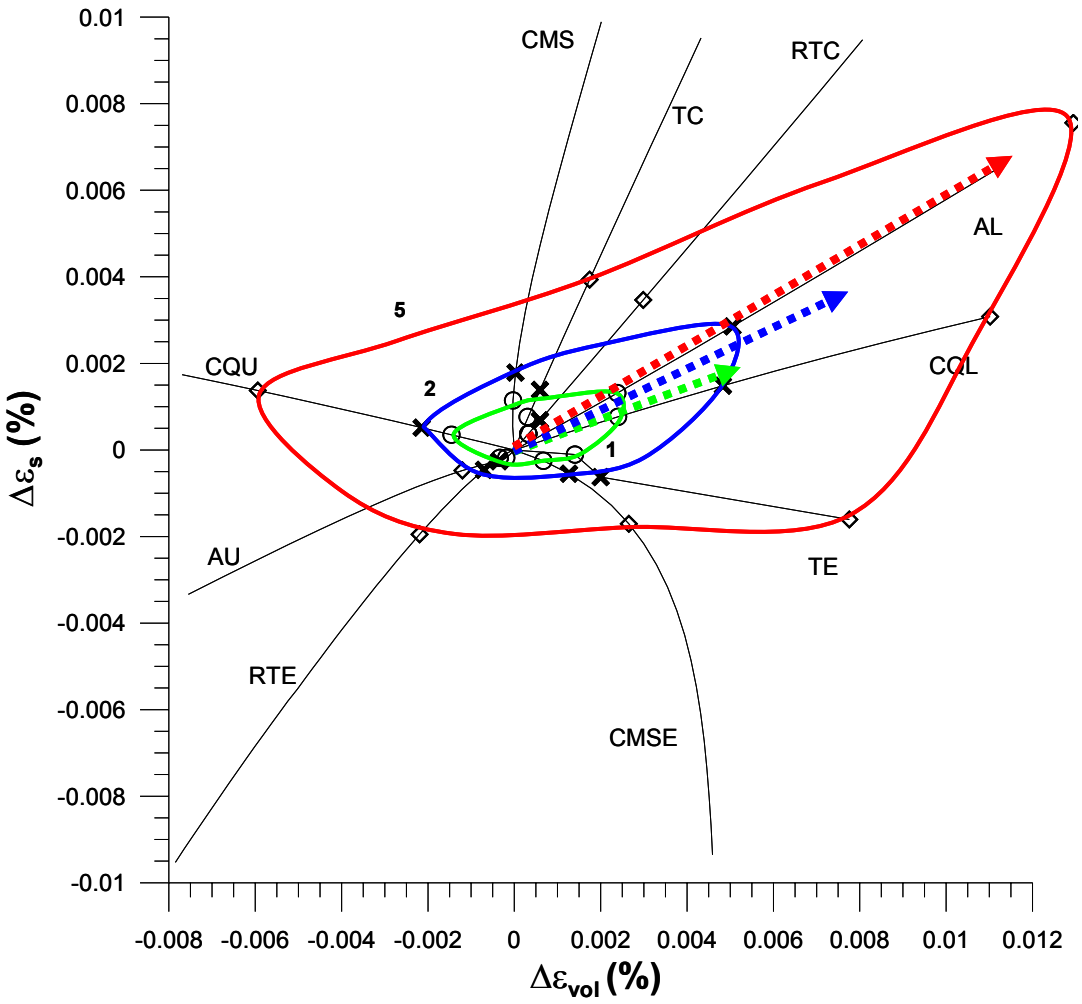

Figure 4-25 Strain response envelopes for small strain levels, R_σ=1, 2, and 5 kPa

4.5. LIMIT STATES AND FAILURE BEHAVIOR

4.5.1. Limit State Response of Chicago Glacial Clays

A limit state or yield surface traditionally represents a stress boundary between "small" and "large" strain behavior. Thus, defining this point is a useful approach to quantify deformation behavior of clays within the context of elasto-plasticity. To do so, one must

specify a procedure used to define the stress state at yielding. Though the basic idea is to find a marked bend in the stress-strain curve, there are a number of approaches one can take to quantify this change in response (e.g. Callisto and Calabresi 1998; Graham et al. 1983; Mitchell 1970; Tavenas et al. 1979). Most of them are categorized in two ways: (i) locate the yield strains at the intersection of the rectilinear extrapolations of the pre- and post yield portions of the stress-strain curves (Callisto and Calabresi 1995), and (ii) find a discontinuity in a plot of strain energy and same stress or strain measure (Tavenas et al. 1979).

The first method is applied herein to define yield, and the results are plotted on in q-p′ space with strain energy contours. As shown in Figure 4-26, a yield point is defined herein at the intersection of rectilinear extrapolations of the pre- and post-yield portions of the stress-strain curve. For each stress path, such points were identified both in the p' - ε_{vol} curve and in the q - ε_s curve, then the average stress was taken as a yield point. Figure 4-27 shows the location of yield points on the stress-strain curves for every stress probe.

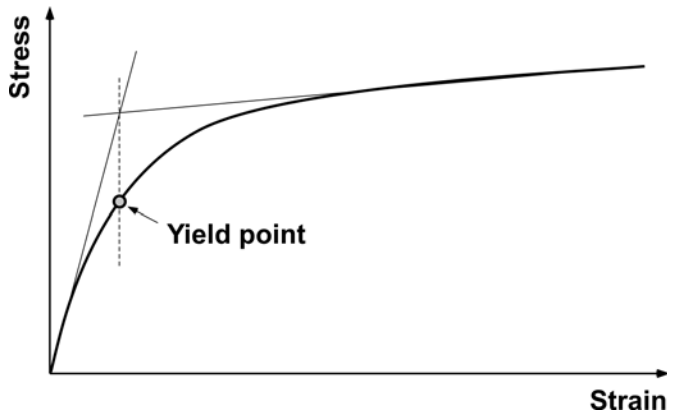

Figure 4-26 Definition of the yield point

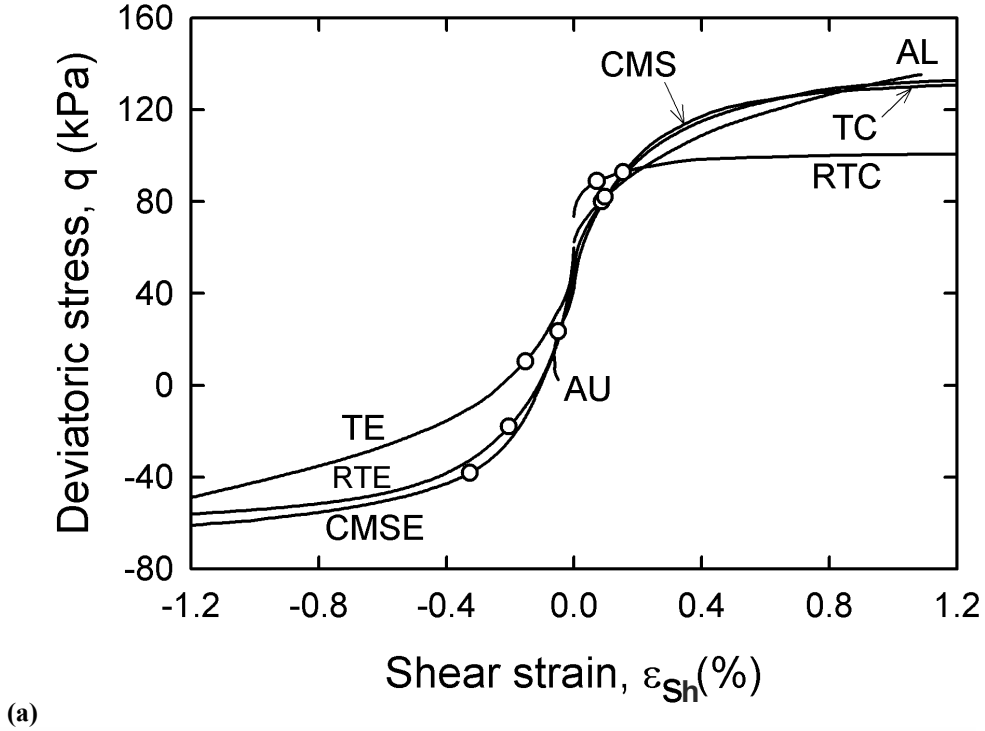

(a)

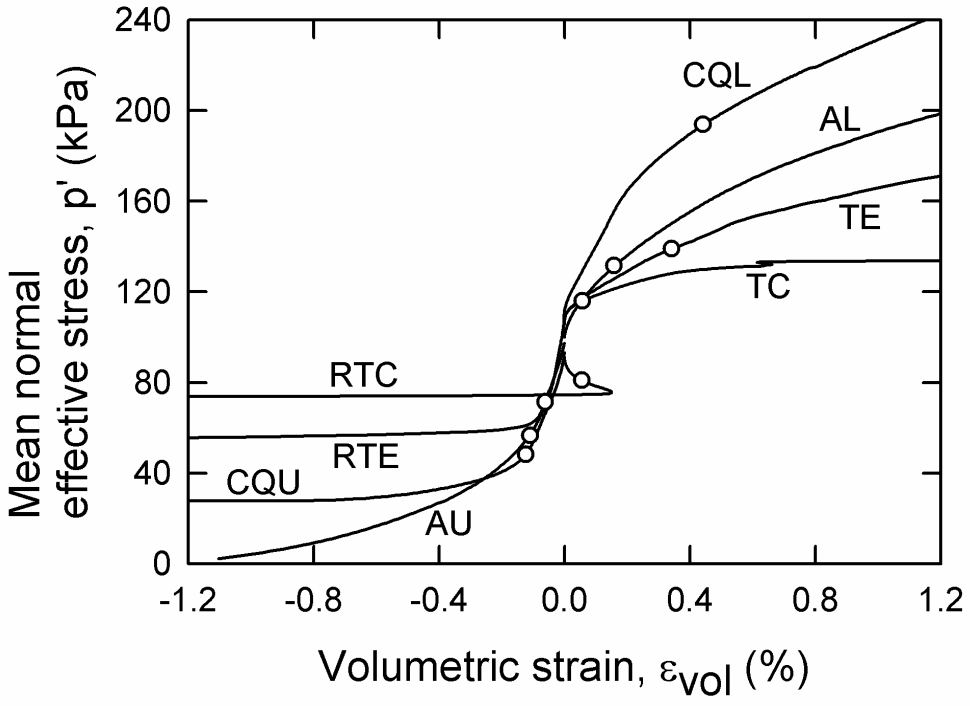

(b)

Figure 4-27 Location of yield points on the stress-strain curves for every stress probe

Figure 4-28 presents the yield points selected from the stress strain data plotted in q-p´ space upon strain energy contours based on the same stress-strain data. Herein the strain energy is defined as

$$W = \int (p' d\varepsilon_{vol} + q d\varepsilon_s) \qquad (4\text{-}8)$$

where the expression is integrated between the starting stress point of the shearing phase of an experiment, and the current values of p' and q.

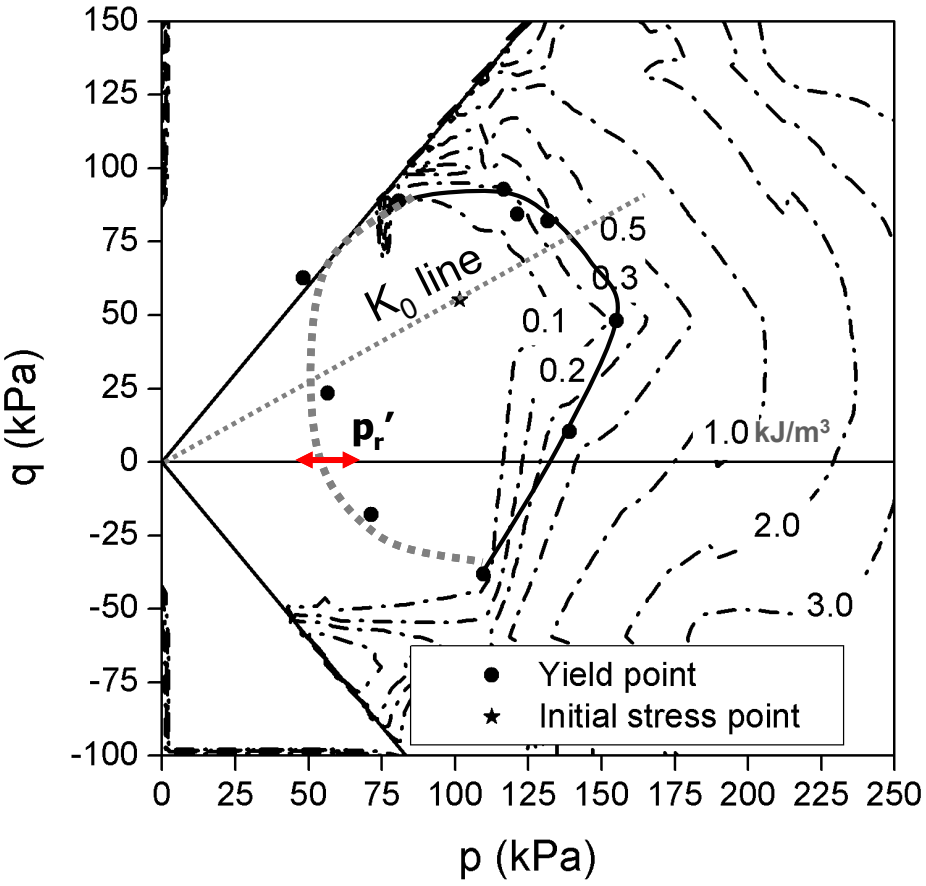

Figure 4-28 Yield points and equal strain energy contours

The K_0 line is also presented based on an average value of K_0 measured after the creep stage of all tests. As has been observed for anisotropic clays, the experimental limit

state surface approximates the shape of a distorted ellipse that is asymmetric about the K_0 line. The peak of the surface occurs near the data points corresponding to the TC and CMS stress probes, but below the failure points. The apex of the interpreted limit state surface is approximately located at the intersection of the K_0 line and this surface. The apparent lowest point on the surface occurs near the data points corresponding to CMSE stress probe. The unloading probes AU represent anisotropic unloading along constant η lines, approximately equal to the slope of the K_0 recompression path. Based on the occurrence of measurable limit points for the unloading probes AU, the limit state surface can be drawn closed and does not have to extend back to the origin of p',q stress space. Similar behavior was observed by Holman (2005) for specimens obtained from the Blodgett layer, a softer stratum of Chicago clays.

It is hard to compare results shown on Figure 4-28 to previous research because most of the previous work on the yield surface (e.g. Crooks and Graham 1976; Tavenas et al. 1979; Smith et al. 1992; Callisto and Calabresi 1998) did not include unloading stress paths other than CMSE path, implicitly assuming that the yield surface extends to the origin of p', q stress space. Thus, the limit state surface found in Figure 4-28 agrees with past work based on yield points determined from compression and CMSE paths. However, unloading path data collected during this study suggest that the limit state does not extend through the origin.

If the limit state indeed does not include the origin in p'-q space, then the residual effective stress of the sample should be located inside the surface otherwise the specimen would "yield" during K_0 reconsolidation and the structure would be subject to significant

alterations. The measured residual effective stress ranged from 40 to 65 kPa as marked in the figure. The majority of this range is inside the interpreted limit state lines as marked in dashed lines. Thus, saturation with effective stress less than the measured residual effective stress can induce "yield" during saturation and K_0 reconsolidation.

As seen in Figure 4-28 with 3 exceptions, the strain energy contour roughly coincides with the yield surface that was determined by geometric constructions. The required strain energy to achieve the yield for the stress paths, TC, CMS, RTC, CQL, TE, CMSE and CQU, is 0.2 to 0.3 kJ/m^3, while the AU, and RTE paths require less strain energy to yield. The yield points are generally matched with the equal strain energy line around between 0.2 to 0.3 kJ/m^3, except the RTE and AU paths where both stress ratio and mean normal effective stress decreases. The closer intervals in the stress ratio, η loading directions between energy contour lines indicates that the distortional deformation occurs much faster in these paths than the other η unloading paths.

Similar results are found in previous work on block specimens cut from the Blodgett stratum at a site in Chicago (Holman 2005, Jung et al. 2007). Figure 4-29 shows the yield locus of Blodgett layer, which is a softer material than the Deerfield layer used in this study. It shows the same trend that the good agreement between yield locus and equal energy line in stress ratio loading and it deviates from the equal energy line when the stress ratio decreases. However, in both cases, the deviation between the yield locus and the equal strain energy is within 0.2 kJ/m^3.

The measured residual effective stresses were also marked in the figure. The range was similar to that of this work, 35-50 kPa. The interpreted limit state should

include the p_r' range, but in that program the specimens were saturated at 10 kPa which was clearly outside of the interpreted limit state line and as a result, the test data during K_0 reconsolidation and shearing showed an alteration of the structure during the saturation. The detailed analyses are presented in Appendix A.

Crooks and Graham (1976) postulated that the limit state surface corresponded to a contour of equal strain energy, but Tavenas et al (1979) showed that for a number of sensitive, lightly overconsolidated Canadian clays, the limit state surface was not uniquely identified with a constant contour of strain energy. Smith et al (1992) verified that this variable strain energy contour was also the case for the yield surface of the soft Bothkennar clays. Callisto and Calabresi (1998) reached similar conclusion for the yield locus of soft Pisa clays based on the triaxial and true triaxial test results.

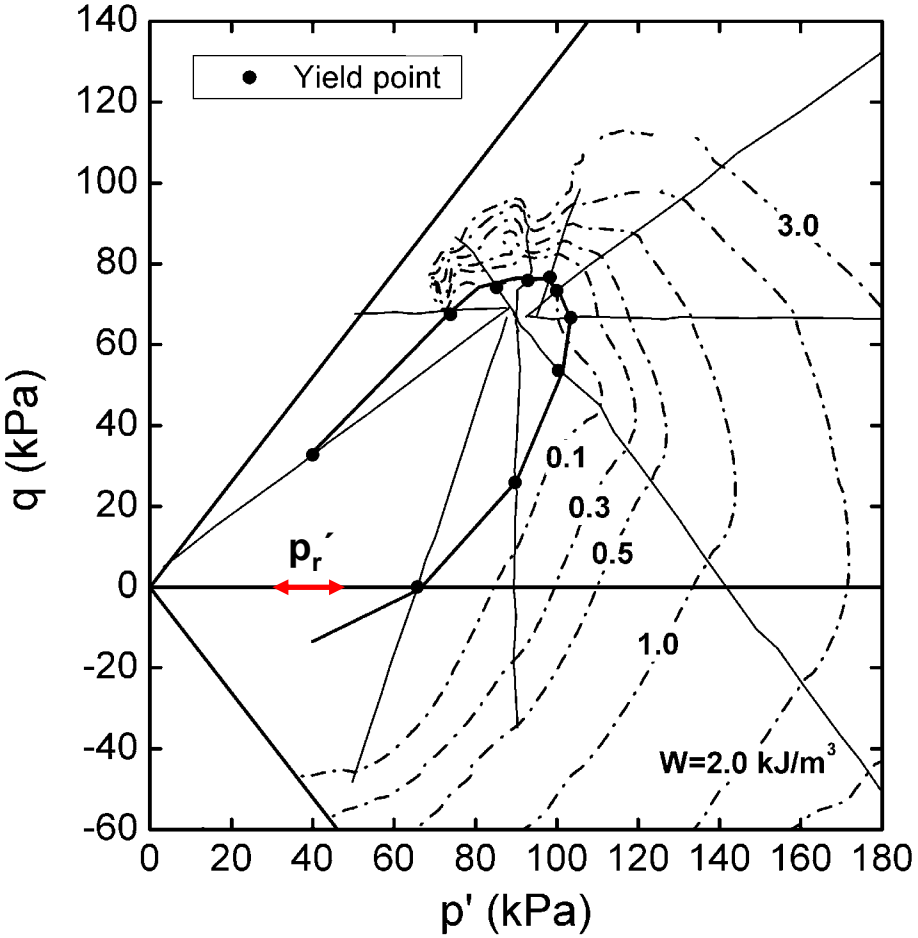

Figure 4-29 Yield points and equal strain energy contours of lower Blodgett layer (Jung et al. 2007)

However, the previous work showed quite a good agreement between the yield points, but the equal strain energy line in stress loading paths and the yield points deviated from equal strain energy line when loaded in paths where the stress ratio decreased. For example, Figure 4-30 show the yield locus plotted in the p´-q plane with equal strain energy contours for soft Pisa clays (Callisto and Calabresi 1998). The yield locus agrees well with equal strain energy line until it passes around the CQL path, and the discrepancy becomes greater than 1 kJ/m^3 as for the TE and CMSE paths. Compared

to this deviation, the maximum discrepancy occurred at the CMSE path shown in the research on Chicago clays is relatively small, less than 0.2 kJ/m^3. Compared to other reported data, the yield locus of compressible Chicago glacial clays plots reasonably agree on an equal strain energy line.

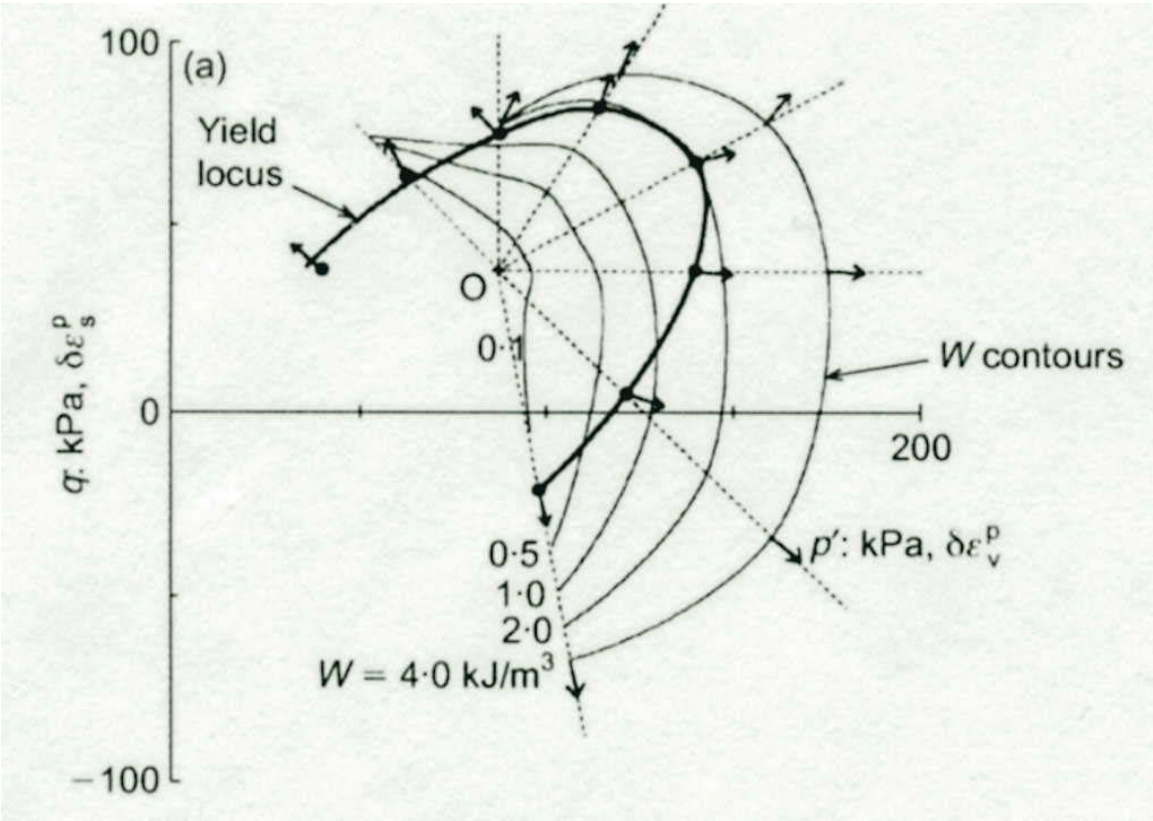

Figure 4-30 Yield locus plotted in the p′-q plane with equal energy contour of soft Pisa clays (Callisto and Calabresi 1998)

4.5.2. Failure Behavior of Chicago Glacial Clays

Failure conditions were achieved for a limited number of natural and reconstituted specimens, primarily for the compression-type stress probes. Due to the limited range of

strains measurable by the internal measurement system, large strain failure behavior was generally observed from the externally measured data. In this study, failure was defined in terms of reaching a peak or constant effective stress ratio σ_1'/σ_3' at large strain levels.

The failure points are plotted in Figures 4-31 and the stress ratio at failure for compression and extension are 1.1 and 0.83, respectively. Clearly, there is discrepancy between the estimated failure line from the TC and CMS and the failure points at the RTC and CQU tests. This "bump" region marked as grey dotted lines a result of the induced overconsolidated state of a specimen during CQU, RTC and RTE loadings.

Based on the distance between the yield points to failure points, abrupt failures are shown in the compression paths, while progressive ones are observed in unloading paths. The failure state found in this study generally agrees with previous research on Chicago clay (Finno and Chung 1992).

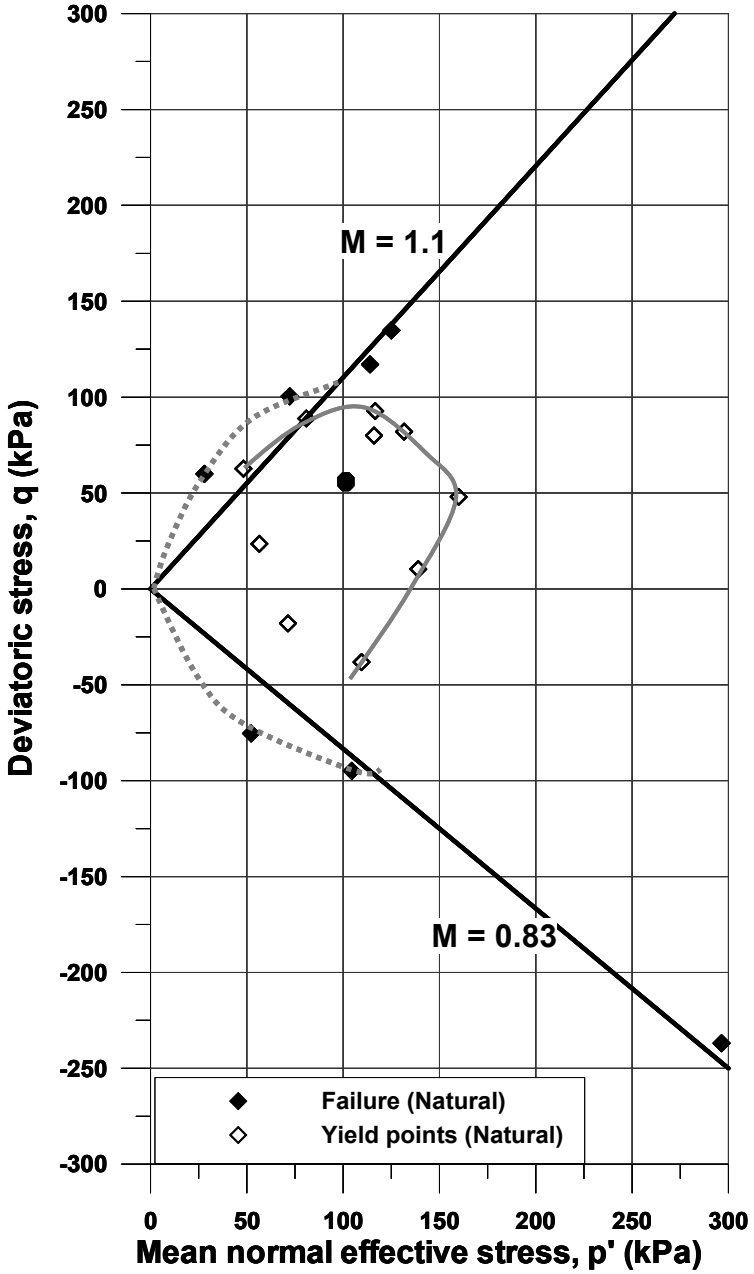

Figure 4-31 Failure points and the stress ratio at failure

4.6. SUMMARY AND CONCLUSIONS

The average index properties for each block sample used in this study were found to be very similar. In particular, natural water contents, void ratios, and plasticity (Atterberg

limits) were nearly identical. The stress history of the blocks, measured in oedometer tests and characterized by σ_p', is also the same, with σ_p' values ranging from 220 to 235 kPa. The similarities in index properties and one-dimensional stress history suggest that block samples are nominally identical and are therefore suitable for use in this research to characterize small strain behavior.

The mean residual effective stress p_r' measured for the block samples was 44 kPa with a standard deviation of 6 kPa. The ratio between the measured residual effective stress and the in-situ vertical effective stress indicates that there is other disturbance than that from the stress relief. To control the swelling, the specimens were saturated at the measured residual stress.

K_0 consolidation responses for each specimen resulted in the achievement of nearly identical end stress states, which was necessary in order to consider each stress probe to have started from the same point. The mean end stress state was (p', q) = (100.4 kPa, 58.5 kPa). The creep behavior at the end of K_0 reconsolidation was very similar for each specimen, with like slopes η and lengths of the creep stress path. The creep phases resulted in stress path rotations of approximately 90°, increases in p' and σ_r', and reductions in q. The mean axial strains, measured by the internal measurement system, were less than 0.5%, which indicated that the triaxial specimens were "very good" to "excellent," based on the qualitative systems of assessing sample disturbance.

The stress-strain response from the directional stress probes was examined in terms of shearing, volumetric, and two coupling relationship – mean normal effective stress and shear strain and deviatoric stress and volumetric strain. Natural variation

between the samples was found as much as 10 to 15% of the stiffness in the same stress path tests. The dependence of stress-strain behavior on the stress probe direction was observed for both shearing and volumetric behaviors. The deviatoric stress-shear strain responses do not show the zones of linear behavior at small strain levels while the p′ loading type of stress paths show the linear behavior up to 0.02%. The stress ratio, η loading probes resulted in significantly smaller shear moduli at all strain levels than the η unloading probes. Similarly, p′ loading paths show smaller bulk moduli than p′ unloading paths. The dependence on the stress path direction decreases with strains in both shearing and volumetric behaviors. The cross-coupling between shear and volumetric behavior was observed for all stress probes. The coupling between $\Delta p'$ and ε_{sh} is less than that between Δq and ε_{vol}. The cross-coupling relationship between the shear and volumetric behaviors clearly suggests that compressible Chicago clays are not an isotropic elastic material and the each coupling effect should be considered exclusively for the modeling framework.

The strain response envelopes (SREs) graphically depict this constitutive response through their asymmetry, orientation, and location with respect to the strain origin, even at small strains. The SREs also show the directional dependence and the evolution of coupling with increased strains. The SREs comparisons with 3 different strain levels show that the different spacing of SREs in loading and unloading directions decrease with increased strain levels. The SREs show that the major axis, under the assumption of elliptical shape, rotates from around the horizontal to AL path as strain increases. This

agrees with the finding from the stress-strain data that the cross-coupling effects become larger with increased strains.

The experimental results presented herein clearly show that the stiffness of compressible Chicago clays is highly dependent on loading direction as well as strain level. The significant variability of the shear and bulk moduli with stress path direction and strain level suggest that the Chicago clays are incrementally nonlinear.

Limit state and failure conditions were examined. The limit state for each stress probe was defined by locating the yield strains at the intersection of the rectilinear extrapolations of the pre- and post yield portions of the stress-strain curves. The shape of the yield surface is a distorted ellipse that is asymmetric about the K_0 line, providing another evidence of anisotropy. The values of strain energy corresponding to each limit state point agree well in the stress ratio loading path and limit state points deviate from equal strain energy line when stress ratio of stress path decreases. However, the limit state of Chicago Glacial clays roughly matches with the constant strain energy line. Based on the distance between the yield points to failure points, abrupt failures are shown in the compression paths, while progressive ones are observed in unloading paths.

CHAPTER 5 RECENT STRESS HISTORY EFFECTS ON SMALL STRAIN BEHAVIOR

This chapter presents analyses of stress probe test results to investigate recent stress history effects on the small strain stiffness. These effects are expressed in terms of modulus degradation, directional dependence and strain response envelopes. In contrast to the first type of stress probe tests, herein, called "post-K_0" probes discussed in Chapter 4, these stress probe tests were performed at a stress state unloaded via an RTE path from the in-situ stress state, herein called "post-unloading" probes.

Section 5.1 explains the two types of the stress probe tests in terms of input stress paths and stress-strain responses. Section 5.2 presents the modulus degradation characteristics of each stress probe tests. Section 5.3 presents those modulus degradation curves with the respective angle change between the current stress path and pre-shear stress path and with the current stress path angle from horizontal or vertical axis. There will also be discussions on issues on the analysis of the directionality. Section 5.4 discusses the strain response envelops of the two different types of stress probe tests and the incremental nonlinearity related to the experimental results. Section 5.5 summarizes the experimental findings.

5.1. STRESS-STRAIN RESPONSES OF STRESS PROBES TO EVALUATE RECENT STRESS HISTORY EFFECTS

5.1.1. Input stress path for two types of stress probe tests

To investigate recent stress history effects, a stress probe test was performed on specimens from a different stress state as those described in Chapter 4. The loading history prior to the actual stress probe simulates the stress relief arising from an excavation unloading path.

As explained in Chapter 3.3.5, the "post-unloading" probe started at the stress state resulting from unloading from the in-situ stress condition, as shown in Figure 5-1(a). The initial stress point of the probing tests was located inside the limit state defined from the set stress probe tests in Chapter 4, because previous research (e.g., Burland 1989; Hight and Higgins 1995; Atkinson and Sallfors, 1991) showed that the measured ground strain levels surrounding foundations and retaining structures were typically less than 0.2% of strain values, which are generally less than the strains associated with the limit state. After K_0 reconsolidation to the in-situ stress condition, the specimens were unloaded via a RTE path to the stress state where the deviatoric stress is a half of the in-situ stress condition (q = 30 kPa). Due to block sample availability, 5 stress probes, CMS, CMSE, CQL, CQU and AU, were applied to investigate the recent stress history effects on the shear, bulk and two cross-coupling moduli, J_s and J_v (couplings between shear stress and volumetric strain and between mean normal effective stress and shear strain).

The input stress path data for the "post-unloading" probe tests are presented in Figure 5-1 (b). The paths shown in the figure are for natural specimens trimmed from block samples FB3. All stress paths are shown in terms of changes in stress, $\Delta p'$, Δq after the start of each path. The

incremental path is shown because of the relatively small variation in the end stress states following K_0 consolidation, creep, unloading and creep. The length and direction of each stress path represents the actual data. All paths follow straight lines of constant slope η due to the drained nature of the stress paths. Small variations in intended path directions and straightness resulted from minor fluctuations in the CKC e/p loading system and the development of small excess pore pressures, generally on the order of 2 to 3 kPa as a maximum, measured at the ends of the specimen.

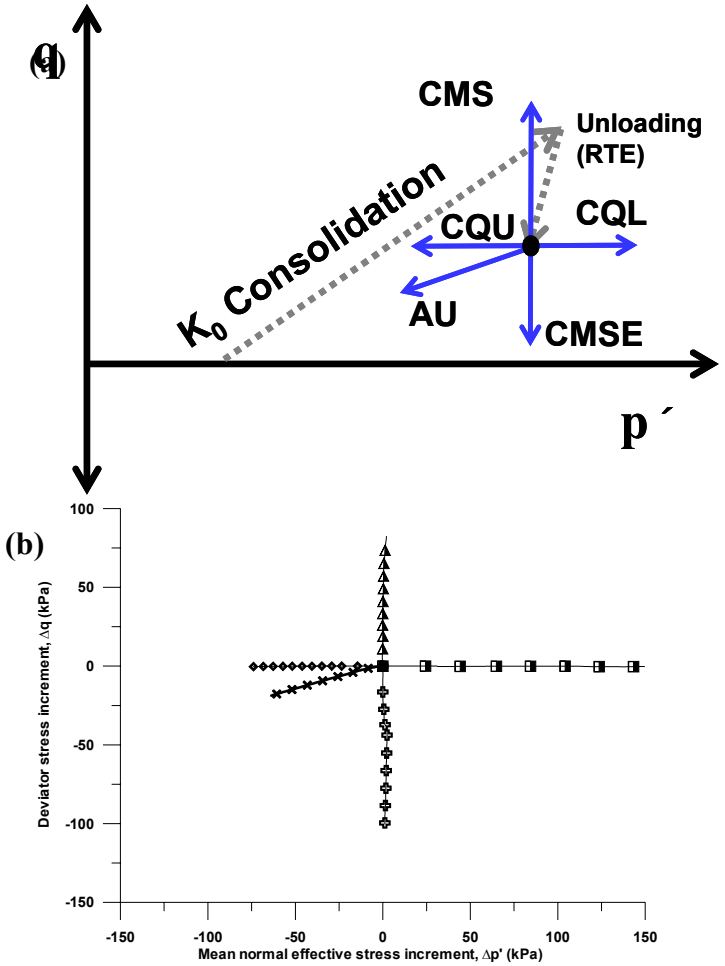

Figure 5-1 "Post-unloading" stress probe tests (a) schematic diagram of the experimental program (b) input stress probe

5.1.2. Unloading behavior before the "post-unloading" probe

Figure 5-2 shows the K_0 reconsolidation and unloading stress paths for these probes. Similar to the first set of probes, the initial stress points of the specimens are scattered in a range of 10 kPa in mean normal effective stress and 2 to 3 kPa of deviatoric stress. This scatter arose from the K_0 reconsolidation process following the recompression method (Bjerrum, 1973; Jamiolkowski et al, 1985). As mentioned before in Chapter 3.3.4, during the K_0 reconsolidation phase, the stress condition at the end of consolidation is not pre-determined; the final stresses after K_0 reconsolidation is a direct function of residual stress which can be influenced by many factors such as the composition of the sample, sampling, handling and trimming disturbance and drying of the sample (Hight et al. 1992). This scatter could have been avoided if the sample was consolidated in anisotropic way to the in-situ stress condition but in that case, the anisotropic consolidation method may have induced the alteration of the natural structure of the clay, which can be crucial to the small strain responses.

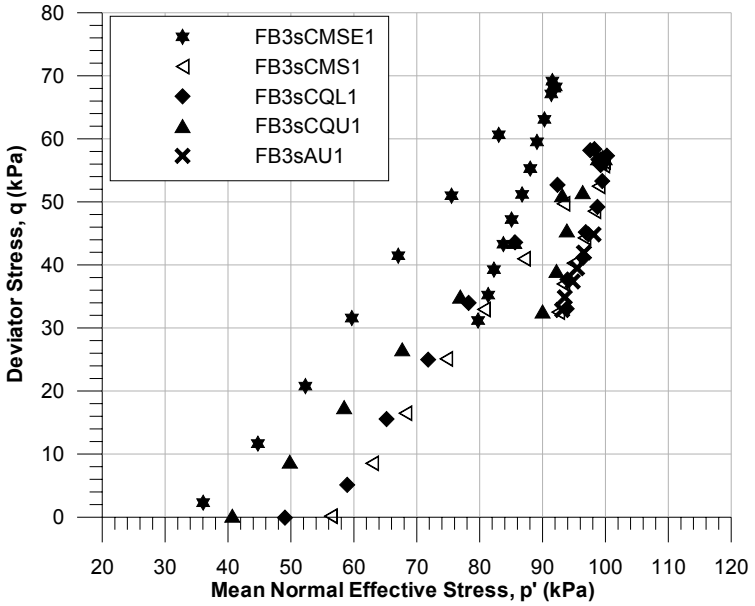

Figure 5-2 K_0 reconsolidation and unloading stress paths in second stress probe tests

All specimens in the "post-unloading" probe tests were subjected to a RTE stress path after K_0 reconsolidation. Though the unloading stress paths do not reach either the failure or yield states, it is worth comparing the observed responses with those from the RTE stress path performed as part of "post-K_0" probe tests. This comparison provides a measure of the natural variability of the specimen and the consistency level of the tests.

Figure 5-3 shows the stress-strain response during the unloading stage of the "post-unloading" probe tests. Even though the beginning stress state of the unloading is slightly different for each specimen, the overall responses are consistent. The shear strains developed during unloading ranged from 0.01 to 0.05 % and volumetric strain varied from 0.016 to 0.07%. The differences between the RTE path and the unloading paths in "post-unloading" probing tests in volumetric behavior can be attributed to the more variation in the initial mean normal effective stress. Furthermore, the comparison with the RTE path in the "post-K_0" probe tests also supports the consistency and small natural variability of the samples used in the second stress probe tests.

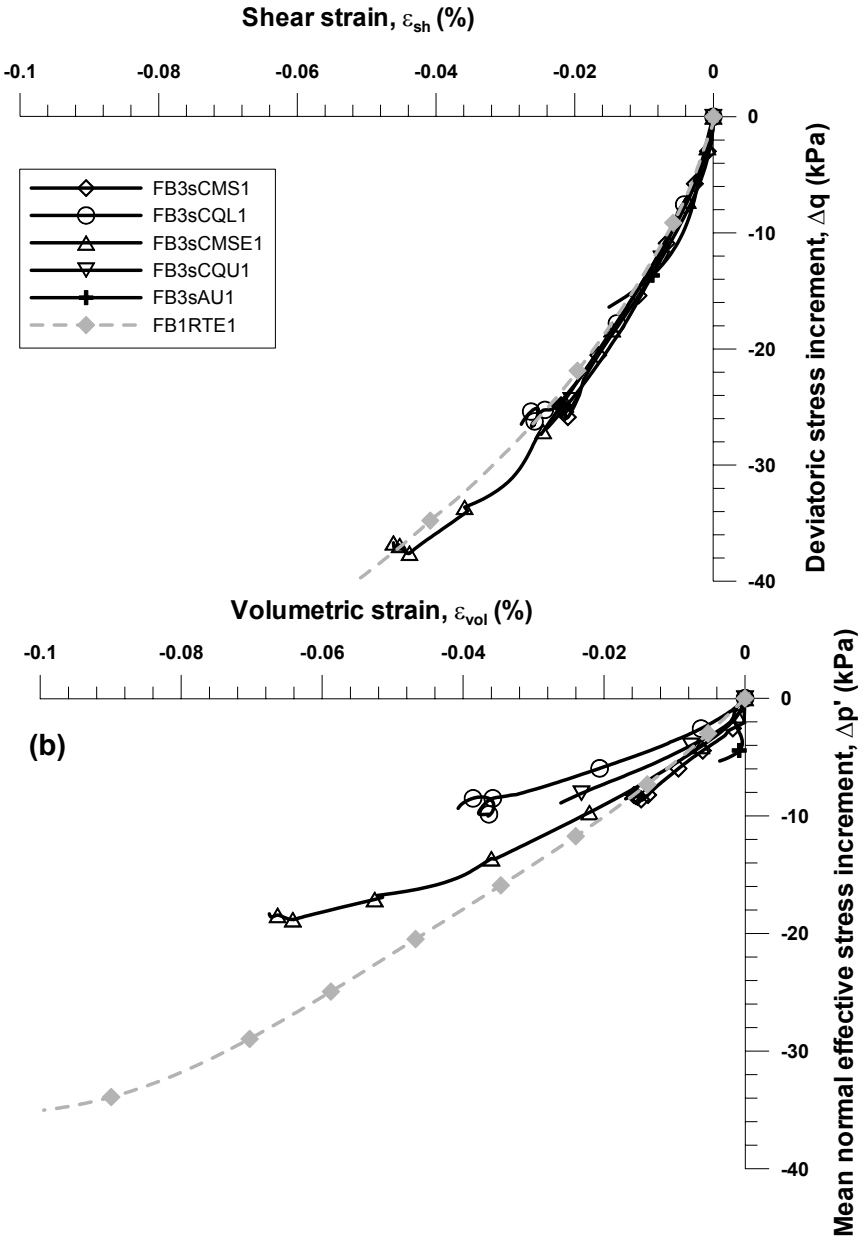

Figure 5-3 Stress-strain response during unloading (a) deviatoric stress – shear strain (b) mean normal effective stress – volumetric strain

5.1.3. Stress-strain response comparisons

In axisymmetric condition, the soil response can be divided into volumetric and shear behavior and their cross coupling as shown in Equation (5-1).

$$\begin{Bmatrix} \Delta\varepsilon_v \\ \Delta\varepsilon_s \end{Bmatrix} = \begin{bmatrix} 1/K & 1/J_v \\ 1/J_s & 1/3G \end{bmatrix} \begin{Bmatrix} \Delta p' \\ \Delta q \end{Bmatrix} \quad (5\text{-}1)$$

where ε_v and ε_s are volumetric strain and shear strain, while p' and q are mean normal effective stress and deviatoric stress, respectively.

In light of Equation (5-1), the stress probe data were processed to generate the plots to investigate the shear, volumetric behavior and the cross-coupling. CMS, CMSE, CQL, CQU and AU data from the two types of stress probe tests are compared to investigate the recent stress history effects on the stress-strain responses. This comparison illustrates the effects of pre-shear stress paths, even though the initial stress conditions are not exactly the same.

Figure 5-4 through 5-7 presents $\Delta p'$-ε_{vol}, Δq-ε_{sh}, $\Delta p'$-ε_{sh} and Δq-ε_{vol} plots for available paths among CMS, CMSE, CQU, CQL and AU stress paths in both the "post-K_0" and "post-unloading" probes. In these figures, the stress path from the "post-unloading" probe is represented by open symbols and adding "s" before the stress path label. The test data in Figure 5-4 through 5-7 are presented at "large" strain scales up to ±1% internal strains and small strains up to 0.1% to illustrate the effects of stress path directions on large and small strain behaviors.

The volumetric stress-strain response is contained in Figures 5-4. At large strains (Figure 5-4(a)), the all $\Delta p'$-ε_{vol} responses but AU for the "post-K_0" probe are similar to those in the "post-unloading" probe in terms of the general data trends and apparent stiffness. The AU of the first stress probe shows a stiffer response because the p´ at the start of shear in "post-K_0" stress probing tests is greater than that for the "post-unloading" stress probing tests. CQU and AU paths for the "post-unloading" probes show less volumetric strains developed due to the

relatively short stress paths to the end of tests. Other than the stiffer response in the AU for the "post-K_0" probes, the overall $\Delta p'$-ε_{vol} responses are similar.

At small strains (Figure 5-4(b)), the CQU and AU paths from "post-K_0" probes and the CQU path show very similar response. In spite of the lower p´ at the beginning of the shear for the "post-unloading" probes, the CQL for the "post-unloading" probes show stiffer response. However, this initial stiffer response is reversed after 0.1% of volumetric strain. This difference in responses is more than 20% in stresses at the volumetric strain of 0.05%, which is larger than the natural variation reported in Section 4.3.2.

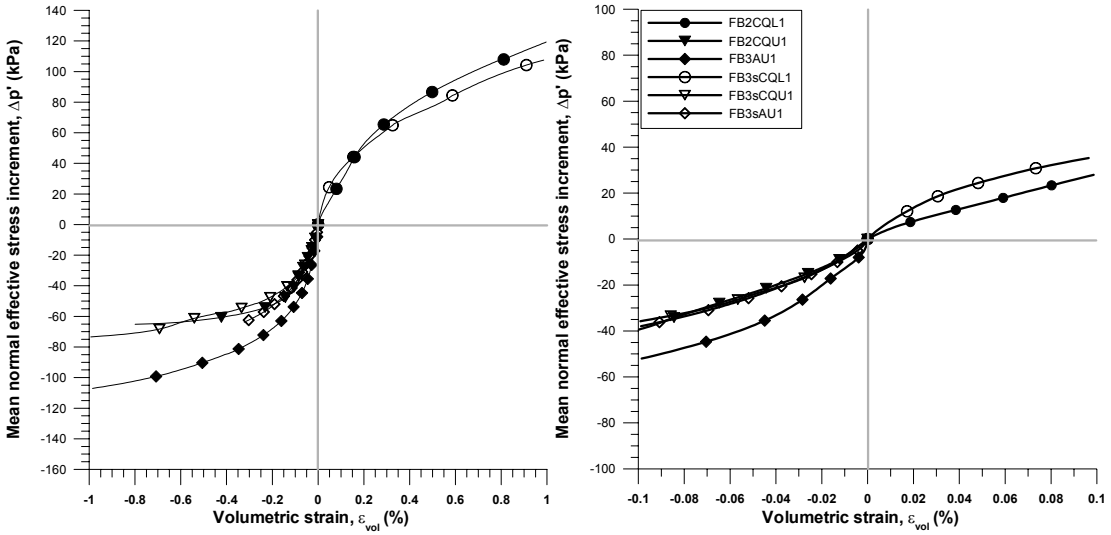

Figure 5-4 $\Delta p'$ versus ε_{vol} for CQL, CQU and AU stress paths in both stress probe tests (a) large strain data up to 1%, (b) small strain data for ε_{vl} ±0.01%

The deviatoric stress-shear strain response is shown in Figure 5-5 for large and small strains. In both large and small strain behavior, the primary differences are the slightly stiffer response for the "post-unloading" probes in loading direction (CMS) and the "post-K_0" probes in unloading direction (CMSE and AU).

In addition, as mentioned earlier in Chapter 4, the smaller developed shear strain during the AU tests than the strain during CQU also supports that the shear strain is not only a function of deviatoric stress, but also the stress ratio (q/p´).

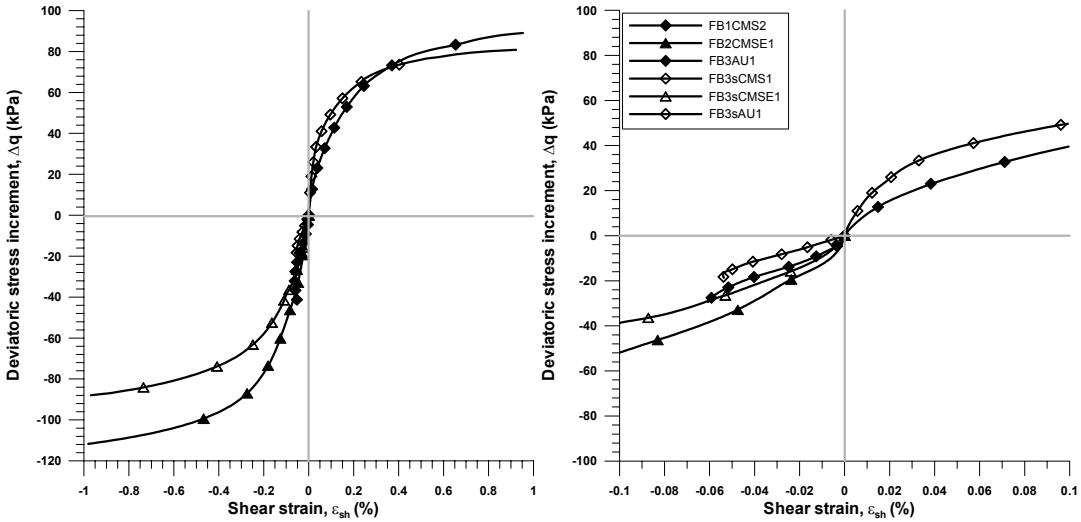

Figure 5-5 Δq versus ε_{sh} for CMS, CMSE and AU stress paths in both stress probe tests (a) large strain data up to 1%, (b) small strain data for ε_{vl} ±0.01%

Previous research on the recent stress history effects focused on the undrained Young's modulus (Santagata 1998), shear and bulk modulus (Atkinson et al 1990; Smith et al 1992) and ignored the cross-coupling effects between the volumetric and shear behavior though it is widely known that soil is not an isotropic elastic material.

Figure 5-6 and 5-7 present the cross-coupling between shear and volumetric behaviors. As mentioned in Chapter 4, even though these two couplings are generally assumed equal under the assumption of isotropic elasticity, it was shown not to be true for compressible Chicago glacial clays. Thus, it is worth to compare those coupling behaviors for two different recent stress histories.

Figure 5-6 shows the mean normal effective stress and shear strain relationship. At large strains (Figure 5-6(a)), there is no "apparent" coupling from -50 to 90 kPa and -50 to 30 kPa for the "post-K_0" and "post-unloading" probes, respectively. The CQL path of the "post-K_0" probes shows stiffer response while the CQU and AU paths for both probes show very similar responses. At small strains for the closer look (Figure 5-6(b)), the response of CQL path of the "post-K_0" probes shows an initially positive shear strain (0.02%) up to 90 kPa increase in mean normal effective stress, followed by a transition to negative shear strain whereas the CQL for the "post-unloading" probes shows initially very stiff responses up to 20 kPa in $\Delta p'$ and softer afterwards. Similarly, the CQU path for the "post-unloading" probes shows 0.01% of negative shear strain up to 40 kPa unloading while the same path for the "post-K_0" probes shows positive shear strain from the beginning. For the AU path, the first probe shows slightly stiffer response, but the overall responses are very similar. This rather complicated coupling between $\Delta p'$ and ε_{sh} suggests that the recent stress history also affects the coupling responses.

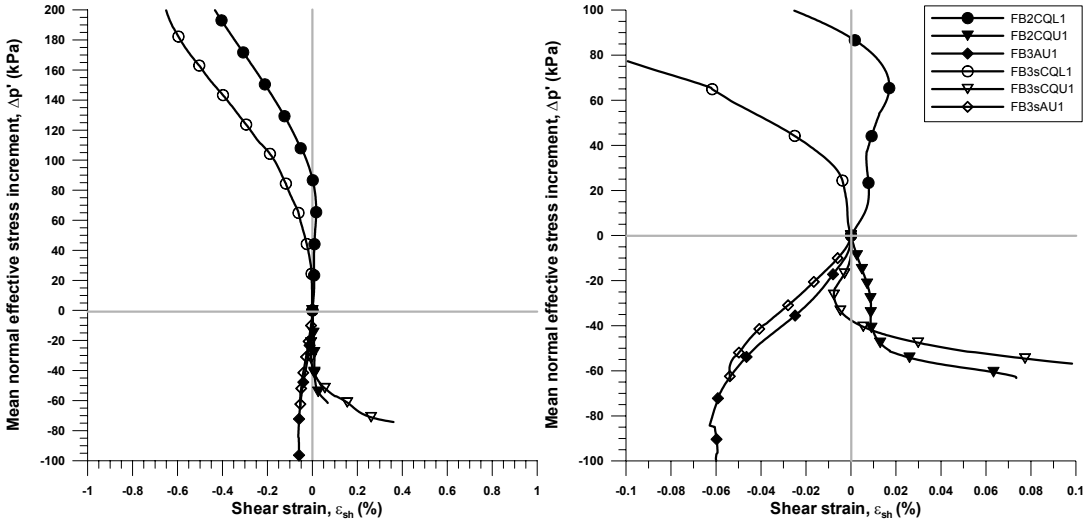

Figure 5-6 $\Delta p'$ versus ε_{sh} for CQL, CQU and AU stress paths in both stress probe tests (a) large strain data up to 1%, (b) small strain data for ε_{vl} ±0.01%

Figure 5-7 shows the deviatoric stress and volumetric strain relationship. At large strains (Figure 5-7(a)), differences between the two probes is more clearly shown in unloading paths (CMSE and AU) than the compression paths (CMS). While CMS paths for the two probes show relatively similar responses, the CMSE and AU paths of the "post-K_0" show stiffer responses. The "post-K_0" probes yield at larger deviatoric stress in both compression and extension. However, considering there is 25 to 35 kPa deviatoric stress difference in the initial stress points between the two probes, the yield stress difference can be negligible. At small strains(Figure 5-7(b)), the CMSE path for the "post-unloading" probes and the CMS path for the "post-K_0" probes show very stiffer responses, indicating little coupling between Δq and ε_{vol}. Overall, the shear induced contraction is occurred in compression as expected in lightly overconsolidated clays. The differences of the two probes suggest that the recent stress history also affects the coupling responses between Δq and ε_{vol}.

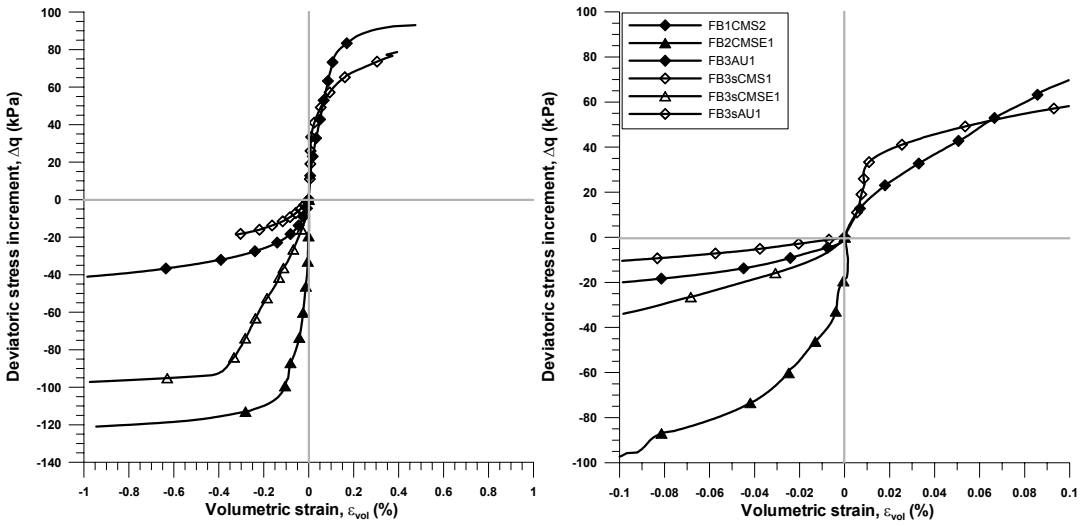

Figure 5-7 Δq versus ε_{vol} for CMS, CMSE and AU stress paths in both stress probe tests (a) large strain data up to 1%, (b) small strain data for ε_{vl} ±0.01%

All the stress-strain relationships between the shear, volumetric and their cross-coupling show that the recent stress history affect the stress-strain response. It is not easy to quantify the difference of the responses between the "post-K_0" and the "post-unloading" stress probes in terms of the stress-strain relationships. Thus, the next section will present the modulus degradation curves of the two stress probe tests.

5.2. MODULUS DEGRADATION BEHAVIOR

Stress-strain data presented in the previous section show that overall similar response in large strain behavior between the two and the differences are clearly shown in small strain range. Unlike the "post-K_0" probe tests presenting stiffer responses in unloading stress paths, the "post-unloading" probe tests show stiffer in loading stress paths.

In this section, the influences of recent stress history on shear, bulk moduli are presented. For the purpose of analysis, interpretation, and discussion of the stress-strain data presented in Chapter 5.1, the following definitions of shear, bulk and two cross coupling secant moduli used in isotropic elasticity are employed:

$$G_{\sec} = \frac{\Delta q}{3\Delta \varepsilon_s} \tag{5-2}$$

$$K_{\sec} = \frac{\Delta p'}{\Delta \varepsilon_v} \tag{5-3}$$

$$J_{v\sec} = \frac{\Delta q}{\Delta \varepsilon_v} \tag{5-4}$$

$$J_{s\sec} = \frac{\Delta p'}{\Delta \varepsilon_s} \tag{5-5}$$

5.2.1. Secant Shear Modulus

The secant shear modulus is plotted versus triaxial shear strain for selected natural specimens whose stress probes involved changes in the deviatoric stress q. Figure 5-8 presents these shear stiffness degradation curves up to 1% shear strain for CMS and CMSE paths of the two probe tests.

As already mentioned in Chapter 4, results of the "post-K_0" probe tests show dependence on loading direction even with the same recent stress history. This is illustrated for both types of probes in Figure 5-8. For example, the stiffness found in the loading (CMS) path at 0.002% shear strain is 44 MPa, while that found in the unloading (CMSE) path is 84 MPa, almost double.

For the "post-unloading" probe tests with a different recent stress history than the "post-K_0" probes, similar patterns are observed. The stiffness of "loading" path (sCMS), which in this case is subjected to a stress reversal, is 85 MPa, while that of "unloading" path (sCMSE) with smaller angular difference is 45 MPa. It is interesting that this value is almost a half of the loading path in the "post-unloading" probes and very similar to that in the unloading path (CMSE) of the "post-K_0" probes.

Considering the differences in the initial stress conditions of the shear between the two stress probe tests, this shear stiffness result implies that the recent stress history impacts on the stress-strain response more than the current stress state at least for these stress differences. However, considering that the second stress probe tests were subjected creep period twice before shear, it might be induced partly by creep effects.

All the findings from the shear moduli between the two stress probes provide clear indication of the recent stress history effects. Also, little difference noted at strains larger than 0.1%.

In addition, the stress paths shown in Figure 5-8 do not contain obvious zones of constant G_{sec} at shear strains greater than or equal to 0.002%. Thus, the very small strain stiffness values must be found from results of the bender element tests, will be discussed in Chapter 6.

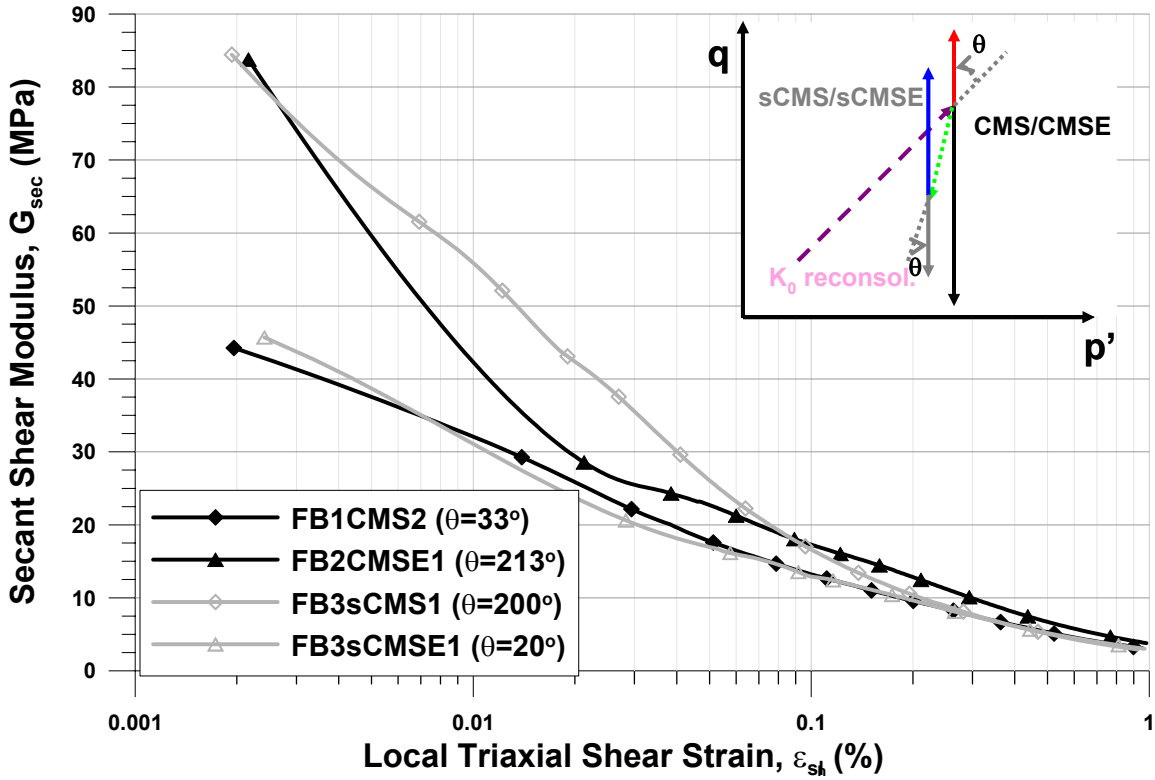

Figure 5-8 Secant shear modulus degradation as a function of shear strain for CMS and CMSE stress paths

5.2.2. Secant Bulk Modulus

The secant bulk modulus K_{sec} is plotted versus the volumetric strain ε_{vl} for stress paths involving changes in the mean normal effective stress p'. The secant bulk modulus degradation curves for CQL and CQU paths of both types of stress probe tests are shown in Figure 5-9. Data are

presented between ε_{vol} of 0.005% to 1.0%. The smallest reliable value of volumetric strain is considered as 0.005%. Here, volumetric strain is calculated from the measurements by on-specimen axial and radial LVDTs.

Similar patterns as shown in the shear modulus degradation can also be observed in bulk modulus degradation curves. In the "post-K_0" probe tests, the loading (CQL) path shows 50 MPa of bulk modulus at 0.005% of volumetric strain while the unloading path exhibits 90 MPa, which is almost twice of that in the loading path. Interestingly, in the "post-unloading" probes, both loading (sCQL) and unloading (sCQU) paths show very similar to each other. There is around 10 MPa difference at 0.005% volumetric strain between the two paths and they become almost identical after 0.01%. Also, like shear moduli, little difference is noted at strains larger than 0.15%.

This seems different than the results shown in shear modulus degradation patterns, a more complete evaluation of the differences in stiffness as a function of the angle between pre-shear stress path and current stress path will be made in the next section.

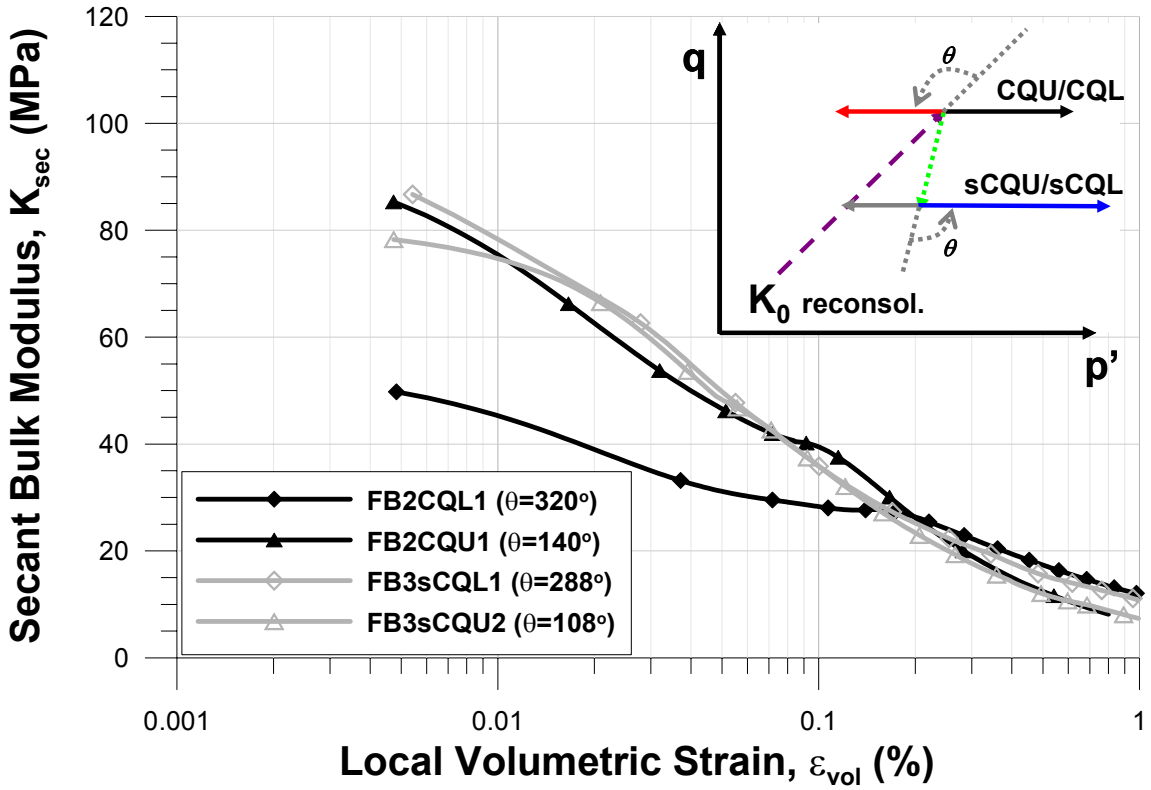

Figure 5-9 Secant bulk modulus degradation as a function of volumetric strain for selected natural specimens

5.3. DIRECTIONALITY OF SOIL STIFFNESS

5.3.1. Directionality of Shear Stiffness

Based on the data presented in Figures 5-8 and 5-9, it is shown that the recent stress history or the pre-shear stress path has an effect on the stress-strain response. Thus, it is interesting to compare the stiffness at various strain level with angular changes to investigate the directionality, effects of both current stress path direction and recent stress history. The experimental data are presented herein with the angular changes between the stress path directions both from an arbitrary initial point to focus on the effects of current stress path direction and from the pre-shear stress path direction to investigate the effects of recent stress history.

Figure 5-10 presents the shear stiffness data of the first and second stress probe tests at shear strain level of 0.002%, 0.01% and 0.1% with the angular change from a horizontal line in *q-p´* space, also the CQL path as also shown in a sketch in the same figure.

To investigate the effect of current stress path direction on the stiffness, first the angle is defined from a horizontal line. The secant shear modulus is technically indeterminate in CQL and CQU paths because there is no change in *q* for those probes. Thus, the curve should be discontinuous at CQU point (θ = 180), but the data trend is very strong to either side.

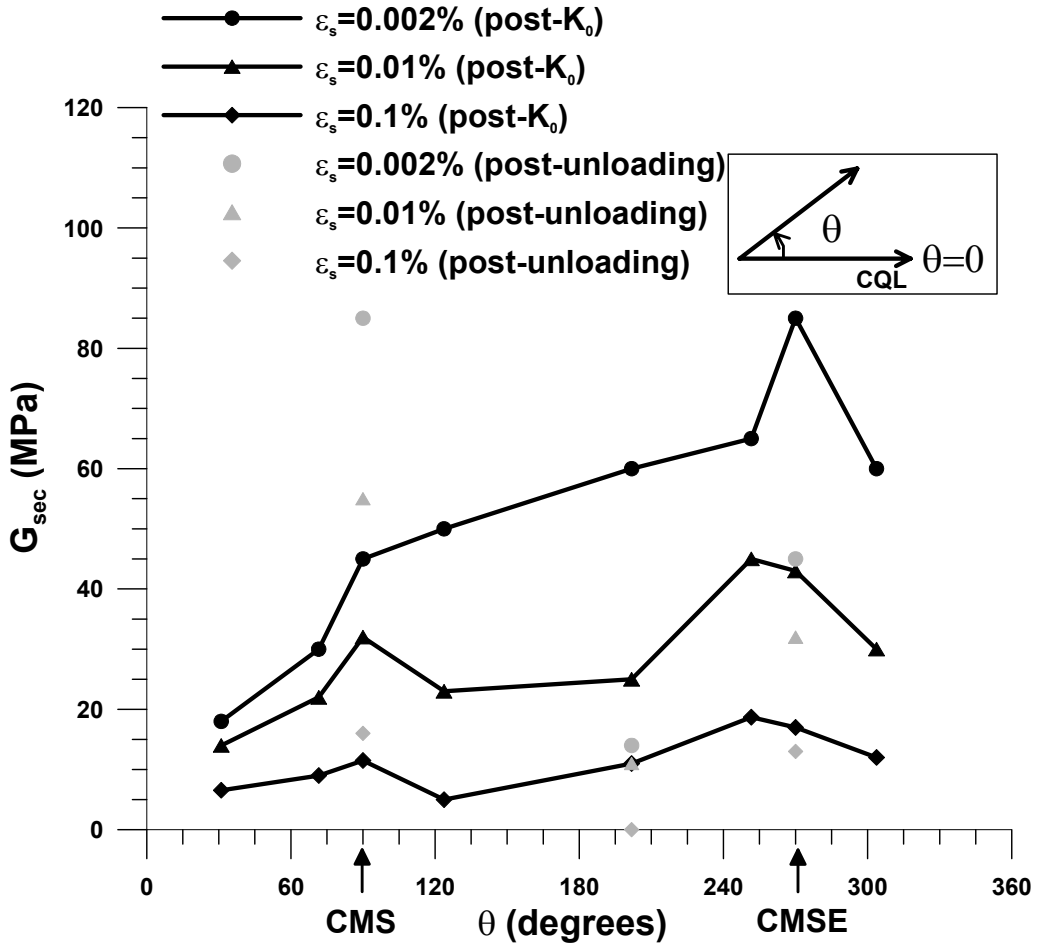

Figure 5-10 Variation of G_{sec} as a function of angular difference θ in stress probe direction with respect to CQL path

The results of the "post-K_0" probes strongly indicate the effects of current stress path direction, but the results of the "post-unloading" probes show a significantly different pattern with lower stiffness in unloading direction (CMSE) and higher stiffness in loading direction (CMS). This apparent discrepancy between the two types of stress probes results suggests one must consider the recent stress history effects.

To this end, Figure 5-11 presents the stiffness in the similar way to Figure 5-10 but with a definition of the angle in terms of the stress direction prior to application on the stress probe, or "recent stress history." The recent stress history of the "post-K_0" probes is assumed to be the K_0 reconsolidation path and that of the "post-unloading" probes is an unloading path (RTE) from the in-situ stress state. AL and RTE paths are assumed to represent the orientation of θ=0 for the "post-K_0" and "post-unloading" probes, respectively. This definition is used in spite of the drained creep under conditions of zero lateral strain which resulted in a nearly 90° change in stress path direction at the ends of both reconsolidation and the unloading path. The length of the creep stress path is generally less than 5 kPa and was not considered large enough to have any significant influence on the directionally-dependent stiffness. These definitions of θ are consistent with that used by Atkinson et al (1990), who defined stress path rotation in terms of the angular difference θ between the previous stress path direction and a new stress path direction. This definition of stress path rotation, as illustrated in upper right cartoons of Figure 5-11, will be used in the following discussions. The angle θ is also defined to be positive counterclockwise.

Using these definitions, with the angular change from CQL, the trend in shear stiffness variation with angular difference in stress path direction of the "post-unloading" probes

conforms to that of the "post-K_0" probes. For example, the loading path (CMS) of the first probe tests and the unloading path (CMSE) of the second probe tests are very similar in terms of the angular differences form the pre-shear stress path even though the current stress path direction is exactly the opposite. It is hard to draw definitive conclusions with the limited data in Figure 5-11, but the overall trend of the data clearly indicates the effect of recent stress history on shear stiffness.

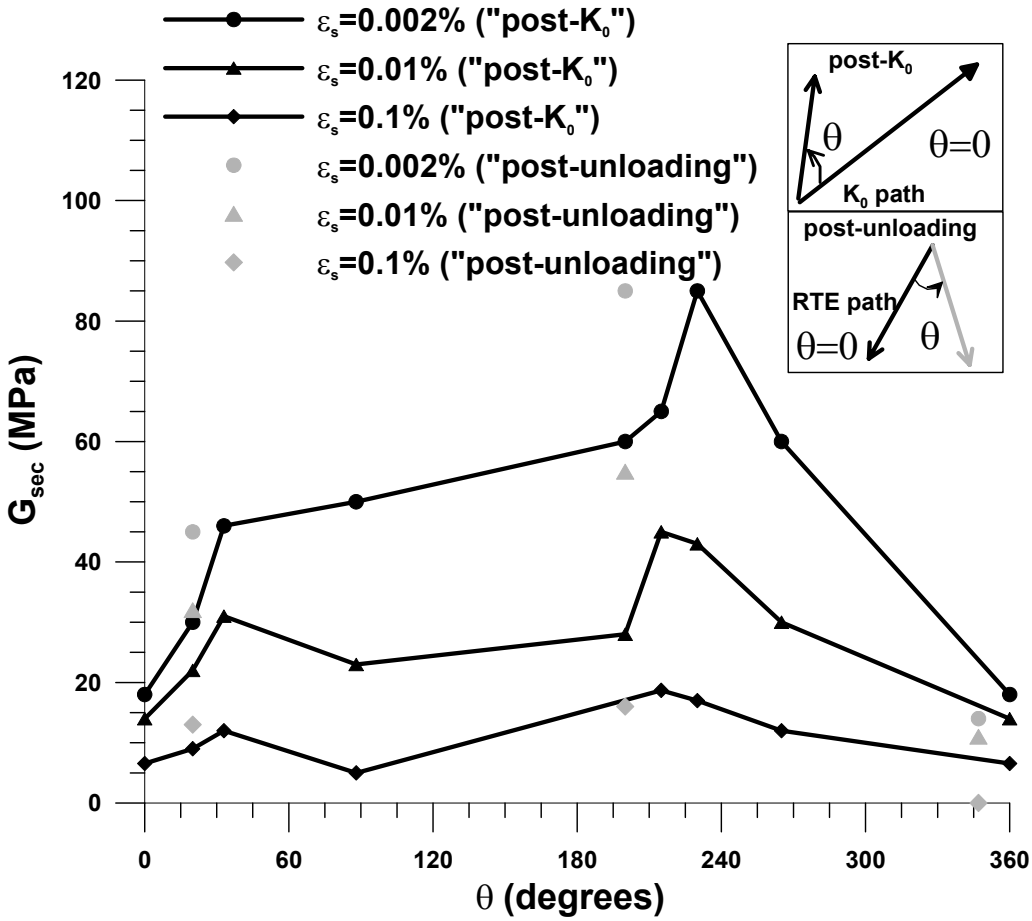

Figure 5-11 Variation of G_{sec} as a function of angular difference θ in stress probe direction with respect to the previous stress history

5.3.2. Directionality of Bulk Stiffness

For the bulk modulus, the similar approaches are employed to investigate the directionality. Figure 5-12 shows the bulk moduli at 0.005%, 0.01% and 0.1% with the angular differences with respect to the CMS path. The CMS path is taken as a zero axis, because the bulk modulus can not be obtained from the path with constant mean normal effective loading and unloading paths (CMS & CMSE). Again, the bulk moduli at 180 degree should be discontinuous but the trend from the "post-K_0" probes is very clear to either side.

As was the case with the shear moduli, the bulk moduli from the "post-unloading" probes do not exhibit the same path dependency as does the results of the "post-K_0" probes. Large differences are noted at 280^o. As was with shear moduli, much smaller differences are noted at the 0.1% strain level.

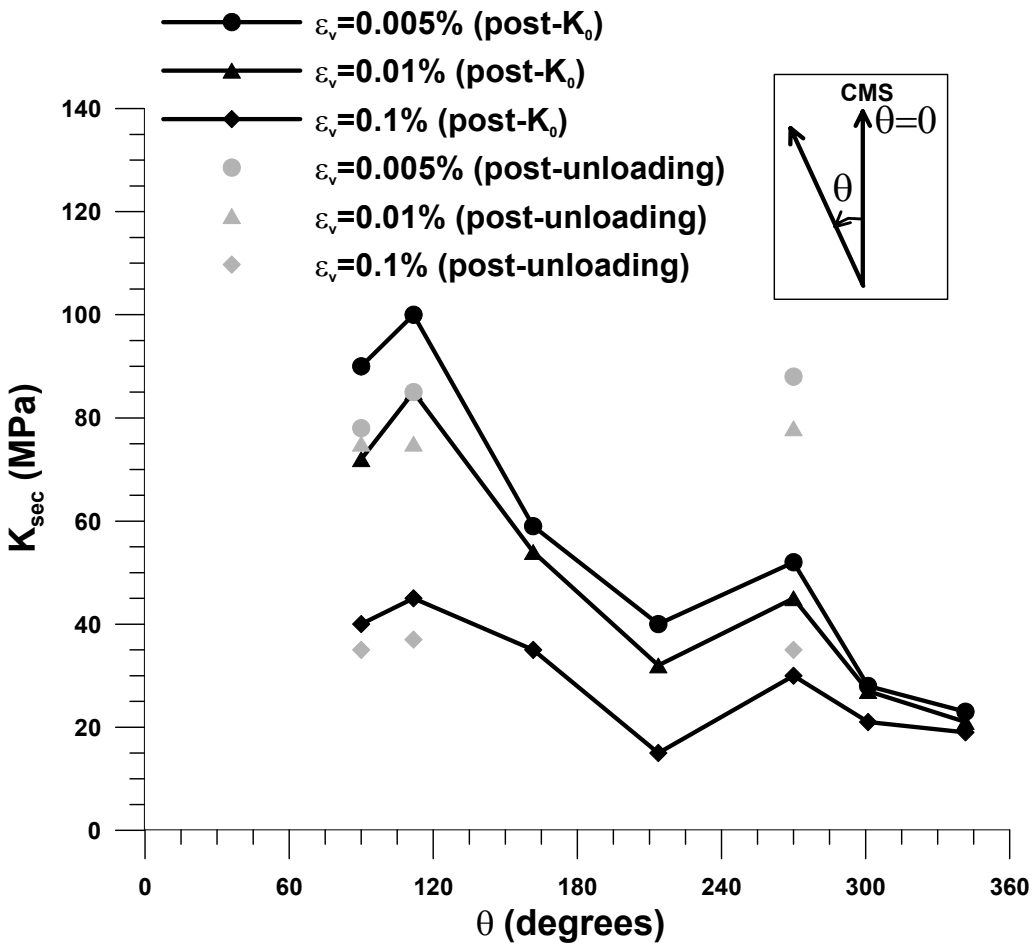

Figure 5-12 Variation of K_{sec} as a function of angular difference θ in stress path direction with respect to CMS path

Figure 5-13 shows the bulk moduli as a function of angular difference in the current stress path direction with respect to the pre-shear stress path. The definitions of angular difference θ in both stress probe tests are illustrated in sketches in Figure 5-13. Unlike the case of shear moduli, it is hard to find any pattern between the two stress probe tests results.

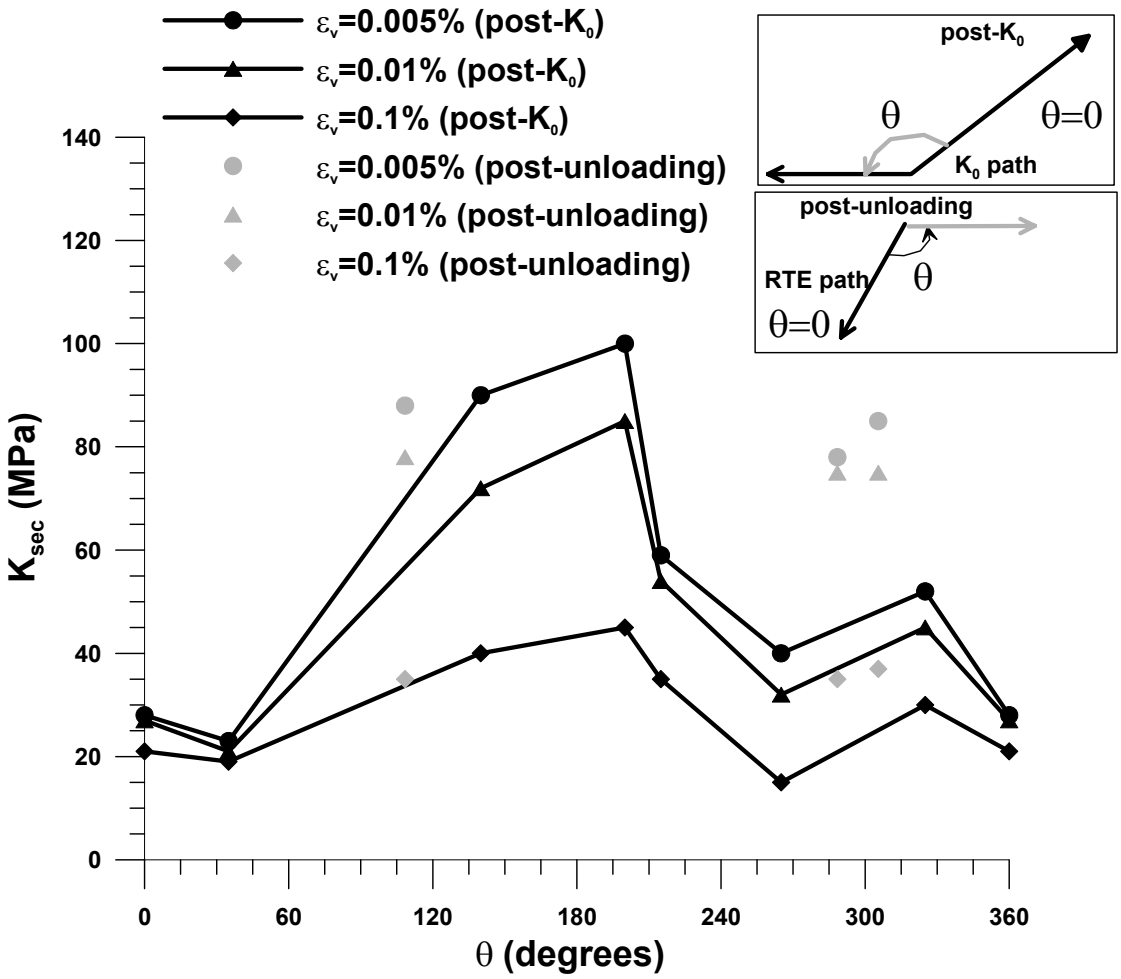

Figure 5-13 Variation of K_{sec} as a function of angular difference θ in stress path direction with respect to the previous stress history

It is hard to find a pattern with only 3 test results especially when those results are not spaced enough in θ to exhibit any pattern. While the "post-unloading" data seem to agree with the "post-K_0" data when θ is defined with respect to a single direction, and hence be little impacted by recent stress history effects. Further work is needed to evaluate the trends in bulk modulus.

5.3.3. Discussions on Directionality of Compressible Chicago Glacial Clays

In Section 5.1 and 5.2, the influences of the current stress path direction and the recent stress history on the stress-strain response are presented. The results of drained directional stress probes on compressible Chicago glacial clay specimens obtained from the Ford Center excavation site clearly demonstrate the dependence of soil stiffness on stress path direction in terms of general p'-q space and the recent stress history. The data obtained in this study and presented in Figures 5-5 through 5-13 can be compared to results of other research described in Chapter 2. Consequently, shear and bulk moduli, the two pseudo elastic parameters analyzed, vary strongly as a function of stress path direction and recent stress history and a magnitude of strain.

Therefore, the experimental data presented in Sections 5.1 and 5.2 reinforces the concept that there is no unique shear or bulk modulus value that can be used to adequately link stress and strain behavior for general stress changes of compressible Chicago glacial clays.

Several recent studies (Atkinson and Stallebrass 1991;Gasparre et al. 2007) uses the conceptual soil model with 3 yield surfaces suggested by Jardine (1995) to explain the effects of recent stress history effects. The 3 yield surface model may in fact be used to describe the directionality of compressible Chicago glacial clays, but there are several reasons to be reluctant to apply that model framework.

First, the soil which provides the insight of the conceptual model is totally different from the soil focused on this research. Their material is a marine-derived highly overconsolidated clay with OCR more than 40, while the soil of this research is a fresh-water slightly overconsolidated clay with OCR of less than 2.

Second, the experimental procedures used herein can not define the linear elastic zone mechanically, thought to occur at very small strain ranges generally as less than 0.001%. While this is in part due to the limitation of research instrumentation used herein, but previous research (Clayton and Heymann 2001) showed that it is not easy to detect the Y_1 surface in most soils. It is logically easier to define the Y_1 surface, which bounds the linear elastic zone for very stiff soils such as highly overconsolidated clay or soft rocks like chalks, but it is not guaranteed that there is linearly elastic zone at the strain level smaller than our measurable range. Though it is possible to define the third yield surface,Y_3 from this experimental work, Y_3 is the same as a conventional yield or bounding surface, depending on the theoretical framework. It would not make any sense to apply a soil model to a particular soil if some of the characteristics of those models are not observed from experimental results.

Third, there is subjectivity in the definition of the second yield surface which plays an important role in explaining the recent stress history effects. According to Jardine (1995), Y_2 is defined as "the limit to recoverable, but non-linear behavior," which meant Y_2 should be defined by unloading and reloading tests in drained condition with small stress increment until it showed distinct plastic strain. As an alternative, Jardine (1995) also addressed that Y_2 can be mapped from monotonic drained probing tests by the location where the strain increment vector may change direction and the rate of plastic strain development accelerates. This more or less ambiguous definition brings up the questions which elastic modulus should be applied to define the elastic strain to discriminate the plastic strain out of total strain. Also there is another method to define Y_2 using coaxiality of shear strain and volumetric strains (Gasparre et al 2007). This seems to eliminate the subjectivity of the definition, but it comes down to a matter of which

scales should be used to define the nonlinearity of the two strains, particularly for the compressible Chicago glacial clays which exhibit highly nonlinear response from the very beginning of the shear.

Fourth, some of the results such as the RTC and sign change in the cross coupling moduli. Even though some of the previous research on stiff natural Gault clays (Lings et al 2000) showed favorable results to the conceptual model based on an anisotropic elasto-plastic model, this is not the case here with compressible Chicago clays. It is hard to define the coupling moduli in the conventional manner with strains because the sign changes during the stress path. The cross-coupling moduli of other soils presented in the previous research do not show this kind behavior. The volumetric responses of a RTC sample and negative moduli in cross-coupling behavior are contrary to the theory of elasticity, implying that these compressible Chicago clays are neither isotropic nor elastic.

Additional comments should be made with regard to the creep effects. First, the ratio between the shear rate during a drained stress probe and the creep rate should be large enough to ignore the creep rate effects on the directionality of the stiffness. Previous research (Santagata 1998; Clayton and Heymann 2001) showed that the directionality of shear stiffness would disappear if the creep rate was 30-50 times smaller than the shearing rate. The shearing rate is controlled to be at least 30 times faster than the creep rate throughout this experimental program; with this rate, according to Santagata (1998) and Clayton and Heymann (2001), no directionality should be observed. Data presented in this Chapter shows otherwise.

One additional experiment was performed with the extended creep period (7days). Figure 5-14 shows the shear stiffness of the 2 triaxial compression tests with different creep periods and

one reduced triaxial extension tests. The ratio between the shear rate and the creep rate is more than 300 but still the directionality can be observed. Also the data confirmed the previous research (Anderson and Stokoe 1978; Tatsuoka et al. 1997; Santagata 2007) that the extended creep or aging can increase the shear stiffness throughout the measured strain range.

Furthermore, since the "post-unloading" probe tests were subjected to the creep twice before the stress probe eventually applied, creep effects must be considered in the analysis of the "post-unloading" probes. Recall in Figure 5-8, the maximum stiffness in the "post-K_0" probes occurred in the CMSE path while that in the "post-unloading" probes occurred in the CMS path. Surprisingly, those two maximum values of shear stiffness of the two stress probe tests showed very similar values even though the "post-unloading" probes started from the lower mean normal effective stress and deviatoric stress. This may be related to the creep effects. However, this question needs to be further studied.

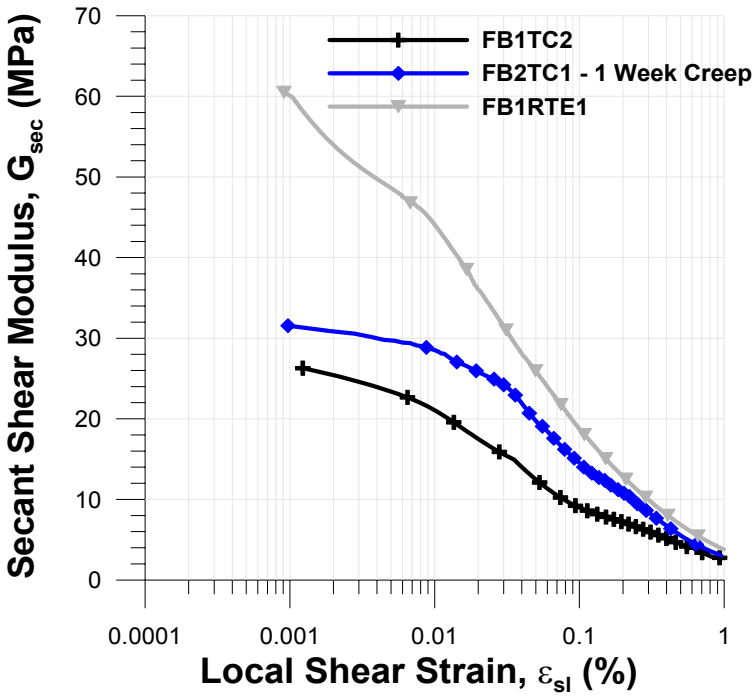

Figure 5-14 Triaxial compression tests results with two different creep period (36 hrs and 170 hrs)

5.4. STRAIN RESPONSE ENVELOPES

Strain response envelopes (SREs) of the two probes are generated to depict the differences in stress-strain response for all possible strain path directions and incremental stress probe magnitudes. Nonlinear and irreversible soil responses also can be seen by examining the SREs. Furthermore, the comparisons of SREs for the two probes will be useful to understand the evolution of the directionality with increased strain.

5.4.1. SREs comparisons between the two types of stress probes

Strain response envelopes are created using the stress-strain data from the two types of stress probes. SREs are plotted at various strain levels to illustrate the evolution of the directionally-dependent Chicago clay behavior as a function of strain level. The SREs can be used to provide insight into the irreversible, nonlinear response of these compressible Chicago clays as well as the general secant compliance as a function of stress path direction. The secant stiffness that is indicated by an SRE is related to the typical definitions for modulus (i.e. shear or bulk).

Figure 5-15 presents the stress probe input circles for R_σ=10, 15, 30, 40, and 50 kPa for both types of probes. R_σ of 1, 2, 5, 10, 15, 30, 40 and 50 kPa were applied to investigate the non linearity and directionality differences due to the different pre-shear stress path.

Figure 5-16 shows the SREs of the two stress probe tests at large strain for R_σ= 15, 30, 40 and 50 kPa. From the upper figure of Figure 5-16, the SREs of the "post-K_0" probes, widely differing behavior between loading and unloading probes is suggested even at relatively large strain levels. The spacing between contours is a function of the general stiffness of the soil for a given loading direction. It is apparent that the softest response occurs when the probe points are in the direction of continued loading (AL) and stiffer responses occur in case of an unloading

stress path (AU). This is consistent with the results presented in the previous sections for G_{sec} and K_{sec}. All SREs are markedly non-symmetric about the origin of the strain increment space, which represents genuine experimental evidence of incremental non-linearity. In particular, the lack of symmetry strongly suggests that soil response is inelastic (Costanzo et al 2006).

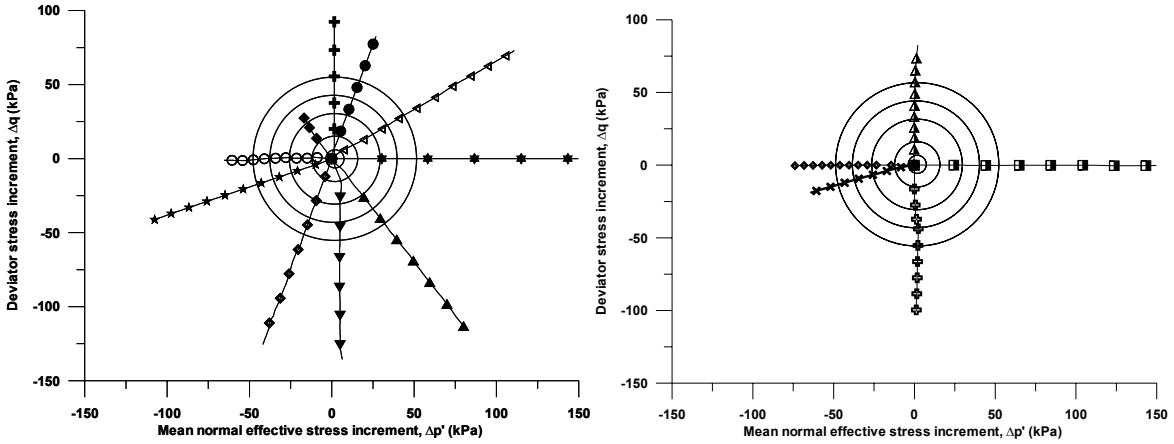

Figure 5-15 Stress probe input circles for R_σ=25, 50, 75, and 100 kPa

Furthermore, assuming SRE is an elliptical shape, the major axis is rotated toward the vertical axis. As explained before, this indicates that the cross-coupling exists. In this case, a mean normal effective stress increase induces the positive shear strains and a deviatoric stress increase induces the positive volumetric strains.

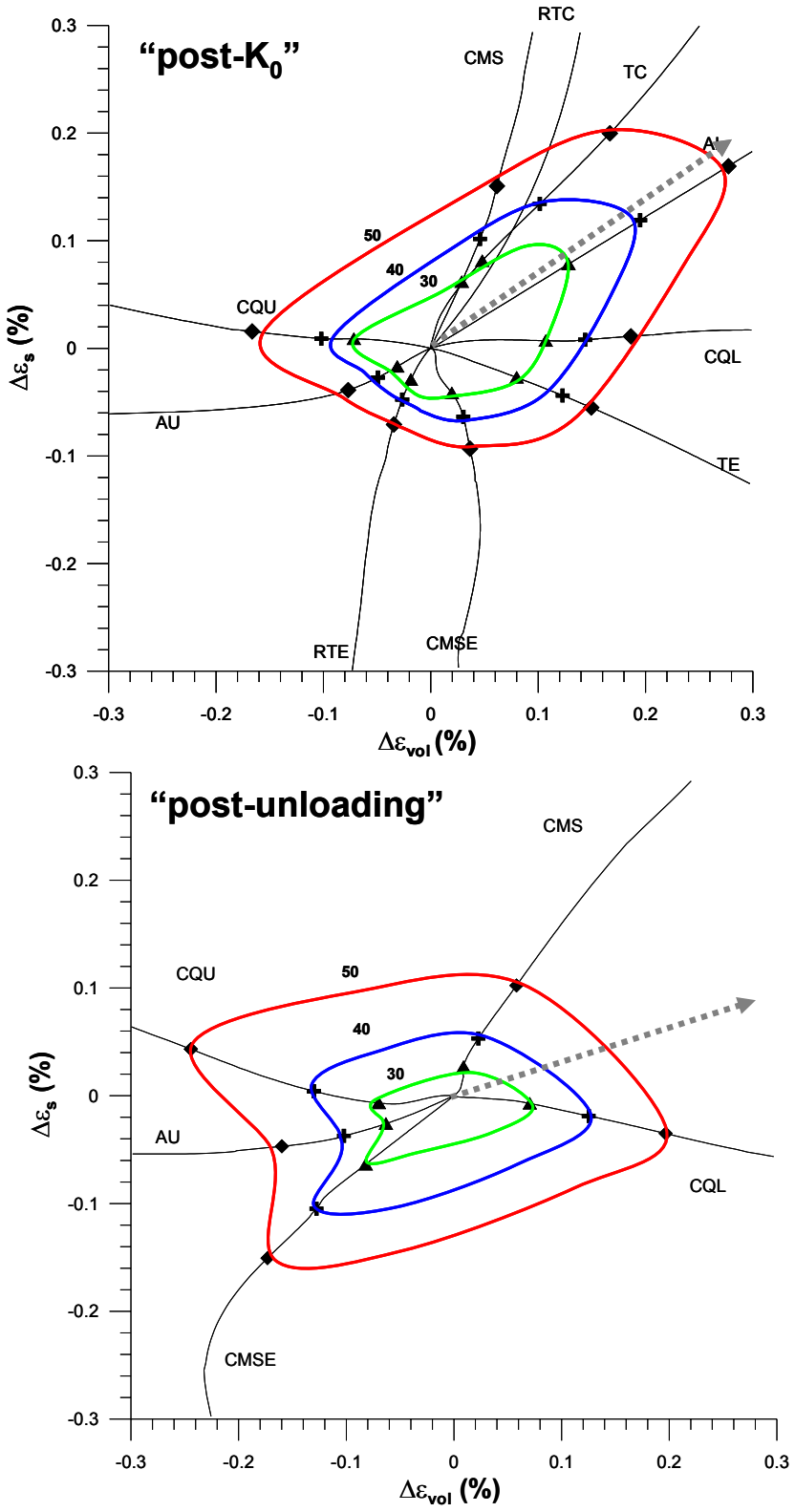

Figure 5-16 Strain response envelopes for small to large-strain levels, R_σ=10, 20, 25, 30, and 50 kPa

The characteristics of the SREs for the "post-unloading" probes are very different. There is relatively equal spacing between contours for the "post-unloading" probes in all directions at large strain level. In contrast to the stiffer response as noted by shorter spacing between the contours, in unloading directions observed in the "post-K_0" probes. However, this is not the case at smaller strain levels as will be shown later with smaller SREs. The rotation of the major axis, shown as a grey dotted arrow, is smaller than that of the "post-K_0" probes and more symmetrical, but still non-symmetric, from the origin under the assumption of an elliptical shape. This indicates that the cross-coupling moduli are also influenced by the recent stress history.

The size of SRE at the given stress level represent the overall stiffness. In general the SRE size of the "post-unloading" probes is smaller than that of the "post-K_0" probes, which means former results show stiffer response than the first probe tests. This size difference is larger at smaller strain levels, as will be shown subsequently.

Small strain responses based on smaller R_σ input values are shown in Figure 5-17. This figure shows SREs for strains between -0.04 and 0.06% for R_σ of 2, 5, 10 and 15 kPa. SREs for the "post-unloading" probes are clearly smaller than that for the "post-K_0" probes. As explained in Section 5.3.3, the stiffer response of the "post-unloading" probes may be a result of the lower initial shear stress state. However, more work needs to be done to identify the cause of this behavior.

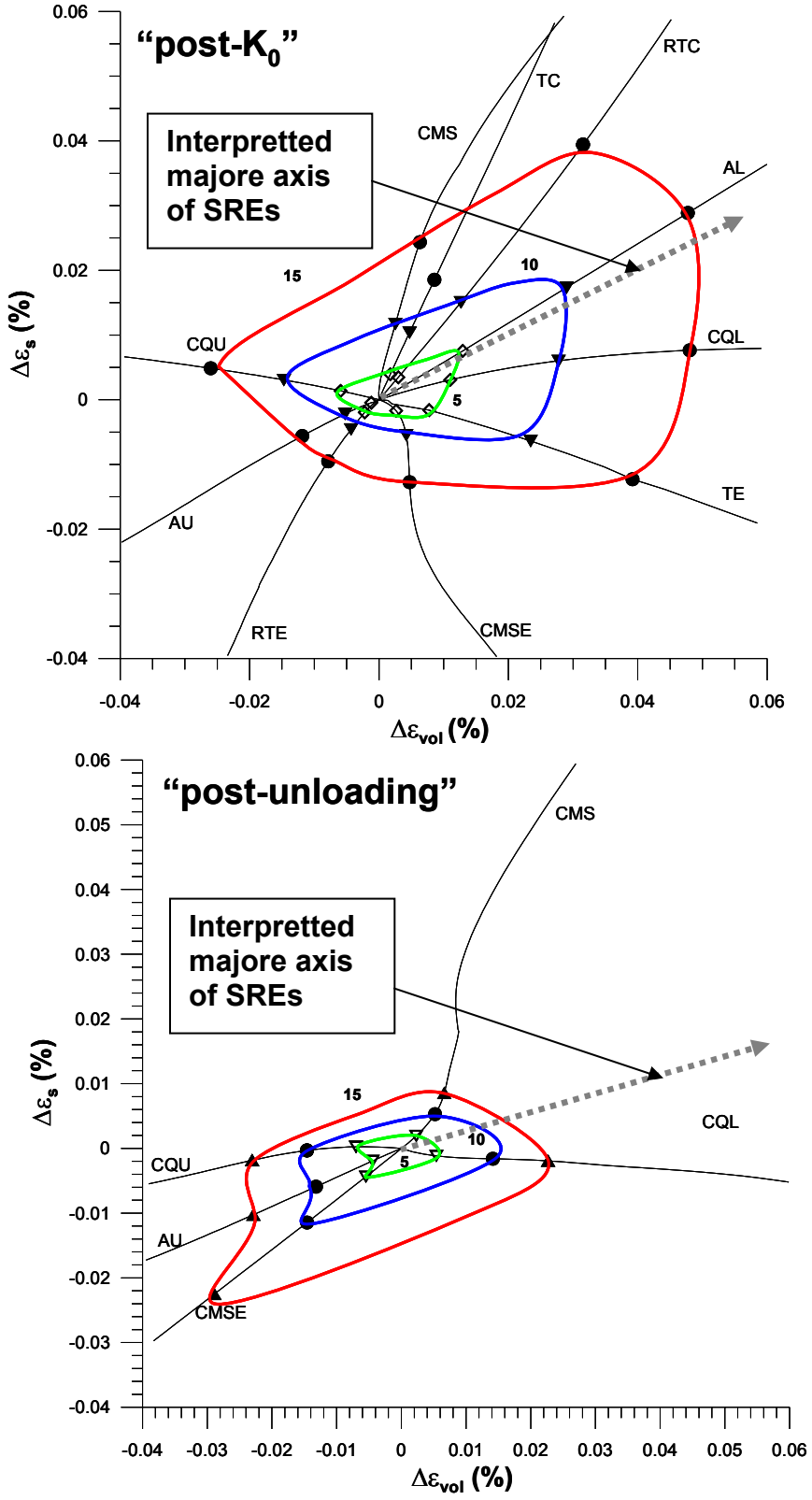

Figure 5-17 Strain response envelopes for small strain levels, R_σ=2, 5, 10, and 15 kPa

In addition, the relatively dense spacing of SREs in the "post-unloading" probes occurs in the (original) loading direction while the dense spacing of SRE in the "post-K_0" probes occurs in (original) unloading direction. Thus, different responses in terms of the current stress path directions, but similar responses are observed in terms of the pre-shear stress path direction, in that the stiffer response results from a stress path reversal from the pre-shear stress path direction.

The above mentioned different characteristics become more distinct in SREs of even smaller strain (±0.01%) with smaller $R_\sigma$of 1, 2, and 5 kPa as shown in Figure 5-18. Stiffer responses in stress reversal location and the smaller size of SREs in the "post-unloading" probes and the major axis rotation of elliptical shape are clear even at the smallest scale obtainable in this investigation. The SREs comparisons with 3 different strain levels show that the differences in the two SREs decrease with increased strain levels, which agrees with the findings of Atkinson (1990) that the stiffness differences between loading and unloading stress path becomes negligible after 0.5% strain. Note that the SRE with R_σ = 1 and 2 are drawn even though some of the strain points are smaller than that can be guaranteed to be accurate because the trend of the smaller SRE with R_σ of 1 and 2 follows the overall trend.

From the comparison between the SREs from the two different types of stress probes, it is shown that the recent stress history plays an important role in the soil response. While the SREs of the "post-K_0" probes progressively shift upward to the right, those in the "post-unloading" probes do not shift much from the horizontal axis. The stiffer responses are observed where the stress path is reversed, and the shear, bulk and two cross-coupling moduli are affected by the recent stress history.

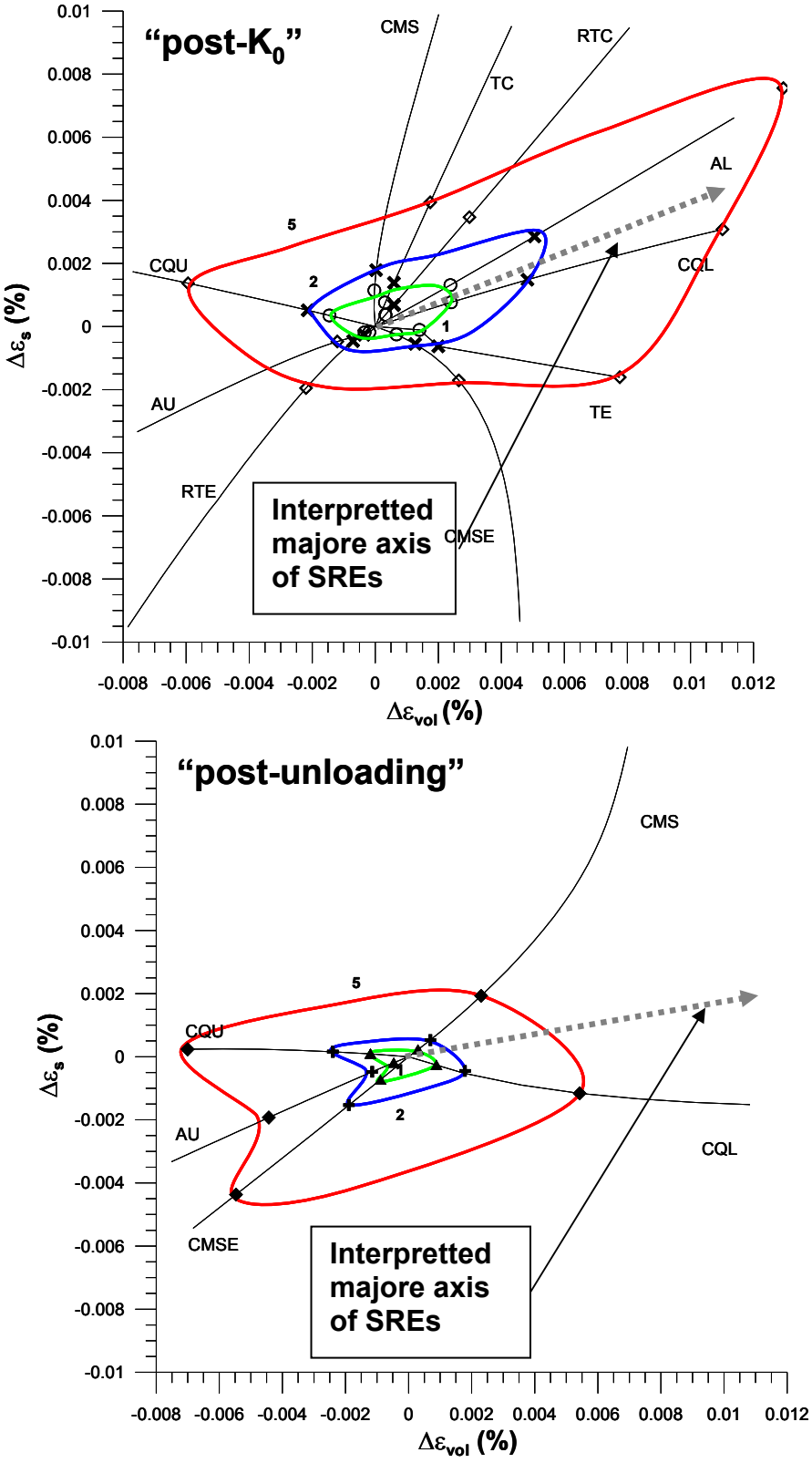

Figure 5-18 Strain response envelopes for small strain levels, R_σ=1, 2, and 5 kPa

5.4.2. Incremental Nonlinearity

Various approaches have been suggested in literature to represent non-linearity of soils. The use of classical elasto-plastic model with multiple yield surfaces or kinematic hardening concepts with multiple nested surfaces have been used to deal with both non-linearity and recent stress history (e.g. Jardine 1995; Atkinson and Stallebrass 1997). However, as explained in Section 5.3.3, there are several reasons to be reluctant to employ these elasto-plastic frameworks.

However, an incremental non-linearity approach can explain the current stress path and recent stress history effects without resorting on the elastoplasticity. Incremental non-linearity, as defined by Tamagnini and Viggiani (2002), is material behavior wherein a rate-type constitutive function, $\dot{G}$, is a continuously nonlinear function of the strain rate (or increment) $\dot{\varepsilon}$ over the entirety of strain space. As a result, it is impossible for general loading and unloading stiffness to be equal. Furthermore, according to this qualitative definition, the tangent stiffness tensor D shows continuously nonlinear dependence on the strain rate direction (Viggiani and Tamagnini, 1999). The experimental results clearly indicate that the response of compressible Chicago glacial clays is inelastic and highly dependent on current stress path direction and recent stress history, as well as on strain magnitude. These behaviors provide evidence that the clays investigated in this program may be classified as incrementally nonlinear. Compared to the elastic SRE in Figure 5-16, which is symmetric in shape and centered about the strain origin, the experimental SREs are clearly nonlinear and inelastic. The non-symmetric shape, shifted origin of the assumed ellipse, and the directional compliance stiffness all support the incrementally non-linear nature of the compressible Chicago glacial clays.

5.5. SUMMARY AND CONCLUSIONS

Results of two types of stress probes with different pre-shear stress paths were compared to investigate the effects of recent stress history and the current stress path dependency. Those two effects are combined herein as "Directionality" because in reality those two effects do not exist separately.

The stress-strain data and modulus degradation behavior for each directional stress probe with two different pre-shear stress paths were presented and discussed in terms of shear and volumetric behavior. Based on the comparisons of stress-strain data and moulus degradation curves between the two types of stress probes, directionality was shown in all data presented. The locations of the maximum shear and bulk moduli occurred at θ corresponding to complete or nearly complete stress reversals; this finding is generally consistent with the experimental data published by Atkinson et al (1990). Current stress path and recent stress history affect not only shear and bulk moduli, but also the cross-coupling moduli. The non-linearity of the stiffness was observed from the beginning of the tests at least at strains that were reliably determined; more than 0.002% of shear strain and 0.005% of volumetric strain.

Incremental strain response envelopes (SRE) in the general p'-q stress and ε_{vol}-ε_{sh} strain spaces can be used to graphically represent the complete nonlinear, irreversible, and directionally dependent response of an entire group of stress probes about an initial stress state. The comparisons of SREs for the two types probes graphically showed the directionality of the Chicago clay. While the SREs of the "post-K_0" probes progressively shifted upward to the right, whereas those in the "post-unloading" slightly shift from the horizontal line as the length of stress path increased. The stiffer responses, illustrated by the narrowest stress contours, were

observed in stress-path reversal orientations. Shear, bulk and two cross-coupling moduli were all affected by the recent stress history. However, this influence became smaller with larger strains.

The experimental results presented herein showed that the stiffness of compressible Chicago clays is highly dependent on loading direction as well as strain level. The significant variability of the shear and bulk moduli with stress path direction and strain level provide experimental evidence that the Chicago clays are incrementally nonlinear.

CHAPTER 6 BENDER ELEMENT TESTS RESULTS

Emphasis has been placed on elastic properties of soil in static problems since Burland (1989) suggested that strains developed in situ under the working load conditions were smaller than previous thought. To investigate soil elasticity, sophisticated measurement systems have become an essential component of advanced laboratory testing devices (Tatsuoka et al. 2001). Among the measuring devices, bender elements provide a simple technique to determine elastic (small-strain) shear stiffness. Bender elements (Shirley and Hampton 1978), in which an elastic modulus is derived based on wave propagation theory, enhance the capacities of triaxial testing devices so that one can simultaneously measure both dynamic and static properties of soils subjected to axisymmetric stress conditions. Because the bender elements induce very small strains which keep the specimen intact during loading, synchronous measurement of elastic and elastic-plastic responses during a static loading is possible (Callisto and Calabresi 1998; Callisto and Rampello 2002; Kuwano and Jardine 2002).

At the beginning of this experimental program, triaxial testing equipment with a vertical bender element set was used. Later, the equipment was upgraded to include two more sets of horizontally-oriented bender elements to investigate the anisotropic nature of compressible Chicago glacial clays. Herein, most of analysis is based on $G_{BE(vh)}$ due to the limited quantity of the other two bender element data, $G_{BE(hh)}$ and $G_{BE(hv)}$.

This chapter presents results of the bender element (BE) tests performed on natural specimens during K_0 reconsolidation, creep, and directional stress probing. Section 6.1 presents the bender element results during K_0 reconsolidation. An empirical relationship between the stress state and the shear stiffness based on the bender element test results is established.

Moreover, the anisotropy ratio ($G_{BE(hh)}/G_{BE(vh)}$) for limited sets of tests is presented. Section 6.2 presents the bender element results during stress probing. The evolution of anisotropy during shearing is presented and the limit state obtained from the bender element tests is compared with that based on the stress-strain data. Section 6.3 compares the dynamic shear stiffness based on the bender element tests results with in-situ sCPT test results and the mechanical shear stiffness obtained from the stress-strain data. Comparison between results of field seismic tests and bender element tests will help to clarify the sampling effects in the laboratory test results and close the gap between the stiffness obtained from the triaxial apparatus with on-specimen measurement systems and the field measurement. Finally, Section 6.4 summarizes this work and presents its conclusions.

6.1. G_{BE} DURING K_0 RECONSOLIDATION

As explained earlier in Chapter 3, the elastic shear wave velocity, V_{BE}, is calculated herein using the wave travel time determined by the cross correlation method (Viggiani and Atkinson 1995) and the tip-to-tip distance between transmitting and receiving bender elements. Assuming that the triaxial specimen represented an infinite, isotropic, elastic medium, G_{BE} can be calculated as:

$$G_{BE(ij)} = \rho V_{BE(ij)}^2 \qquad (6\text{-}1)$$

where ρ is the total mass density of the specimen when V_{BE} was measured. The shear moduli and shear wave velocities are given a double suffix, the first referring to the direction of propagation of the wave, the second referring to the direction of polarization or particle motion.

6.1.1. G_{BE} Relationship to Effective Stress

As discussed in Chapter 2, many researchers have investigated the factors influencing soil

elasticity. From the results of resonant column tests on sands and clays, Hardin and Black (1966, 1968) and Hardin and Blandford (1989) suggested the following empirical relation:

$$G_{ij}^0 = S_{ij} f(e)(\text{OCR})^k (\sigma'_i)^{ni} (\sigma'_j)^{nj} \qquad (6\text{-}2)$$

where G_{ij}^0 is the elastic shear modulus in the $i-j$ plane, S_{ij} is a material constant (or fabric constant), $f(e)$ is a void ratio function, e is the void ratio, OCR is the overconsolidation ratio, σ'_i is the normal effective stress in the i-direction, and ni, nj and k are exponents for σ'_i, σ'_j and OCR, respectively. While numerous testing data have supported the applicability of Equation (6-2), effort also has been devoted to simplify it. A number of researchers (e.g. Ishihara 1982; Tatsuoka and Shibuya 1992; Jamiolkowski et al. 1994; Shibuya et al. 1997; Santagata et al. 2005) ignored the effect of OCR on the elastic shear modulus, and proposed alternative expressions with different void ratio functions. Viggiani (1992) replaced $f(e)$ with a function of the mean normal effective stress based on plastic hardening of clays under isotropic loading (Houlsby and Wroth 1991). Rampello et al. (1997) extended Viggiani's equation to anisotropic stress conditions based on experimental results of a reconstituted clay subjected to a constant stress ratio. Thus, elastic stiffness of soils can be expressed in terms of the stress components, as well as by relationships between void ratio and stresses.

Values of $G_{BE(vh)}$ were related to void ratio and the axial and radial effective stresses based on the data measured during K_0 consolidationby :

$$\frac{G_{BE(vh)}}{p_a} = Af(e)\left(\frac{\sigma'_a}{p_a}\right)^{na}\left(\frac{\sigma'_r}{p_a}\right)^{nr} \qquad (6\text{-}3)$$

where p_a is atmospheric pressure (101.3kPa), used as a normalizing constant, $f(e)$ is a void

ratio function, and A, na, and nr are material constants. The reference void ratio, 0.7455 was calculated by averaging void ratios at the end of the consolidation stage. The 36 hour creep period resulted in an increase in σ'_r, which when coupled with the ageing effects, resulted in an increased G_{BE}. To maintain the compatibility of the analysis, the data measured during the creep stage were not considered specifically when deriving Equation (6-3).

Based on the data set of G_{BE} obtained from the consolidation data, the exponents of Equation (6-3), na and nr, were obtained by a least square regression to yield:

$$\frac{G_{BE(vh)}}{p_a} = 609\left(\frac{\sigma'_a}{p_a}\right)^{0.285}\left(\frac{\sigma'_r}{p_a}\right)^{0.163} \qquad (6\text{-}4)$$

Note that $Af(e)$ is taken as a constant equal to 609. Figure 6-1 compares the measured data and the line computed based on Equation (6-4). Even though the variation of void ratio is not taken into account in Equation (6-4), the computed line agrees well with the measured data because of small change of void ratio in the overconsolidated state during consolidation.

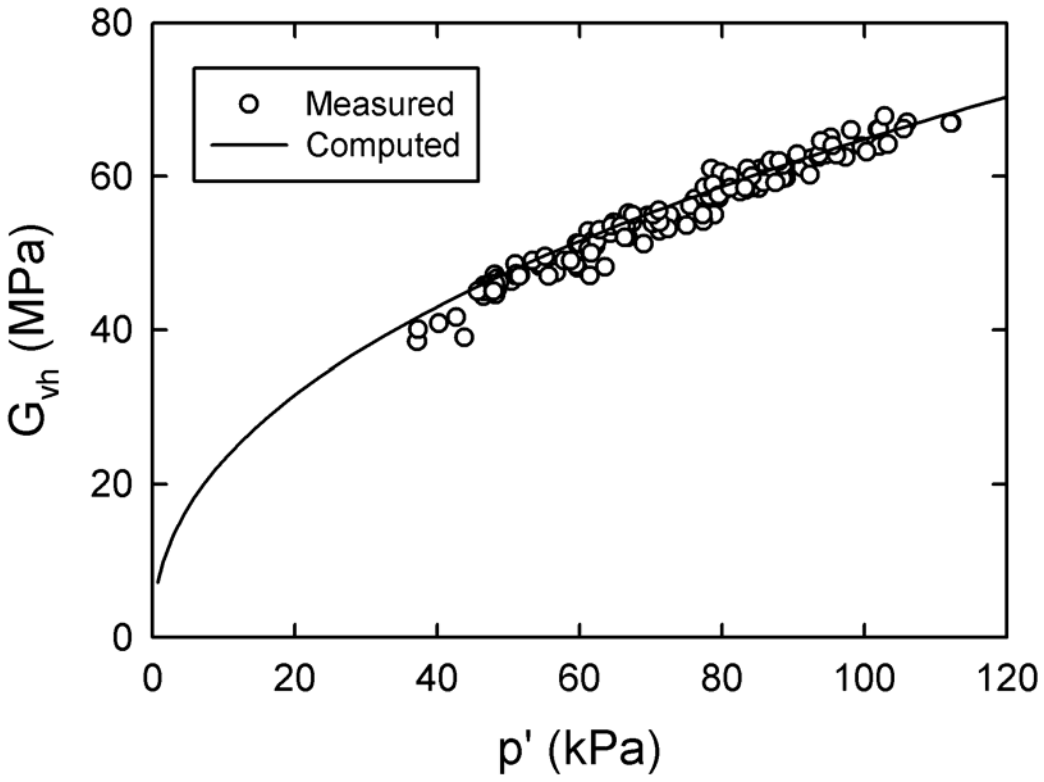

Figure 6-1 Comparison between measured and computed $G_{BE(vh)}$ from Equation (6-4)

6.1.2. Anisotropy of Very Small Strain Stiffness

The addition of two sets of horizontal bender element sets to the experimental device during the course of this work made it possible to investigate the anisotropic nature of compressible Chicago glacial clays.

The horizontal bender elements measure the horizontally-propagated, horizontally-polarized wave velocity, V_{hh}, and the horizontally-propagated, vertically-polarized wave velocity, V_{hv}. With the same procedure applied in Section 6.1.1, an empirical equation for $G_{BE(hh)}$ was determined to be:

$$\frac{G_{BE(hh)}}{p_a} = 859.6\left(\frac{\sigma'_r}{p_a}\right)^{0.603} \qquad (6\text{-}5)$$

Note that $Af(e)$ is taken as a constant equal to 859.6. Figure 6-2 compares the measured data and the line computed based on Equation (6-5). Here, the scatter is larger than that in Figure 6-1, possibly as a result of difference in the installation method for the vertical and the horizontal bender elements and the shorter distance between the horizontal bender elements. While the vertical bender elements are inserted in the top cap and bottom pedestal, the horizontal bender elements has to be inserted by hand and is thus possibly subjected to more alignment errors than a vertical set. Also, the shorter travel distance for the horizontal set of bender elements makes the same absolute error in defining the arrival time result in a larger error in propagation velocity.

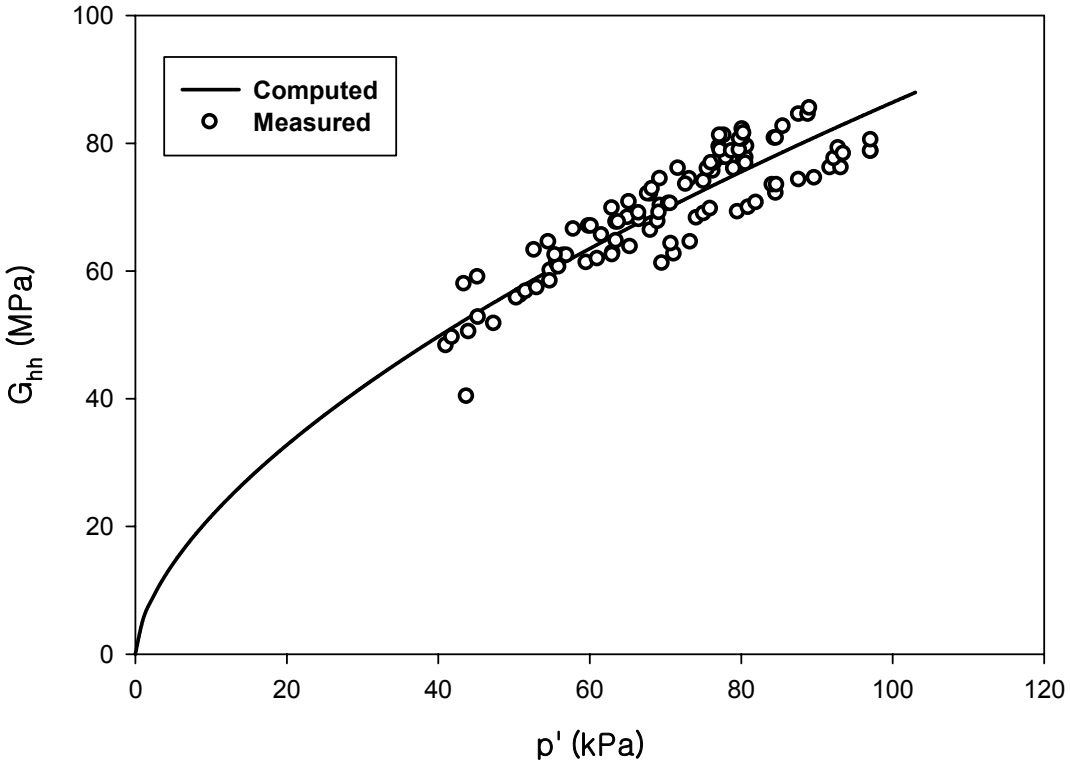

Figure 6-2 Comparison between measured and computed $G_{BE(vh)}$ from Equation (6-5)

The shear moduli calculated from the propagation velocities measured in the 3 sets of bender elements from Equation (6-1) during K_0 reconsolidation are plotted in Figure 6-3. The trend of three different shear moduli, (i.e. $G_{hh} >> G_{hv} \cong G_{vh}$), agrees with the general pattern of directional moduli in a cross-anisotropic soil experiencing one-dimensional deposition (Pennington et al. 1997; Jovicic and Coop 1998). The modulus ratio, either E_h/E_v or G_{hh}/G_{vh}, is commonly used to report the degree of stiffness anisotropy in a given stress condition. Conventionally, shear modulus ratio G_{hh}/G_{vh} is used more often for clay and plotted in Figure 6-4.

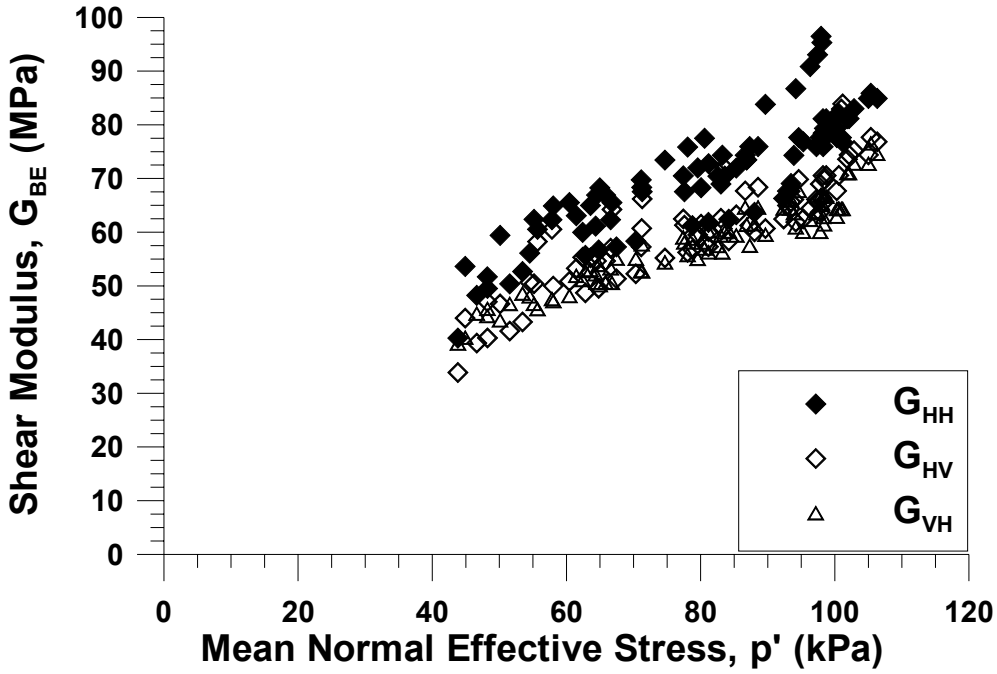

Figure 6-3 Shear modulus based on bender elements results during K_0 consolidation

In addition, G_{hh}/G_{hv} values are also plotted to check the suitability of cross-anisotropy. The shear moduli ratios of other soils (Jamiolkowski et al. 1995; Pennington et al. 1997; Jovicic and Coop 1998; Lings et al. 2000) was shown in Table 2-2. The ratios for normally consolidated

or lightly overconsolidated clays ranged from 1.2 to 1.7 and those for the heavily overconsolidated clays were more than 2.2. The ratio G_{hh}/G_{vh} of soft Chicago glacial clay varied from 1 to 1.4 with an average of 1.18 and a standard deviation of 0.03. This ratio can be placed in the lower bound of the reported values.

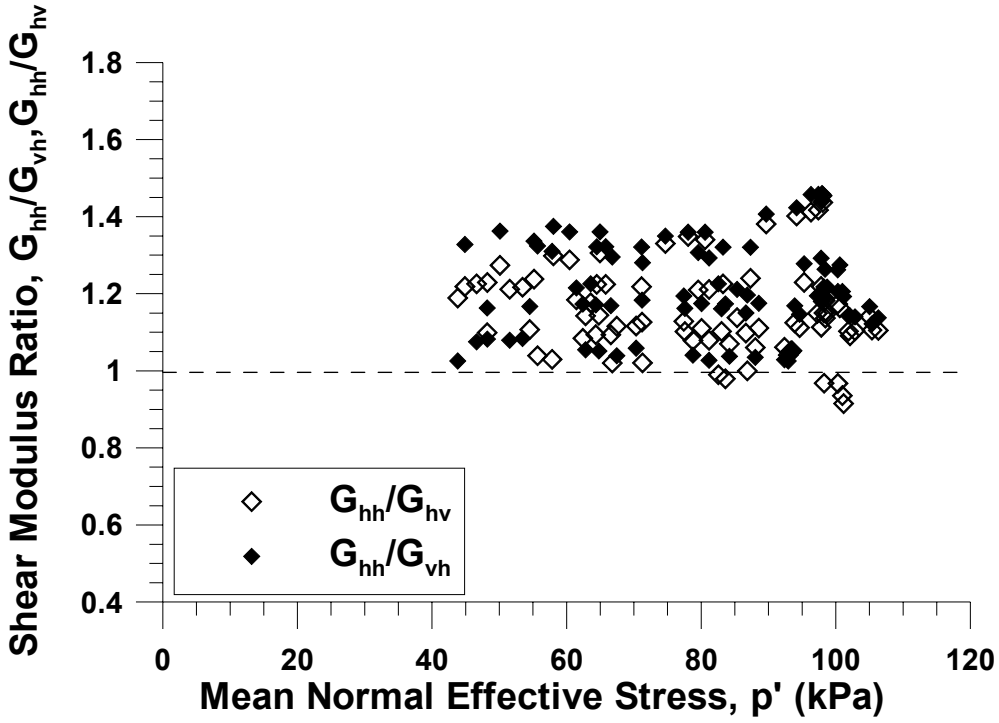

Figure 6-4 Shear modulus ratio during K_0 consolidation

Furthermore, the initial stiffness is inherently anisotropic due to the depositional fabric of a clay (Pennington et al. 1997), as evidenced by the constant ratio (=1.18) throughout the consolidation phase. Even in the beginning of the k_0 reconsolidation which is isotropic state at the measured residual stress, the anisotropy ratio is a constant (=1.2). Inherent anisotropy is dominant and the stress-induced anisotropy is relatively small during K_0 reconsolidation, as Jovicic and Coop (1997) reported for kaolin and London clay.

In addition to the tests conducted on individual specimen, bender element tests were performed on the Blocks #2 and #3 before any specimens were cut to evaluate the initial

anisotropy of the blocks. 5 bender element tests were performed with 25 wave-stacking in each test. Table 6-1 summarizes bender element tests performed on uncut Block #2 and #3. The average anisotropy ratio, ($G_{hh}/G_{hv}=V_{hh}^2/V_{vh}^2$) of Block #2 and #3 were 1.08 and 1, respectively. Block #2 showed similar values in V_{vh} and V_{hv} but Block #3 showed V_{hv} less than the other two. The measured residual effective stress in each specimen before the triaxial testing ranges similar in the two blocks. This smaller ratio compared to the values from the specimen likely occurred because the tests on uncut blocks contained more uncertainty in path lengths. The uncut block tests were subjected to more the alignment errors because the two sides of the block facing each other were not parallel and the bender element sets were installed by hand.

Table 6-1 Bender element test results on uncut block #2 and #3

		V_{vh} (m/s)	V_{hv} (m/s)	V_{hh} (m/s)	Ratio (V_{hh}^2/V_{vh}^2)
Block #2 (37 kPa<p_r'<51 kPa)	1	160	161	167	1.09
	2	162	161	169	1.09
	3	159	162	167	1.10
	4	159	160	166	1.09
	5	162	161	165	1.04
	Average	161	161	167	1.08
Block #3 (35 kPa<p_r'<54 kPa)	1	136	127	137	1.01
	2	134	127	133	0.99
	3	133	129	134	1.02
	4	135	128	138	1.05
	5	136	128	133	0.96
	Average	135	128	135	1.00

6.1.3. $G_{BE(vh)}$ during creep period

In the triaxial testing procedure, a drained creep period under conditions of zero lateral strain was imposed on each specimen before the start of the stress probing portion of the test. This creep cycle is applied to avoid any confusing interactions related to previous loading history. The

average time of creep was 36 hours, but one test was performed to investigate the extended creep effect. The creep period was considered complete when the internally-measured axial strain rate was less than 0.002%/day.

Table 6-2 shows the increase of G_{BE} value during the creep period. Values of G_{BE} at the end of K_0 consolidation and at the end of creep period are compared. Average 4% of increase during 36 hours of creep was observed, which is comparable to 6% of increase from the previous findings on block specimens of Chicago clays taken from the Blodgett stratum (Holman 2003).

However, the extended creep period (1 week) increased G_{BE} by 8.3%. In that specimen, there was around 5% of increase during the first 36 hours which is comparable to the average of the other specimen and the 3% increase occurred during the rest of the time (132 hours). Thus, the creep period affects the very small strain stiffness of Chicago clays, in agreement with Shibuya et al. (1997)' obsevations that the structure of clays induced by ageing or creep affects the very small strain stiffness measured by bender element tests.

Table 6-2 $G_{BE(vh)}$ comparison at the end of K_0 reconsolidation and at the end of 36 hrs creep

	G_{BE} at the end of K_0 Consol. (Mpa)	G_{BE} at the end of creep (Mpa)	Increase (%)
FB1CMS2	68.09	69.76	2.46
FB2CMSE1	63.96	68.66	7.34
FB2CQL1	68.10	71.57	5.09
FB2CQU1	67.43	67.45	0.03
FB2TC2	72.39	76.15	5.19
FB1RTE1	63.53	65.02	2.35
FB1TE1	66.44	69.69	4.90
FB1RTC2	65.58	68.81	4.93
FB3AL1	64.00	67.00	4.69
FB3AU1	68.00	69.00	1.47
FB3sCMS1	63.00	64.00	1.59
FB3sCMSE1	64.00	66.00	3.13
FB3sCQL1	58.00	63.00	8.62
FB3sCQU1	65.00	65.00	0.00
FB2TC1*	68.00	71.5 (73.71)	5.15 (8.38)
		AVERAGE (%)	3.79

6.2. G_{BE} DURING STRESS PROBE TESTS

Bender element tests were conducted during each stress probe to evaluate the influence of stress changes and strains on the bender element modulus G_{BE}. Based on previous work by Viggiani and Atkinson (1995), it was expected that small increments of stress and strain during the stress probes would not result in significant changes in G_{BE}. Large stress and strain increments were anticipated to cause more significant changes in the dynamic properties.

6.2.1. Effect of Large-strain Yielding on Elastic Shear Stiffness

To investigate the yielding effects on the bender element test results, the ratio between measured and predicted values of $G_{BE(vh)}$ (herein after called G_{BE} ratio) is plotted against the length of stress path (LSP) in Figure 6-5. LSP is defined as:

$$\text{LSP} = \sqrt{(p' - p'_0)^2 + (q - q_0)^2} \qquad (6\text{-}7)$$

where p'_0 and q_0 refer to the stresses prior to the application of the stress probe. Figure 6-5(a) shows the variation of the G_{BE} ratios during consolidation. Except for the small scattering at the beginning of consolidation due to variation in the void ratio under low effective confining stresses, the values of the G_{BE} ratio vary between 0.97 and 1.03. In contrast, Figure 6-5(b) shows that the G_{BE} ratio for a number of stress probes is much smaller than these values. To highlight the reduction of the G_{BE} ratio, straight lines are drawn through data that deviates from the limit expected based on the data in Figure 6-5(a). It may be noted that, even though an apparent reduction of G_{BE} ratios is observed during shearing, a limited number of data points were available because of the limitation of measurement near failure in the stress-controlled tests.

A clear reduction of G_{BE} ratio is found in the AU, CMS, CMSE, CQU, RTE, TC, and

RTC stress paths. The G_{BE} ratio decreases more quickly in the RTC, CQU, and CMS stress paths wherein the stress ratio ($\eta = q / p'$) increases with constant or decreasing p'. It is clear that an increasing stress ratio contributes to the reduction of the G_{BE} ratio.

By selecting the LSP in Figure 6-5(b) at the intersection of the straight line marking the reduction of the G_{BE} ratio and the horizontal line where G_{BE} ratio is equal to one, one can locate a stress point in p'-q space, hereafter called the reduction point. The reduction points are given in Figure 6-6, together with the yield points and yield surface. The reduction points are surprisingly close to the yield surface, as defined previously. This similarity implies that the decrease of elastic shear stiffness reflected in the G_{BE} ratio, directly relates to post-yield behavior of clays. This suggests that the reduction of the G_{BE} ratio by distortional deformation results from the change of the internal route inside the soil structure through which the elastic waves propagate, as described previously. Under such distortion by changing stress ratios, the existing soil structure that has been established *in-situ* and during consolidation starts to change, as indicated by the yield surface and the reduction of the G_{BE} ratio. Note that this does not imply that the response within the yield surface is elastic. Clearly, data presented in Chapter 4 show that the responses are nonlinear and path-dependent within this surface, and although no unload-reload cycles were included in the probes, the responses likely included irrecoverable deformations.

Furthermore, the locations of the reduction points for the RTE, CMSE, and AU paths in p'-q space in Figure 6-6 show the stress ratios clearly differ from those at the reduction points of the η-loading paths. Thus, the decrease in elastic stiffness is not initiated at a specific magnitude of the stress ratio, as Hoque and Tatsuok (2004) concluded for the response of sands, because the structure of clays is more affected by previous stress history than that of sand.

There is no apparent reduction of G_{BE} ratio for the paths of AL, CQL, and TE in Figure 6-5(b). Such consistency between the measured values and those predicted by Equation (6-4) indicates that Equation (6-4) remains valid for these paths at stresses beyond those defined by the yield curves defined in Section 4.5. Plastic volumetric compression likely is a major cause of the yielding for these compression paths wherein the initial yield surface is exceeded during probing. The soil structure *in-situ* and during consolidation maintains geometrical similarity to that during probing for the compression paths, implying the direction of the internal route for shear wave propagation would not change significantly. Empirical expressions for G_{BE} such as Equation (6-4) account for the decrease of void ratio induced by the plastic volumetric compression through the void ratio function. For the TE path wherein the stress ratio decreases as p' increases, the volumetric compression after yield apparently compensates for the distortion affecting the shear wave propagation. Thus Equation (6-4) was applicable for this path, at least for the magnitude of loading induced in this test. Because of limitation in the on-sample instrumentation, the TE probe did not reach failure.

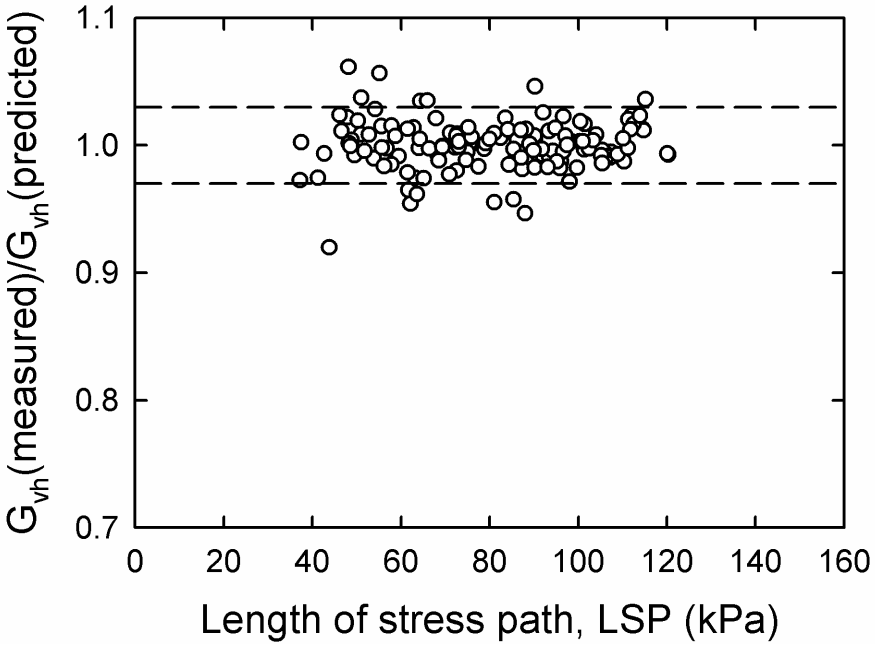

(a)

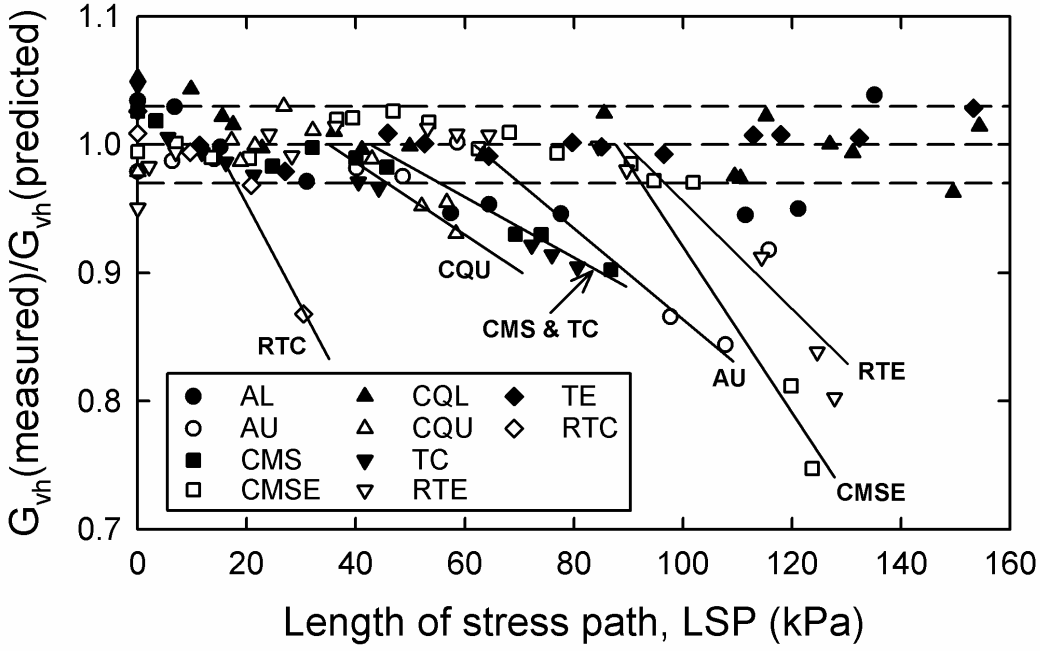

(b)

Figure 6-5 Reduction point (a) during consolidation (b) during stress probe tests

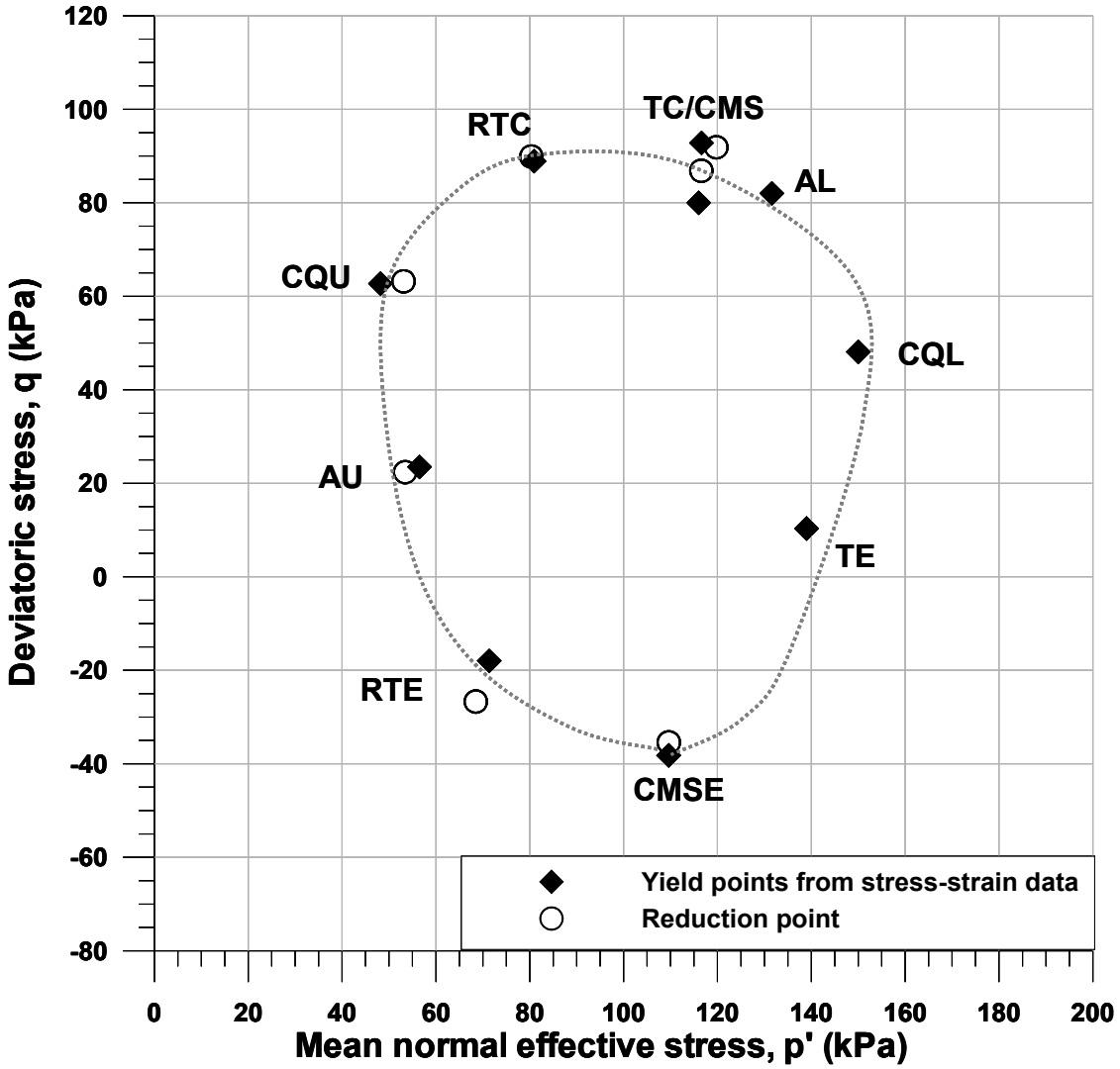

Figure 6-6 Yield point from reduction points and from stress-strain data

6.2.2. Evolution of Anisotropic Stiffness during Shear

As the experimental program progressed, two sets of bender elements were added to the system. Probes, AL, AU and TC were performed with the three sets of bender elements. Figure 6-7 shows the results of three tests during K_0 reconsolidation, creep and shearing. The AU path shown in Figure 6-7(a), indicates the convergence of all three values of G_{BE}. However, it is worth noting that the convergence occurred around the residual effective stress (=51 kPa). The

TC path shown in Figure 6-7(b), shows clear reduction of all three values of G_{BE}. It is clearly shown that as the specimen sheared toward failure, the anisotropic state became isotropic. In contrast, the AL path in Figure 6-7(c) shows that the ratio remained constant ratio as the loading progressed. As explained in the previous section, the soil structure *in-situ* and during consolidation maintains geometrical similarity to that during probing for AL path, implying the direction of the internal route for shear wave propagation would not change significantly. However, the distortion of soil particles during TC and AU paths has also impact on the other two dynamic shear moduli, $G_{BE(hh)}$ and $G_{BE(hv)}$. It is also interesting the data show that the anisotropy ratio $G_{BE(hh)}/G_{BE(vh)}$ becomes 1 around the yield state. In addition, the convergence in the AU path after the residual effective stress supports the previous finding that the saturation with the effective stress less than the measured residual stress affects the structure of the clay.

Due to the limited data, it is hard to draw any definitive conclusions, but it is clearly shown that all three dynamic shear moduli are affected during shear. It will be interesting to investigate the reduction point and reduction rate of each dynamic shear moduli in various stress paths.

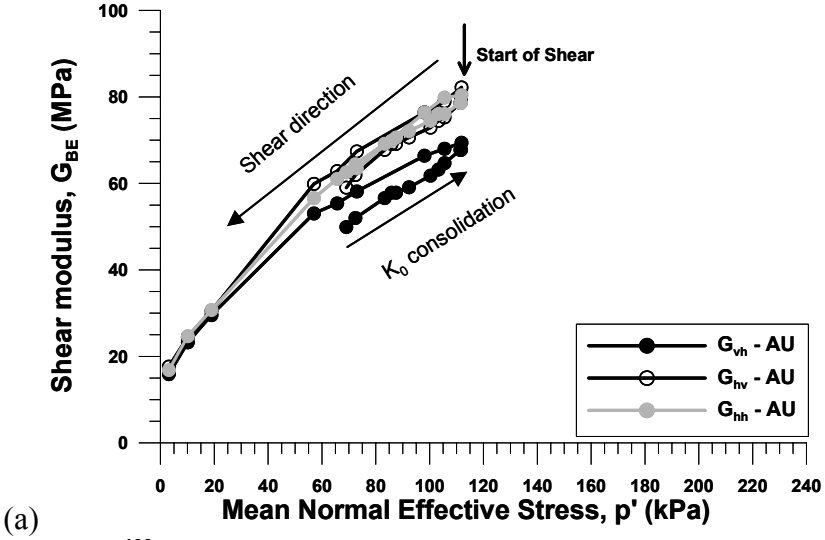

(a)

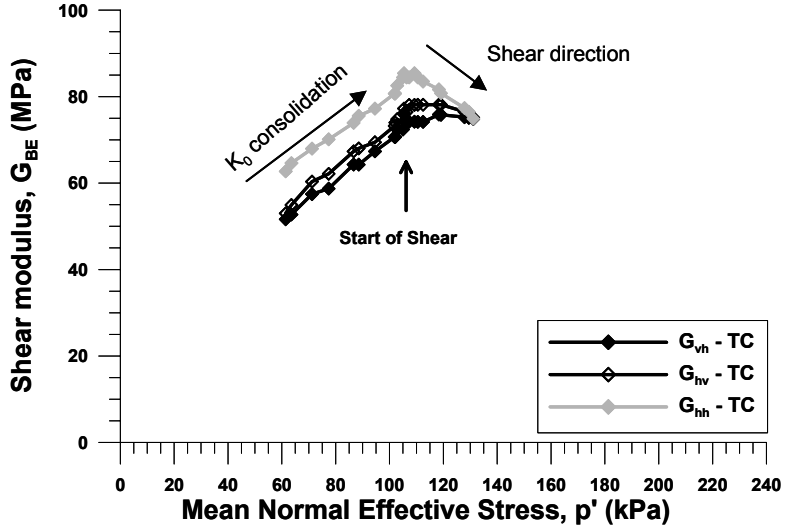

(b)

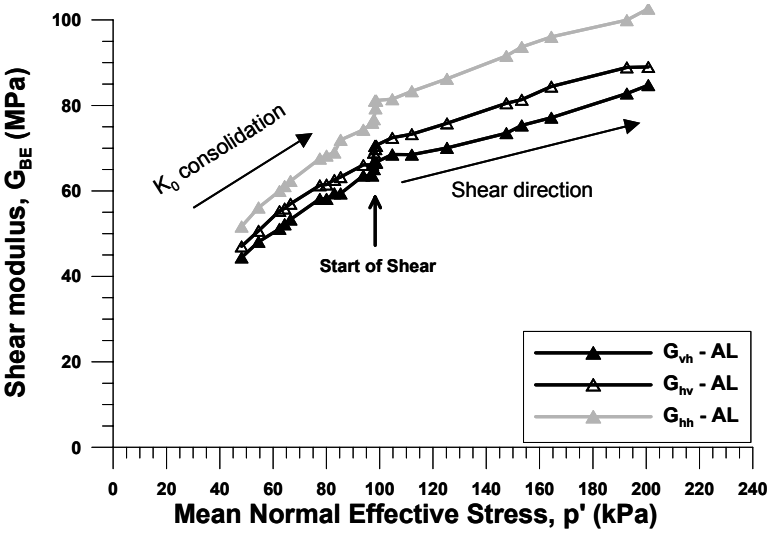

(c)

Figure 6-7 $G_{BE(vh)}$, $G_{BE(hh)}$ and $G_{BE(hv)}$ during stress probe tests: (a)AU, (b) TC, and (c) AL path

6.3. DYNAMIC VERSUS MECHANICAL SOIL STIFFNESS

Dynamically-determined soil stiffness has been frequently equated with the maximum or initial soil stiffness determined through mechanical means such as triaxial testing, even for soft clays (Clayton and Heymann, 1999). The assumed strain level from 0.0001 to 0.001% for dynamic testing could lead one to believe that no greater stiffness could be measured, particularly without performing laboratory studies such as this where mechanical shear stiffness is measured accurately to nearly 0.001%. G_{BE} is commonly assumed to represent the maximum shear modulus G_{max} at these small strain levels (Dyvik and Madshus, 1985). To evaluate this hypothesis, it is important to compare the laboratory-measured bender element modulus to field-measured dynamic moduli. The mechanically-measured stiffness at the smallest measurable strain levels can then be compared to G_{BE}.

6.3.1. Comparison between G_{BE} and field data

Seismic cone penetration testing (SCPT) was performed at the site of the Ford Center excavation. These field data are compared herein to the laboratory bender element data. The testing was performed during July 2003 by the In-Situ Testing Research Group at the Georgia Institute of Technology under the direction of Professor Paul Mayne. The testing program at the Ford site consisted of conventional piezocone testing and seismic cone testing using the true interval method, in which the travel time for the shear wave is not measured from the ground surface to a single geophone receiver, but between two geophones mounted within the cone. Nearly continuous profiles of the shear wave velocity V_s can be made using this method and compared with the bender element propagation velocity V_{BE}. Due to the location of the source and the

receiver and the wave propagation and polarization direction, this seismic cone penetration test results can be compared to V_{vh} from the bender element test results.

Figure 6-8 presents the continuous profile of V_s with depth. The in-situ shear wave velocity V_s was approximately 185 to 225 m/s at an elevation of about – 5 m in ECD, where the block samples were obtained. The V_{BE} at the end of creep for the entire set of triaxial specimens ranges 180 to 195 m/s, within the range of data for the in-situ shear wave velocity at the similar elevation. This suggests that the laboratory dynamic stiffness is essentially in the lower bound of the field measurements. This also conforms well to the previous research that G_{max} measured in-situ is approximately equal to that measured in laboratory tests on very high quality specimens (Clayton and Heymann, 1999; Matthews et al, 2001).

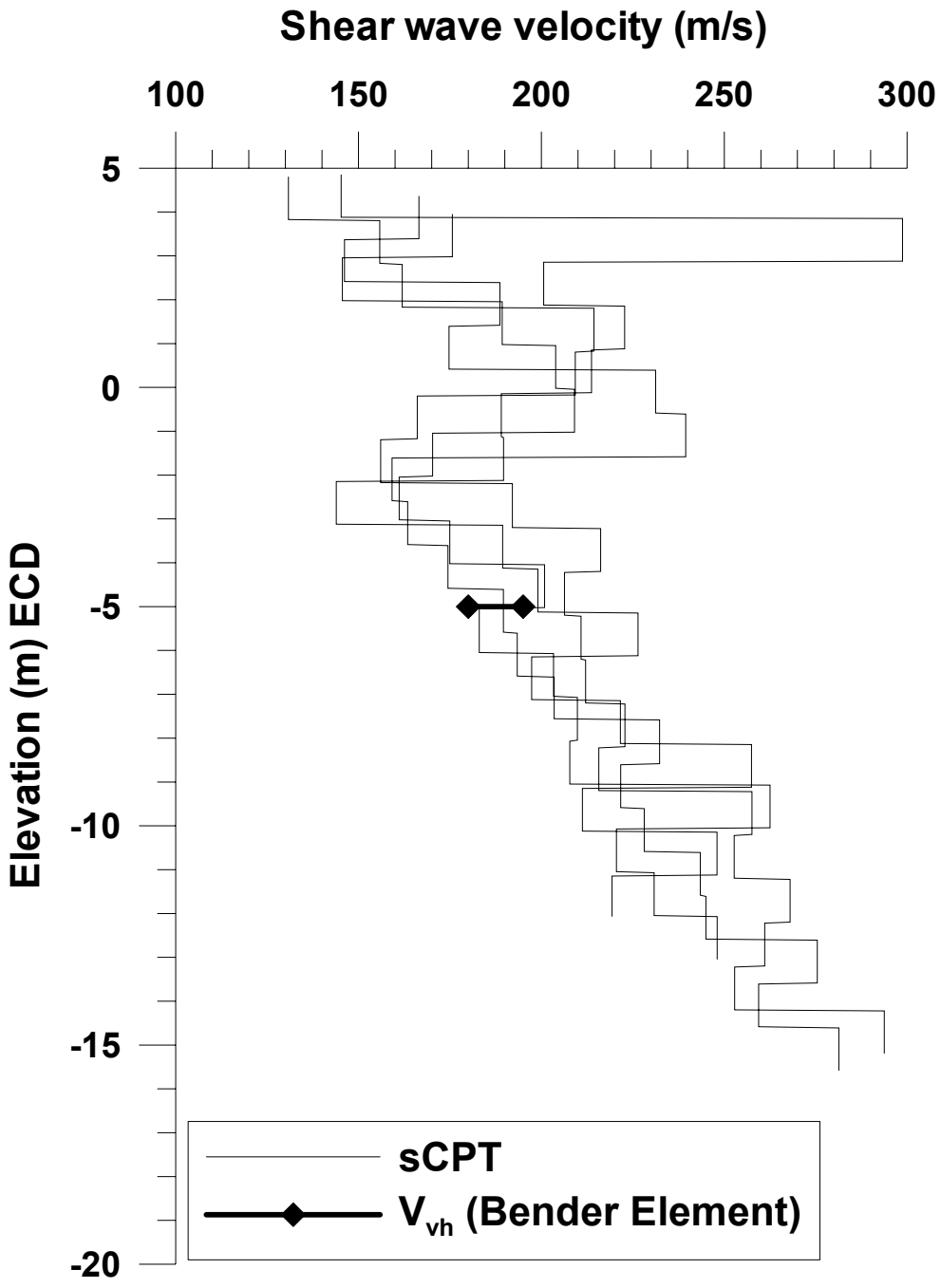

Figure 6-8 Continuous in-situ shear wave velocity V_s profile with depth at the Ford Engineering Center site

6.3.2. Comparison between Dynamic and Mechanical Stiffness

The bender element modulus $G_{BE(vh)}$, which is presumed to occur at dynamic strains between 0.0001 to 0.001%, can be compared with the secant shear modulus G_{sec} from the triaxial tests.

Figure 6-9 shows that the shear moduli from the stress probe tests with the $G_{BE(vh)}$ range obtained at the end of K_0 reconsolidation and creep periods.

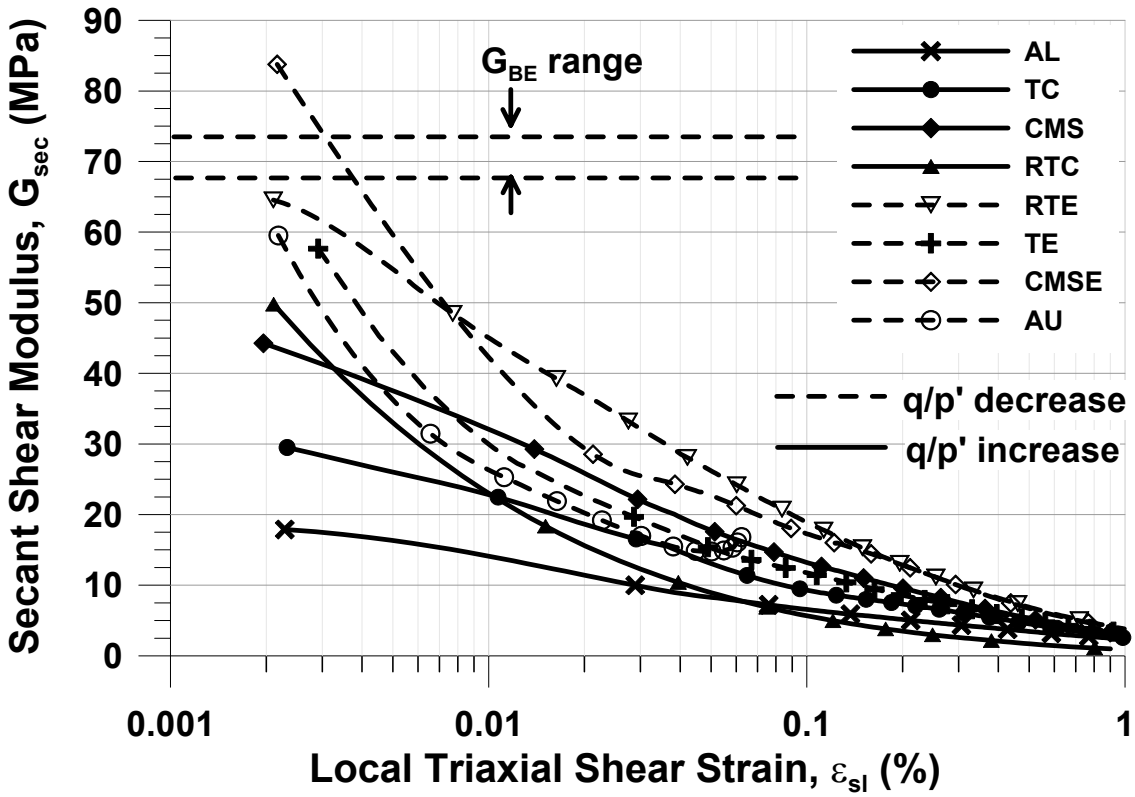

Figure 6-9 Comparison of shear moduli between triaxial tests and bender element tests

The dynamic modulus, $G_{BE(vh)}$ from the bender element tests does not directly correspond to any of the mechanically measured values of G_{sec} at the smallest reliably-measurable strain of 0.002%. The range of $G_{BE(vh)}$ at the end of K_0 creep was 68 to 73 MPa. This range is similar to those from CMSE and RTE stress paths. It is reasonable to expect elastic behavior selected in the mechanical moduli from unloading stress paths. These trends agree with previous research on Bothkennar clay and London clays (e.g. Smith et al, 1992; Gasparre et al. 2007).

6.4. SUMMARY AND CONCLUSIONS

The bender element data obtained during the K_0 consolidation process indicate that the empirical correlation of $G_{BE(ij)}$, which was established based on the data during consolidation to the in situ effective stress, is valid within the stress space defined by mechanical yield.

Deviations of measured values of $G_{BE(vh)}$ from the empirical correlation can be used to define stresses that correspond to mechanically-defined yield points. For the stress paths where the stress ratio varies with constant or decreasing p´, the stress points initiating such changes of $G_{BE(vh)}$ are located close to the yield surface. Distortion induced by the variation of stress ratio apparently leads to the alteration of the pathway for shear wave propagation, resulting in the reduction of $G_{BE(vh)}$ after yield.

The empirical correlation for G_{BE} represents the variation in elastic shear stiffness in compression paths CQL and AL wherein p' increases with little or no change in stress ratio. After yield, the changes of volumetric strain are described by the void ratio function in the empirical correlation. The soil structure *in-situ* and during consolidation apparently maintains geometrical similarity to that during probing for these compression paths, implying the direction of the internal route for shear wave propagation does not change significantly.

Three sets of bender element test results show that soft Chicago glacial clay is a cross-anisotropic material with G_{BEhh}/G_{BEhv} =1.18, a relatively small anisotropy ratio compared to the reported values for other clays such as London, Gault and Pisa clays. $G_{BE(hh)}$ also shows a similar reduction during shearing but due to the limited quantity of the data with 3 bender elements set , it is hard to draw definitive conclusions.

The shear modulus at the end of the K_0 creep portion of the tests based on the shear wave velocity in axial direction (G_{vh}) agrees well with the field measured shear wave velocity by seismic CPT tests.

Based on the results of the stress probes, the bender element modulus does not directly correspond to a particular value of G_{sec} at the smallest strain levels measured, 0.002%. Comparison of the G_{BE} values at the end of creep with $G_{0.001}$ values indicates that G_{BE} is approximately equal to the mechanically-measured secant modulus for an unloading probe direction similar to RTE or CMSE. For these lightly overconsolidated clays, it is reasonable to conclude that an unloading probe would produce small strain moduli similar to those from dynamic tests.

CHAPTER 7 BEHAVIOR OF RECONSTITUTED SAMPLES OF COMPRESSIBLE CHICAGO GLACIAL CLAYS

A series of reconstituted blocks were created from cuttings and spent soil samples from the block samples taken from the Ford Design Engineering Center. Results of stress probe tests on these reconstituted blocks were compared to results of stress probe tests on natural samples. The comparisons quantify the effects of inhomogeneity and ageing in natural samples, and also help to understand the mechanical behavior of natural soils.

The results of stress probe tests of the reconstituted specimens will be presented in terms of stress-strain response, modulus degradation, bender element test results and the strain response envelopes. These responses will be compared to those of the natural specimen to evaluate the suitability of reconstituted specimens to represent the mechanical behavior of natural samples.

Section 7.1 presents the index properties and oedometer test results of the reconstituted samples. Section 7.2 compares the K_0 reconsolidation responses with those of the natural samples in terms of stress-strain response and dynamic properties obtained from bender element tests. Section 7.3 presents the responses of reconstituted samples during stress probe tests in the context of stress-strain behavior, and modulus degradation. Section 7.4 compares the strain response envelopes of the reconstituted samples with those of the natural samples. Section 7.5 compares the limit states and failure behavior of the two sample types. Section 7.6 presents the discussion about the results in this study and previous research on the reconstituted samples of Chicago clays. Section 7.7 summarizes the results and draws conclusions.

7.1. INDEX PROPERTIES AND OEDOMETER TEST RESULTS

Reconstituted samples were created using slurry consolidation techniques (Sheeran and Krizek 1971). As explained in Chapter 3, dried Chicago clay, consisting of trimmings and spent specimens from the natural samples, was crushed and passed through a 0.425 mm sieve to remove the coarse and medium sized sand particles. This process generally resulted in a 10% loss of total weight of dried soil. The slurry with a water content of twice the liquid limit of the natural samples, was placed into a large consolidometer (203.2 mm diameter) and loaded in several stages until the applied pressure reached the maximum past pressure previously determined from oedometer tests (Chapter 3.1) on the natural samples. The reconstituted samples from batch # 3, 4 and 6 are used in this study and the index properties and oedometer test results of which are compared with those of the natural samples in Table 7-1 and Figure 7-1. Hereafter, natural samples are designated "block" or "B" and reconstituted samples are "R."

Table 7-1 Comparison of index properties and 1D consolidation characteristics of natural and reconstituted samples

	Natural	R-#3	R-#4	R-#6
Natural Water Content (%)	24.6-25.2	26-26.3	25.7-26.5	26-26.5
Liquid Limit (%)	29.5-31	39-41	37-40	38-41
Plasticity Index (%)	14.2-16.4	19-21	17-20	18-20
Specific Gravity	2.71-2.72	2.71-2.72	2.71-2.72	2.71-2.72
Max. Past Pressure (kPa)	220-230	210-220	210-220	210-220
OCR	1.7	NA	NA	NA
Compression Index, C_c	0.2	0.21	0.22	0.21
Recompression Index, C_r	0.028	0.03	0.04	0.035

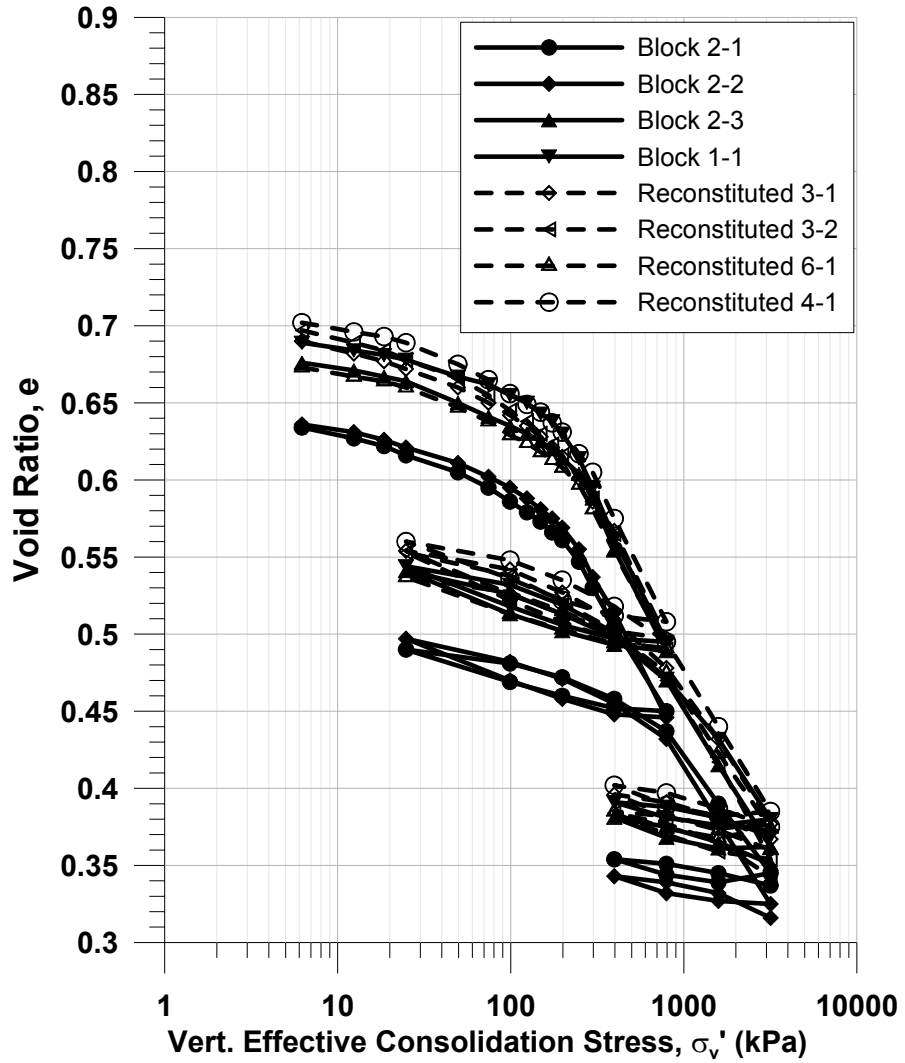

Figure 7-1 Oedometer test results comparison between natural block samples and reconstituted samples

The variation in the index properties among the reconstituted samples is very small. There is less than 1% of water content variation. The maximum past pressure varied from 10 to 15 kPa with an apparent average value slightly less than that of the natural samples.

There is a slight difference between natural and reconstituted samples in terms of plasticity index likely because removal of the sand resulted in slight higher PI. Overall, the reconstituted samples are quite similar to the natural samples in terms of index properties and stress history obtained from oedometer tests.

7.2. SATURATION AND K_0 RECONSOLIDATION BEHAVIOR OF RECONSTITUTED SAMPLES

7.2.1. Residual Effective Stress and Saturation Behavior

The residual effective stress, p_r', was determined for all reconstituted triaxial specimens using the pore water pressure method detailed in Section 3.3.3. Results for each specimen are listed in Table 7-2, as are the results of the natural specimens. The mean value of p_r' for the reconstituted specimens was 48 kPa, with a range of 40 to 53 kPa and a standard deviation was 5 kPa, corresponding to a coefficient of variation (COV) of 0.1. This range of residual effective stress itself is quite similar to that of the natural samples. However, the ratio between the residual effective stress and the vertical effective stress of the natural and reconstituted specimens are 0.32 and 0.22, respectively. The vertical effective stress of reconstituted samples was taken as 220 kPa for this computation, because the reconstituted samples were in a virgin compression state prior to removal from the slurry consolidation. The OCR of 1.7 was imposed by reconsolidating to 137 kPa in the triaxial cell during K_0 reconsolidation.

The reconstituted specimens are presumed to have undergone less disturbance than the natural samples because they were only extruded from the slurry consolidometer and placed in a low temperature storage room (and hence were not subjected to disturbance from field trimming and transportation). A possible reason for the difference in p_r'/σ_{v0}' between the two specimen types is related to the amount of ageing each sample type experienced. Ageing, assumed here to result from creep under constant vertical effective stress, results in strengthening of interparticle bonds between soil particles and affects soil stress-strain response at small strain levels (Tatsuoka et al, 1997). For the natural Chicago glacial clays, the ageing period may have been

up to 8000 years depending on the actual end of deposition and the effects of the unloading-reloading history discussed in Section 3.1.1. The reconstituted samples were aged under constant vertical stress for only approximately 7 days, or 0.02 years.

The applied effective stress during the back pressure saturation was maintained to be the measured residual stress and no significant strain developed during this period.

Table 7-2 Residual effective stress of natural and reconstituted specimens

Test	Residual stress (p_r')	Test	Residual stress (p_r')
FB1TC1	37.42	FB3AL1	47.00
FB1RTC1	44.30	FB3sCMS1	47.71
FB1RTE1	38.27	FB3sCQL1	47.17
FB1TE1	49.65	FB3sCMSE1	35.28
FB1TC2	51.15	FB3sCQU1	54.26
FB1RTC2	33.45	FB3AU1	51.82
FB1CMS1	38.30	FB3sCQU2	40.26
FB1CMS2	64.21	FB3sAU1	49.25
FB1CQL1	32.66	FB3 Average	46.59 (6.13)
FB1 Average	43.27 (10.22)	Average	43.92 (6.20)
Test	Residual stress (p_r')	**Test**	**Residual stress (p_r')**
FB2TC1	37.42	**FR3TC1**	**53.39**
FB2CQL1	42.07	**FR3RTE1**	**46.82**
FB2CMSE1	42.04	**FR6CQL1**	**48.08**
FB2CQU1	39.00	**FR6CMSE1**	**40.45**
FB2TC2	51.00	**FR6CQU1**	**52.83**
FB2AU1	42.00	**FR6CMS1**	**46.51**
FB2TC3	38.42	**FR Average**	**48.01 (4.75)**
FB2 Average	41.71 (4.53)		

7.2.2. K_0 Reconsolidation Behavior

Each specimen was reconsolidated under K_0 conditions to a σ_{vc}' of 137 kPa after the back pressure saturation process. As explained in Section 3.3.4, the K_0 reconsolidation process allows the soil sample to reach a predetermined vertical effective stress while changing the effective radial stress to maintain one-dimensional consolidation conditions.

The effect of these boundary conditions and the method of test control is that the effective radial stress σ_r' is not forced to be the same for each "identical" specimen, and is allowed to change as a function of the constitutive behavior of the specimen. As a result, the principal stress difference or deviatoric stress, q at the final σ_{vc}' is not necessarily the same for each specimen, nor is the mean normal effective stress p'. This stress state at the end of K_0 reconsolidation and creep is influenced by the effective stress during the saturation, which is the measured residual effective stress. Stress paths of reconstituted samples and natural samples during K_0 reconsolidation and creep period are presented in Figure 7-2. The stress paths of reconstituted samples at the end of K_0 reconsolidation and creep are similar to those of the natural samples, but the mean of K_0 value of the reconstituted samples was 0.64, 5% larger than that of the natural samples. The variation of the stress state of the reconstituted samples at the end of K_0 reconsolidation and creep is also similar to that of the natural samples as seen on the inset in Figure 7-2. During the creep period, radial effective stress was controlled to maintain the K_0 condition. As a result, radial effective stress increased during creep and consequently the deviatoric stress decreased to maintain the predetermined σ_{v0}'. Based on the difference in mean slopes of the recompression and creep stages, the change in stress path direction was approximately 88 to 95 degrees. Considering the potential effects of significant stress path rotations such as these on the subsequent stress-strain behavior, the stress path lengths varied approximately 6 to 10 kPa, which is also very similar to those for the natural samples.

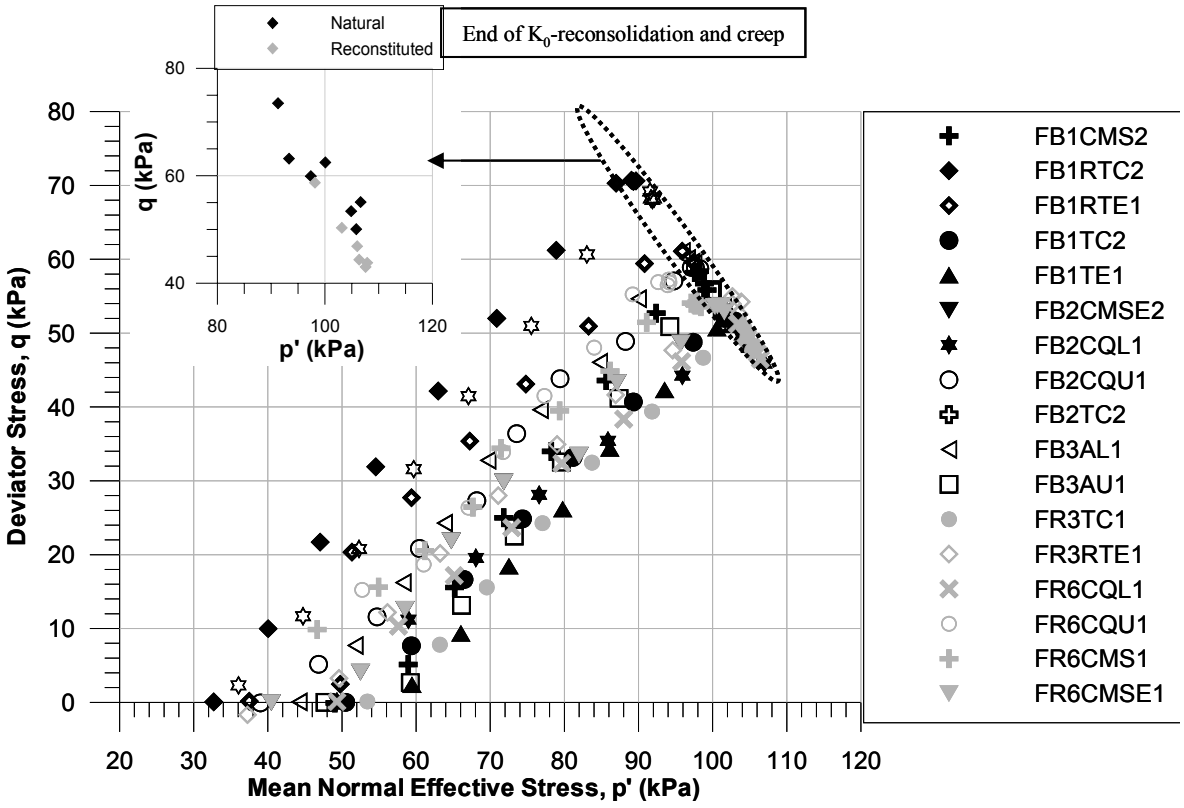

Figure 7-2 Stress paths of natural samples and reconstituted samples during K_0 reconsolidation and creep

Table 7-3 summarizes the stress state at the end of K_0 reconsolidation and creep based on the internal measurement system. The mean σ_{vc}' measured in the internal measurement system was 139 kPa with standard deviations of 1 kPa. The K_0 value at this σ_{vc}' was 0.64, and the ranged from 0.61 to 0.68 and averaged 0.64, which is 5% larger than that of natural samples. The p' ranged from 101 to 106 kPa with a mean value of 105 kPa and a standard deviation of 2.3 kPa. The mean deviatoric stress q was. The values of q varied from 44.0 to 60.0 kPa with a mean of 51 kPa and a standard deviation of 5.7 kPa. As already seen in Figure 7-2, the consolidated stress states of the reconstituted and natural samples are not significantly different.

Table 7-3 Stress state at the end of K_0 consolidation and creep

Test	p' (kPa)	q (kPa)	σ_{vo} ' (kPa)	K_0 value
FB1TC2	103	54	139	0.61
FB1RTE1	98	61	139	0.56
FB2CQL1	109	48	140	0.66
FB2CMSE1	105	55	140	0.61
FB2CQU1	100	63	142	0.56
FB1CMS2	106	50	138	0.64
FB Average	**103.9**	**55.1**	**140**	**0.61**
Stdev	3.4	5.6	1.2	0.039
FR3TC1	101	50.88	137	0.64
FR3RTE1	103	55.23	139	0.61
FR6CQL1	102	44.39	140	0.64
FR6CMSE1	106	59.95	140	0.62
FR6CQU1	105	47.80	139	0.68
FR6CMS1	106	47.88	139	0.66
FR Average	**105.1**	**51.02**	**139.1**	**0.64**
Stdev	2.3	5.7	1	0.03

Table 7-4 summarizes the axial and volumetric strains that occurred during K_0 reconsolidation and creep for reconstituted and the natural samples subjected to the same stress probes as applied to the reconstituted samples. Overall, the K_0 condition was well maintained because the difference between volumetric and axial strains was less than 0.1% in all cases. The recompression strains of less than 1% show that the reconstituted samples are of "excellent" quality according to the Sample Quality Designation (Terzaghi et al. 1994). While it may seem odd to evaluate the quality of reconstituted samples, they were subjected to the laboratory-induced disturbance such as those disturbances due to trimming and cutting. The recompression strains of reconstituted samples are very small, and almost twice of that of the natural samples, as expected based on the measured values of C_r in Table 7.1. However, reconstituted samples developed about 4 times larger axial strains during the K_0 creep period than did the natural

samples, likely as a result of the short aging of reconstituted samples, as explained earlier in this section.

Table 7-4 Strains at end of K_0 consolidation and creep for natural samples

Test	ε_a (%)	ε_{vol} (%)	ε_a (Creep) (%)
FB1TC2	0.287	0.340	0.013
FB1RTE1	0.262	0.416	0.011
FB2CQL1	0.263	0.183	0.016
FB2CMSE1	0.139	0.143	0.013
FB2CQU1	0.128	0.108	0.015
FB1CMS2	0.440	0.295	0.014
FB Average	**0.253**	**0.247**	**0.014**
Stdev	0.114	0.121	0.002
FR3TC1	0.520	0.513	0.065
FR3RTE1	0.740	0.860	0.080
FR6CQL1	0.473	0.579	0.052
FR6CMSE1	0.150	0.158	0.026
FR6CQU1	0.301	0.330	0.032
FR6CMS1	0.415	0.430	0.050
FR Average	**0.433**	**0.478**	**0.051**
Stdev	0.201	0.238	0.020

The strain response during K_0 reconsolidation is quite different for the two types of samples. Figure 7-3 compares typical internally-measured strains during the K_0 reconsolidation for the two types of samples. As explained in Section 4.2.2.1, at the beginning of the K_0 reconsolidation, the triaxial machine increases the deviatoric stress and reduces the effective radial stress while checking the axial and volumetric strain. Once there is a change in axial and volumetric strain, the deviatoric stress is reduced and the effective radial stress increases to reduce the differences between the axial and volumetric strains. This process generally took less than 20 minutes, but during this time, the natural samples exhibited negligible strains while the reconstituted samples underwent axial strains as large as -0.3%, as shown in Figure 7-3(b). This

behavior was boserved in all the reconstituted samples; these initial negative strains ranged from 0.2 to 0.3%.

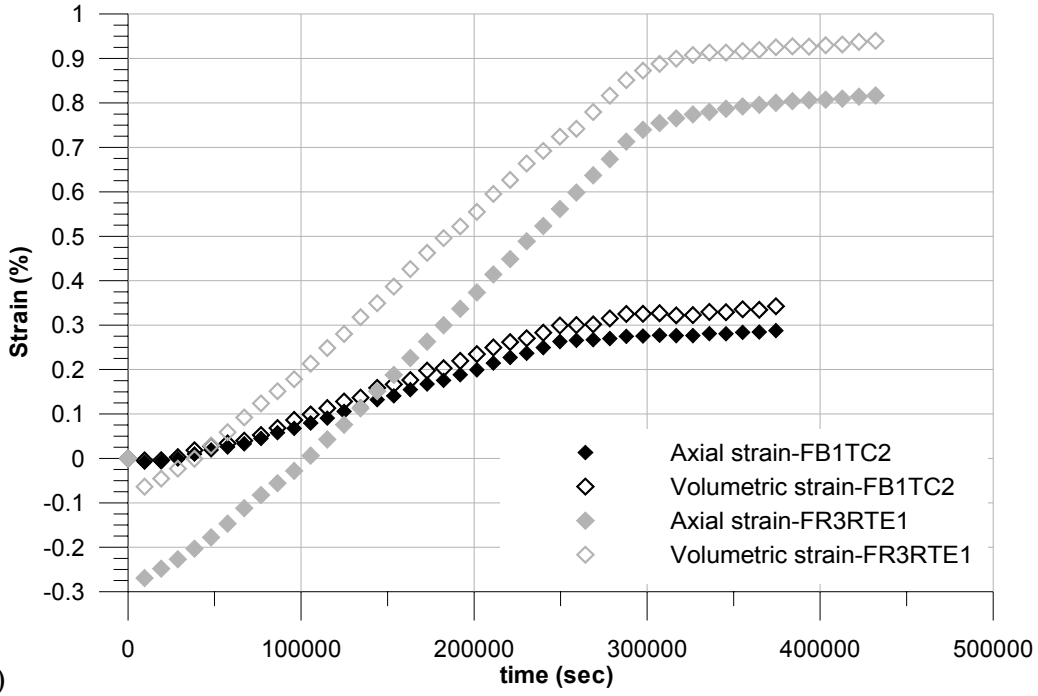

(a)

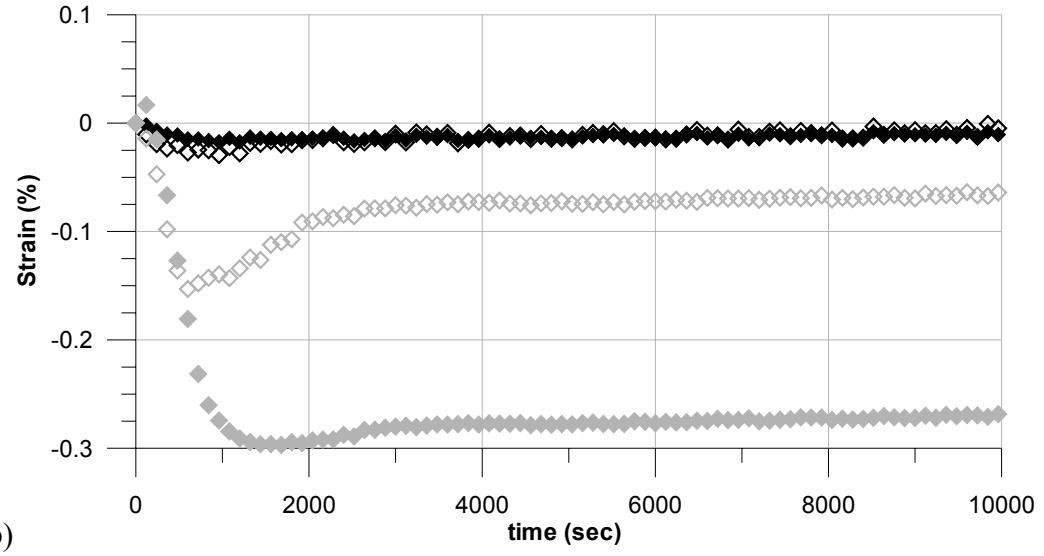

(b)

Figure 7-3 Strain response of natural and reconstituted samples during K_0 reconsolidation and creep at two time scales

In summary, larger K_0 values, larger recompression strains during K_0 consolidation, larger strains during creep and the initial negative strains during K_0 consolidation for the reconstituted samples suggest that the constitutive responses of the two sample types are different.

The "identical" behavior among the reconstituted samples was expected because procedures for reconstituting and preparing each sample were nominally identical. Differences could arise from different periods of laboratory aging, or the duration of time the samples rested between extruding each sample from slurry consolidometer and conducting a particular experiment, because laboratory aging was not exactly the same. However, these reconstituted samples had laboratory aging periods less than two months. From the K_0 reconsolidation results, the variabilities were observed between the specimens from the same reconstituted block. This may be because there were usually two or three week differences in each testing and also K_0 reconsolidation behaviors depend on the residual effective stress which can be influenced by laboratory disturbance such as trimming and setting up disturbance.

7.2.3. Bender Element Test Results during K_0 Reconsolidation and creep

As explained earlier in Chapter 3, the elastic shear wave velocity, V_{BE}, was calculated using the wave travel time determined by the cross correlation method (Viggiani and Atkinson 1995) and the tip-to-tip distance between transmitting and receiving bender elements. Assuming that the triaxial specimen can be represented as an infinite, isotropic, elastic medium, G_{BE} can be calculated as:

$$G_{BE(ij)} = \rho V_{BE(ij)}^2 \qquad (7\text{-}1)$$

where ρ is the total mass density of the specimen when V_{BE} was measured. Only vertical bender elements were used on the reconstituted specimens, and thus G_{BE} and V_{BE} are obtained from the vertically propagated and horizontally polarized waves.

Figure 7-4 shows the measured shear wave velocity during K_0 consolidation and creep. Clearly, shear wave velocities of reconstituted samples are lower than those of natural samples. To investigate the dynamic response during the K_0 reconsolidation, the approach in Section 6.1.1 is used to define the relationship between G_{BE} and current effective stress state for the reconstituted samples.

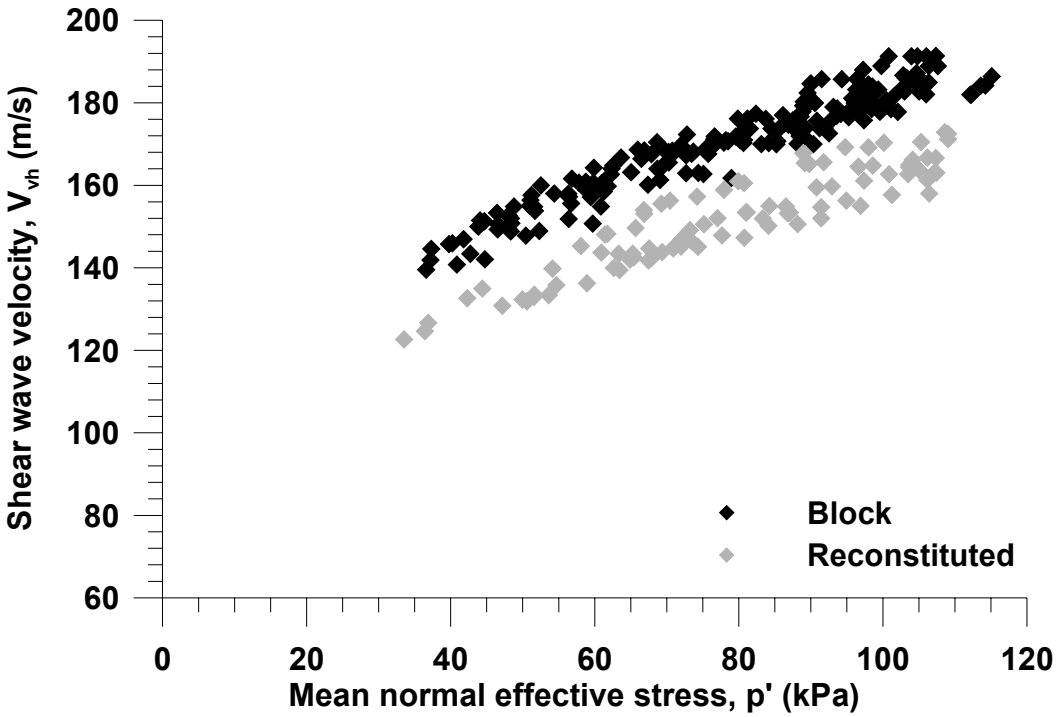

Figure 7-4 Shear wave velocity, V_{vh} comparisons between natural and reconstituted samples

Values of $G_{BE(vh)}$ were related to void ratio and the axial and radial effective stresses based on the data measured during consolidation; the resulting relationship is expressed as:

$$\frac{G_{BE(vh)}}{p_a} = Af(e)\left(\frac{\sigma'_a}{p_a}\right)^{na}\left(\frac{\sigma'_r}{p_a}\right)^{nr} \qquad (7\text{-}2)$$

where p_a is atmospheric pressure (101.3kPa), used as a normalizing constant, $f(e)$ is a void ratio function, and A, na, and nr are material constants. The reference void ratio, 0.7671 was calculated by averaging void ratios at the end of the consolidation stage. This average void ratio is very similar to 0.7455 of natural samples. The 36 hour creep period resulted in an increase in σ'_r, which when coupled with the ageing effects, resulted in an increased G_{BE}. To maintain the compatibility of the analysis, the data measured during the creep stage were not considered specifically when deriving the constants for Equation (7-2).

Based on the values set of G_{BE} obtained during the consolidation, the exponents of Equation (7-2), na and nr, were obtained by a least square regression to yield:

$$\frac{G_{BE(vh)}}{p_a} = 565\left(\frac{\sigma'_a}{p_a}\right)^{0.130}\left(\frac{\sigma'_r}{p_a}\right)^{0.459} \qquad (7\text{-}3)$$

Note that $Af(e)$ is taken as a constant equal to 565.

Clearly, the values of $Af(e)$ of reconstituted samples is different from $Af(e)$ of the natural samples, = 609, as are the na and nr values. For the natural samples, na is 0.285 and nr is 0.163, whereas the reconstituted values are 0.13 and 0.459, respectively. These differences indicate that G_{BE} of the natural samples is more influenced by the vertical effective stress and that of the reconstituted samples are more affected by the radial effective stress. This suggests that the structure of reconstituted samples is different from that of the natural samples.

Figure 7-5 compares the measured data and the line computed based on Equation (7-3) as well as the corresponding data for the natural samples. This comparison clearly shows that reconstituted samples are softer than the natural samples during K_0 reconsolidation.

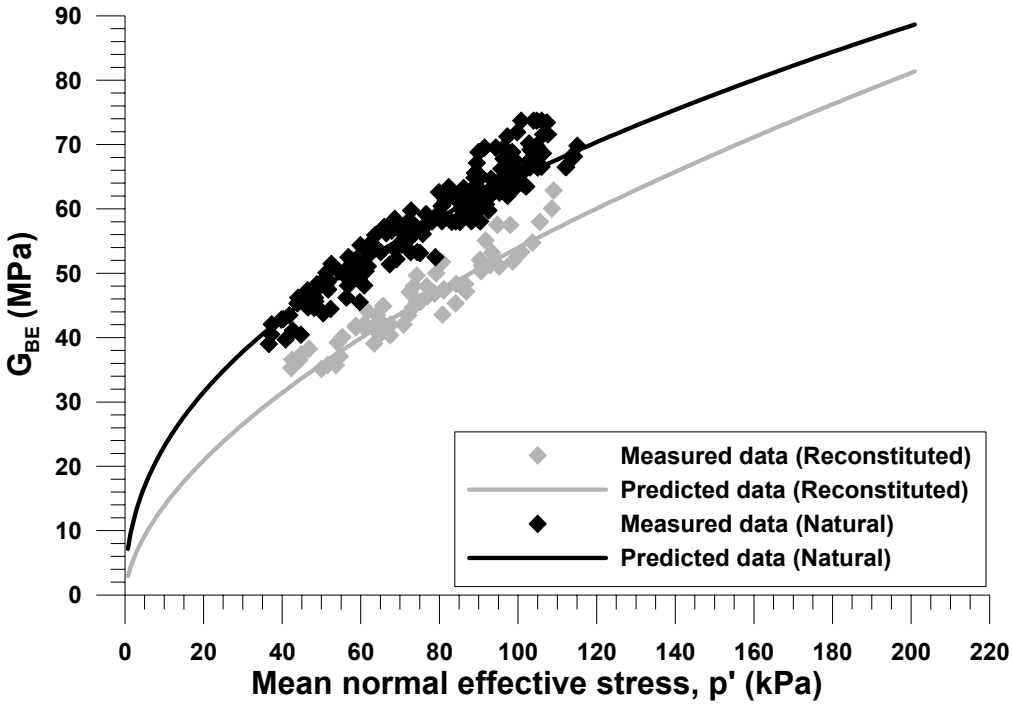

Figure 7-5 Comparison of measured data and predicted values for natural and reconstituted samples

As presented in Section 6.1.3, G_{BE} of natural samples increased 4% during the creep period. The average creep period was 36 hours and generally 3 bender element tests were performed. Table 7-5 shows the summary of G_{BE} of reconstituted samples at the end of consolidation and at the end of creep. For reconstituted samples, the average increased amount of G_{BE} during creep is 7.2% which is almost twice that of natural samples, which is likely to be a result of the large axial strain of the reconstituted samples during creep.

Table 7-5 G_{BE} of reconstituted samples comparison at the end of K_0 reconsolidation and at the end of 36 hrs creep

	G_{BE} at the end of K_0 Consol. (Mpa)	G_{BE} at the end of creep (Mpa)	Increase (%)
FR3RTE1	51.82	55.24	6.60
FR3TC1	57.99	60.68	4.64
FR6CMS1	60.06	64.33	7.11
FR6CMSE1	49.99	55.55	11.11
FR6CQL1	54.76	58.55	6.92
FR6CQU1	54.58	58.32	6.84
AVERAGE (%)	54.87	58.78	7.20

7.3. STRESS-STRAIN RESPONSE OF RECONSTITUTED SAMPLES

7.3.1. Stress Probes

Reconstituted specimens were subjected to the six stress probes shown in Figure 7-6 in q-p' space. The notations for these probes are summarized in Table 7-6. The stress probes include triaxial compression and extension as well as stress paths for investigating coupling effects, constant q loading and unloading constant mean normal stress loading and unloading. All paths follow straight lines of constant slope η from their initial points due to the drained nature of the testing program. The small variations in intended path directions and straightness noted in Figure 7-6 resulted from minor fluctuations in the CKC e/p loading system and the development of small excess pore pressures, generally 2 to 3 kPa measured at the ends of a specimen.

Table 7-6 Notation for directional stress probe

Label	Description	Label	Description
TC	Triaxial compression	RTE	Reduced triaxial extension
CMS	Constant mean normal stress	CMSE	Reduced constant mean normal stress
CQL	Constant shear loading	CQU	Constant shear unloading

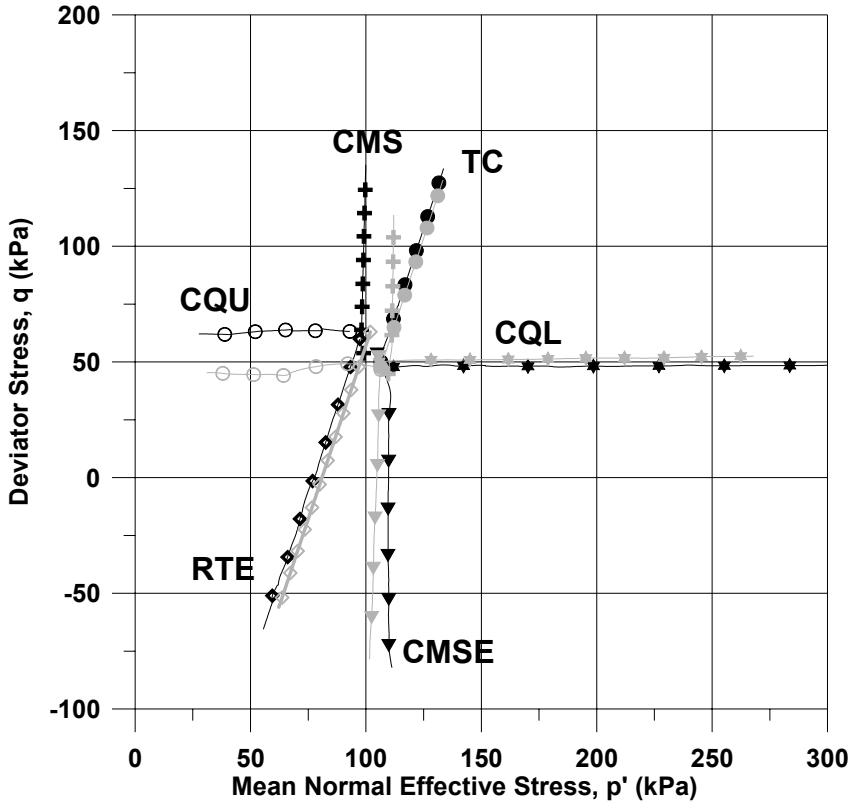

Figure 7-6 Stress paths for selected natural specimens in *p'*-*q* space

Figure 7-7 presents the deviatoric stress-axial strain response and volumetric strain response measured from internal measurement system for TC, RTE, CMS, and CMSE paths for both reconstituted and natural specimens. For CQL and CQU paths, mean normal effective stress-axial strain response and volumetric response are plotted because deviatoric stress remains constant in those paths. Overall, reconstituted samples show softer responses than the natural samples in both loading and unloading paths. Another distinct difference is the axial strain that occurred near the end of the CQU probe. Whereas the natural sample show negligible axial strain, the reconstituted sample compressed (positive axial strain) for the same unloading path. These different responses in the same path indicate the different anisotropic nature of the two samples.

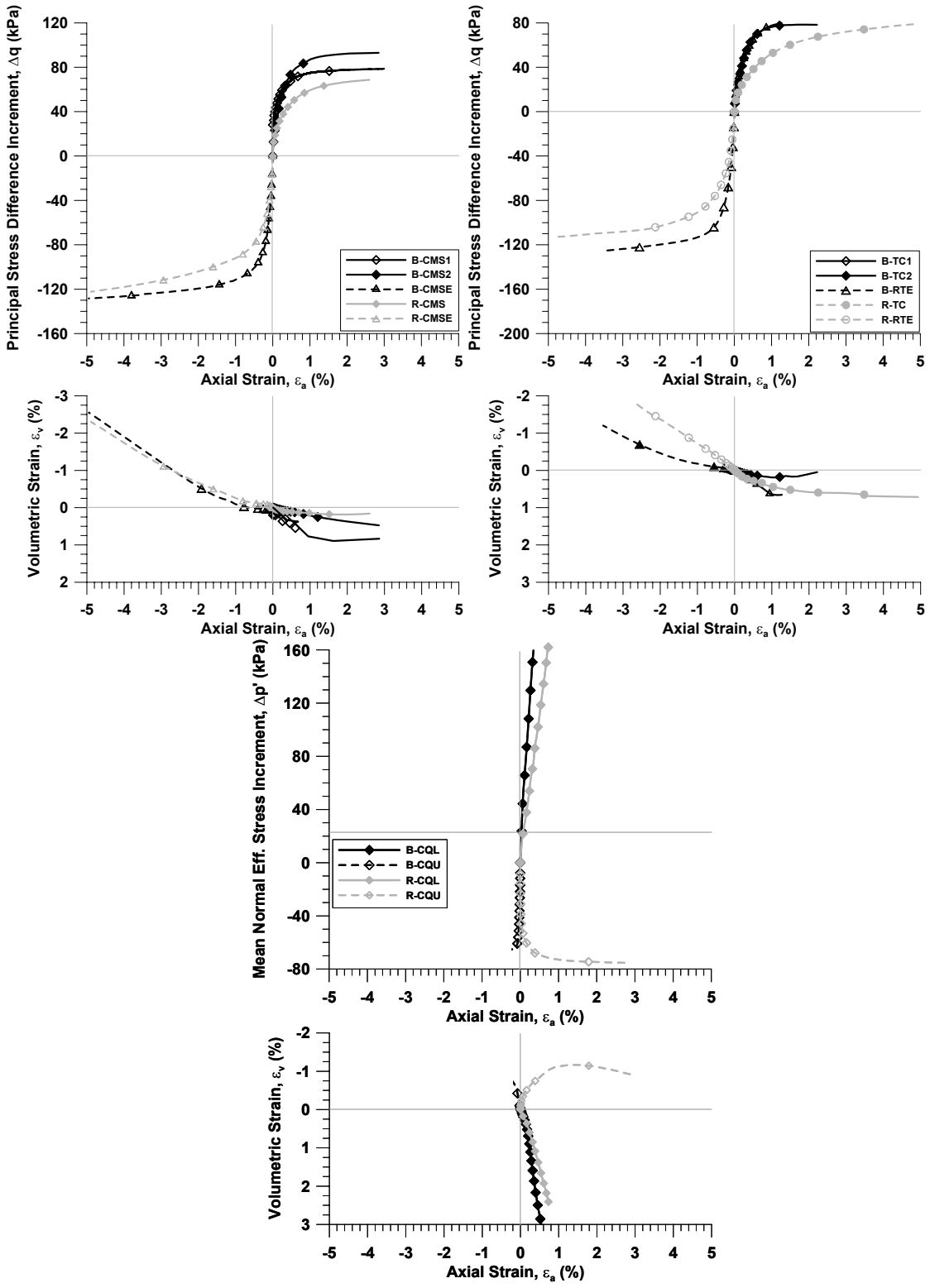

Figure 7-7 Stress-strain data of natural and reconstituted samples

7.3.2. Stress-Strain Response of Reconstituted Specimens

In axisymmetric conditions, soil responses can be divided into volumetric, shear and coupled responses, as shown in Equation (7-4).

$$\begin{Bmatrix} \Delta\varepsilon_v \\ \Delta\varepsilon_s \end{Bmatrix} = \begin{bmatrix} 1/K & 1/J_v \\ 1/J_s & 1/3G \end{bmatrix} \begin{Bmatrix} \Delta p' \\ \Delta q \end{Bmatrix} \tag{7-4}$$

In the following sections, stress-strain responses of reconstituted samples are compared with that of the natural samples in terms of shear, bulk and the two cross-coupling moduli assuming in isotropic elasticity:

$$G_{\text{sec}} = \frac{\Delta q}{3\Delta\varepsilon_s} \tag{7-5}$$

$$K_{\text{sec}} = \frac{\Delta p'}{\Delta\varepsilon_v} \tag{7-6}$$

$$J_{v\,\text{sec}} = \frac{\Delta q}{\Delta\varepsilon_v} \tag{7-7}$$

$$J_{s\,\text{sec}} = \frac{\Delta p'}{\Delta\varepsilon_s} \tag{7-8}$$

7.3.3. Deviatoric Stress-Shear Strain Comparison

Figure 7-8 shows the Δq-ε_{sh} plots for natural and reconstituted specimens at two shear strain scales: large strain up to ±2% and small strains up to ±0.01%. At the large strain in Figure 7-8(a), all the reconstituted samples show softer responses than natural samples. The CMSE and RTE responses are almost identical behavior for each sample type. The CMS responses are stiffer than the TC responses for each sample type. All the paths reach the failure, as discussed in detail in Section 7.5.2.

The small-strain response to the directional stress probes is presented in Figure 7-8(b). The data are plotted for $-0.01\% \leq \varepsilon_{sh} \leq 0.01\%$ to accentuate the behavior just beyond ±0.002% strain, the accepted lower limit of small strains. At these levels of strains, the differences in Δq-ε_{sh} behavior are much more visible than in Figure 7-8(a). The probe data of both samples generally indicate that at small ε_{sh}, the slopes of the Δq-ε_{sh} curves are relatively smaller in compression than in extension paths. Softer responses for the reconstituted samples also are found for each path.

To further examine the shear stiffness at the small strain range, secant shear modulus are plotted versus shear strain in Figure 7-9.

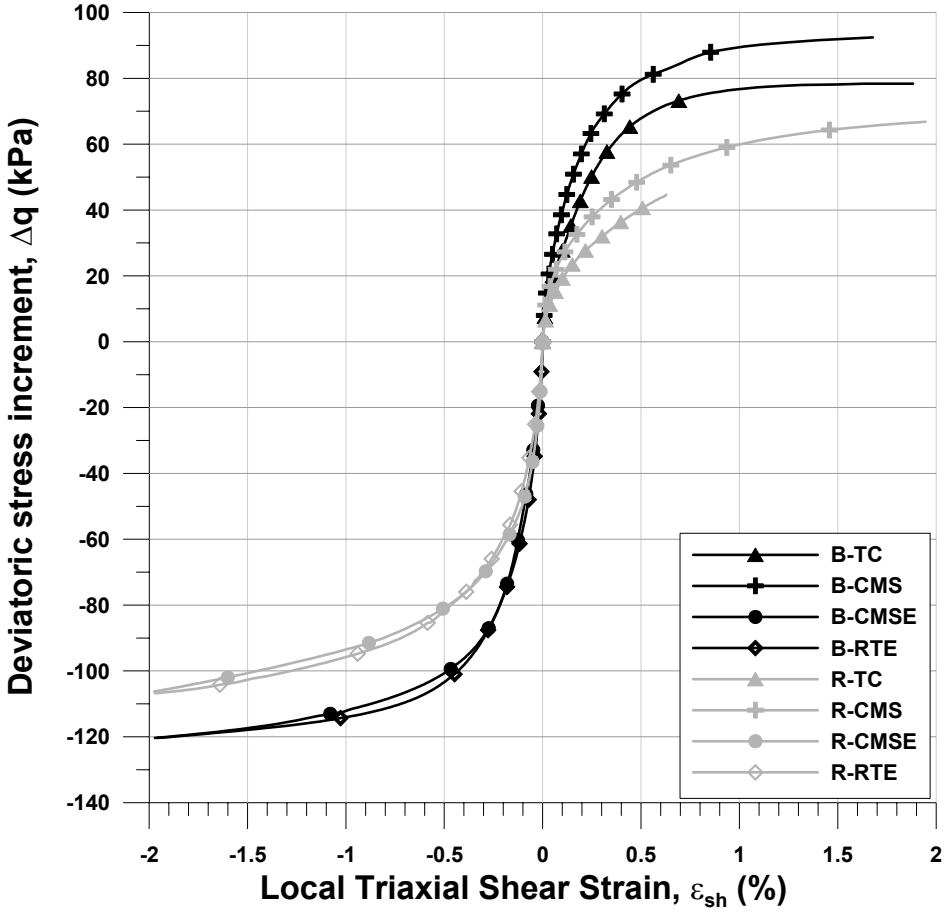

(a)

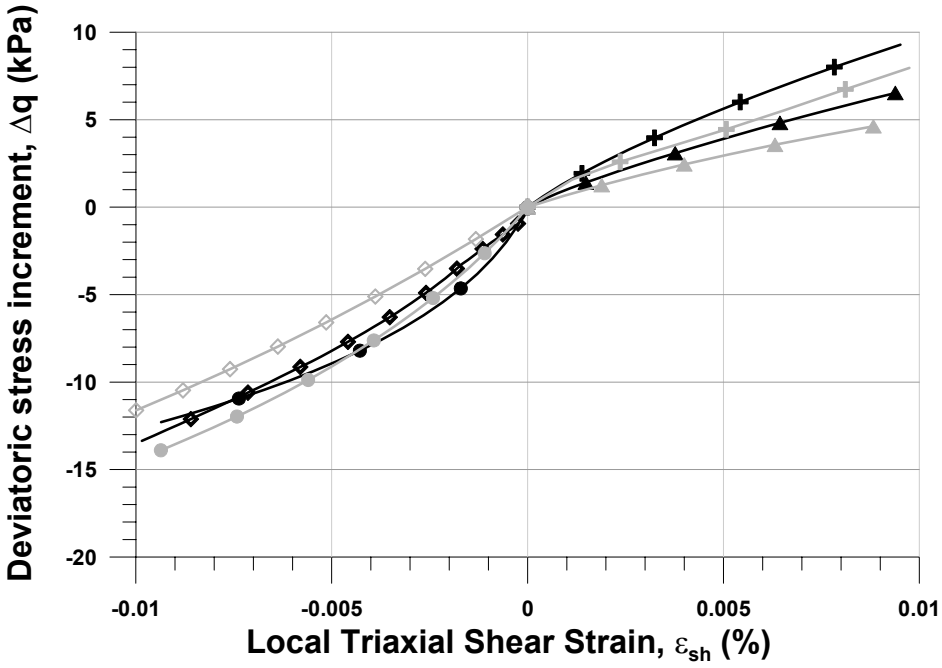

(b)

Figure 7-8 Change in deviatoric stress q versus shear strain ε_{sh} for natural and reconstituted specimens (a) complete test data, (b) test data for ε_{sh} ±0.01%

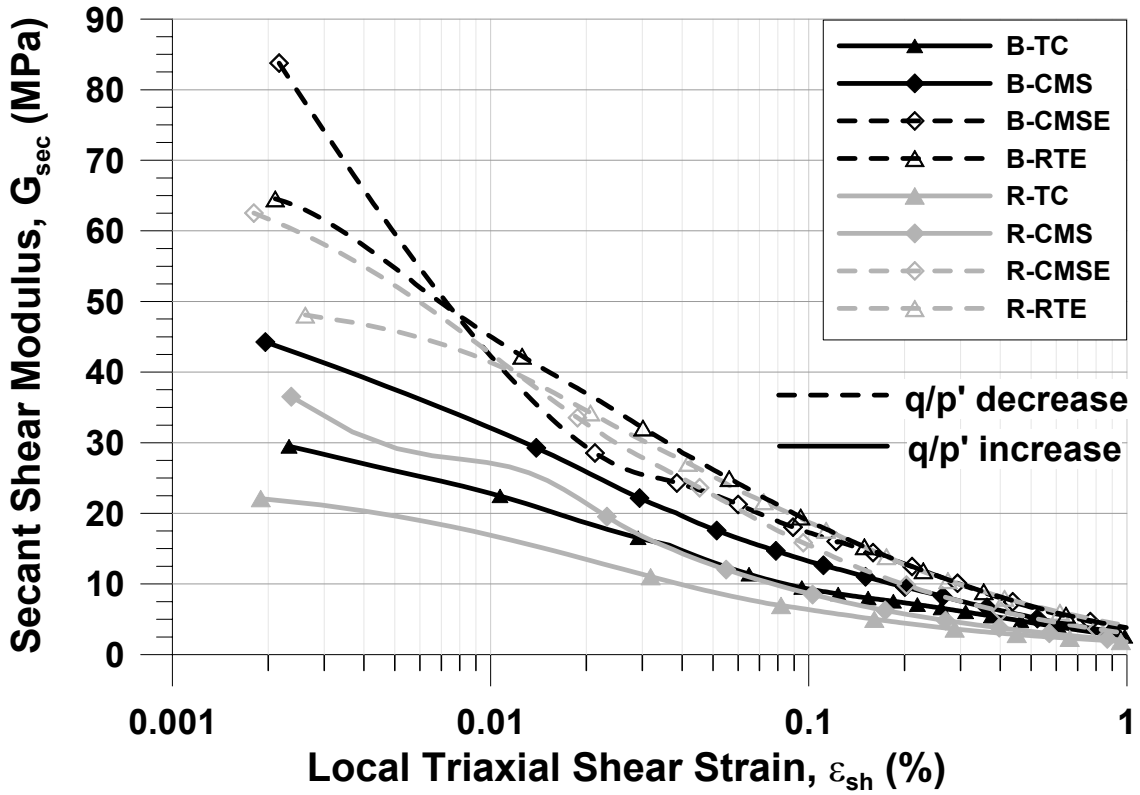

Figure 7-9 Shear stiffness degradation curves of natural and reconstituted samples for stress probe tests

The maximum and minimum calculated G_{sec} values of reconstituted samples at ε_{sh} of 0.002% are 62 MPa and 22 MPa for probes CMSE and TC, respectively, which are 25% less than those of the natural samples for the same paths. As is the case for the natural samples, the secant shear moduli decrease continually, suggesting that a linear elastic region is not found in reconstituted samples, at strain levels greater than 0.002%.

As explained in Section 4.3, the shear moduli of natural Chicago glacial clay strongly depend on the stress path direction. The shear moduli in the stress probes wherein q and the stress ratio, $\eta = q/p'$, is increased ("loading") are smaller than those in the stress probes where q and η initially decrease ("unloading"). Similar patterns are observed in reconstituted samples. Figure 7-10 shows the angle θ, the angular difference from the CQL path as shown in the inset.

The values of G_{sec} for 0.002%, 0.01%, and 0.1% strains plotted versus the angle θ for each of the stress probe. Data points for path CQL are shown at 0° and 360°. To compare the general trends, the G_{sec} values for the natural specimens subjected to other stress paths, AL, AU, RTC and TE also are plotted. The trends are similar for the reconstituted and natural samples, but the magnitude of shear moduli is smaller in the reconstituted samples. The dependence of the shear moduli of the reconstituted samples on θ is large at 0.002% and 0.01% shear strain, and the apparent directional dependence decreases as the strains reach and exceed 0.1%. In addition, the differences in moduli of the two sample types also decrease with increased strain.

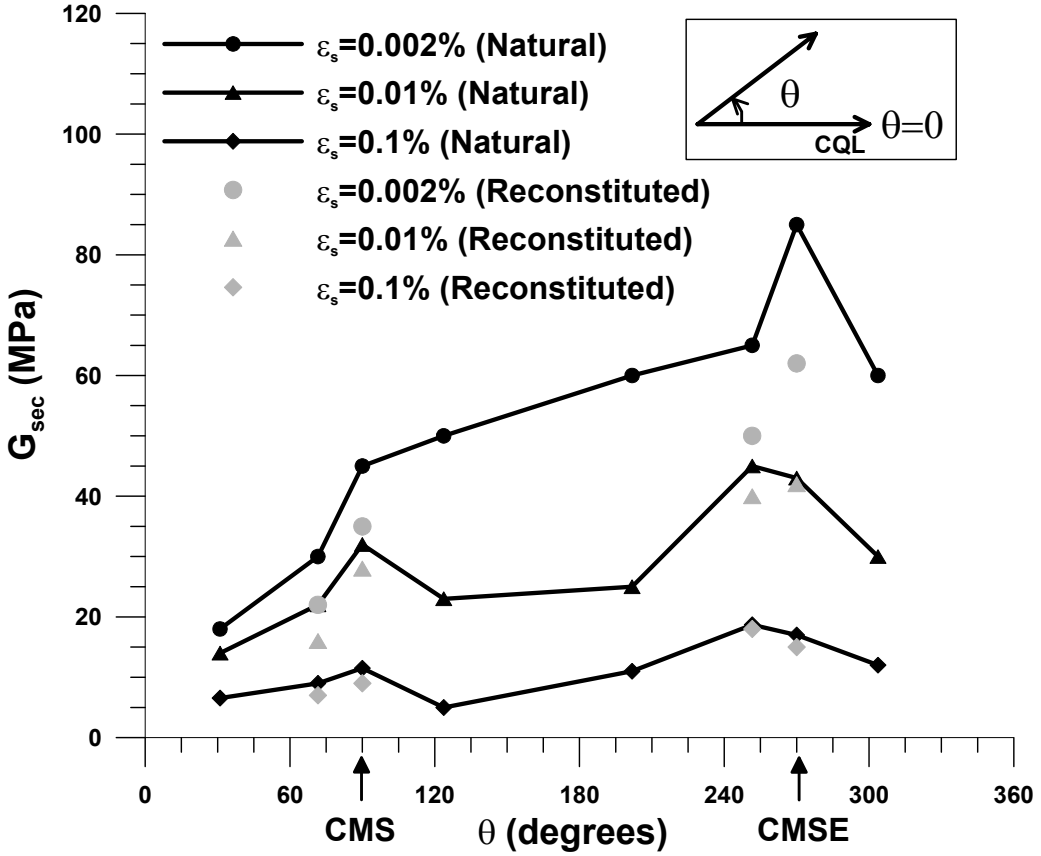

Figure 7-10 Variation of secant shear modulus G_{sec} of natural and reconstituted samples as a function of angular difference in stress probe direction

7.3.4. Mean Normal Effective Stress-Volumetric Strain Comparison

Figure 7-11 shows the of $\Delta p'$-ε_{vol} plots for natural and reconstituted specimens at two strain scales: large strains up to ±2% and small strains up to ±0.01%. For the present discussion, loading paths will refer to probes for which $\Delta p'$ increased (CQL, and TC) and unloading paths refer to probes for which $\Delta p'$ decreased (CQU and RTE). Similarly to the deviatoric stress and shear strain data, the volumetric responses of reconstituted samples are softer than those of the natural samples. At large strains shown in Figure 7-11(a), the loading paths indicated constant K value at strains larger than 0.5%. In contrast, the response for unloading paths indicates that the initial behavior is stiff, followed by volumetric yielding. As explained Section 4.3.3, the large volumetric strain around failure is because the internally measured volumetric strain is calculated from the measurements of axial and radial LVDTs which show radical movements around the failure. The volumetric behavior at small strains is shown in Figure 7-11(b). Overall softer response of the reconstituted samples is shown for all stress paths. For both natural and reconstituted samples, unloading paths show stiffer response than the corresponding loading path. To further study the volumetric behavior at small strains, secant bulk moduli are plotted versus volumetric strain in Figure 7-12.

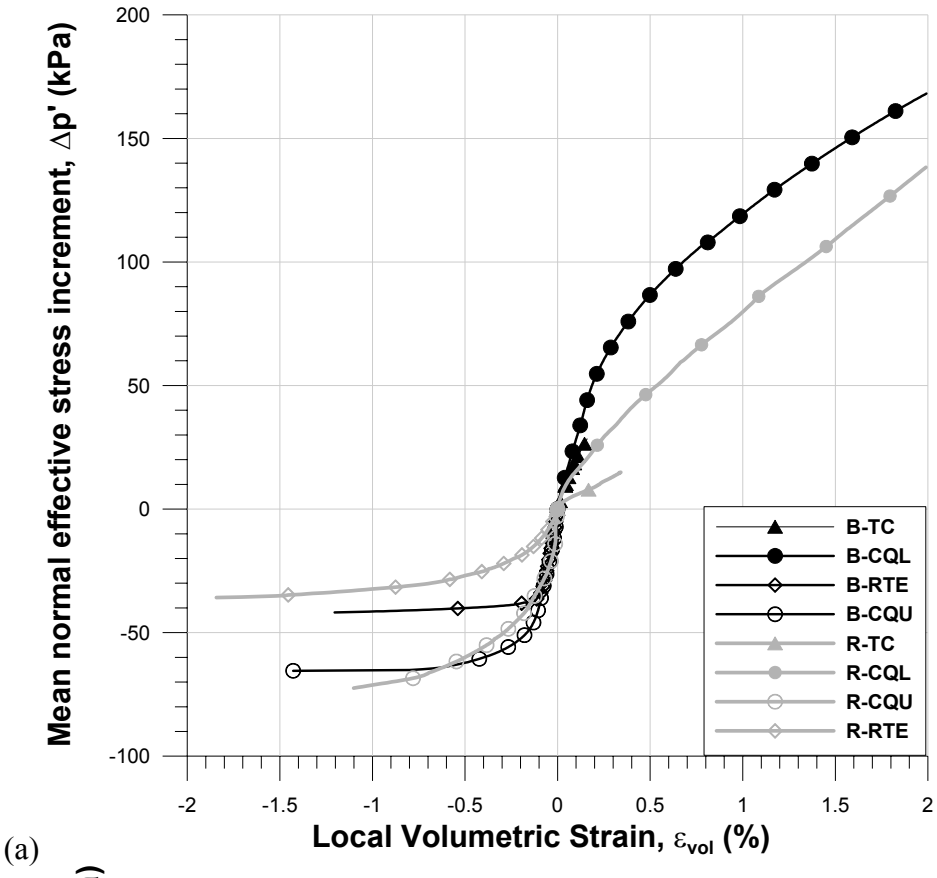

(a)

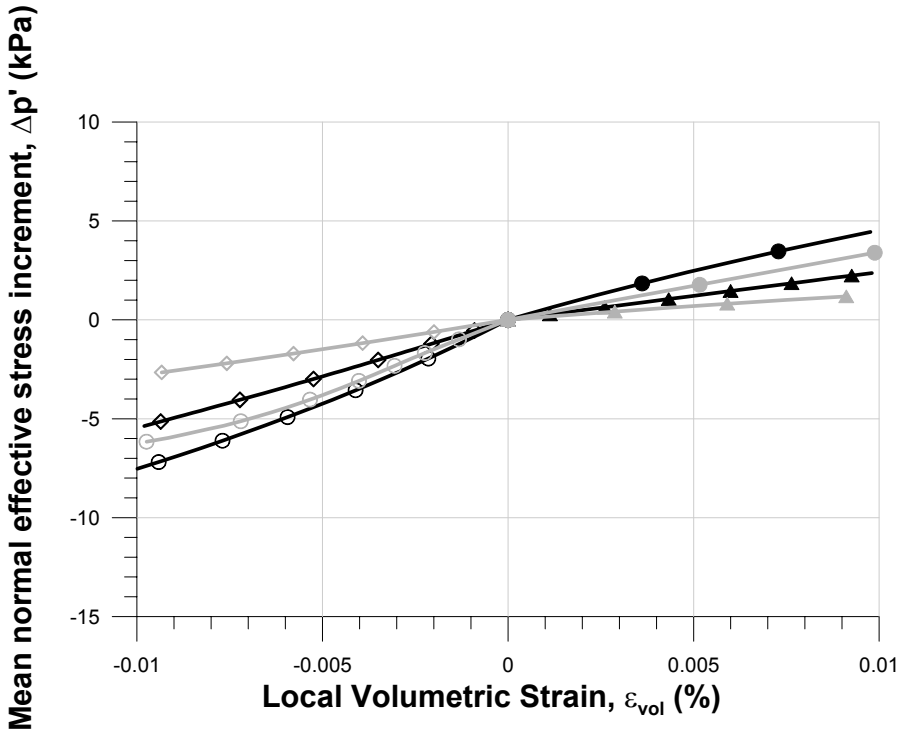

(b)

Figure 7-11 Change in mean normal effective stress p' versus local volumetric strain ε_{vol} for selected natural specimens (a) complete test data, (b) test data for ε_{vol} ±0.01%

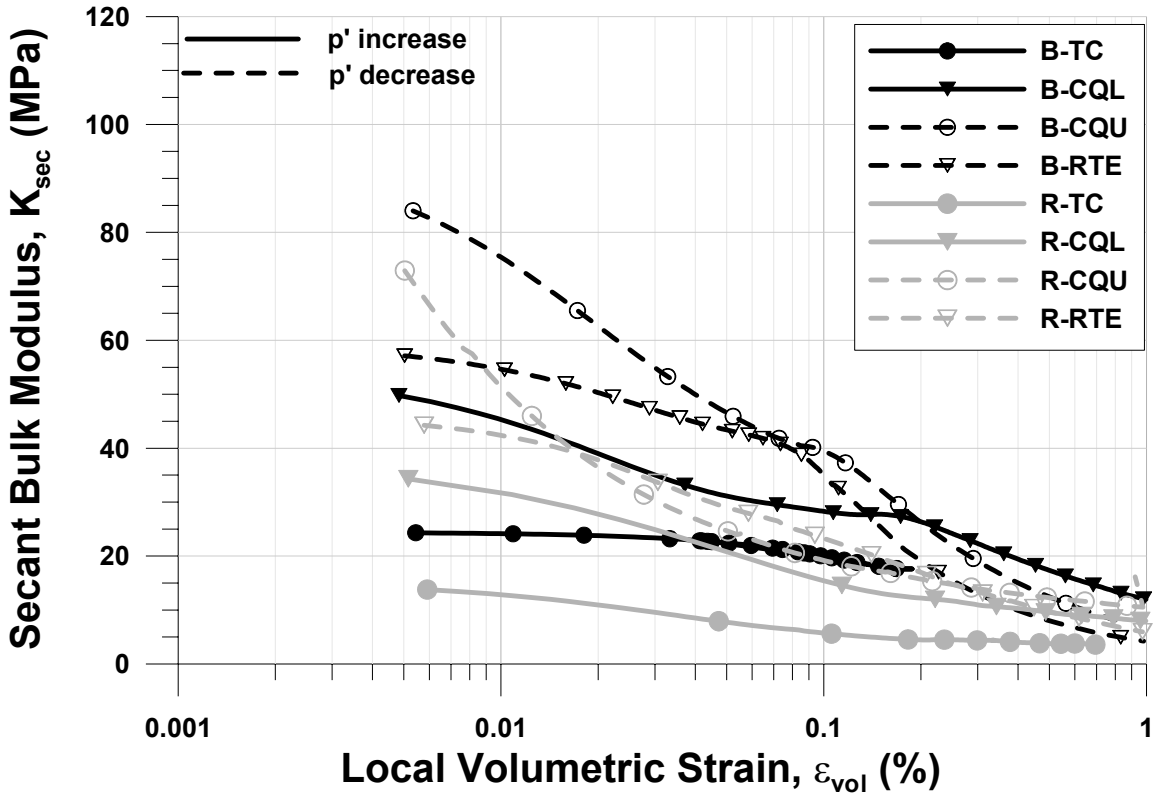

Figure 7-12 Bulk modulus degradation curves of block samples for stress probe tests

The maximum and minimum calculated K_{sec} values of reconstituted samples at ε_{vol} of 0.005% are 72 MPa and 14 MPa for probes CQU and TC, respectively. They are also 15% and 45% smaller than those of the natural samples for the same paths. Unlike the natural samples that showed a constant bulk modulus in a TC path, the reconstituted samples show no such inferred linear elastic zone for volumetric strains smaller than 0.4%. As discussed in Section 4.3, the bulk moduli of natural Chicago clay strongly depend on the stress path direction. The bulk moduli in the stress probes wherein p' is increased ("loading") are smaller than those in the stress probes where p' initially decrease ("unloading"). This stress path dependency of bulk moduli also is seen in the reconstituted sample data. The reconstituted samples show softer responses in each direction than natural ones.

The pattern of bulk moduli of the two is very similar to that of the shear moduli when both are plotted against the direction of loading. Figure 7-13 shows plots of K_{sec} for 0.005%, 0.01%, and 0.1% strains plotted against θ. To compare the general trends, the K_{sec} values for the natural specimens subjected to other stress paths, AL, AU, RTC, TE are also plotted.

For both types of samples, the dependence of bulk modulus on θ is large at 0.005% and 0.01% ε_{vol}, but the directional dependence decreases as the strains reach and exceed 0.1%. Unlike the shear behavior, the differences between natural and reconstituted samples do not decrease with increased strains. Even at ε_{vol} of 0.1%, the difference between the two is clearly seen.

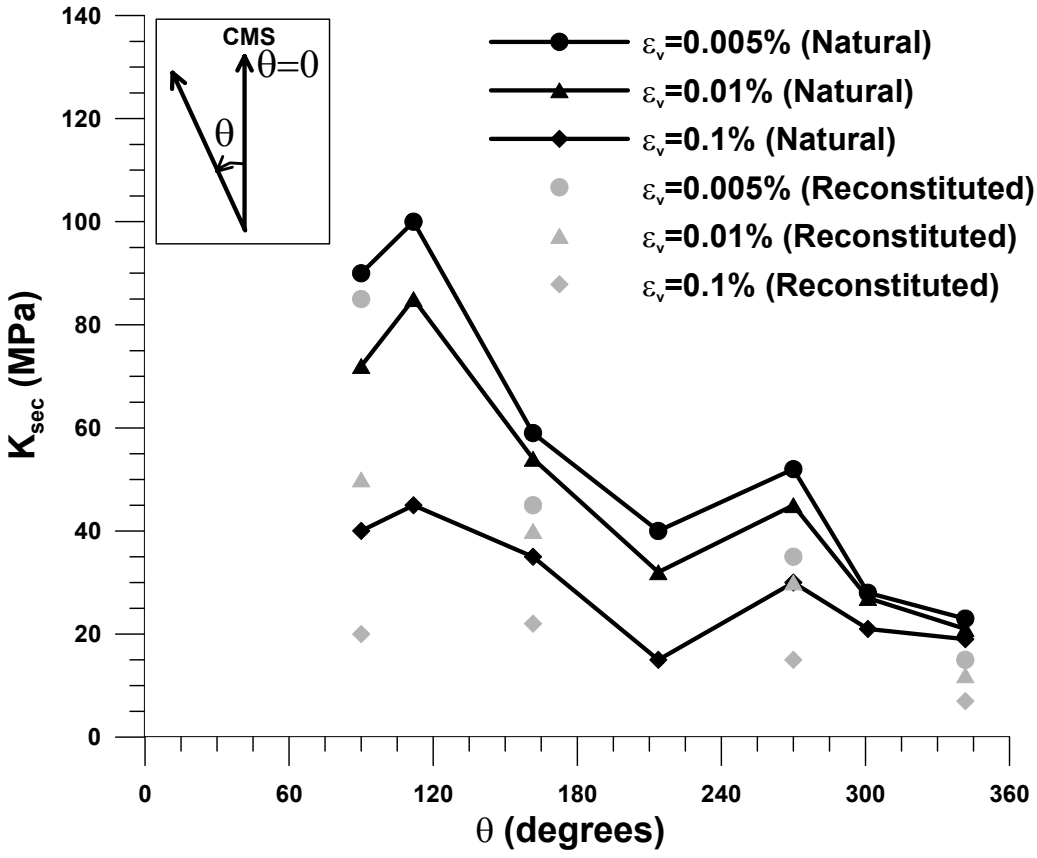

Figure 7-13 Variation of secant bulk modulus K_{sec} of natural and reconstituted samples as a function of angular difference in stress probe direction

7.3.5. Coupling Stress-Strain Behavior

Figure 7-14 shows the mean normal effective stress and shear strain relationship to investigate the cross coupling behavior of the natural and reconstituted samples. Softer response of the reconstituted samples also is found in the cross coupling responses. At large strains, the CQL paths for both sample types show no apparent coupling for increments as large as 90 kPa for natural samples and 50 kPa for reconstituted samples. While the CQU path for the natural sample shows no coupling for $\Delta p'$ as large as -50 kPa, the reconstituted sample shows coupling from the beginning of the CQU path.

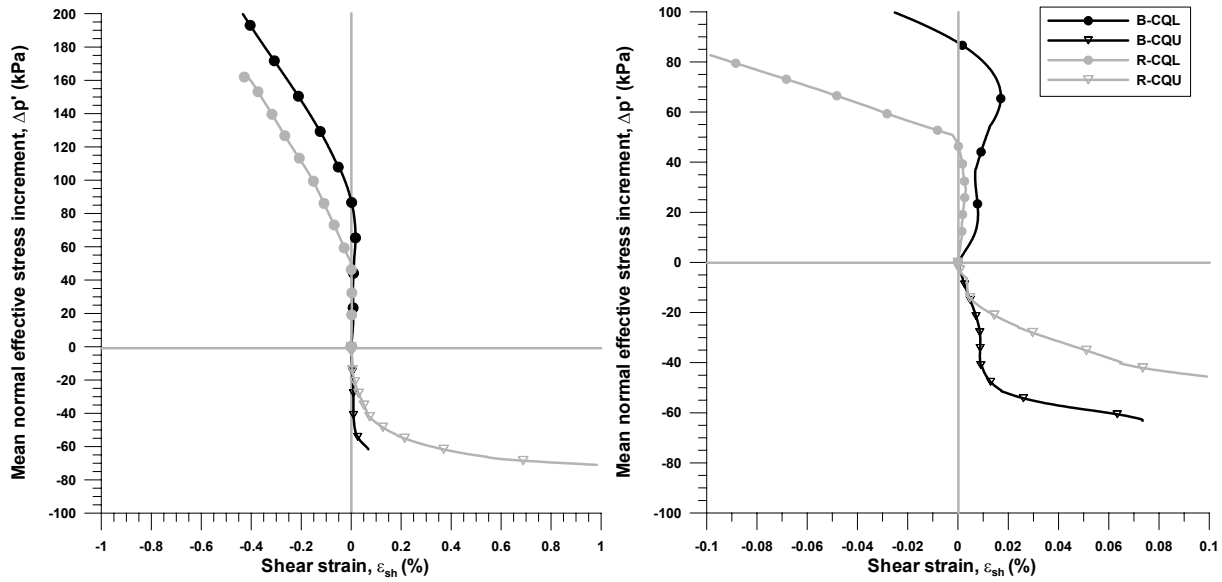

Figure 7-14 $\Delta p'$ versus ε_{sh} for CQL and CQU stress paths of natural and reconstituted samples (a) large strain data up to 1%, (b) small strain data for ε_{vl} ±0.01%

Figure 7-15 shows the deviatoric stress and volumetric strain relationships for the natural and reconstituted samples. Softer q-ε_{vol} responses are found in all reconstituted samples when compared to the corresponding path for natural samples. Unlike the mean normal effective stress and shear strain relationship, the CMS data for both types of samples exhibit coupling responses

from the beginning of the test. For the unloading CMSE path, the natural sample shows no coupling for stress changes as large as 20 kPa, whereas the reconstituted sample show coupling as soon as the test starts. Overall, for both sample types, shear-induced contraction occurred in compression loadings, as expected for lightly overconsolidated clays.

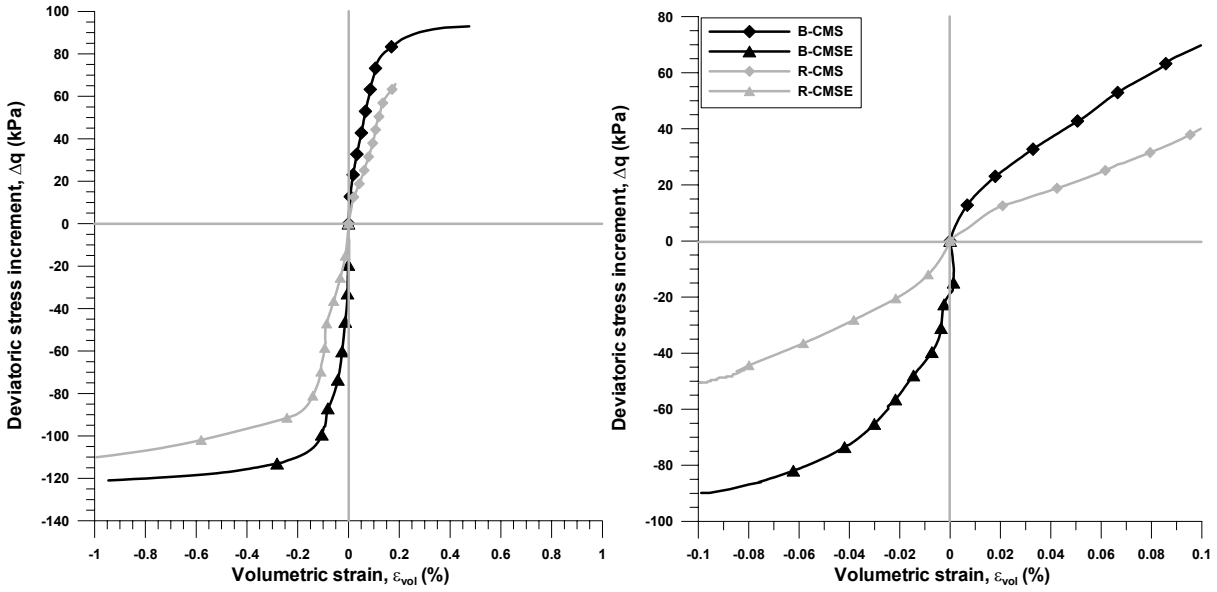

Figure 7-15 Δq versus ε_{vol} for CMS and CMSE stress paths of natural and reconstituted samples (a) large strain data up to 1%, (b) small strain data for ε_{vl} ±0.01%

7.4. STRAIN RESPONSE ENVELOPE

Strain response envelopes (SREs) for the natural and reconstituted samples are generated and compared to depict stress-strain response differences for all possible strain path directions and incremental stress probe magnitudes. Nonlinear and irreversible soil responses also can be seen by examining the SREs. Detailed theory and development of strain response envelopes have been presented in Section 4.4.1.

7.4.1. Strain Response Envelopes of Natural and Reconstituted samples

Figure 7-16 presents the stress probe input circles for $R_\sigma(=\sqrt{(\Delta p)^2+(\Delta q)^2})$ =5, 10, 15, 30, 40, and 50 kPa for both types of samples. R_σ of 5, 10, 15, 30, 40 and 50 kPa were applied to compare the non linearity and directionality differences. All the stress probes are used to generate general SREs for the natural samples.

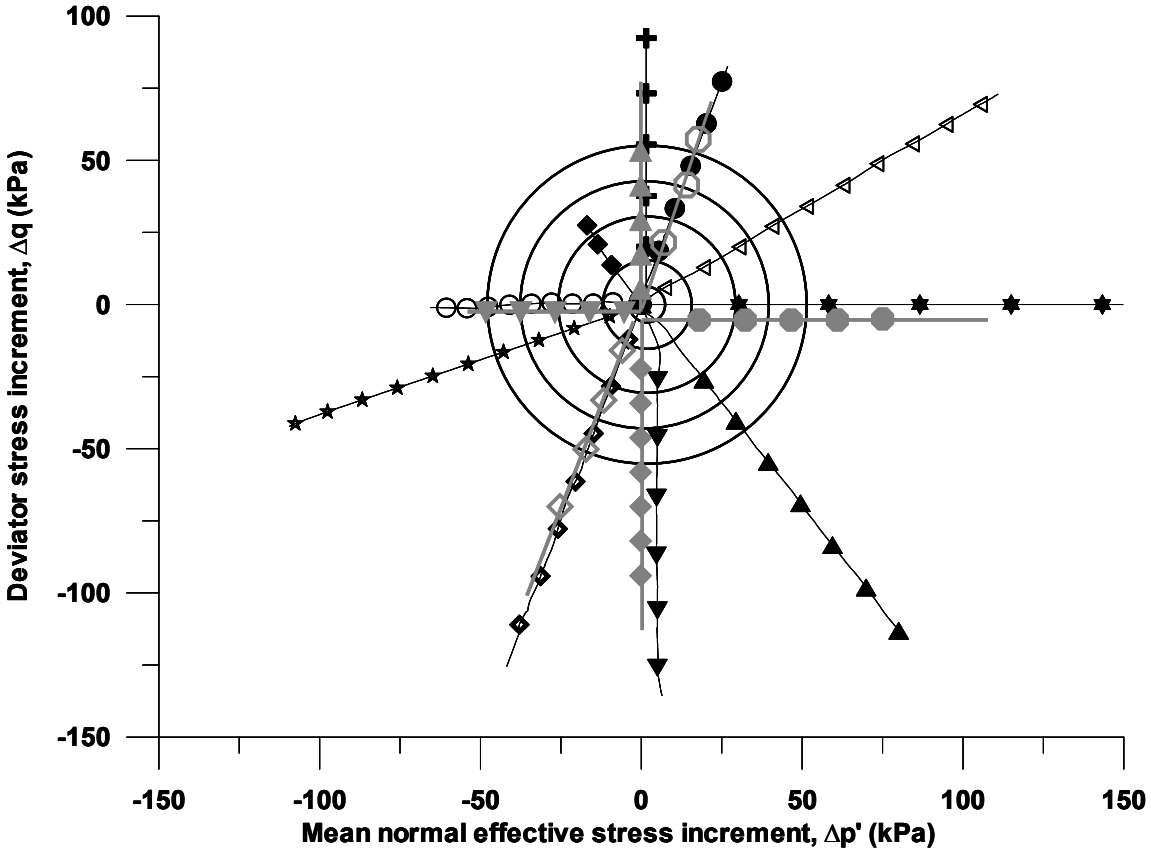

Figure 7-16 Stress probe input circles for R_σ=25, 50, 75, and 100 kPa

Figure 7-17 shows the SREs of the two types of samples at large strains for R_σ= 30, 40 and 50 kPa. The overall trends of the two samples indicate that the origin of the SREs shifts towards up and to the right suggesting the directional dependence of the stiffness of the soil. Due to the absence of an AL path for the reconstituted samples, the major axis of the SREs, assuming

an elliptical shape, can not be directly shown. However, the data trends clearly show that the "major axis" is shifted the same direction as natural samples. This rotation proves that there are cross-coupling effects in relatively large strain. Note that the "major axis" rotation is induced by mixed effects of $\Delta p'$-ε_{sh} and Δq-ε_{vol} relationship as explained in Section 4.4.1.

A noticeable difference is the size of the SREs for each sample type. Even though the input stress level is the same, the SREs of the reconstituted samples are much larger than those of the natural samples, which shows softer responses of the reconstituted samples. The spacing of the SREs contours also shows the softer response of reconstituted samples because this spacing is a function of the stiffness of the soil for a given loading direction. The differences in size and spacing indicate that reconstituted samples are not only softer at the same stress level, but also become softer at a greater rate than the natural samples.

Figure 7-18 shows both natural and reconstituted SREs for strains between -0.04 and 0.1% with R_σ of 5, 10 and 15 kPa. In this strain range, the difference in sizes between the two is less noticeable, but the shape of SRE for the reconstituted sample becomes longer in the horizontal direction. This change implies softer volumetric responses than shear responses. The rotations of the major axes in the SREs for both samples are observed from the small stress increment. This suggests that cross-coupling responses also influence the general stress-strain responses of the reconstituted samples at small strain levels.

All SREs of both samples in large and small strain ranges are markedly non-symmetric about the origin of the strain increment space, which represents genuine experimental evidence of incremental non-linearity. The comparison of SREs of the natural and reconstituted samples shows that reconstituted samples are softer than the natural samples and, in particular, the differences in cross coupling of the two types of samples results in different shapes of SREs.

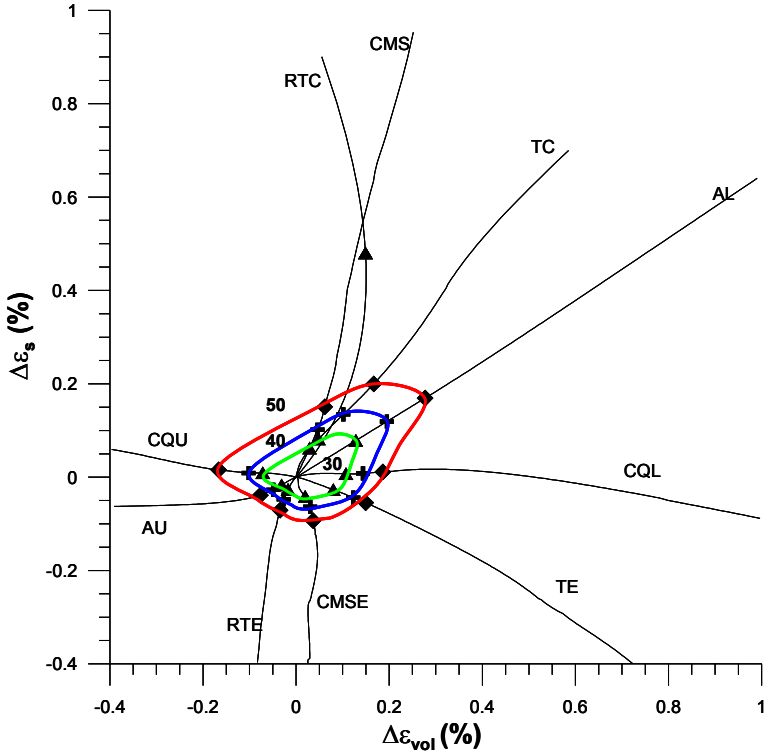

(a)

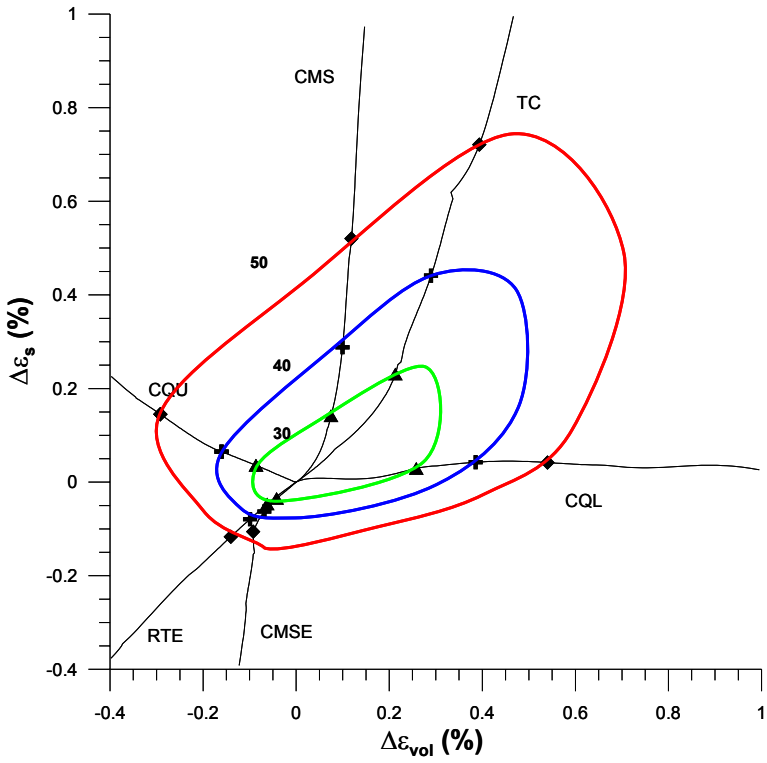

(b)

Figure 7-17 Strain response envelopes of (a) natural and (b) reconstituted samples for large-strain levels, R_σ= 30, 40 and 50 kPa

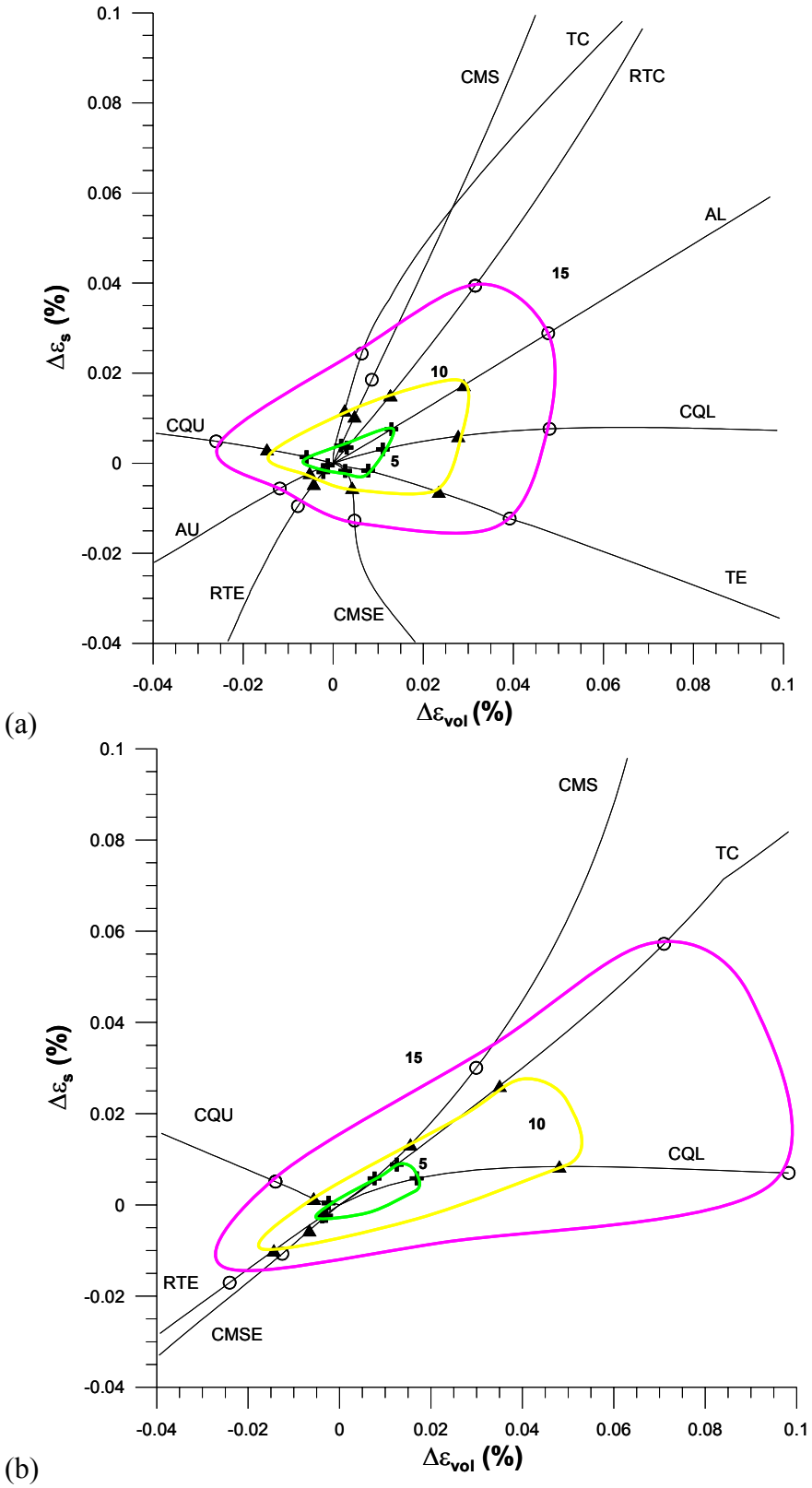

Figure 7-18 Strain response envelopes of (a) natural and (b) reconstituted samples for small-strain levels, R_σ= 5, 10 and 15 kPa

7.5. LIMIT STATES AND FAILURE BEHAVIOR OF NATURAL AND RECONSTITUTED CHICAGO CLAYS

Limit states and failure conditions were examined for the two types of specimens. Procedures to evaluate the limit and failure states were discussed in Section 4.5.1 and 4.5.2, respectively. Figure 7-19 shows the location of yield points on the stress-strain curves for every stress probe.

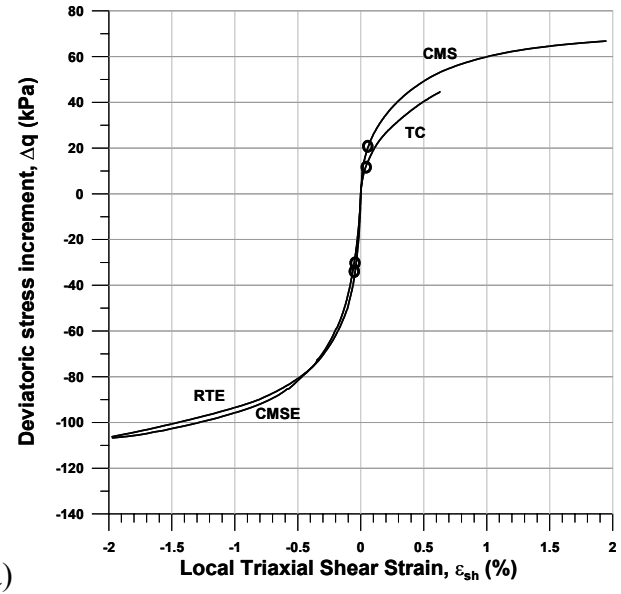

(a)

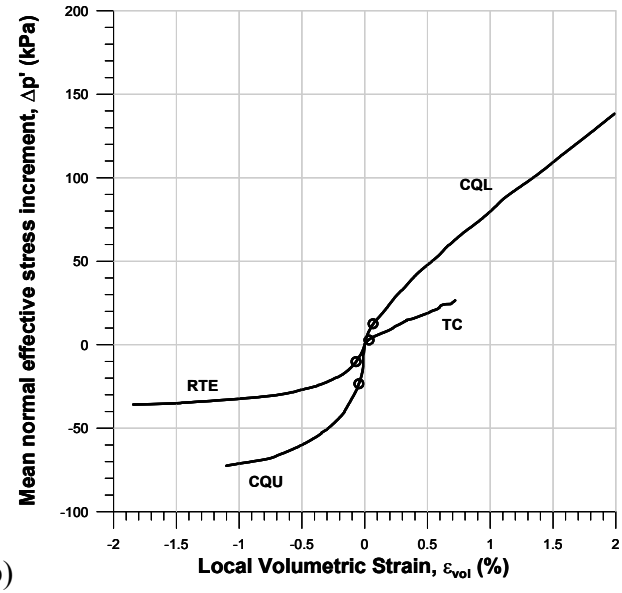

(b)

Figure 7-19 Location of yield points of reconstituted samples on the stress-strain curves

Figure 7-20 shows limit and failure states of both natural and reconstituted samples. Both samples show the distorted elliptical shape of limit states, indicating that both samples are anisotropic materials. However, the limit state of the reconstituted samples is smaller, especially in the CQU and CQL paths, than that of the natural samples. This implies that the reconstituted samples show softer responses in volumetric behaviors. From the comparisons of the limit states in volumetric behaviors between the natural (Figure 4-27(b)) and reconstituted samples (Figure 7-19(b)), the RTE and TC paths of the reconstituted samples also reach the limit state with less volumetric strains. This might be due to the loss of fines during the reconstituting procedures as explained in Section 3.1.2, because volumetric responses are more affected by the permeability, which is a function of the amount of fines.

Unlike limit states, the failure points are very similar and the stress ratio at failure for normally consolidated states in compression and extension are 1.1 and 0.83, respectively. Also, the "bump" region of the failure lines also is observed in the reconstituted samples. As explained 4.5.2, this region is due to highly OC state of the specimen. Due to the similar failure values and smaller limit state, overall failure responses of the reconstituted samples are progressive while those of the natural samples are abrupt especially in stress ratio, η loading paths. This progressive failure indicates the lack of structure in the reconstituted samples.

In addition, the limit state of the RTE path for the reconstituted samples is located near the limit state of the CQU path. This implies the closing of limit state lines, even though it is hard to draw any definitive conclusion without performing the AU tests.

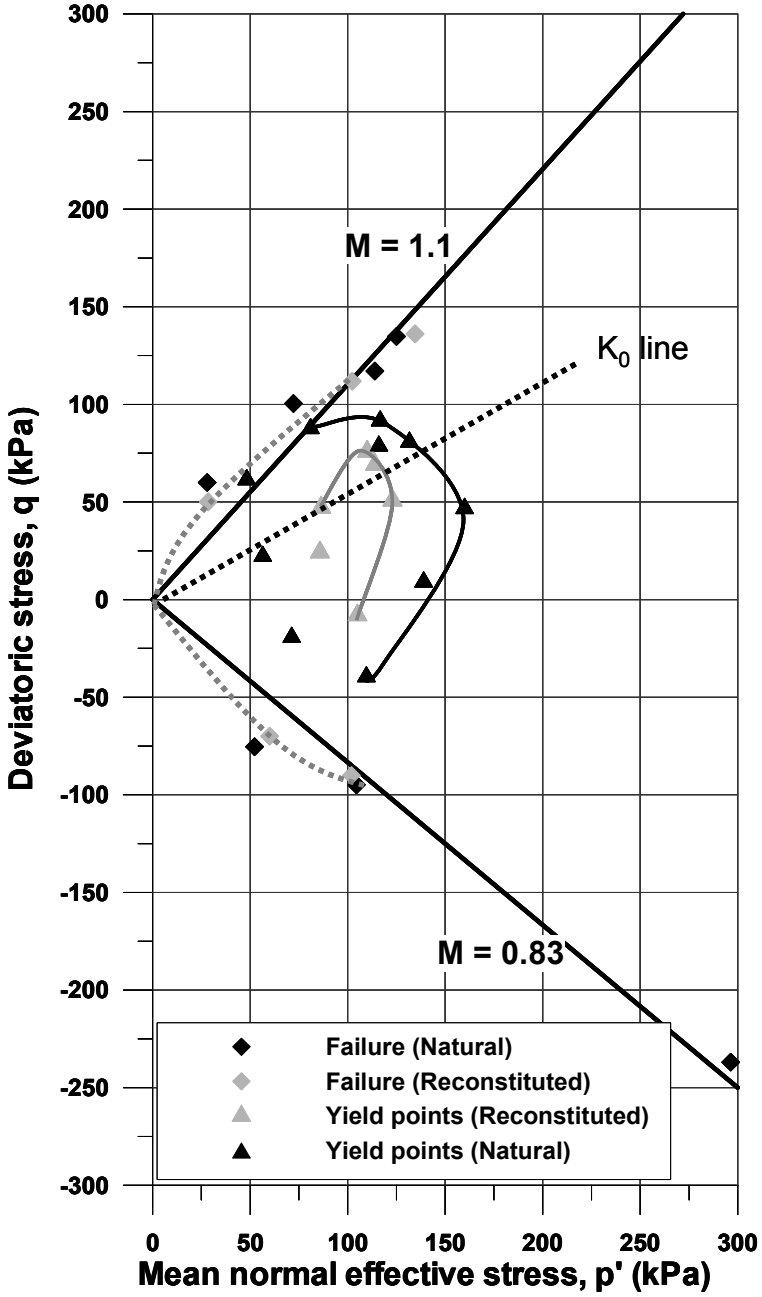

Figure 7-20 Limit states and failure comparison of natural and reconstituted samples

7.6. DISCUSSION

From the comparisons between the natural and reconstituted samples presented in this dissertation, it is shown that the responses of the reconstituted samples during K_0 reconsolidation,

K_0 creep and shearing are different from those of natural samples, with the exception of similar failure states.

In the literature, there are several comparisons between the natural and reconstituted samples. The recent research of Holman (2005) on the reconstituted and natural samples of Blodgett strata shows a "perfect" match between the two in terms of index properties, consolidation and stiffness. However, the natural samples experienced large swelling during saturation in Holman's program. Because of the swelling effect, the direct comparison is not appropriate because swelling strains can destructure natural clays. In the comparisons between natural and reconstituted samples of Boston Blue clays, a good agreement in undrained strength was found (Santagata 1998), but the type of natural samples was not specified and different K_0 values were reported for the two types of samples. Research on natural and reconstituted Pisa clays showed the initial stiffnesses from the true triaxial and triaxial test results were similar, but the reconstituted samples show yielding at lower stress levels than the natural samples (Callisto and Calabresi 1998).

The reconstituting procedure applied herein was to make normally consolidated reconstituted samples with a maximum past pressure similar to the natural samples, and then obtain the appropriate OCR by reconsolidating the reconstituted specimens in the triaxial system to the in-situ vertical effective stress. This procedure has advantages in that the reconstituted specimens with same maximum past pressure, but with various OCR, can be generated during reconsolidation by applying different vertical effective stresses in the triaxial cell. However, with this procedure, the reconstituted block was subjected to a rapid change in stress condition during extraction from the slurry consolidometer from K_0 to isotropic. To eliminate the disturbance due to this rapid change, the reconstituting procedure used at MIT (Santagata, 1998) includes a stage

of hydrostatic stress condition before the extrusion of the sample. Estimating K_0 values from the other reconstituted samples in triaxial tests, the vertical effective stress is controlled to be the same as the radial stress before the extrusion. In future tests, it will be worth while to make reconstituted samples with similar values of OCR by unloading from the maximum past pressure to the vertical effective stress in the slurry consolidometer. This comparison can provide the validity of the method used herein. Furthermore, to elucidate the effects of aging, it is worth reconstituting samples with much longer creep period to compare with results from the reconstituted samples with creep periods of 7 days.

In addition, literatures related to reconstituted samples are marine clays. In the process of making the slurry as a first step in the reconstitution procedures, NaCL was added in the mixture to facilitate the flocculation of the clays. However, these flocculating additives cannot be used for fresh-water deposited materials such as Chicago clays, another reason why it is hard to reproduce the structure of the Chicago clays.

Reconstituted samples are widely used for the general stress-strain-stiffness responses study for its virtually infinite supply and minimal variability. However, more work needs to be done to evaluate the characteristics of reconstituted Chicago clays compared to the natural ones in terms of stiffness and yield characteristics.

7.7. SUMMARY AND CONCLUSIONS

Responses of reconstituted samples were compared with those of natural samples in terms of index properties, stress history, residual effective stress, K_0 reconsolidation, and creep, and stress-strain responses during stress probing.

Both natural samples and reconstituted samples show very similar index properties and stress history. While the magnitude of the residual stresses also was similar, the ratio p_r'/σ_{v0}' is much lower for the reconstituted samples. This may be related to the short period of aging compared to the natural samples. Similarly, stress-strain responses during K_0 reconsolidation are different and in particular 4 times larger creep strain was observed in reconstituted samples though both samples show very small recompression strains.

Bender element test results show clear difference between the two samples. Empirical equations for G_{BE} based on the effective stress show the values of G_{BE} of the reconstituted samples are 20-30% lower than those of the natural samples at the end of K_0 reconsolidation.

Stress-strain responses during stress probe test consistently show the softer response of reconstituted samples in shear, volumetric and cross coupling of shear and volumetric behaviors. However, overall characteristics of natural samples such as stress path and strain level dependency of stiffness and cross coupling are also shown in reconstituted samples.

Though the yield surface of reconstituted samples is smaller than that of natural samples, the failure points are very similar and the stress ratio at failure for compression and extension are 1.1 and 0.83, respectively. The reconstituted samples show progressive failure in both η loading and η unloading paths, while the natural samples show abrupt failure in η loading paths.

In spite of the similarity of the index properties and stress history, reconstituted samples show very different behaviors from natural samples. This might be due to the short period of creep/aging but the bender element test results suggest both samples show different structures. Reconstituted samples can be used for the investigation of the mechanical behavior of clays because data show that they exhibit the general characteristics of natural clays. However, overall softer responses, different dynamic responses based on bender element test results and smaller

yield surface presented in this Chapter suggest that it is hard for reconstituted samples to represent the natural samples of compressible Chicago glacial clays.

CHAPTER 8 SUMMARY AND CONCLUSIONS

8.1. SUMMARY

Geotechnical engineering analyses of deformations around new or existing structures requires consideration of the strain-level dependent nature of soil stiffness (i.e. modulus degradation), effects of stress path directions and recent stress history. Measured displacement fields around serviceable structures, such as well-designed deep excavations, demonstrate that strains are typically lower than predicted in conventional analysis. This overestimation of deformations is due to the strain-level dependency of soil stiffness and the effects of stress path direction. Complete characterization of soil small strain behavior requires the measurement of soil moduli over at least 3 orders of strain magnitude, from below 0.001% to 0.1%, typically using combinations of wave propagation techniques such as bender elements or seismic cone penetration testing (SCPT) and very sensitive LVDTs mounted directly on soil specimens. The modulus of lightly overconsolidated soils at very small and small strains are influenced by sample disturbance, current state and stress history, stress path direction and reversals, anisotropy, and age/creep. Stress history has a very significant influence on the stiffness degradation behavior of clays, and may result in widely differing soil response for stress path directions rotated from the direction of the previous stress history.

The experimental program undertaken to investigate the small strain properties of compressible Chicago glacial clays included sophisticated testing of block samples and reconstituted specimens, with a specially-designed small strain testing system composed of

bender elements and very sensitive subminiature LVDTs in a computer-controlled triaxial stress path system.

The index properties for each block sample used in this study were found to be very similar. The stress history of the blocks, as measured in oedometer tests and characterized by σ_p', also is very similar, with σ_p' values ranging from 220 to 235 kPa. The mean residual effective stress, p_r', measured for the block samples was 44 kPa with a standard deviation of 6 kPa. The ratio between the measured residual effective stress and the in-situ vertical effective stress indicated that there was disturbance other than that from the stress relief. To minimize the swelling during saturation and possible structural alternation, the specimens were saturated at the measured residual stress.

K_0 consolidation responses for each specimen resulted in the achievement of nearly identical end stress states, which was necessary to consider each stress probe to have started from the same point. The mean end stress state was in terms of $p'$and q was 100.4 and 58.5 kPa, respectively. The creep behavior at the end of the K_0 reconsolidation was very similar for each specimen, similar path direction and lengths of the creep stress path. The creep phases resulted in stress path rotations of approximately 90°, increases in p' and σ_r', and reductions in q. The mean axial strains, measured by the internal measurement system, were less than 0.5%, which indicated that the triaxial specimens were "very good" to "excellent," based on the Sample Quality Designation method of assessing sample disturbance.

The stress-strain response from the directional stress probes was examined in terms of shearing, volumetric, and two coupling relationships – the mean normal effective stress-shear strain coupling and deviatoric stress-volumetric strain coupling. Natural and experimental

variation resulted in 10-15% of modulus difference in the same stress path tests. The dependence of stress-strain behavior on stress probe direction was observed for both shearing and volumetric behaviors. The deviatoric stress-shear strain responses do not show the zones of linear behavior at small strain levels, i.e. apparent linear elastic response, while the p' loading type of stress paths show linear behavior up to 0.02%. The stress ratio, η (=q/p'), loading probes resulted in significantly smaller shear moduli at all strain levels than the η unloading probes. Similarly, p' loading paths show smaller bulk moduli than p′ unloading paths. The dependence on the stress path direction decreases with strains in both the shearing and volumetric behaviors. Shear-volumetric coupling was observed for all stress probes in the large strain range while the coupling was relatively weak in small strain range.

The strain response envelopes (SREs) graphically depict this constitutive response through their asymmetry, orientation, and location with respect to the strain origin, even at small strains. The SREs also show the directional dependence and the evolution of coupling with increased strains. The SREs at 3 different strain levels show that the different spacing of SREs in loading and unloading directions decreases with increasing strains. The SREs show that the major axis, under the assumption of an elliptical shape, rotates from around the horizontal to the AL path in q-p' space as strain increases, suggesting that the cross-coupling effects become larger as strain increases.

Limit state and failure conditions were examined. The limit state for each stress probe was defined by locating the yield strains at the intersection of the rectilinear extrapolations of the pre- and post yield portions of the stress-strain curves. For the stress paths when stress ratio, η

(=q/p') increases, the values of strain energy are essentially constant to each limit state. However, the limit state points have quite different strain energies when stress paths with decreasing η.

The results of two types of stress probe tests with different pre-shear stress paths were compared to investigate the effects of recent stress history and the current stress path dependency. Those two effects are combined herein as "directionality" because in reality those two effects do not exist separately. Based on the comparisons of the stress-strain data and moulus degradation curves of the two types of stress probe tests, directionality was apparent in all data presented. The peak shear and bulk moduli are located at an orientation θ, the angular difference between the current stress path and pre-shear stress path, corresponding to complete or nearly complete stress reversals. Current stress path and recent stress history affect not only shear and bulk moduli but also the cross-coupling moduli.

The comparisons of SREs between the two stress probe tests graphically illustrate the directionality of the Chicago clay. The stiffer responses, shown by the closest stress contours, were observed in stress-path reversal points and shear, bulk and two cross-coupling moduli are all affected by the recent stress history. This influence becomes smaller with larger strains.

The bender element data obtained during the K_0 consolidation process was used to establish a relationship between the bender element modulus G_{BE} and the effective stress. Deviations of measured values of $G_{BE(vh)}$ from the empirical correlation during stress probing tests were used to define stresses that correspond to mechanically-defined limit state points. For the stress paths where the stress ratio increases, the stress points initiating such deviations of $G_{BE(vh)}$ are located close to the yield surface.

Three sets of bender element test results show that soft Chicago glacial clay is a cross-anisotropic material with G_{BEhh}/G_{BEhv} =1.2, which is relatively small anisotropy ratio compared to those reported values for other clays. Values of $G_{BE(hh)}$ follow the same trend during shearing as $G_{BE(vh)}$ but conclusions cannot be drawn due to the limited quantity of the data with 3 bender elements. Also, the shear modulus based on the shear wave velocity in axial direction (G_{vh}) agrees well with the field measured shear wave velocity by seismic CPT tests.

Based on the results of the stress probes, the bender element modulus does not directly correspond to a particular value of G_{sec} at the smallest, reliably-measured strain levels, 0.002%. Comparison of the G_{BE} values at the end of creep with $G_{0.001}$ values indicates that G_{BE} is closest to a mechanically measured secant modulus for the stress path directions rotated 180 to 230 degrees from the previous stress history.

Reconstituted samples were created with slurry consolidation techniques to compare their responses during shear probing with those of the natural block samples. Reconstituted samples were compared with natural samples in terms of index properties, stress history, residual effective stress, K_0 reconsolidation and creep behaviors, and stress-strain responses during shear.

Both natural samples and reconstituted samples show very similar index properties and stress history. A similar range of residual stress also was found. However, the ratio p_r'/σ_{v0}' is much lower in reconstituted samples. Similarly, stress-strain responses during K_0 reconsolidation are different. In particular, creep strains were 4 times larger in reconstituted samples, although both samples exhibited very small recompression strains. Bender element test results show clear differences between the two samples. Empirical equations for G_{BE} based on the effective stress

are markedly different, suggesting different the two types of samples had different structures, at very small strain responses.

When comparing with reconstituted and natural samples, stress-strain responses during stress probe tests consistently showed softer responses for the reconstituted samples in shear, volumetric and cross coupling of shear and volumetric behaviors. However, the overall characteristics of the natural samples, such as stress path and strain level dependency of stiffness and cross coupling, also are shown in the reconstituted responses. Though the limit state surface of reconstituted samples is smaller than that of natural samples, the failure points are very similar and the stress ratio at failure for compression and extension are 1.1 and 0.83, respectively.

8.2. CONCLUSIONS

The results of this research clearly indicate that the small strain behavior of the compressible Chicago glacial clays exhibits the dependence on the current stress path and pre-shear stress path, i.e. “recent stress history” as well as on the strain level. Through the data collected by the three different instrumentation systems used in this study, bender elements, on-specimen measurement systems and external measurement systems, the stress-strain behavior of natural specimens trimmed from block samples and reconstituted specimens successfully was measured at very small to large strains in multiple stress path directions.

The stress-strain responses observed from the directional stress probes indicated there were significant differences between loading and unloading stress paths. The shear and bulk moduli degrade as a function of increasing strain level; however, the comparisons of results of the two types of stress probe tests with different pre-shear stress paths showed clear evidence of “directionality” of stiffness in compressible Chicago glacial clays. This “directionality”

combines the dependency on both the current stress path and recent stress history, because in reality those two effects do not exist separately. The significant directionality and non-linearity of the stiffness provide experimental evidence that the Chicago clays are incrementally nonlinear.

The very small strain shear modulus G_{BE}, as measured by bender element tests, is dependent on the effective stress state for the Chicago clays during K_0 reconsolidation. The G_{BE} values essentially are the same as the dynamic modulus from sCPT data and the mechanically measured shear modulus at the stress path directions rotated 180 to 230 degrees from the previous stress history. The cross-anisotropy of natural Chicago clays was observed via results of tests that employed three sets of bender elements. The degree of anisotropy was in lower bound of previously reported values for normally to lightly overconsolidated clays. Deviations of measured values of $G_{BE(vh)}$ from the empirical correlation during stress probes can be used to define stresses that correspond to mechanically-defined limit points.

Results of reconstituted samples can be used to investigate the effective stress at failure conditions of compressible Chicago clays because the failure conditions are the same for the reconstituted and natural samples. However, in spite of similarity of index properties and stress history, overall softer responses, softer dynamic responses based on bender element test results and smaller limit state surface, suggest that reconstituted samples do not represent the *in-situ* behavior of compressible Chicago glacial clays. Because the two types of specimens exhibit similar trends in responses, proper correction factor can be developed after more experiments so that the reconstituted results can be scaled to the *in-situ* behavior.

REFERENCES

Addenbrooke T.I., Potts D.M. and Puzrin A.M. (1997). The influence of pre-failure soil stiffness on the numerical analysis of tunnel construction. *Geotechnique*, Vol. 47, No.3, pp. 693-712.

Amorosi, A., Callisto, L., and Rampello, S. (1999). Observed behavior of reconstituted clay along stress paths typical of excavations. *Proceedings of the Second International Symposium on Pre-failure Deformation Characteristics of Geomaterials*, Torino, Vol. 1, 35-42.

Andresen, A., and Kolstad, P. (1979). "The NGI 54 mm sampler for undisturbed sampling of clays and representative sampling of coarser materials." *Norwegian Geotechnical Institute Publication*, 130, 13-21.

Arulnathan, R., Boulanger, R.W., and Riemer, M.F. (1998). Analysis of bender element tests. *Geotechnical Testing Journal*, ASTM, Vol. 21, No. 2, 120-131.

Atkinson, J.H. (2000). Non-linear soil stiffness in routine design: 40th Rankine Lecture. *Geotechnique*, Vol. 50, No. 5, 487-508.

Atkinson, J.H. and Sallfors, G. (1991). Experimental determination of stress-strain-time characteristics in laboratory and in situ tests. *Proceedings of the 10th European Conference on Soil Mechanics and Foundation Engineering*, Florence, Vol. 3, 915-956.

Atkinson, J.H., Richardson, D., and Stallebrass, S.E. (1990). Effect of recent stress history on the stiffness of overconsolidated soil. *Geotechnique*, Vol. 40, No. 4, 531-540.

Baldi, G., and Hight, D. W. (1988). "State-of-the-art: A reevaluation of conventional triaxial test methods." *Advanced triaxial testing of soil and rock, ASTM STP*, 977, 219-263.

Bishop, A.W., and Henkel, D.J. (1957). *The Measurement of Soil Properties in the Triaxial Test*, London, Edward Arnold, Ltd.

Bjerrum, L. (1973). "Problems of Soil Mechanics and Construction on Soft Clay: State of Art Report." *Proceedings of the 8th Internation Conference on Soil Mechanics and Foundation Engineering*, Moscow, 173-184.

Blackburn, J. T. (2005). "Automated sensing and three-dimensional analysis of internally braced excavations," Ph.D thesis, Northwestern University, Evanston.

Burland, J.B. (1989). 'Small is beautiful' – the stiffness of soils at small strains: Ninth Laurits Bjerrum Memorial Lecture. *Canadian Geotechnical Journal* **26**, 499-516.

Burland, J.B., and Symes, M.J. (1982). A simple axial displacement gauge for use in the triaxial apparatus. *Geotechnique*, Vol. 32, No. 1, 62-65.

Calabresi, G., and Scarpelli, G. (1985). "Effects of swelling caused by unloading in over-consolidated clays." *Proc. 11th Int. Conf. Soil Mech. Found. Engng*, San Francisco, 411-414.

Callisto, L. and Rampello, S. (2002). Shear strength and small-strain stiffness of a natural clay under general stress conditions. *Geotechnique*, Vol. 52, No. 8, 547-560.

Callisto, L. and Calabresi, G. (1998). Mechanical behavior of a natural soft clay. *Geotechnique*, Vol. 48, No. 4, 495-513.

Chan, C. K. (1981). "An electropneumatic cyclic loading system." *Geotechnical Testing Journal*, 4(4), 183-187.

Chung, C.K. (1991). *Stress-strain-strength behavior of compressible Chicago glacial clay tills*. Ph.D. Dissertation, Northwestern University, Evanston.

Chung, C.K. and Finno, R.J. (1992). Influence of depositional processes on the geotechnical parameters of Chicago glacial clays. *Engineering Geology*, Vol. 32, 225-242.

Clayton, C. R. I., Hight, D. W., and Hopper, R. J. (1992). "Progressive Destructuring of Bothkennar Clay - Implications for Sampling and Reconsolidation Procedures." *Geotechnique*, 42(2), 219-239.

Clayton, C.R.I., and Heymann, G. (2001). Stiffness of geomaterials at very small strains. *Geotechnique*, Vol. 51, No. 3, 245-255.

Clayton, C.R.I., and Heymann, G. (1999). Stiffness of geomaterials from small strain triaxial and field geophysical tests. *Proceedings of the Second International Symposium on Pre-failure Deformation Characteristics of Geomaterials*, Torino, Vol. 1, 65-71.

Clayton, C.R.I., Hight, D.W., and Hopper, R.J. (1992). Progressive destructuring of Bothkennar clay: implications for sampling and reconsolidation procedures. *Geotechnique*, Vol. 42, No. 2, 219-239.

Clayton, C.R.I., and Khatrush, S.A. (1986). A new device for measuring local axial strains on triaxial specimens. *Geotechnique*, Vol. 36, No. 4, 593-597.

Clough, G.W., and O'Rourke, T.D. (1990). Construction induced movements of insitu walls. *Proceedings of a Conference in Design and Performance of Earth Retaining Structures*, ASCE Geotechnical Special Publication No. 25, Ithaca, 439-470.

Costanzo, D., Tamagnini, C., and Viggiani, G. (2003). Incremental behavior of a reconstituted clay subjected to stress probing tests. *Proceedings of the International Workshop on Geotechnics of Soft Soils-Theory and Practice*, 6 pp.

Crooks, J.H.A., and Graham, J. (1976). Geotechnical properties of the Belfast estuarine deposits. *Geotechnique*, Vol. 26, No. 2, 293-325.

Cuccovillo, T., and Coop, M.R. (1997). The measurement of local axial strains in triaxial tests using LVDTs. *Geotechnique*, Vol. 47, No. 1, 167-171.

DaRe, G. Santagata, M.C., and Germaine, J.T. (2001). LVDT based system for the measurement of prefailure behavior of geomaterials. *Geotechnical Testing Journal, ASTM*, Vol. 24, No. 3, 288-298.

Dyvik, R., and Madshus, C. (1985). Laboratory measurements of G_{max} using bender elements. In *Advances in the Art of Testing Soils under Cyclic Conditions (edited by V. Khousla)*, Detroit, ASCE, New York, 186-196.

Fahey, M. (1999). Deformation and in-situ stress measurement. *Proceedings of the First International Conference on Site Characterization ISC-98*, Atlanta, Vol. 1, 49-68.

Finno, R. J., and Chung, C. K. (1992). "Stress-Strain-Strength Responses of Compressible Chicago Glacial Clays." *Journal of Geotechnical Engineering-Asce*, 118(10), 1607-1625.

Finno, R.J., and Roboski, J.F. (2005). Three-dimensional response of a tied-back excavation through clay. *Journal of Geotechnical and Geoenvironmental Engineering*, ASCE, Vol. 131, No. 3, 273-282.

Gasparre, A, Nishimura, S, Minh, NA, Coop, MR, Jardine, RJ, The stiffness of natural London Clay, *Geotechnique*, 2007, Vol: 57, Pages: 33 - 47

Goto, S., Tatsuoka, F., Shibuya, S., Kim, Y-S., and Sato, T. (1991). A simple gauge for local small strain measurements in the laboratory. *Soils and Foundations*, Vol. 31, No. 1, 169-180.

Graff, K.F. (1975). *Wave Motion in Elastic Solids*. Oxford, Clarendon Press.

Graham, J., Noonan, M.L., and Lew, K.V. (1983). Yield states and stress-strain relationships in a natural plastic clay. *Canadian Geotechnical Journal*, Vol. 20, 502-516.

Gudehus, G. (1979). A comparison of some constitutive laws for soils under radially symmetric loading and unloading. *Proceedings of the 3rd International Conference on Numerical Methods in Geomechanics*, Aachen, 1309-1324.

Hardin, B.O. (1978). The nature of stress-strain behavior of soils, *Proceedings of the ASCE Geotechnical Engineering Division Specialty Conference on Earthquake Engineering and Soil Dynamics*, Vol. 1, 3-89.

Hardin, B. O., and Black, W. L. (1966). "Sand stiffness under various triaxial stresses." *J. Soil Mech. Found. Div.*, 92(2), 27-42.

Hardin, B. O., and Black, W. L. (1968). "Vibration modulus of normally consolidated clay." *J. Soil Mech. Found. Div.*, 94(SM2), 353-369.

Hardin, B. O., and Blandford, G. E. (1989). "Elasticity of particulate materials." *J. Geotech. Eng.*, 115(6), 788-805.

Hardin, B. O., and Richart, F. E. J. (1963). "Elastic wave velocities in granular soils." *J. Soil Mech. Found. Eng.*, 89(SM1), 33-65.

Heymann, G., Clayton, C.R.I., and Reed, G.T. (1997). Laser interferometry to evaluate the performance of local displacement transducers. *Geotechnique*, Vol. 47, No. 3, 399-405.

Hight, D.W. (2001). Sampling effects on soft clay: An update on Ladd and Lambe (1963). *Proceedings of the Symposium on Soil Behavior and Soft Ground Construction*, ASCE Geotechnical Special Publication No. 119, Cambridge, 86-121.

Hight, D.W., and Higgins, K.G. (1995). An approach to the prediction of ground movements in engineering practice: Background and application. *Proceedings of First International Conference on Pre-Failure Deformation Characteristics of Geomaterials*, Sapporo, Vol. 2, 909-945.

Hight, D. W. (2003). "Sampling effects in soft clay: An update on Ladd and Lambe (1963)." *Soil Behavior And Soft Ground Construction*, Cambridge, MA, United States, 86-121.

Hight, D. W., Boese, R., Butcher, A. P., Clayton, C. R. I., and Smith, P. R. (1992). "Disturbance of the Bothkennar Clay Prior to Laboratory Testing." *Geotechnique*, 42(2), 199-217.

Holman, T.P. and Finno, R.J. (2005). Maximum shear modulus and incrementally nonlinear soils. *Proceedings of the 16th International Conference on Soil Mechanics and Geotechnical Engineering*, Osaka, accepted for publication.

Holman, T. P. (2005). "Small strain behavior of compressible Chicago glacial clay," PhD thesis, Northwestern University, Evanston, IL.

Hoque, E., and Tatsuoka, F. (2004). "Effects of stress ratio on small-strain stiffness during triaxial shearing." *Geotechnique*, 54(7), 429-439.

Houlsby, G.T. and Wroth, C.P. (1991). The variation of shear modulus of a clay with pressure and overconsolidation ratio. *Soils and Foundations*, Vol. 31, No. 3, 138-143.

Ishihara, K. (1982). "Evaluation of soil properties for use in earthquake response analysis." *Proc. Int. Symp. Numer. Models Geomech.*, Balkema, Rotterdam, Netherland, 237-259.

Jamiolkowski, M., Ladd, C.C., Germaine, J.T., and Lancelotta, R. (1985). New developments in field and laboratory testing of soils – Theme Lecture 2. *Proceedings of the 11th International Conference on Soil Mechanics and Foundation Engineering*, San Francisco, Vol. 1, 57-153.

Jamiolkowski, M., Lancellotta, R., and LoPresti, D.C.F. (1995). Remarks on the stiffness at small strains of six Italian clays. *Proceedings of First International Conference on Pre-Failure Deformation Characteristics of Geomaterials*, Sapporo, Vol. 2, 817-836.

Jardine, R.J. (1992). Some observations on the kinematic nature of soil stiffness. *Soils and Foundations*, Vol. 32, No. 2, 111-124.

Jardine, R.J., St. John, H.D., Hight, D.W., and Potts, D.W. (1991). Some practical applications of a nonlinear ground model. *Proceedings of the 10th European Conference on Soil Mechanics and Foundation Engineering*, Florence, 223-228.

Jardine, R.J., Potts, D.M., Fourie, A.B., and Burland, J.B. (1986). Studies of the influence of non-linear stress-strain characteristics in soil-structure interaction. *Geotechnique*, Vol. 36, No. 2, 377-396.

Jardine, R.J., Symes, M.J., and Burland, J.B. (1984). The measurement of soil stiffness in the triaxial apparatus. *Geotechnique*, Vol. 34, No. 3, 323-340.

Jovicic, V., and Coop, M.R. (1998). The measurement of stiffness anisotropy in clays with bender element tests in the triaxial apparatus. *Geotechnical Testing Journal, ASTM*, Vol. 21, No. 1, 3-10.

Jovicic, V., Coop, M.R., and Simic, M. (1996). Objective criteria for determining G_{max} from bender element tests. *Geotechnique*, Vol. 46, No. 2, 357-362.

Jung, Y.-H., Cho, W. and Finno, R.J., Defining Yielding from Bender Element Measurements in Triaxial Stress Probe Experiments, Journal of Geotechnical and Geoenvironmental Engineering, ASCE, accepted for publication.

Kuwano, R., and Jardine, R. J. (2002). "On the applicability of cross-anisotropic elasticity to granular materials at very small strains." *Geotechnique*, 52(10), 727-749.

Lacasse, S. (1985). "Testing of special soils: ocean floor soils." *Proc. 11th Int. Conf. Soil Mech. Found. Engng*, San Francisco, 5, 2683-2686.

Ladd, C.C., and Lambe, T.W. (1963). The strength of undisturbed clay determined from undrained tests. *Laboratory Shear Testing of Soils*, ASTM Special Technical Publication No. 361, Philadelphia, 342-371.

Ladd, C.C. and Foote, R. (1974). A new design procedure for stability of soft clays. *Journal of the Geotechnical Engineering Division*, ASCE, Vol. 100, No. 7, 763-768.

Lings, M.L. and Greening, P.D. (2001). A novel bender/extender element for soil testing. *Geotechnique*, Vol. 51, No. 8, 713-717.

Lings, M.L., Pennington, D.S., and Nash, D.F.T. (2000). Anisotropic stiffness parameters and their measurement in a stiff natural clay. *Geotechnique*, Vol. 50, No. 2. 109-125.

Lunne, T., Berre, T., and Strandvik, S. (1997). Sample disturbance effects in soft low plasticity Norwegian clay. *Proceedings of the Symposium on Recent Developments in Soil and Pavement Mechanics*, Rio de Janeiro, 81-102.

Lunne, T., Robertson, P.K., and Powell, J.J.M. (1997). *Cone Penetration Testing in Geotechnical Practice*. London, E&FN Spon.

Mair, R.J., and Wood, D.M. (1987) *Pressuremeter Testing, Methods and Interpretation*, CIRIA Ground Engineering Report. London, Butterworths.

Matthews, M.C., Clayton, C.R.I., and Own, Y. (2000). The use of field geophysical techniques to determine geotechnical stiffness parameters. *Geotechnical Engineering, Proceedings of the Institution of Civil Engineers*, Vol. 143, January, 31-42.

Mayne, P.W. (2003). Personal communication, unpublished data.

Mayne, P. W., and Kulhawy, F. H. (1982). "Ko-Ocr Relationships in Soil." *Journal of the Geotechnical Engineering Division-Asce*, 108(6), 851-872.

Mesri, G.R,, Lo, D.O., and Feng, T-W. (1994). Settlement of embankments on soft clay. *Proceedings of Settlement '94, Vertical and Horizontal Deformations of Foundations and Embankments*, ASCE Geotechnical Special Publication No. 40, Vol. 1, 8-56.

Nishio, S. y., and Tamaoki, K. (1988). "Measurement of shear wave velocities in diluvial gravel samples under triaxial conditions." *Soils Found.*, 28(2), 35-48.

Peck, R. B., and Reed, W. C. (1954). "Engineering properties of Chicago subsoils." Engineering Experimental Station, Univ. of Illinois, Urbana, IL.

Pennington, D.S., Nash, D.F.T., and Lings, M.L. (1997). Anisotropy of G_0 shear stiffness in Gault Clay. *Geotechnique*, Vol. 47, No. 3, 391-398.

Phoon, K.K. and Kulhawy, F.H. (1999). Characterization of geotechnical variability. *Canadian Geotechnical Journal*, Vol. 36, 612-624.

Powrie, W., Pantelidou, H., and Stallebrass, S.E. (1998). Soil stiffness in stress paths relevant to diaphragm walls in clay. *Geotechnique*, Vol. 48, No. 4, 483-494.

Rampello, S., Viggiani, G.M.B., and Amorosi, A. (1997). Small-strain stiffness of reconstituted clay compressed along constant triaxial effective stress paths. *Geotechnique*, Vol. 47, No. 3, 475-489.

Rolo, R. (2003) "Anisotropic stress-strain-strength behaviour of brittle sediments," PhD thesis, University of London, Imperial College of Science, Technology and Medicine, London, England.

Santagata, M., Germaine, J. T., and Ladd, C. C. (2005). "Factors affecting the initial stiffness of cohesive soils." *J. Geotech. Geoenv. Eng.*, 131(4), 430-441.

Santagata, M. C., and Germaine, J. T. (2002). "Sampling disturbance effects in normally consolidated clays." *Journal of Geotechnical and Geoenvironmental Engineering*, 128(12), 997-1006.

Santagata, M.C. (1998). *Factors Affecting the Initial Stiffness and Stiffness Degradation of Cohesive Soils.* Ph.D. Dissertation, Massachusetts Institute of Technology, Cambridge.

Scholey, G.K., Frost, J.D., LoPresti, D.C., and Jamiolkowski, M. (1994). A review of instrumentation for measuring small strains during triaxial testing of soil specimens. *Geotechnical Testing Journal, ASTM*, Vol. 18, No. 2, 137-156.

Sheeran, D.E. and Krizek, R.J. (1971). Preparation of homogeneous soil samples by slurry consolidation. *Journal of Materials, ASTM*, Vol. 6, No. 2, 356-373.

Shibata, T., and Soelarno, D. S. (1978). "Stress-strain characteristics of clays under cyclic loading." *J. Japan. Soc. Civ. Engrs.*, 276, 101-110.

Shibuya, S. (2000). "Assessing structure of aged natural sedimentary clays." *Soils and Foundations*, 40(3), 1-16.

Shibuya, S., Hawang, S. C., and Mitachi, T. (1997). "Elastic shear modulus of soft clays from shear wave velocity." *Geotechnqiue*, 47(3), 593-601.

Shirley, D. J., and Hampton, L. D. (1978). "Shear-wave measurements in laboratory sediments." *J. Acoust. Soc. Am.*, 63(2), 607-613.

Skempton, A.W. and Sowa, V.A. (1963). The behavior of saturated clays during sampling and testing. *Geotechnique*, Vol. 13, No. 4, 269-290.

Smith, P.R., Jardine, R.J., and Hight, D.W. (1992). Yielding of Bothkennar clay. *Geotechnique*, Vol. 42, No. 2, 257-274.

Stallebrass, S. E., and Taylor, R.N. (1997). The development and evaluation of a constitutive model for the prediction of ground movements in overconsolidated clay. *Geotechnique*, Vol. 47, No. 2, 235-253.

Sully, J.P. and Campanella, R.G. (1995). Evaluation of in situ anisotropy from crosshole and downhole shear wave velocity measurements. *Geotechnique*, Vol. 45, No. 2, 267-282.

Sun, C.H. and Mok, Y.J. (2006) Development and application of a source for crosshole seismic method to determine body wave velocity with depth at multi-layered sites. *Journal of Korean Geotechnical Society*, Vol. 9, No. 3, 193-206

Takahasi, A., Fung, D. W. H., and Jardine, R. J. (2005). "Swelling effects on mechanical behaviour of natural London Clay." *Proc. 16th Int. Conf. Soil Mech. Geotech. Engng*, Osaka, Japan, 443-446.

Tamagnini, C. and Viggiani, G. (2002). On the incremental nonlinearity of soils. Part 1-theoretical aspects. *Rivista Italiano di Geotecnica*, 44-61.

Tanaka, H. (2000). Re-examination of established relations between index properties and soil parameters. *Keynote Lecture, Proceedings of the International Symposium on Coastal Geotechnical Engineering in Practice*, Yokohama, 2-24.

Tanaka, H., Sharma, P., Tsuchida, T., and Tanaka, M. (1996). "Comparative study on sample quality using several different types of samplers." *Soils and Foundations*, 36(2), 67-68.

Tatsuoka, F., Jardine, R.J., LoPresti, D., DiBenedetto, H., and Kodaka, T. (1997). Theme Lecture: Characterizing the pre-failure deformation properties of geomaterials. *Proceedings of the 14th International Conference on Soil Mechanics and Foundation Engineering*, Hamburg, 2129-2164.

Tatsuoka, F., and Shibuya, S. (1992). "Deformation characteristics of soils and rocks from field and laboratory tests." *Proc. 9th Asian Regional Conf. on Soil. Mech. Found. Eng.*, Vol. 2, Bangkok, 101-170.

Tatsuoka, F., Shibuya, S., and Kuwano, R. (2001). *Advanced laboratory stress-strain testing of geomaterials*, Exton, Lisse, Pa., Lisse.

Tavenas, F., Des Rosiers, J-P., Leroueil, S., La Rochelle, P., and Roy, M. (1979). The use of strain energy as a yield and creep criterion for lightly overconsolidated clays. *Geotechnique*, Vol. 29, No. 3, 285-303.

Terzaghi, K., Peck, R. B., and Mesri, G. (1996). *Soil Mechanics in Engineering Practice*, John wiley & Sons, Inc., New York, 43-44.

Timoshenko, S.J. and Goodier, J.N. (1970). *Theory of Elasticity, 3rd Ed*. New York, McGraw Hill Book Co.

Tu, X. (2007). "An Incrementally Non-linear Model for Clays with Directional Stiffness and a Small Strain Emphasis," PhD thesis, Northwestern University, Evanston, IL.

Viggiani, G. and Tamagnini, C. (1999). Hypoplasticity for modeling soil nonlinearity in excavation problems. *Proceedings of the Second International Symposium on Pre-failure Deformation Characteristics of Geomaterials*, Torino, Vol. 2, 581-588.

Viggiani, G., and Atkinson, J.H. (1995). Interpretation of bender element tests. *Geotechnique*, Vol. 45, No. 1, 149-154.

Viggiani, G., and Atkinson, J.H. (1995). Stiffness of fine-grained soil at very small strains. *Geotechnique*, Vol. 45, No. 2, 249-265.

Viggiani, G. (1992). "Small strain stiffness of fine grained soils," Ph.D. thesis, City University, London.

Whittle, A.J., DeGroot, D.J., Ladd, C.C., and Seah T-H. (1994). Model prediction of the anisotropic behavior of Boston blue clay. *Journal of Geotechnical Engineering*, ASCE, Vol. 120, No. 1, 199-224.

APPENDIX A

Paper accepted to the Geotechnical Testing Journal

Wanjei Cho[1], Terence P. Holman [2], Young-Hoon Jung [3], and Richard J. Finno[4]

Effects of swelling during saturation in triaxial tests in clays

---

Abstract: Effects of swelling during saturation in triaxial tests on compressible Chicago glacial clays are assessed from results of triaxial compression tests on block samples cut from excavations, thin wall Shelby tube samples and reconstituted specimens. The results are presented in terms of the stress-strain response during saturation, k_0 reconsolidation and shearing. Bender element tests were also performed to investigate the effects of swelling on the shear wave velocities during k_0 reconsolidation. Results showed that the swelling during saturation lowered the shear wave velocity, thereby inferring a change in the original structure of natural clay. Responses at strains less than 0.01% were most affected by the saturation-induced swelling. To minimize these changes, it is recommended that the measured residual stress is applied prior to saturating the soil. Based on these results, the saturation stage should be considered as much a part of a triaxial test as consolidation and shearing.

Keywords: Residual stress, Clay, Saturation, Swelling.

[1] Grad. Res. Ass't., Dept. of Civil and Env. Engrg., Northwestern Univ., Evanston, IL 60208
[2] Senior Engineer, Moretrench Geotec, Rockaway, NJ, 07866
[3] Post-doctoral fellow, Dept. of Civil and Env. Engrg., Northwestern Univ., Evanston, IL 60208
[4] Professor, Dept. of Civil and Env. Engrg., Northwestern Univ., Evanston, IL 60208 e-mail: r-finno@northwestern.edu

INTRODUCTION

An important guiding principle in laboratory experimental programs is to reproduce during an experiment both the initial in-situ stresses and the changes in stress expected in the field. The first portion of this principle is challenging to follow because of well-known sample disturbance effects (Clayton et al. 1992; Hight 2003). To minimize sample disturbance effects, one can use either the recompression technique (Bjerrum 1973) to bring the specimen to its in-situ state of stress or a normalized soil properties approach (Ladd and Foott 1974). Efforts in the past to quantify sample disturbance have focused primarily on quantifying the departure from an "ideal" recompression behavior. Andresen and Kolstad (1979) used the measured volumetric strain to the initial vertical effective stress, σ_{v0}', under the assumption that a "perfect sample" (Ladd and Lambe 1964) should develop little strain as it is recompressed to σ_{v0}'. Lunne et al. (1999) used a normalized change in void ratio in their categorization based upon subjective observations of sample quality. Other methods (Lacasse 1985; Terzaghi et al. 1996) have followed similar approaches. These methods assess sample quality in a global sense such that all sources of sample disturbance are included.

Most research on sample quality and sample disturbance effects focused on the disturbance due to sampling methods or during sampling procedures (Hight et al. 1992; Santagata and Germaine 2002; Tanaka et al. 1996). One less recognized contributor to sample disturbance in a triaxial test specimen is the swelling that occurs during the saturation phase of the experiment. While the detrimental effects of swelling on highly overconsolidated or plastic clays are well documented (e.g. Calabresi and Scarpelli 1985; Takahasi et al. 2005), these effects are generally considered inconsequential when testing lightly overconsolidated or fresh water clays. Furthermore, strains during saturation are rarely measured in a triaxial test, so their magnitudes

are generally unknown and their impacts on the subsequent stress-strain responses are not quantified.

This paper addresses the effects of swelling during saturation in triaxial tests on compressible Chicago glacial clays. These effects are assessed from results of triaxial compression tests on block samples cut from excavations, thin wall Shelby tube samples and reconstituted specimens. Experiments were conducted with on-specimen instrumentation in triaxial cells fitted with bender elements. Responses during saturation, k_0 reconsolidation and drained shearing are presented. Saturation-induced swelling resulted in lower quality specimens as reflected by sample quality designations, lower k_0 values and smaller stiffness at axial strains less than 0.01%. It is shown that saturating specimens at the measured residual effective stress can minimize the subsequent saturation-induced swelling.

EXPERIMENTAL PROGRAM

Soils

Block samples of compressible Chicago glacial clay were obtained at two sites. At the Robert H. Lurie Cancer Research Center in downtown Chicago (Finno and Roboski 2005), samples were hand-cut from the bottom of the excavation (Holman 2005). Geologically, the sample is from the Blodgett layer, a supraglacial till, characterized by its relatively wide range of water contents (Peck and Reed 1954). At the Ford Motor Company Engineering Design Center in Evanston (Blackburn 2005), samples were obtained from a waterlain paratill, characterized by its uniform texture. Both deposits have overconsolidation ratios less than 1.7. The geology of these compressible Chicago glacial clays is presented in more detail by Chung and Finno (1992).

Reconstituted samples were created using slurry consolidation techniques (Sheeran and Krizek 1971). Dried Chicago clay, consisting of trimmings and tested specimens from the block samples, was crushed and dry-sieved through a 0.425 mm sieve to remove coarse and medium sand particles, which leads to 10% loss of total weight of dried soil. The slurry with a water content of twice the liquid limit of the block samples, was placed into a large consolidometer (203.2 mm diameter) and loaded in several stages until the applied pressure reached the maximum past pressure previously determined from standard oedometer tests on the block samples.

Thin-walled tube samples were collected at each site from similar depths as the two block samples.

Figure 1 summarizes the void ratio-vertical effective stress curves obtained from a series of standard oedometer tests for the block and reconstituted samples. The index properties and the results of oedometer tests for each specimen are summarized in Table 1. All specimens are classified as low plasticity (CL) clay. The overconsolidation in the block samples arises in these clays from a post-depositional drop and subsequent rise of the water table and ageing effects (Finno and Chung 1992). Note that index properties and 1-D compression responses of the block and reconstituted samples are very similar.

Experimental Procedures

Testing was performed using a CKC e/p Cyclic Loader, an automated, feedback-controlled triaxial testing system (Chan 1981). This system was modified to accommodate the internal instrumentation, two axial and one radial on-specimen subminiature LVDTs, an internal load cell,

and three pairs of bender elements manufactured by GDS Instruments. This modification and application of internal measurement system eliminates the effects of seating errors and allows the investigation of saturation effects on both the small and large strain responses. The internal deformation measurements made by subminiature LVDTs mounted directly on the specimen were used to calculated axial and radial strain values. Each LVDT has a linear range of ±2.5 mm about the electrical zero and the gage length of 46 mm was used for the axial strain calculation. The radial caliper constructed of lightweight anodized aluminum is styled after that proposed by Bishop and Henkel (1957). This small strain measurement system is capable of resolving 0.002% of shear strain, and 0.015 kPa of axial stress. The axial load was measured using an internal load cell (submersible type, measurement range of ±4 kN) and corresponding axial stresses were calculated using the measured axial load and the instantaneous specimen area from the measured radial deformation. Cell and pore pressures were measured using external differential pressure transducers. The readings of the axial LVDTs were averaged to produce a single axial deformation response, assumed to be representative of the centerline deformations within the middle one-third of a specimen. The data obtained from two axial and one radial LVDTs, the pressure transducers, and the load cell were plotted against testing time, and then fit with a polynomial function to attain smoothed responses.

Bender element tests were conducted during the reconsolidation phase of each experiment. Axial bender elements were fixed to the pedestal and the top cap, whereas the two lateral elements were inserted into rubber grommets attached to diametrically opposite sides of the latex membrane. The two lateral bender elements are positioned so that horizontally and vertically polarized waves can be transmitted. The width and thickness of the bender element are 11 mm and 1 mm, respectively, and are inserted about 1 mm into the specimen. Bender element tests

typically were conducted using a single-pulse sinusoidal input signal with frequencies of 2 kHz for vertical and 10 kHz for lateral wave propagations. Peak-to-peak input voltage was set to 14 V. Tip-to-tip distance was used to calculate the wave travel distance. Travel times were computed after averaging 20 bender element shots using the cross correlation method (Viggiani and Atkinson 1995). Further details of the experimental equipment and testing procedure can be found in Holman (2005). Figure 2 shows a specimen with on-specimen gages (two axial and one radial LVDTs), a vertical bender element set embedded in top cap and bottom pedestal and two sets of horizontal bender elements attached on the sides of the specimen.

Table 2 summarizes the triaxial tests conducted for this work. Triaxial specimens with a nominal diameter of 71 mm and a height-to-diameter ratio between 2.1 and 2.3 were hand-trimmed from the block samples. After mounting a specimen in the triaxial cell, the residual stress, p_r', was measured by a pore-water pressure measurement technique (Ladd and Lambe 1964), as discussed later. The specimen then was saturated either at 10 kPa or at its residual stress. Each specimen subsequently was reconsolidated until the axial stress reached the in-situ vertical effective stress, subjected to a 36 hour drained creep cycle, and then sheared in drained triaxial compression. During shearing, the axial stress was applied at a rate of 1.2 kPa/hour to minimize accumulation of excess pore water pressure within the specimen.

Figure 3 illustrates the different stress paths between for the saturation at 10 kPa and for the saturation at the residual stress. In axisymmetric conditions, the mean normal effective stress, p', and the deviator stress, q, are defined as:

$$p' = (\sigma'_a + 2\sigma'_r)/3; \quad q = \sigma'_a - \sigma'_r \tag{1}$$

and the corresponding volumetric strain, ε_{vol}, shear strain, ε_{sh}, and secant shear modulus, G_{sec}

are given by:

$$\varepsilon_{vol} = \frac{1}{3}\left(\varepsilon_a + 2\varepsilon_r\right);\ \varepsilon_{sh} = \frac{2}{3}\left(\varepsilon_a - \varepsilon_r\right);\ G_{\sec} = \frac{q}{3\varepsilon_s} \quad (2)$$

where σ'_a, σ'_r, ε_a, and ε_r are axial effective stress, radial effective stress, axial strain and radial strain, respectively.

RESIDUAL EFFECTIVE STRESS

Residual effective stress, also called stored effective stress, initial mean effective stress, or effective stress after sampling, is the effective stress remaining in the soil sample after sampling, storage and handling (Hight 2003; Ladd and Lambe 1964; Skempton and Sowa 1963). This concept is rooted in the perfect sampling concept (Ladd and Lambe 1964) where there is no other disturbance, but that from the stress relief. The difference between the perfect sampling effective stress and the residual effective stress, p_r', is caused by disturbance rather than stress relief, implying that the residual stress can be used as a qualitative measure of sample disturbance (Baldi and Hight 1988; Ladd and Lambe 1964).

The residual effective stress, p_r', was evaluated prior to saturation via the response of excess pore-water pressure as isotropic stress increments are applied to a specimen with the drainage lines closed (Ladd and Lambe 1964; Skempton and Sowa 1963). Typically, the total confining stress, σ_c, was increased in 50 kPa increments until the total stress reached 300 kPa, and then σ_c was decreased in 100 kPa increments to 100 kPa. In each step, the pore-water pressure, u, was allowed to equilibrate and then was recorded. Pore pressures usually stabilized within 30 to 60 minutes in each loading step. Typical responses of u to σ_c are shown in Figure 4.

Using linear regression on this data, the matric suction within the soil sample, u_m, was taken as the value of u at σ_c=0. Following the general concept of effective stress, the residual effective stress, p_r', is defined as:

$$p_r' = -u_m \tag{3}$$

RESULTS OF EXPERIMENTS

Responses during Saturation

After measuring residual stress, the specimen was saturated by increasing both the cell and back pressures while maintaining the effective stress at either 10 kPa or p_r'. After saturation, the B values of all specimens were greater than 0.98.

Figure 5 compares the axial and radial strains of Ford block specimens saturated at 10 kPa and p_r'. As shown in Figure 5, negligible strains developed when a specimen was saturated at the residual stress, whereas the specimen saturated at 10 kPa swelled to produce 0.5% radial strain and 0.2% axial strain. This difference between axial and radial strains may be caused by an unexpected deviatoric stress of 2 to 4 kPa which was independently measured by the internal load cell, even though the external measurements consistently indicated no applied deviatoric stress. The same amount of deviatoric stress also occurred in specimens saturated at the residual stress; however, such 2 to 4 kPa stress had less impact on the behavior of these latter specimens saturated at residual stresses of 40 to 50 kPa.

The volumetric strain during saturation, ε_{sat}, is plotted against the ratio between the saturation stress and the residual stress, σ_{sat}'/p_r', in Figure 6. As can be seen in Figure 6, a higher value of σ_{sat}' produces a lower value of ε_{sat}. When σ_{sat}' is increased up to p_r', the volumetric

strain during saturation becomes negligible regardless of sample type. This trend is reasonable because the residual stress, p_r', in principle, represents a matric suction, or negative pore pressure, at zero total stress. In other words, if the (negative) matric suction is greater than the externally applied effective stress during saturation, swelling of the sample occurs as the suction pressure is reduced to the effective confining stress. Test results showed that when a specimen was saturated at the measured residual stress, the volumetric strain during saturation varied between 0.01% and 0.2%. When specimens were saturated at 10 kPa, volumetric strains during saturation ranged from 0.3% to 2.1%. Consequently, sample swelling during saturation can be minimized by applying an effective stress equal to the measured residual stress before adding water to the specimen in the saturation stage.

Responses during k_0-reconsolidation

During k_0 reconsolidation, each soil specimen reached a pre-determined vertical effective stress by applying vertical stress at a rate of 1.25 kPa/hr and adjusting the confining pressure to minimize the differences between the axial and volumetric strains. Figure 7 shows the strains developed in block samples during this portion of the test, as a function of σ_{sat}'. The axial and radial strains are the accumulated strains from the beginning of saturation. Even though the specimens were prepared from the same block sample, at the end of k_0 reconsolidation, the specimen saturated at 10 kPa developed axial strains of 1.2%, four times larger than those observed in the specimen saturated at the residual stress. Similar to the residual stress, the volumetric strain developed during k_0 reconsolidation can be a quantitative measure of sample quality (Andresen and Kolstad 1979). Terzaghi et al. (1996) defined five levels of specimen

quality based on observed volumetric strains during reconsolidation to σ_{v0}': Less than 1% of volumetric strains considered as "very good", between 1% and 2% as "desirable" and more than 2% as "marginally acceptable", and so on. Based on this specimen quality designation method, the specimen saturated at the residual stress can be considered as "very good" while the quality of the specimen saturated at 10 kPa is designated as "desirable" as a consequence of applying different effective stresses prior to saturation. It also is shown clearly that the axial swelling during saturation was recovered during k_0 consolidation.

The volumetric strains during saturation and k_0 reconsolidation are compared in Figure 8. Lurie block samples were saturated at 10 kPa, while all others were saturated at their residual stresses. Except for the Lurie block samples, the expected behavior–block samples are of higher quality than the tube samples—can be seen. For the Lurie block samples, which were saturated at 10 kPa, approximately 80% of the total volumetric strains in the reconsolidation stage can be regarded as the strains recovered from the swelling during saturation. If the sample quality is based only on the volumetric strains during reconsolidation, the apparent quality of the Lurie block samples is similar to those of the tube samples saturated at the residual stress.

Figure 9 shows the ratios of the residual stress to the in-situ vertical effective stress, p_r'/σ_{v0}', another measure of sample quality (Baldi and Hight 1988; Ladd and Lambe 1964), plotted against volumetric strains during reconsolidation. As the value of p_r'/σ_{v0}' increases, the volumetric strain decreases in both the Ford block and tube samples saturated at the residual effective stresses. Even though the Lurie and Ford block samples have similar values of residual effective stress, the Lurie block samples developed more volumetric strains during reconsolidation, clearly indicating that the sample quality of Lurie block samples deteriorated as a result of swelling during the saturation stage.

Figure 10 shows the effect of saturation in terms of stresses in the p′-q diagram. During the k_0 reconsolidation stage, the stress paths are almost parallel, so the stress state at the end of consolidation mainly depends on the initial value of p′. Furthermore, the specimens saturated at 10 kPa do not require as much confining pressure as the specimen saturated at the residual stress to maintain the zero radial strain condition throughout the k_0 reconsolidation.

Figure 11 shows the variation of k_0 values during k_0-reconsolidation. In the reconsolidation phase, the vertical stress gradually increased to the target value, while the radial stress was adjusted to minimize the additional radial strains. The k_0 value decreased from the initial value of 1 for an isotropic stress state until the ageing phase. The final k_0 values of the specimens saturated at 10 kPa are less than those of the specimens saturated at their residual stresses. In addition, the final k_0 values for the specimens saturated at the residual stress agree well with the k_0 value estimated by the expression for k_0: Mayne and Kulhawy (1982)

$$k_0 = (1 - \sin\phi')OCR^{\sin\phi'} \tag{4}$$

where ϕ' is the effective friction angle, and OCR is the overconsolidation ratio.

Figure 12 shows the results of the bender element tests during k_0 reconsolidation. The vertically propagated and horizontally polarized shear wave velocity, V_{vh}, is plotted against the mean normal effective stress. The Ford block samples saturated at their residual stresses exhibit higher values of V_{vh} than the other samples. However, the shear wave velocities of the Ford block samples saturated at 10 kPa are as low as those of the reconstituted samples. These data suggest that the swelling during saturation alters the original structure that transmits the elastic shear wave in the block sample, thus reducing shear wave velocities.

At the Ford site, seismic cone penetration tests (sCPT) were conducted to obtain in-situ

shear wave velocities. The value of V_{vh} for the Ford block samples saturated at their residual stresses corresponds to the values from sCPT while the shear wave velocities of other Ford samples (i.e. Ford reconstituted samples and Ford block samples saturated at 10 kPa) are about 15% less than the velocity from sCPT. This result also suggests that swelling during saturation changes the original structure of the block sample.

To further evaluate the effects of the swelling, additional bender element tests in two horizontal directions were conducted on Ford block samples. The horizontal bender elements measured the horizontally-propagated, horizontally-polarized wave velocity, V_{hh}, and the horizontally-propagated, vertically-polarized wave velocity, V_{hv}. Figure 13 compares three shear wave velocities for the two differently-saturated Ford block samples. For the specimen saturated at the residual stress, the trend of three different velocities, (i.e. $V_{hh} >> V_{hv} \cong V_{vh}$), agrees with the general pattern of directional velocities in a cross-anisotropic soil experiencing one-dimensional deposition (Pennington et al. 1997; Jovicic and Coop 1998). In contrast, the trend in the specimen saturated at 10 kPa, $V_{hv}>V_{vh}>V_{hh}$, is quite different from the trend in the specimen saturated at the residual stress. At the end of k_0 reconsolidation, the V_{hh} of the specimen saturated at 10 kPa is 30% lower than that saturated at its residual stress. This implies that the swelling affected the initial cross-anisotropic structure in the natural clay; The structural change apparently was largest in the horizontal direction, likely because of the larger radial strains that developed during saturation.

It is clearly shown that the response of a specimen saturated at 10 kPa is different than that saturated at p_r' in terms of k_0 and shear wave velocities, which suggests that there were changes in structure caused by swelling during saturation at 10 kPa. Furthermore, similarities between the observed responses of specimens saturated at 10 kPa and the reconstituted specimens suggest

that the swelling during saturation destructures natural clay to the point where the natural Chicago clay is very similar to the reconstituted specimens.

Stress-strain response during drained triaxial compression

After k_0 reconsolidation, all specimens were sheared in drained triaxial compression. Figure 14 presents the deviatoric stress-shear strain response during shearing. When comparing the Ford block and reconstituted specimens, both saturated at their residual stresses, the block samples exhibit stiffer stress-strain behavior and a more abrupt failure, which agrees with the commonly-observed differences in behavior between natural and reconstituted samples arising from the different ageing periods (Shibuya 2000).

Though the stress-strain responses shown in Figure 14 vary, all the specimens have very similar friction angles, as shown in Figure 15, stress path plots in a p′-q diagram. Previous research on soft Chicago glacial clays (Finno and Chung 1992) indicates that the friction angle of the Blodgett layer from which the Lurie samples were taken, ranges from 24 to 32 degrees and the friction angle of the Deerfield layer from which Ford samples were taken, ranges from 28 to 33 degrees. Because measured friction angles for all specimens vary from 25 to 28 degrees, it may be concluded that the swelling during saturation had little influence on the drained failure conditions.

Unlike the failure characteristics, swelling during saturation clearly affects the stress-strain behavior at the small-strain level. Figure 16 shows the deviatoric stress-shear strain responses during shearing for strains as high as 0.1%. For the Ford samples, the block specimens saturated at their residual stresses are stiffer than both the reconstituted specimen saturated at the residual

stress and the block specimen saturated at 10 kPa. Little difference is observed between the responses of the latter specimens. The Lurie block specimen saturated at 10 kPa exhibits similar stress-strain response of the Lurie reconstituted specimen saturated at the residual stress.

Figure 17 emphasizes the differences in the initial portions of the stress-strain responses. While overall patterns of stiffness degradations are similar, the initial stiffness of Ford block specimen saturated at 10 kPa is 30% smaller than the average initial stiffness of the two block specimens saturated at the residual stress. The initial stiffness of the Ford reconstituted specimen saturated at the residual stress also is larger than that of Ford block specimen saturated at 10 kPa. The stiffness degradation of Lurie block specimen saturated at 10 kPa is practically identical to that of Lurie reconstituted sample saturated at the residual stress. The swelling during saturation reduced the initial stiffness of the block specimens, and thus presumably degraded the original structure of the block specimens.

In summary, swelling during saturation leads to damage of the soil structure in natural Chicago clay specimens based on comparisons between responses of specimens saturated at the residual stresses and at 10 kPa. This damage is inferred from (i) the sample quality differences based on the magnitude of volumetric strain during k_0 reconsolidation, (ii) the lower k_0 values in specimens saturated at 10 kPa, (iii) the lower shear wave velocities, V_{vh} and V_{hh} in specimens saturated at 10 kPa, and (v) the softer responses at small strains in specimens saturated at 10 kPa.

CONCLUSIONS

The effects of swelling during saturation on the stress-strain response of fresh-water, compressible Chicago glacial clays have been investigated through drained triaxial compression tests performed on undisturbed block, reconstituted and thin-wall tube samples. The mechanical

responses of the clay were measured via on-specimen measurement gauges and bender element sets.

Specimens saturated at 10 kPa swelled significantly during saturation compared to those saturated at their residual stress. During k_0 reconsolidation, volumetric strains of the specimens saturated at 10 kPa are larger than those of specimens saturated at the residual stress. Results of bender element tests indicate that the swelling resulted in lower shear wave velocity (V_{vh}) when specimens were saturated at an effective stress well below the residual stress, regardless of whether the specimen was block or reconstituted. Block specimens saturated at the residual stress exhibit similar shear wave velocities to those measured by sCPT in the field. The results of horizontal bender element tests show that the original cross-anisotropic structure transmitting directional elastic shear waves in the natural clays was altered by the swelling during saturation. Swelling during saturation reduced the shear stiffness in the small strain range, but had little effect on the friction angles.

To minimize swelling during saturation and subsequent alteration of soil structure in natural clays, the saturation stage should be considered as much a part of a triaxial test as consolidation and shearing. It is recommended that the residual stress be measured before saturating a specimen and the measured residual stress be used as the effective stress during saturation. In this way, possible detrimental effects of swelling during saturation can be minimized.

REFERENCES

Andresen, A., and Kolstad, P. (1979). "The NGI 54 mm sampler for undisturbed sampling of clays and representative sampling of coarser materials." *Norwegian Geotechnical Institute Publication*, 130, 13-21.

Baldi, G., and Hight, D. W. (1988). "State-of-the-art: A reevaluation of conventional triaxial test methods." *Advanced triaxial testing of soil and rock, ASTM STP*, 977, 219-263.

Bishop, A. W., and Henkel, D. J. (1957). *The measurement of soil properties in the triaxial test*, E. Arnold, London, 72-74.

Bjerrum, L. (1973). "Problems of Soil Mechanics and Construction on Soft Clay: State of Art Report." *Proceedings of the 8th Internation Conference on Soil Mechanics and Foundation Engineering*, Moscow, 173-184.

Blackburn, J. T. (2005). "Automated sensing and three-dimensional analysis of internally braced excavations," Ph.D thesis, Northwestern University, Evanston.

Calabresi, G., and Scarpelli, G. (1985). "Effects of swelling caused by unloading in over-consolidated clays." *Proc. 11th Int. Conf. Soil Mech. Found. Engng*, San Francisco, 411-414.

Chan, C. K. (1981). "An electropneumatic cyclic loading system." *Geotechnical Testing Journal*, 4(4), 183-187.

Chung, C. K., and Finno, R. J. (1992). "Influence of Depositional Processes on the Geotechnical Parameters of Chicago Glacial Clays." *Engineering Geology*, 32(4), 225-242.

Clayton, C. R. I., Hight, D. W., and Hopper, R. J. (1992). "Progressive Destructuring of Bothkennar Clay - Implications for Sampling and Reconsolidation Procedures." *Geotechnique*, 42(2), 219-239.

Finno, R. J., and Chung, C. K. (1992). "Stress-Strain-Strength Responses of Compressible Chicago Glacial Clays." *Journal of Geotechnical Engineering-Asce*, 118(10), 1607-1625.

Finno, R. J., and Roboski, J. F. (2005). "Three-dimensional responses of a tied-back excavation through clay." *Journal of Geotechnical and Geoenvironmental Engineering*, 131(3), 273-282.

Hight, D. W. (2003). "Sampling effects in soft clay: An update on Ladd and Lambe (1963)." *Soil*

Behavior And Soft Ground Construction, Cambridge, MA, United States, 86-121.

Hight, D. W., Boese, R., Butcher, A. P., Clayton, C. R. I., and Smith, P. R. (1992). "Disturbance of the Bothkennar Clay Prior to Laboratory Testing." *Geotechnique*, 42(2), 199-217.

Holman, T. P. (2005). "Small strain behavior of compressible Chicago glacial clay," PhD thesis, Northwestern University, Evanston, IL.

Jovicic, V., and Coop, M. R. (1998). "The measurement of stiffness anisotropy in clays with bender element tests in the triaxial apparatus." *Geotechnical Testing Journal*, 21(1), 3-10.

Lacasse, S. (1985). "Testing of special soils: ocean floor soils." *Proc. 11th Int. Conf. Soil Mech. Found. Engng*, San Francisco, 5, 2683-2686.

Ladd, C. C., and Foott, R. (1974). "New design procedure for stability of soft clays." *Journal of Geotechnical Engineering-Asce*, 100(GT7), 763-786.

Ladd, C. C., and Lambe, T. W. (1964). "Strength of "undisturbed" clay determined from undrained tests." American Society for Testing and Materials (ASTM), Philadelphia, PA, United States. (361), 342-371.

Lunne, T., Berre, T., and Strandvik, S. (1999). "Sample disturbance effects in soft low plastic Norwegian clay." *Norges Geotekniske Institutt/Norwegian Geotechnical Institute*(204), 81-102.

Mayne, P. W., and Kulhawy, F. H. (1982). "Ko-Ocr Relationships in Soil." *Journal of the Geotechnical Engineering Division-Asce*, 108(6), 851-872.

Peck, R. B., and Reed, W. C. (1954). "Engineering properties of Chicago subsoils." Engineering Experimental Station, Univ. of Illinois, Urbana, IL.

Pennington, D. S., Nash, D. F. T., and Lings, M. L. (1997). "Anisotropy of G_0 shear stiffness in Gault Clay." *Geotechnique*, 47(3), 391-398.

Santagata, M. C., and Germaine, J. T. (2002). "Sampling disturbance effects in normally consolidated clays." *Journal of Geotechnical and Geoenvironmental Engineering*, 128(12), 997-1006.

Sheeran, D. E., and Krizek, R. J. (1971). "Preparation of Homogeneous Soil Samples by Slurry Consolidation." *Journal of Materials-ASTM*, 6(2), 356-373.

Shibuya, S. (2000). "Assessing structure of aged natural sedimentary clays." *Soils and Foundations*, 40(3), 1-16.

Skempton, A. W., and Sowa, V. A. (1963). "The behavior of saturated clays during sampling and testing." *Geotechnique*, 13(4), 269-290.

Takahasi, A., Fung, D. W. H., and Jardine, R. J. (2005). "Swelling effects on mechanical behaviour of natural London Clay." *Proc. 16th Int. Conf. Soil Mech. Geotech. Engng*, Osaka, Japan, 443-446.

Tanaka, H., Sharma, P., Tsuchida, T., and Tanaka, M. (1996). "Comparative study on sample quality using several different types of samplers." *Soils and Foundations*, 36(2), 67-68.

Terzaghi, K., Peck, R. B., and Mesri, G. (1996). *Soil Mechanics in Engineering Practice*, John wiley & Sons, Inc., New York, 43-44.

Viggiani, G., and Atkinson, J. H. (1995). "Stiffness of fine-grained soil at very small strains." *Geotechnique*, 45(2), 249-265.

List of Tables

Table 1 Summary of index properties and consolidation characteristics

	Lurie Block	Lurie Reconst.	Ford Block	Ford Reconst.	Tube 1 (Lurie)	Tube2 (Ford)
Natural Water Content (%)	28.7-29.7	29-31.2	24.6-25.2	26-26.5	25.6-27.8	21.1-24.5
Liquid Limit (%)	35-37.6	34	29.5-31	38-41	33	28.8-31.0
Plasticity Index (%)	17.6-19.2	17	14.2-16.4	18-20	16.2	13.2-15.2
Specific Gravity	2.71-2.73	2.72	2.71-2.72	2.71-2.72	2.72	2.72
Max. Past Pressure (kPa)	180-190	165-175	220-230	210-220	150	190
OCR	1.4	NA	1.7	NA	1.4	1.5
Compression Index, C_c	0.25	0.27	0.2	0.21	0.26	0.18
Recompression Index, C_r	0.04	0.05	0.028	0.035	0.05	0.026
Coefficient of consolidation ($\times 10^{-7}$ m^2/s)	0.72-1.92	0.86-2.12	0.75-1.90	0.92-1.87	0.76-2.00	0.63-1.93

Table 2 Summary of triaxial tests

Test	Sample Type	p_r' (kPa)	σ'_{sat} (kPa)	$\varepsilon_{vol(sat)}$ (%)	$\varepsilon_{vol(k0)}$ (%)
Ford Block 1	Block	51.2	50.5	-0.09	0.41
Ford Block 2	Block	52.1	51.2	-0.15	0.38
Ford Block 2	Block	47.4	10.1	-1.23	1.35
Lurie Block 1	Block	64.7	10.3	-2.70	3.58
Ford Reconstituted	Reconstituted	49.3	49.9	-0.06	0.56
Lurie Reconstituted	Reconstituted	15.8	16.1	-0.08	1.65
Tube 1 (Lurie)	Tube	18.1	17.9	0.00	1.82
Tube 2 (Ford)	Tube	20.3	19.8	-0.01	1.66

List of Figures

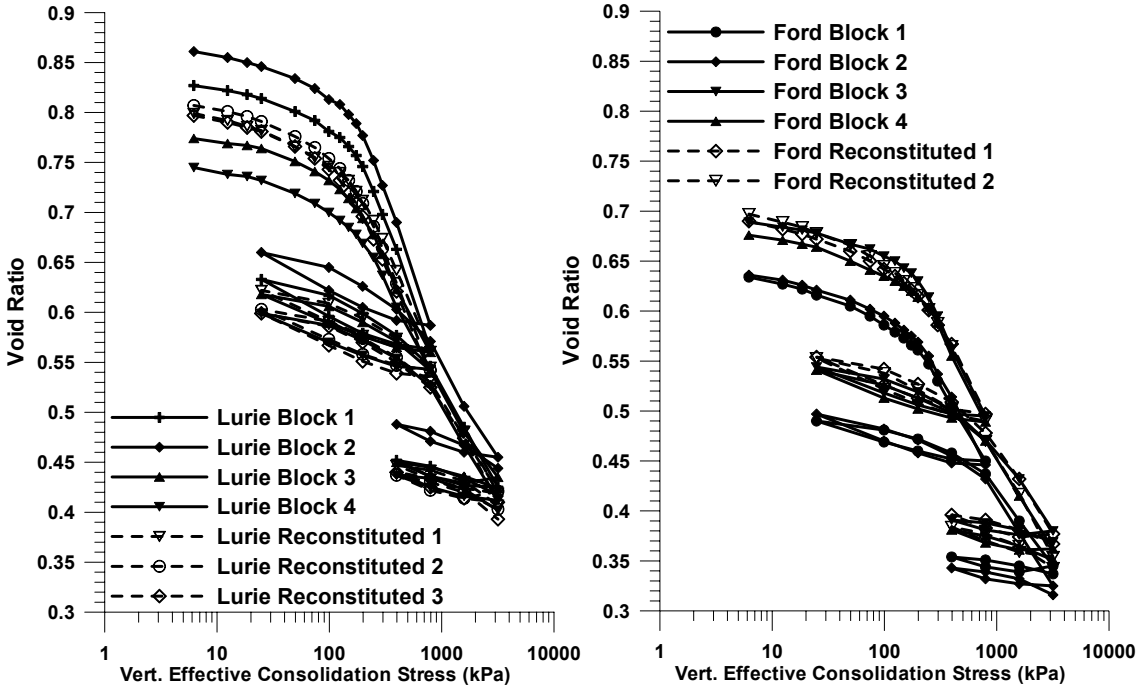

Fig. 1 Consolidation characteristics of natural block and reconstituted samples

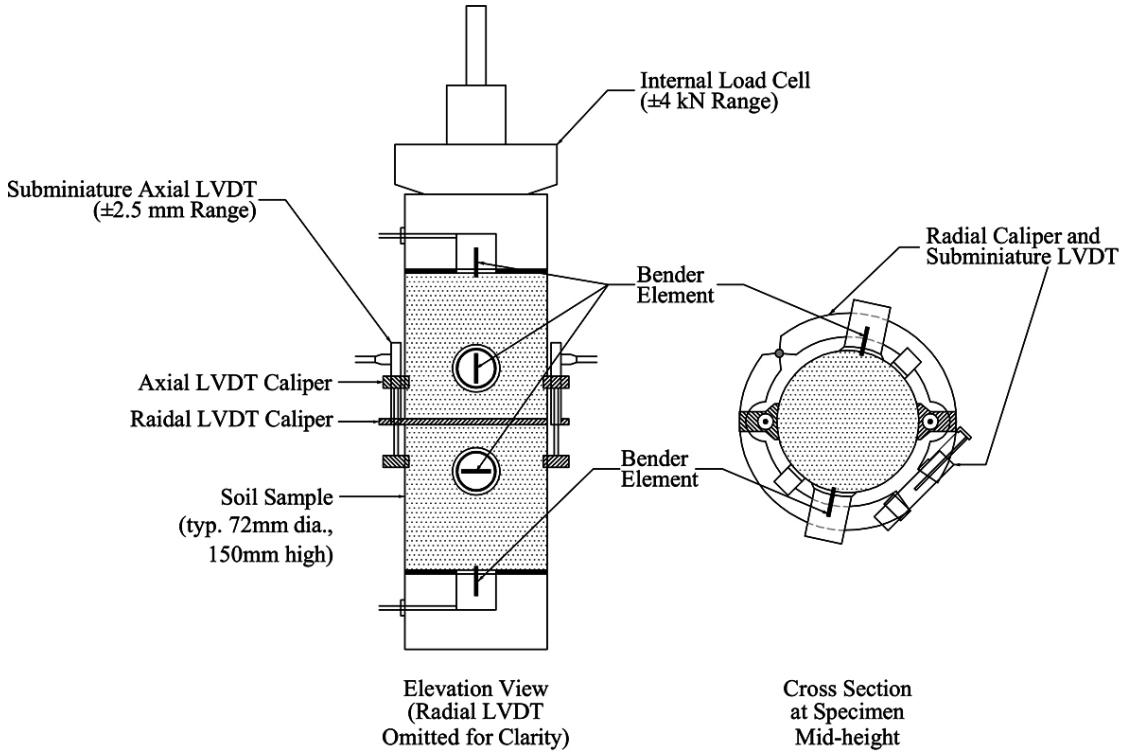

Fig. 2 Schematic diagrams of small strain instrumentation and mounting on typical triaxial specimen

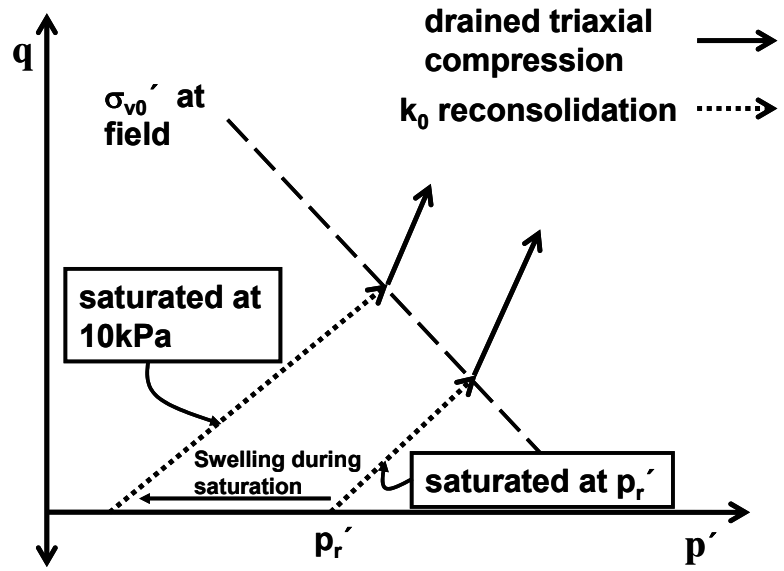

Fig. 3 Triaxial testing plan in p′-q space

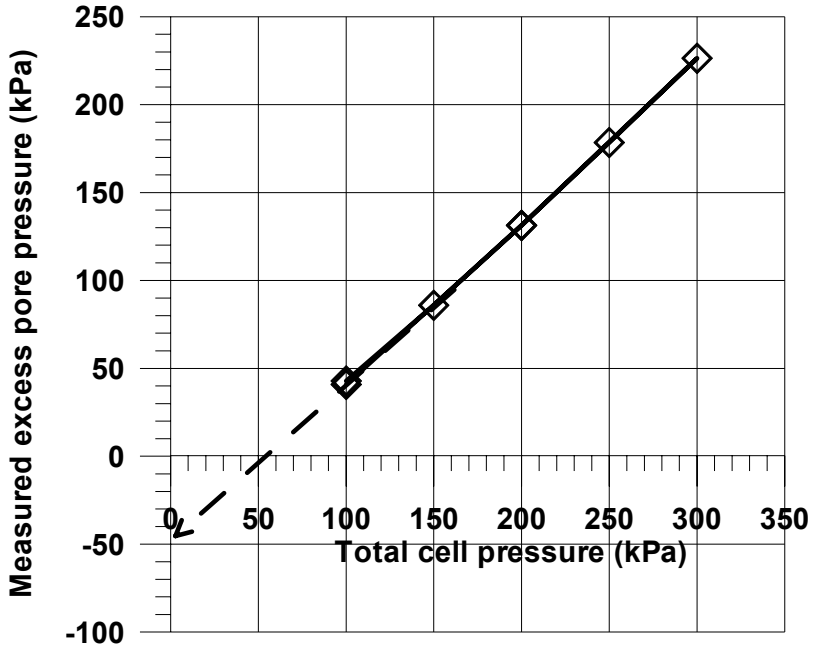

Fig. 4 Linear regression method to determine residual effective stress

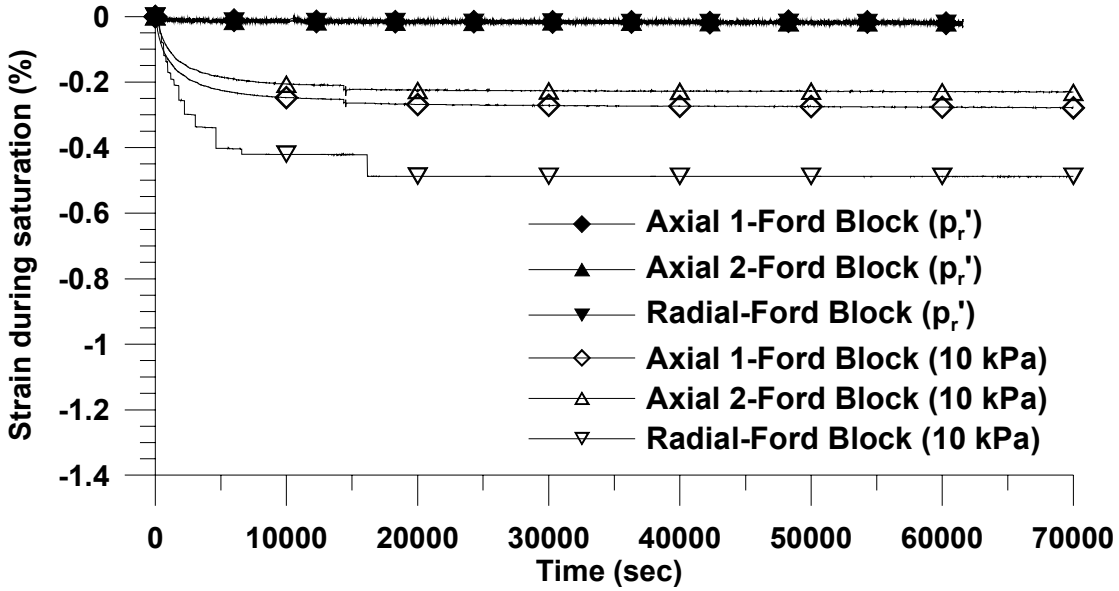

Fig. 5 Axial and radial strain during saturation

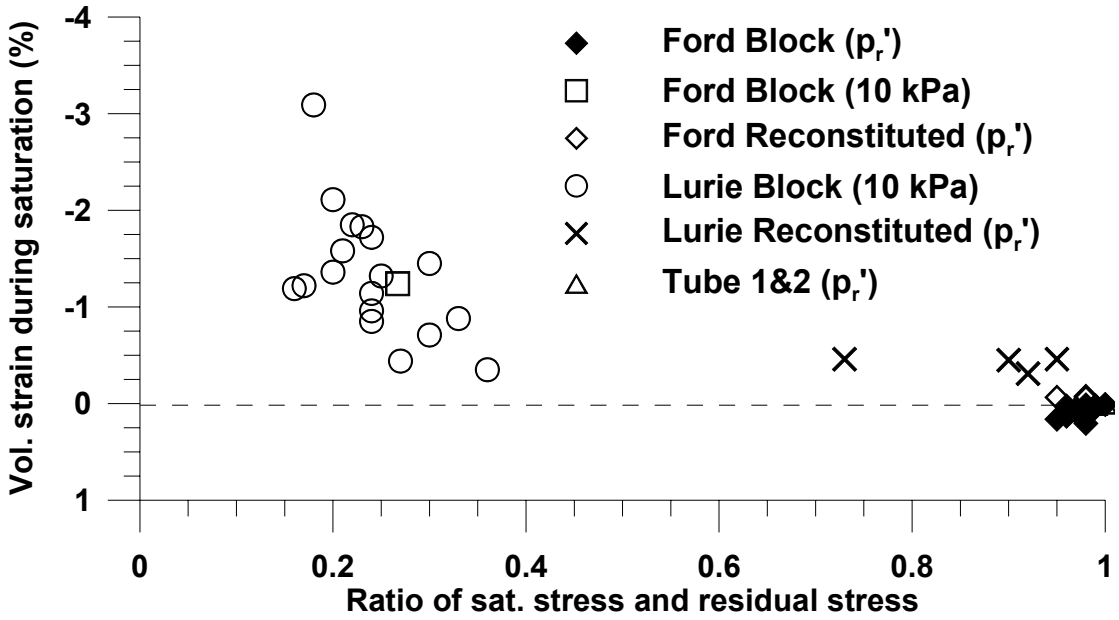

Fig. 6 Relationship between ratio σ_{sat}'/p_r' and vol. strain during saturation

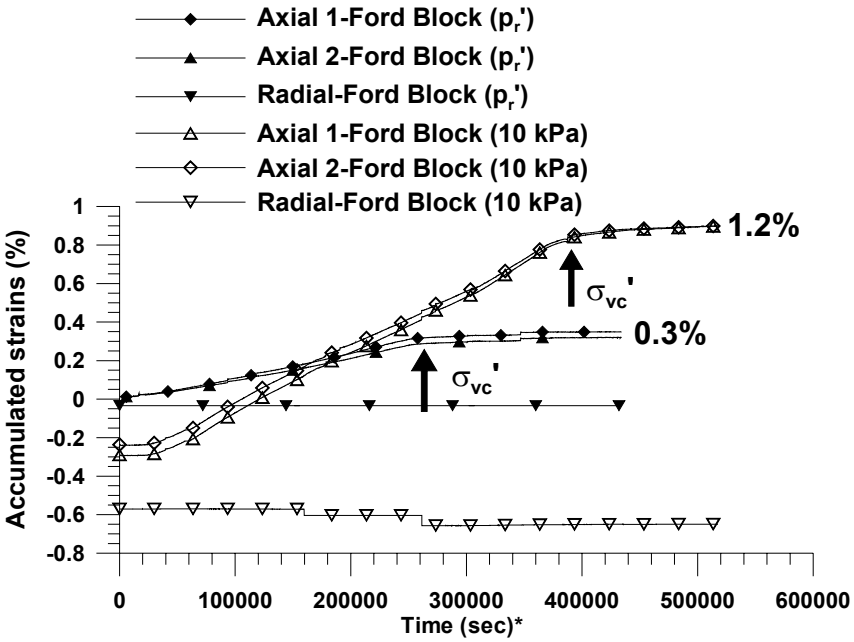

Fig. 7 Axial and radial strain during k_0 reconsolidation

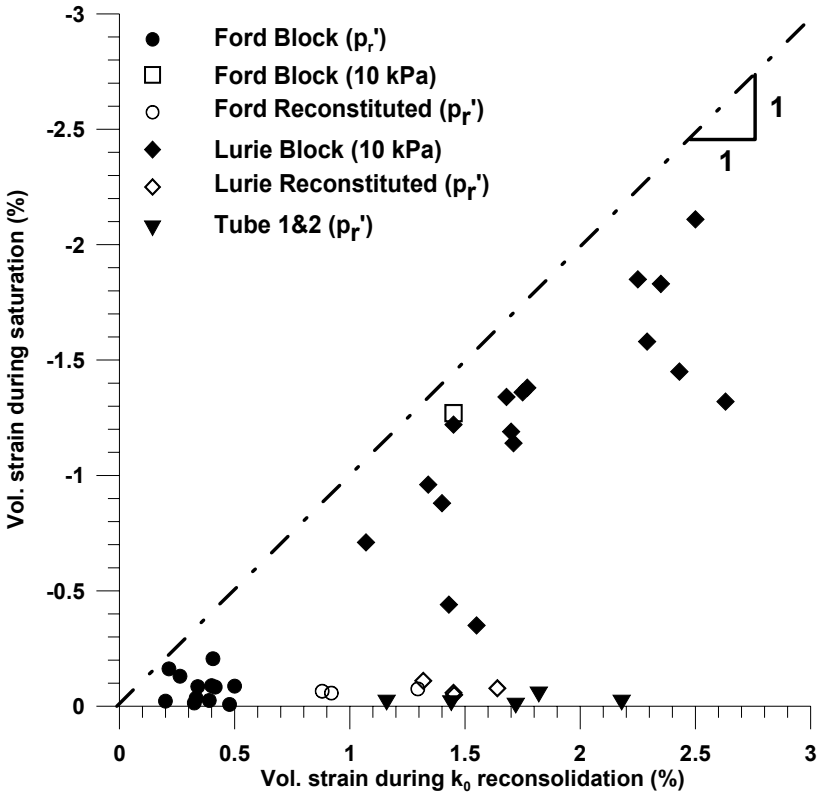

Fig. 8 Relationship between vol. strain during saturation and k_0 reconsolidation

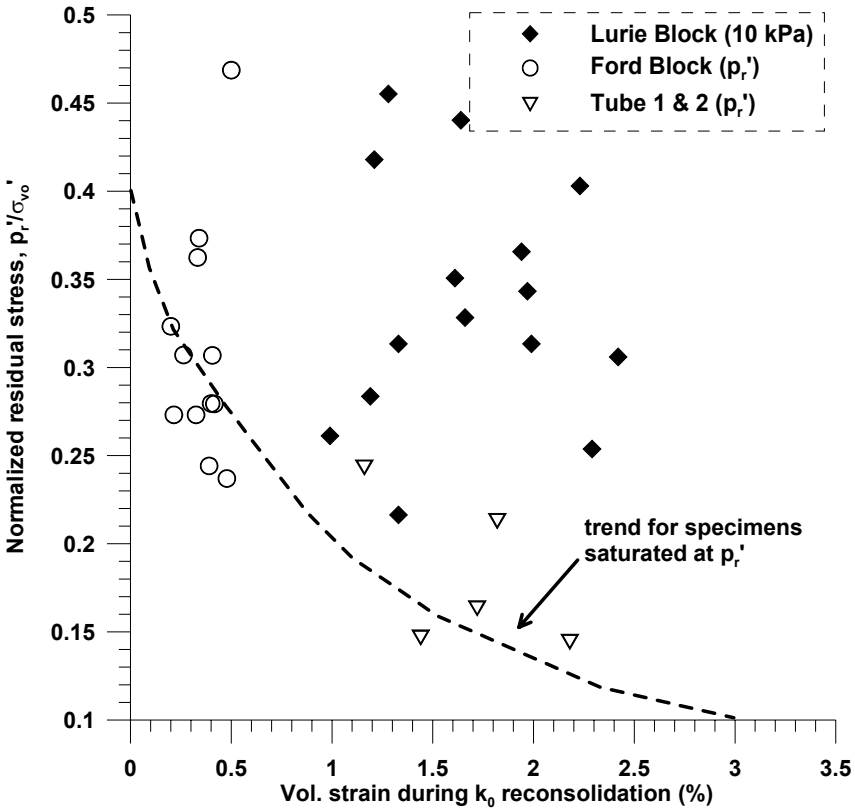

Fig. 9 Relationship between normalized residual stress, p_r'/σ_{v0}' and vol. strain during k_0 reconsolidation

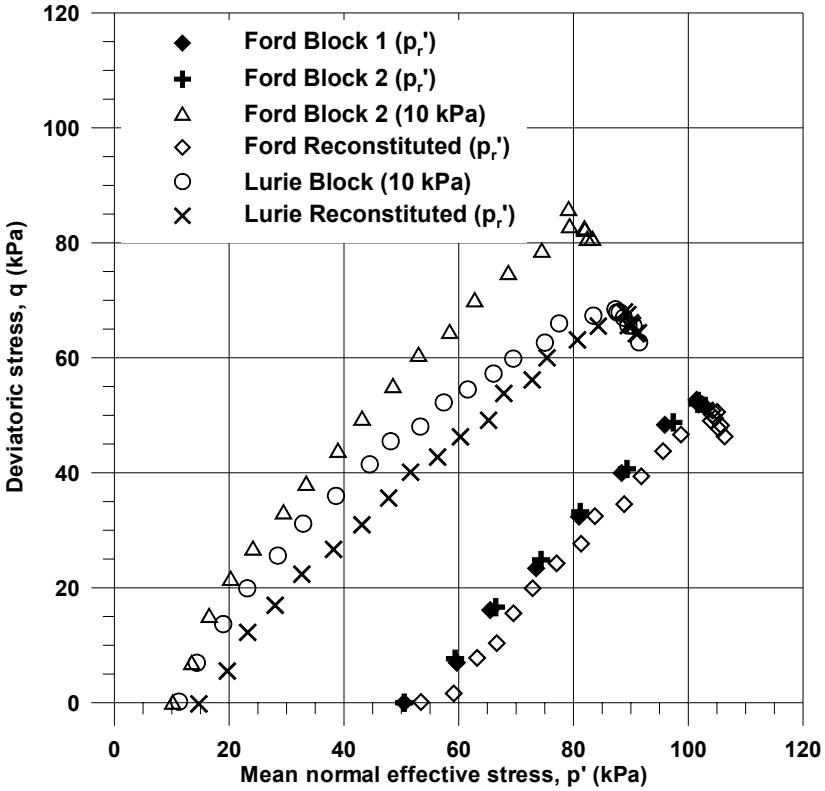

Fig. 10 Stress paths during k_0 reconsolidation

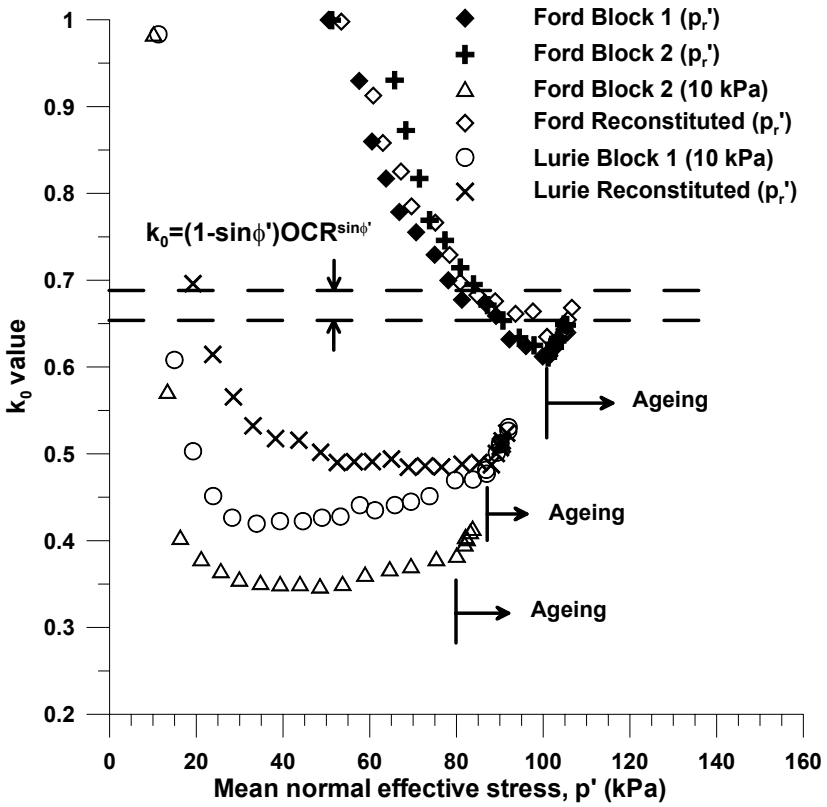

Fig. 11 Variation of k_0 value during k_0 reconsolidation

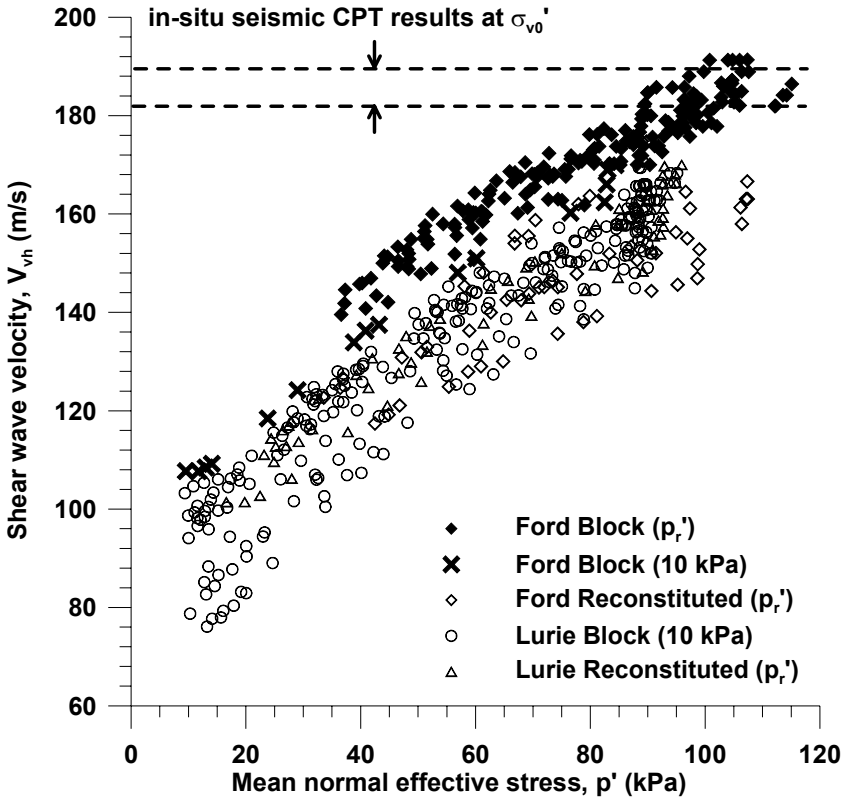

Fig. 12 Bender element test results (V_{vh})

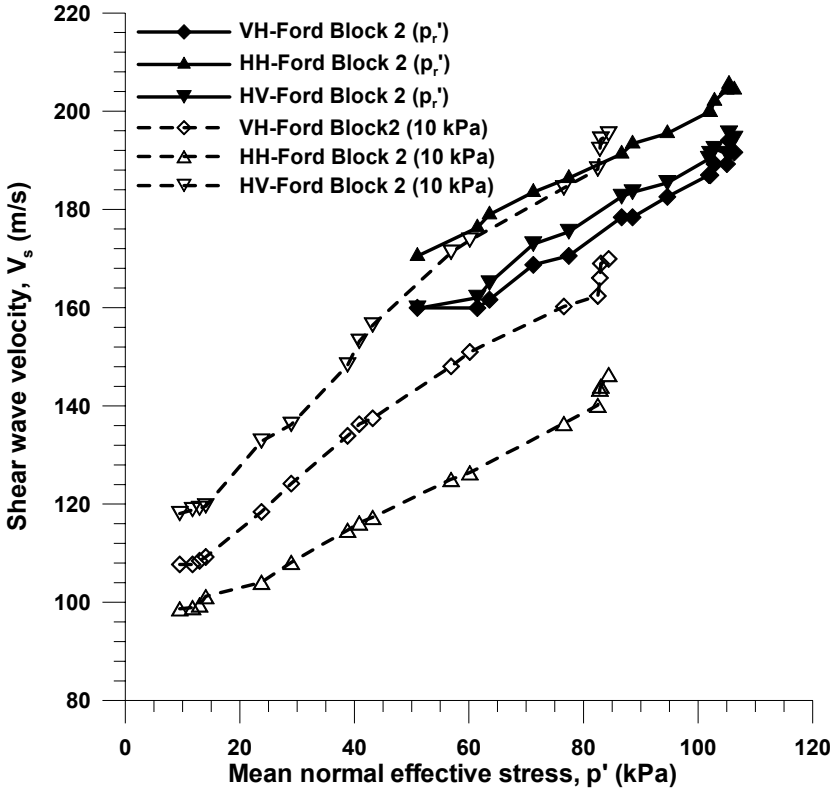

Fig. 13 Bender element test results (V_{hh}, V_{hv} and V_{vh})

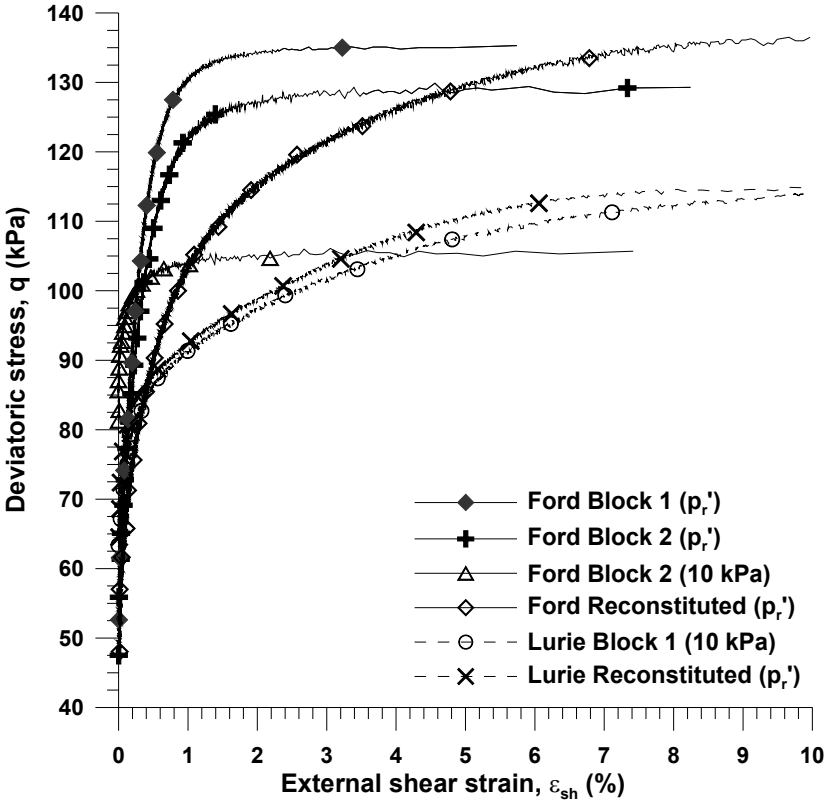

Fig. 14 Stress-strain data from external measurement system

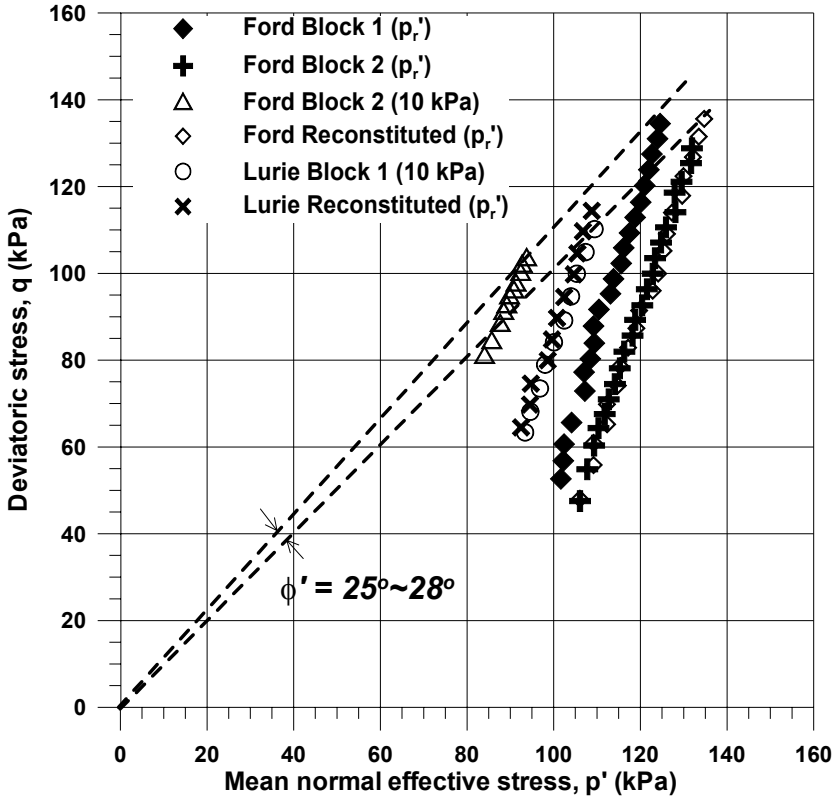

Fig. 15 Triaxial compression stress paths and measured friction angles

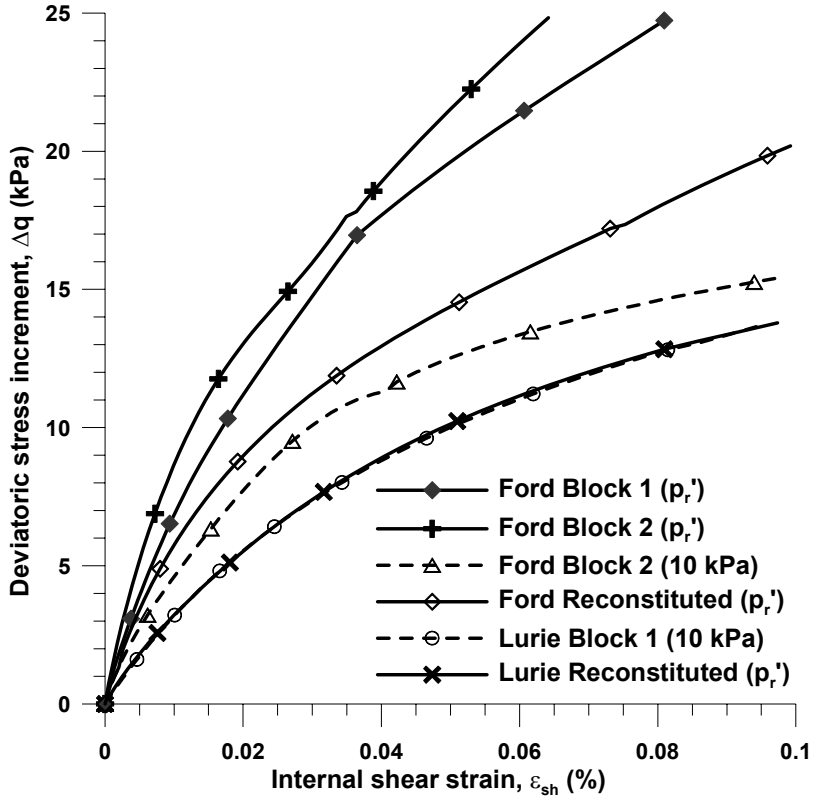

Fig. 16 Stress-strain data from internal measurement system

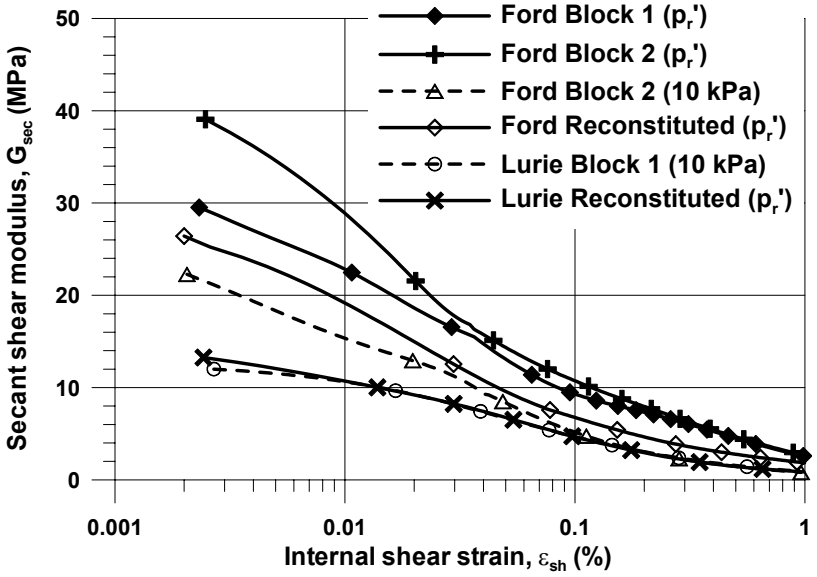

Fig. 17 Secant shear modulus degradation curves